Development of Doped Microcrystalline Silicon Oxide and its Application to Thin-Film Silicon Solar Cells

Ontwikkeling van gedoteerd microkristallijn siliciumoxide en de toepassing in dunne film zonnecellen

(met een samenvatting in het Nederlands)

Proefschrift

ter verkrijging van de graad van doctor aan de Universiteit Utrecht op gezag van de rector magnificus, prof.dr. G.J. van der Zwaan, involge het besluit van het college voor promoties in het openbaar te verdedigen op woensdag 20 mei 2015 des middags te 2.30 uur

door

Andreas Lambertz

geboren op 6 december 1968 te Opladen, Duitsland

Promotor: Prof.dr. R.E.I. Schropp

Copromotor: Dr. F. Finger

Table of Contents

Chapter 1

Introduction

1.1   The growth of photovoltaic system installations

The annual installation of photovoltaic (PV) systems has grown dramatically worldwide, from 0.6 GWp/y in 2003 to over 38 GWp/y in 2013 [1]. The increase in PV installations between 2003 and 2013 (Figure 1.1) corresponds to an annual growth rate of approximately 50%, as indicated by the dashed trend line. Assuming the same growth rate for the next 10 years, the amount of annually installed PV systems will reach 1.9 TWp/y.
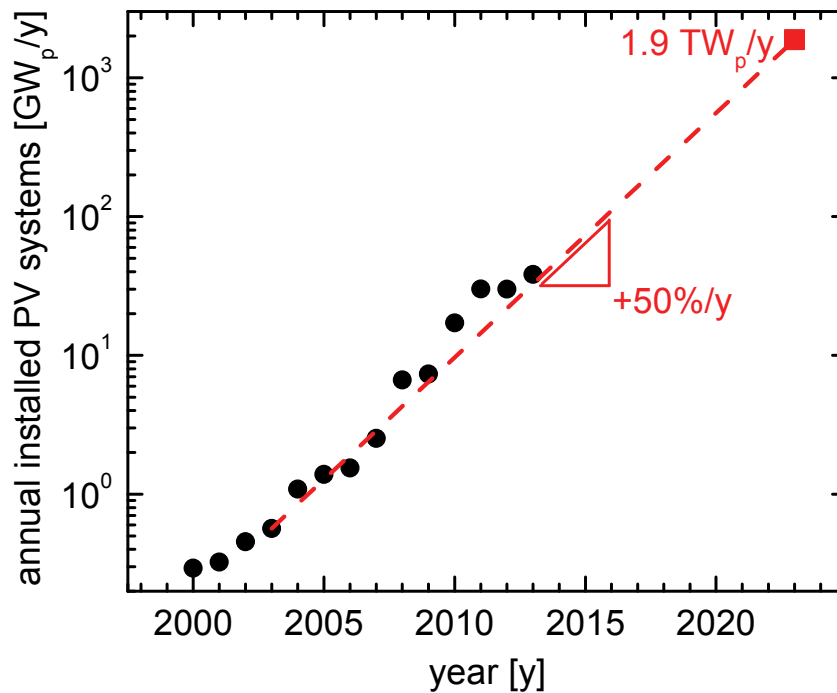
Figure 1.1: The annual installation of photovoltaic (PV) systems from 2000 to 2013 [1]. The trend line indicates an annual growth rate of 50%.

Looking at this growth from the demand side, to generate a substantial share, e.g. >10%, of the global electricity production in the next decade, a growth of 50%/y for PV system installations is necessary [1]. For this growth to continue as predicted, a sustainable PV technology is needed.

Thin-film silicon solar modules have twofold shorter energy pay-back times (EPBT) as compare to wafer based crystalline solar modules and use materials that are abundant and non-toxic [2,3]. The shorter EPBT will become more relevant when the annual installation of PV systems reaches the TWp/y range. In order to produce the required 1.9 TWp/y of currently available crystalline silicon solar modules and assuming an EPBT=1.6 y and a Yield=1600 kWh/(kWp×y), the PV industry would require approximately 4864 TWh/y, which is for example about 8 times the current German annual electricity consumption (600 TWh/y).

In addition to the beneficial shorter energy pay-back time the thin-film silicon solar module equipment technology was being pushed by flat panel display technology because it uses the same kind of production equipment [4].

1.2   Basics of a-Si:H/μc-Si:H tandem solar cells

Figure 1.2 a) shows a thin-film silicon tandem solar cell, which is a stack of two solar cells. This is the state-of-the-art device for current thin-film silicon solar module production technology. The substrate for the device is glass, which is coated with a rough transparent conducting oxide (TCO). The top cell has a hydrogenated amorphous silicon (a-Si:H) intrinsic absorber layer and the bottom cell has a hydrogenated microcrystalline silicon (μc-Si:H) intrinsic absorber layer. The a-Si:H top cell and the μc-Si:H bottom cell consist of a p-i-n structure. Doped thin-film silicon layers have, compared to crystalline silicon, a poor mobility lifetime product. In contrast, intrinsic thin-film silicon layers have a better mobility lifetime product. Therefore, intrinsic layers are used as the absorber layer for the top- and bottom solar cells. However, the p- and n-layers are needed to build up the electric field, which collects the electrons and holes generated in the respective intrinsic absorber layers. The TCO and the back contact are needed to conduct the current to the leads of the solar cell.
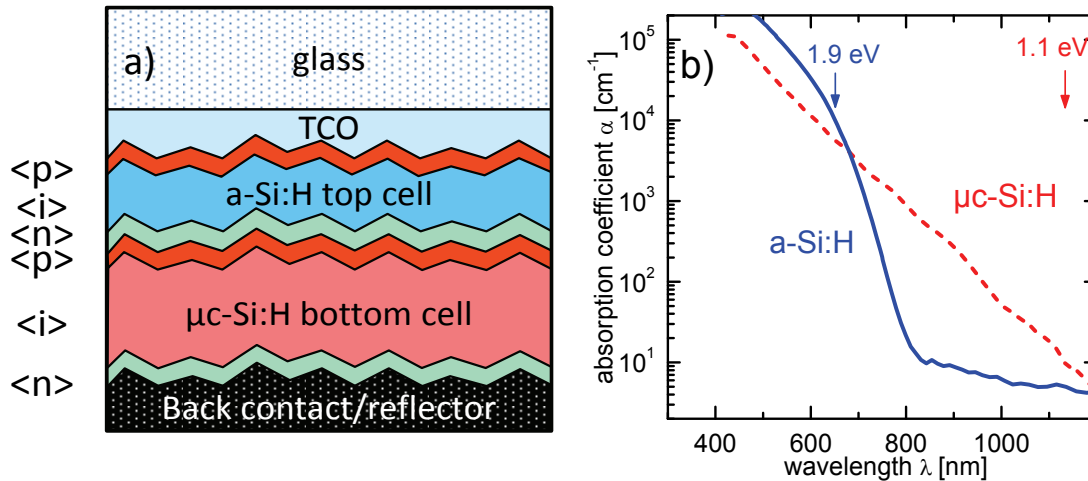
Figure 1.2: a) A schematic of an a-Si:H/µc-Si:H tandem solar cell. The substrate of the device includes the glass and the transparent conducting oxide (TCO). An a-Si:H top solar cell, a µc-Si:H bottom solar cell, and a back contact/reflector are stacked on the TCO. b) The absorption coefficient α versus the wavelength λ of a µc-Si:H i-layer and an a-Si:H i-layer used as absorber layer in the sketched a-Si:H/µc-Si:H tandem solar cell.

Figure 1.2 b) shows an absorption coefficient spectrum for hydrogenated amorphous silicon (a-Si:H) and hydrogenated microcrystalline silicon (µc-Si:H). The a-Si:H top cell absorber layer has an optical band gap of 1.9 eV (≈ 650 nm) and only weakly absorbs the long wavelength segment ($\lambda > 650$ nm) of the solar spectrum. To utilize the long wavelength segment of the solar spectrum ($\lambda > 650$ nm), a bottom cell that has a µc-Si:H absorber layer with an optical band gap of 1.1 eV (Figure 1.2 b) is attached to the a-Si:H top cell [5-8]. The combination of these two optical band gaps corresponds, theoretically, to the almost ideal combination for tandem solar cells [9]. The thickness of absorber layers is typically kept below 340 nm, for the a-Si:H top cell, and below 3 µm for the µc-Si:H bottom cell, because of their, compared to e.g. crystalline silicon, low electron- and hole-mobility lifetime product. The penetration depth of the light is much greater than for typical absorber layer thicknesses; for example, approx. 1 µm in a-Si:H at $\lambda = 650$ nm and approx. 40 µm in µc-Si:H at $\lambda = 900$ nm. Therefore, an increase of the optical path length within the absorber layers is required. The surface of the TCO is rough, as indicated in (Figure 1.2 a). The rough TCO/silicon and the silicon/back reflector interface leads to light scattering and internal reflection. Some of the light can thus be trapped within the solar cell until it is absorbed. This leads to an increase of the optical path length and enables an intrinsic absorber layer thickness that is smaller than the penetration depth.
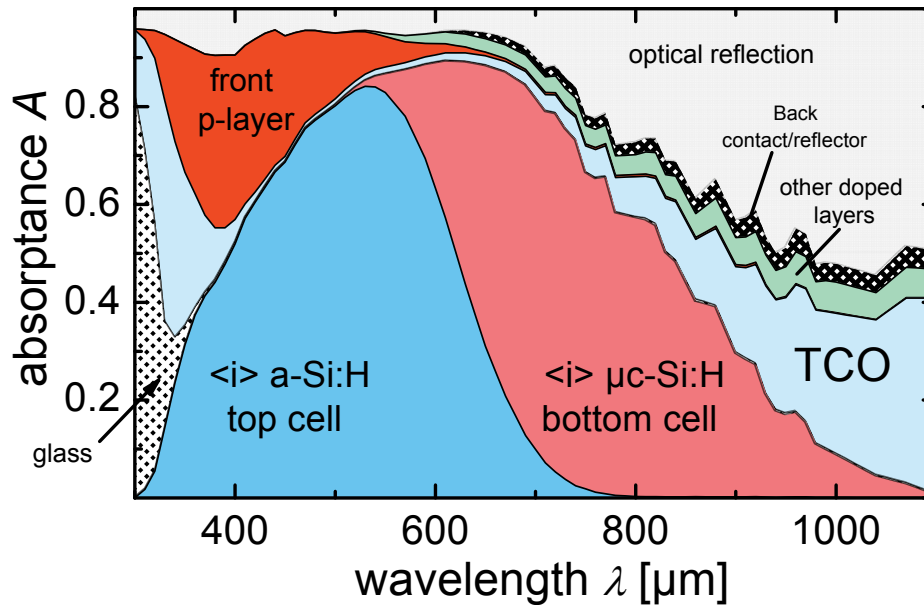
Figure 1.3: The simulated absorptance A versus the wavelength λ of the layers in a typical a-Si:H/µc-Si:H solar cell [10] as shown in Figure 1.2 a).

The next step is to examine the absorptance in the individual layers in more detail. Figure 1.3 shows the simulated absorptance A of the indicated layers versus the wavelength in a typical a-Si:H/µc-Si:H solar cell [10]. This simulation was performed with the numerical device simulator Advanced Semiconductor Analysis (ASA). For the simulation of the absorptance A the electrical and optical input parameters were adjusted by comparing the measured and simulated results [10]. The light absorbed in the a-Si:H i-layer and the µc-Si:H i-layer can contribute to the generation of charge carriers (electrons and holes). In contrast, light absorbed in the doped layers (Figure 1.3) can hardly contribute to the current generation in the solar cell, because of their low electron- and hole-mobility lifetime, which is a result of the high defect density. Therefore, absorption in the doped layers, which is called parasitic absorption, has to be avoided. This parasitic absorption in the a-SiC:H front p-layer [11] reduces the absorptance of the i-layers up to a wavelength of 600 nm. Other doped layers, the n/p contact between the cells, the n-layer of the bottom cell, and the back contact/reflector, start to absorb at $\lambda > 500$ nm within the solar cell. The parasitic absorption of the TCO is considerable for $\lambda > 700$ nm, where the free carrier absorption in the TCO is significant. The optical reflection of the cell is determined by the in-coupling of the light into the cell, the thickness of the absorber layers and the amount of light trapping. The in-coupling of the light is mainly affected by the reflection of the light at the air/glass and the TCO/silicon interfaces, as a result of the stepwise increase of the refractive index (n) from air $n \approx 1$, through TCO $n \approx 2$ to Si $n \approx 3.7$.

One conclusion from this simulation is that a reduction in parasitic absorption in the doped silicon layers, back reflector, together with an improved in-coupling of the light, can lead to a considerable gain in current. Additionally a reduction of the refractive index of the n-layer,

which is in contact with the back reflector, can also lead to a reduced parasitic absorption and therefore a gain in current [12]. The reduction of the parasitic absorption in the doped layers and, therefore, improvement in the current generated by the solar cell will be one focus of the present study.

1.3 Purpose of the intermediate reflector and requirements of the material properties

Another important method to improve the stabilized efficiency of the a-Si:H/μc-Si:H tandem solar cell is to reduce the degradation of the a-Si:H top cell under light illumination. To reduce the effect of light-induced degradation, the intrinsic a-Si:H absorber layer has to be kept as thin as possible, to reduce the amount of light-induced defects and to increase the electric field strength [13,14]. However, reducing the thickness of the a-Si:H i-layer results in a low photocurrent [13-16]. Figure 1.4 shows the external quantum efficiency (*EQE*) versus the wavelength for an a-Si:H top cell and a μc-Si:H bottom cell of an a-Si:H/μc-Si:H tandem solar cell. The current (J_{QE}) calculated from the external quantum efficiency and the AM1.5-G spectra for the solar cells is labelled on the graph. The a-Si:H top cell has a J_{QE} of 10 mA/cm² and the μc-Si:H bottom cell a J_{QE} of 12.7 mA/cm². Since both cells are electrically connected in series, the cell with the lowest current limits the total device current. Consequently, in order to achieve high efficiencies, the currents generated by the a-Si:H top and μc-Si:H bottom cells have to be balanced. As an example, for the tandem cell shown in Figure 1.4, the a-Si:H top cell would limit the current of the device. Particularly if the current of the μc-Si:H bottom cell is increased, e.g. due to better light scattering, a gain in current of the a-Si:H top cell is of particular importance. Figure 1.4 also shows the *EQE* for an a-Si:H single junction cell of the same thickness as the a-Si:H top cell, but with a highly reflective ZnO/Ag back reflector, which increases the J_{QE} of the top cell by 4.5 mA/cm² to 14.5 mA/cm². This indicates that, the amount of light absorbed in the top cell can be increased by using a reflector. Therefore, an increase in the a-Si:H absorber layer thickness, to balance the currents, can be avoided, thus reducing light-induced degradation [13,14].
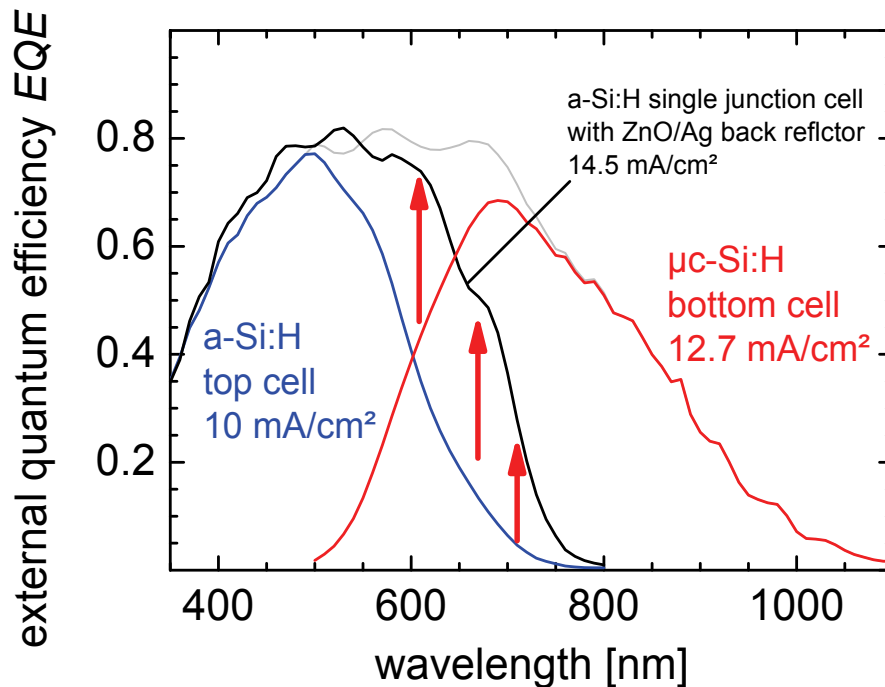
Figure 1.4: External quantum efficiency EQE for the a-Si:H top cell, the µc-Si:H bottom cell, the sum of both EQE in an a-Si:H/µc-Si:H tandem solar cell and an a-Si:H single junction solar cell with ZnO/Ag back reflector.

Using a ZnO/Ag reflector between the cells would lead to a bottom cell without photocurrent; therefore, the reflector has to be transparent for the light, which has an energy below the band gap of the amorphous silicon absorber material. This reflector has to be applied between the a-Si:H top cell and the µc-Si:H bottom cell and is named the intermediate reflector (IR) [17-22]. Such an intermediate reflector (IR) has to fulfil a number of requirements:

low refractive index

The IR has to reflect the light with a wavelength λ below 650 nm back into the a-Si:H top cell. This light reflected by the IR would result effectively in a current transfer from the µc-Si:H bottom cell to the a-Si:H top cell, (the top cell will generate more current; the bottom cell will generate less). To achieve a high internal reflection of the light, a refractive index difference between the IR and the surrounding silicon ($n \approx 3.7$) is necessary. Therefore, a low refractive index n for the IR is required.

low reflectivity for long wavelengths

As shown in Figure 1.4, the a-Si:H top cell can absorb light up to an wavelength of 650 nm when a highly reflective back contact is used, and the µc-Si:H bottom cell can utilize light up to a wavelength of about 1100 nm. Therefore, light with a wavelength of >650 nm should not be reflected, which leads to a further prerequisite for the IR: a low reflectivity for wavelengths λ>650 nm. Consequently, the intermediate reflector would have to selectively reflect the light with λ<650 nm.

low absorption

Light, that penetrates the intermediate reflector, can also be absorbed in the intermediate reflector. Since the IR is placed between the cells, this light does normally not lead to photocurrent that can be collected; consequently, the absorption in the IR has to be as low as possible. To further reduce the parasitic absorption, the IR should not be an extra layer, but preferably replace the doped layers in the tunnel recombination junction between the a-Si:H top cell and the μc-Si:H bottom cell (n/p contact) by more transparent layers.

low electrical resistance in the growth direction

The a-Si:H top solar cell and the μc-Si:H bottom cell are electrically connected in series via the n/p contact between the solar cells. Therefore, the IR has to connect electrically the a-Si:H top and the μc-Si:H bottom cell, which requires a tunnel recombination junction with a low electrical resistance. A sufficiently low electrical resistance in the direction of the current flow between the component cells has to be ensured.

high resistance in the lateral direction

An intermediate reflector with highly conductivity in the lateral direction, e.g. doped zinc oxide (ZnO), could lead to a shunting of the μc-Si:H bottom cell when the solar cell stripes are electrically connected to a solar module. Figure 1.5 a) illustrates the shunting of the μc-Si:H bottom cell via the interconnection between the cell stripes between the highly conductive intermediate reflector and the back contact as illustrated by the arrow.
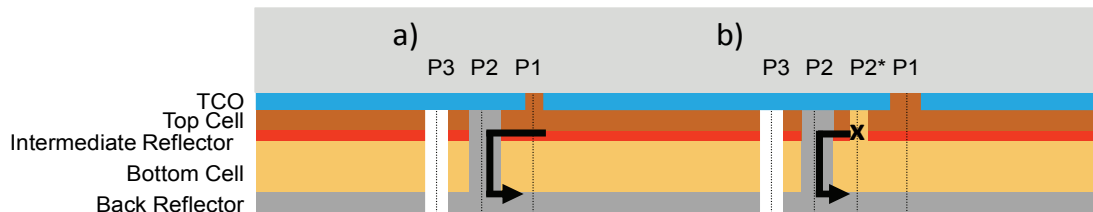
Figure 1.5: A schematic cross section of two cell stripes of a solar module with intermediate reflector. a) On the left side, the bottom solar cell is shunted because of a highly conductive intermediate reflector. b) On the right side, the shunting of the bottom cell is prevented by an additional laser-scribing step P2* after the deposition of the intermediate reflector. The arrows are indicating current flow through the shunt introduced by a highly conductive intermediate reflector.

In Figure 1.5 b) additional laser scribing step (P2*) after the deposition of the intermediate reflector interrupts the current path and therefore avoids the shunting of the bottom cell [23]. A high resistance in the lateral direction of the intermediate reflector would also avoid shunting of the μc-Si:H bottom cell and the standard interconnection process can be applied. Therefore, a high resistance of the intermediate reflector in lateral direction is preferable, while high conductivity in the perpendicular direction should be maintained (anisotropic conductivity).

function as nucleation layer

If the subsequent absorber layer is microcrystalline silicon, the IR should also function as a nucleation layer. Previous studies on the critical dependence of the film properties on the "substrate"-layer morphology [24-29] have already confirmed a substrate dependency, especially in the favourable transition regime between a-Si:H and µc-Si:H growth [30,31].

suitable preparation process

One requirement for the preparation process of the IR is that it should not damage the underlying solar cell; for example, the temperatures should not be above $\approx 200°C$ or the process should not etch or impose energetic ion bombardment on the silicon layers of the underlying solar cell. For an industrial process, high compatibility between the IR deposition process and the silicon deposition would be a great advantage. The most suitable process for the IR deposition is to use preparation conditions similar to those for the a-Si:H top cell and the same equipment as for the silicon deposition.

Zinc oxide (ZnO) has already been investigated as an intermediate reflector [17,20,22,23]. ZnO has a refractive index of approximately 2 and its optical band gap is higher than $3\,eV$. Doping can make ZnO highly conductive, which is desirable, in order to keep the series resistance of the device low. However, on the other hand, a high lateral conductivity of the IR requires an additional laser structuring process step (P2*), subsequent to the IR deposition, when the solar cell stripes are electrically connected to a solar module as shown in Figure 1.5. Furthermore, typical preparation processes for ZnO are low-pressure chemical vapour deposition (LPCVD) or magnetron sputtering, which imply an additional production step using a different deposition technology in the middle of the production flow of the tandem cell.

Other material, such as microcrystalline silicon carbide µc-SiC:H [32], can be prepared with a wide band gap and is also sufficiently conductive due to an intrinsic doping effect. However, in [32], the µc-SiC:H was prepared at a substrate temperature above 200°C, which would damage the a-Si:H top cell.

As shown in [18,33], an intermediate reflector with a refractive index of 1.7 was successfully applied to a-Si:H/µc-Si:H solar cells but details about the material or the preparation conditions were not provided.

1.4   A short history of doped microcrystalline silicon oxide prepared by plasma enhanced chemical deposition

In the present study doped µc-SiO$_x$:H which is a phase mixture of highly crystalline µc-Si:H (crystalline silicon nanoparticles) and amorphous silicon oxide (a-SiO$_x$:H) [34,35] has been investigated. Doped hydrogenated amorphous silicon oxide (a-SiO$_x$:H) without a crystalline

phase prepared by plasma enhanced chemical deposition (PECVD) has been investigated since 1985 [36,37] and has proven its performance as a p-type a-SiO$_x$:H window layer for a-Si:H solar cells [38]. To achieve a higher transparency and conductivity, the same group [34,35] developed doped a-SiO$_x$:H with a doped μc-Si:H phase, which was named doped hydrogenated microcrystalline silicon oxide (μc-SiO$_x$:H). The prominent property of doped μc-SiO$_x$:H is that it has a higher conductivity than its amorphous counterpart with the same band gap, due to its highly conductive doped μc-Si:H phase [34,35].

μc-Si:H consists typically of columns of silicon crystals with a size of few tens of nanometres surrounded by an amorphous silicon tissue [39]. Figure 3.5 in chapter 3 shows a schematic picture of the structure of μc-Si:H. Previous work has demonstrated that the silane concentration in hydrogen strongly influences the crystalline volume fraction [40-42]. From the literature [34,35,43], it is known that the ratio of carbon dioxide flow to silane flow has a pronounced influence on the transparency.

Doped μc-SiO$_x$:H was first applied as a p-type window layer in single junction solar cells [43]. Later the mixed-phase nature of n-type μc-SiO$_x$:H was investigated in more detail [44] and the μc-SiO$_x$:H p- and n-layers were also implemented in stacked a-Si:H/a-Si:H solar cells [45-47] by the Energy Research Unit at Indian Association for the Cultivation of Science, Kolkata, in India. These results about the material properties of the doped μc-SiO$_x$:H [34,35,44] suggested that its application in a-Si:H/μc-Si:H tandem solar cells would also be successful.

1.5   Objectives and outline

The aim of the present study is to improve the performance of tandem solar cells. This will be achieved by two approaches:

(i)   Improvement of the current matching between top and bottom cells, by the use of the doped layers as intermediate reflectors (IR), and

(ii)   the improvement of the doped layers by reduction of the parasitic absorption within these layers.

To achieve such improvements, the preparation and the properties of doped μc-SiO$_x$:H films will be investigated in detail. The required properties for the doped μc-SiO$_x$:H layers are a high transparency, a sufficient electrical conductivity, and a tuneable refractive index. To achieve the required properties for the doped μc-SiO$_x$:H material it is necessary

• to understand the influence of the process parameters on the structure and composition,

• to obtain insights in the contribution of each phase on the optical and electrical properties,

• and to elaborate the interdependence between the optical and electrical properties.

Doped μc-SiO$_x$:H layers with various optical properties implemented in solar cells will help to understand the interdependence between the layer properties and the solar cell performance. Especially, to balance the top cell current and bottom cell current in a-Si:H/μc-Si:H tandem solar cells by the implementation of the μc-SiO$_x$:H intermediate reflector is a part of the present study.

The present study is divided into two parts: (i) the development of doped μc-SiO$_x$:H layers and (ii) their application to thin-film silicon solar cells.

Chapter 2 - "Techniques and methods for the preparation and characterisation of films and solar cells" - is divided into two sections. The first section describes techniques and methods for the characterization of films and solar cells. The second section describes details of the preparation techniques for films and solar cells. It describes the deposition system and details of the processes for the preparation of silicon layers and solar cells. In addition, it also presents the important properties of the silicon layers as used in the solar cells. The gas flow variations for the various gases and the related gas flow parameters for the development of the doped μc-SiO$_x$:H films in the present study are presented.

Chapter 3 describes the background of the silicon oxide alloy. It describes the structure of SiO$_2$ and a-SiO$_x$:H. The concept of the phase mixture of highly crystalline μc-Si:H (crystalline silicon nanoparticles) and amorphous silicon oxide (a-SiO$_x$:H) is presented. The conductivity versus the optical band gap of doped μc-SiO$_x$:H from literature are presented. The basic principles that constitute conductivity in a material consisting of oxygen-rich amorphous silicon phase and the highly crystalline microcrystalline silicon phase, are presented in this chapter.

Chapter 4 presents a detailed description of the development of doped μc-SiO$_x$:H films. This chapter shows the material properties versus the process gas flows parameters for n-type and p-type material in two separate sections. In these sections, the dependencies between material properties, such as the oxygen content, crystalline volume fraction, optical properties, and the electrical conductivity are described. A consistent systematic approach of the material development and data presentation was used for the p-type μc-SiO$_x$:H as for the n-type μc-SiO$_x$:H.

In chapter 5, the dependencies between the gas flow parameters, the material composition and the optical properties for both p- and n-type μc-SiO$_x$:H are summarised. In a ternary diagram, phase compositions with preferable material properties are identified. A survey graph for the optical and electrical properties that are relevant for the proposed applications in thin-film silicon solar cells is presented.

Chapter 6 is separated into three parts. The first part deals with a-Si:H single junction solar cells with μc-SiO$_x$:H as the n-layer. The following section is about μc-Si:H single junction solar cells with doped μc-SiO$_x$:H material as a p- and n-layer. The final section deals with a-Si:H/μc-Si:H tandem solar cells. The influence of applying doped μc-SiO$_x$:H to various doped layers on the solar cell properties is investigated.

Chapter 2

Techniques and methods for the preparation and characterisation of films and solar cells

This chapter describes the techniques and methods used to prepare and characterise films and solar cells. It presents preparation details and typical properties of the silicon layers used in the solar cells. For the development of doped μc-SiO_x:H, gas flow parameters used in the present study are described.

2.1 Techniques and methods for the characterisation of films and solar cells

2.1.1 The thickness of the films and solar cells

To measure the thickness of the films and solar cells, a step profiler from Veeco Instruments type Dektak was used. The accuracy of the thickness measurement is crucial, not only for the determination of the deposition rate; it also directly influences the determination of other material properties such as the electrical conductivity, optical absorption, and refractive index. The measurement uncertainty is influenced by the accuracy of the Dektak and by the quality of the step profile. During the present study, two techniques were used to remove the film locally from the substrate to create a step profile, for the thickness measurement: (i) laser ablation and (ii) mechanical removal with an adhesive tape. For (i), a film that absorbs sufficiently at the applied laser wavelength of 488 nm is required. For (ii), Ag stripes were evaporated previous to the film deposition on the glass surface and then removed with an adhesive tape, together with the film from the glass. The evaporated Ag stripes have a low adhesion to the glass surface;

therefore, they can be removed with an adhesive tape from the glass and consequently resulting in a step from the glass substrate to the surface of the film. The mechanical removal of the film was used to measure the films, e.g. μc-SiO$_x$:H, that do not absorb sufficiently at the laser wavelength used for laser ablation.

2.1.2   The electrical conductivity of the films

The electrical conductivity was measured in a vacuum cryostat, with a voltage from -100 V to $+100$ V. The lower current limit for this setup at 100 V is 0.5 pA. This limit is partly a result of the non-infinite resistance between the conducting leads at the vacuum feed trough. Two co-planar Ag contacts were evaporated on the film with a gap of $0.5\,\text{mm} \times 5\,\text{mm}$ and therefore the conductivity was measured in the planar direction of the film. With this contact geometry and a typical film thickness of 500 nm, the minimum conductivity, which is measurable, is $1 \times 10^{-12}\,(\Omega\text{cm})^{-1}$ for this set-up. To prevent surface contamination of the film by the ambient water vapour and to bring the film to the annealed state, a sequence of annealing at 440 K for 30 min and cooling back to room temperature was applied [48,49]. The temperature of 440 K (167°C) was chosen as a temperature that is well below the deposition temperature to avoid a post-deposition manipulation of the sample by hydrogen diffusion [50]. This is a common procedure to measure the conductivity of a-Si:H films [51].

2.1.3   The optical absorption, optical band gap, and refractive index of the films

The optical properties such as the absorption coefficient $\alpha(\lambda)$ and the refractive index $n(\lambda)$ versus the wavelength λ of the films were determined by measuring the transmittance $T(\lambda)$ and reflectance $R(\lambda)$ using a spectrophotometer. For a film thickness of 500 nm, an absorption coefficient of $100\,\text{cm}^{-1}$ leads to an absorptance of only 0.5%, i.e. only a small fraction is absorbed by the film. It is not possible to measure such low absorptance accurately with a conventional spectrophotometer. The absorbed light will be in the range of the measurement uncertainty [39]. Therefore, photothermal deflection spectroscopy (PDS) was used for low absorption coefficients in the sub-band gap regime [39,52].

Optical band gap

Disordered silicon semiconductors such as a-Si:H or μc-Si:H do not have a defined mobility energy gap, because the absorption coefficient does not decrease steeply at the band edge on the low energy side of the absorption spectrum, due to localized states in the band tails. Additionally, this material does not have a forbidden gap, as crystalline silicon does, because of localized defect states in the band gap. For crystalline silicon, the absorption coefficient α

decreases in the band gap to values below 10^{-7} cm^{-1} [53]. Typical absorption spectra are shown in Appendix B. For a-Si:H for $\alpha > 10^3$ cm^{-1}, on the high energy side of the absorption spectrum, transitions from the valence band to the conduction band dominate. A fit of the Tauc model to this part of the absorption spectrum leads to the definition of the Tauc gap [54]. Below an α of 10^3 cm^{-1}, on the low energy side of the absorption spectrum, the exponential decay of the absorption coefficient to low photon energies is called the Urbach edge and is a consequence of the exponential decrease of the density of states in the shallowest band tails, the valence band tail [55]. The segment of the spectrum with lower absorption (for a-Si:H < 1.5 eV), is often referred to as the sub band gap absorption. This spectral range is dominated by the transitions from the valence band and the conduction band to defect states. The absorption coefficient in this spectral range is a measure of the defect density [56,57].

The Tauc gap is often used as the optical band gap. When determining the Tauc gap [54], one assumes a square root dependency of the density of states on the energy at the band edges of an amorphous semiconductor. Therefore, in the Tauc plot $(\alpha \times E)^{0.5}$ is plotted versus the photon energy E. Subsequently, a linear slope is fitted to $(\alpha \times E)^{0.5}$ and extrapolated to zero. The intersection with the E axis is the Tauc gap.

In the present study, the E_{04} is used as a quantity for the optical band gap. The E_{04} optical band is defined by the photon energy E for which an optical absorption coefficient α of 10^4 cm^{-1} is obtained [39]. The value of 10^4 cm^{-1} for the absorption coefficient, at which the optical band is determined in the present study, is not a unique value but within the range of the absorption coefficient, where the Tauc gap is determined ($\alpha > 10^3$ cm^{-1}). The value of the E_{04} is similar to the value of the Tauc gap [58,59]. However, we used the E_{04} as the optical band gap for the development of doped μc-SiO$_x$:H because, in the most cases, it is less ambiguously determined than the Tauc gap. This uncertainty is not present when determining the E_{04} optical band gap. For example, for the doped μc-SiO$_x$:H investigated in the present study, the linear slope for the determination of the Tauc gap could be fitted in multiple ways. In addition, the E_{04} provides an indication for the photon energy threshold from which the absorptance A is relevant for a typical doped layer ($A \approx 2\%$ at 20 nm thickness, single path).

Using a spectrophotometer, the absorption coefficient $\alpha(\lambda)$ versus the wavelength λ of the films was determined by measuring the transmittance $T(\lambda)$ and reflectance $R(\lambda)$, using the Beer-Lambert law, as suggested by [60], and the equation

$$\alpha(\lambda) = -\frac{1}{d} \times \ln\left(\frac{T(\lambda)}{1-R(\lambda)}\right) \quad (2.1).$$

The film thickness d was measured using the step profiler close to the measurement spot of the spectrophotometer. It is important to measure the transmittance $T(\lambda)$ and the reflectance $R(\lambda)$ at the same spot on the sample, to avoid inaccuracies in the calculated absorption spectra that arise

from non-uniformity of the film thickness [61] and different positions of the reflectance and transmittance minima and maxima in the spectrum.

Refractive index

Two methods were used to determine the refractive index. Both methods used the same transmittance and reflectance data.

Method 1: The refractive index (n) versus the wavelength was determined using the layer thickness (d) measured by a step profiler and the wavelength difference between two maxima or minima (λ_1 and λ_2) of the interference fringes in the optical transmittance or reflectance spectra that were measured with a spectrophotometer.

To calculate the refractive index, we used the equations for the maxima,

$$2 \times d \times n_m = m_m \times \lambda_m \tag{2.2}$$

and for the minima,

$$2 \times d \times n_m = \left(m_m + \frac{1}{2} \right) \times \lambda_m \tag{2.3}$$

where m is the number of the maxima or minima. For two neighbouring extremes, we can write

$$m_2 = m_1 + 1 \tag{2.4}$$

and, using equation (2.2) or (2.3) and (2.4), we obtain

$$n \times \left(\frac{\lambda_1 + \lambda_2}{2} \right) \approx \frac{1}{2 \times d \times \left(\frac{1}{\lambda_2} - \frac{1}{\lambda_1} \right)} \tag{2.5}$$

from which the refractive index for each of the average wavelength λ_1 and λ_2 was determined. This method is applicable only in the wavelength range where the films are highly transparent. From this evaluation, we obtained the refractive index values for the average wavelength λ between two maxima or minima. The difference in the refractive index between two maxima or minima is small; therefore, using the average of λ as the position of the refractive index n is a good approximation. To evaluate the refractive index at $\lambda = 1\,\mu m$, we plotted $1/(n^2-1)$ versus the square of the photon energy (E^2). Using linear regression and extrapolation to $E^2 = 1.1\,eV^2$ ($\lambda = 1\,\mu m$), we determined the refractive index at $\lambda = 1\,\mu m$ [62-66].

Method 2: The other method was to fit the optical properties (refractive index n, absorption coefficient α) to the transmittance and reflectance spectra of the film, using the Fresnel equations and the OJL model [67]. This was done with the optical simulation software Scout [68] or Optics 2 [69].

2.1.4   The oxygen content of the films

Rutherford Backscattering Spectroscopy

Using Rutherford Backscattering Spectroscopy (RBS), one can measure the area-related atomic density of the oxygen atoms and the silicon atoms [70,71] within an error of approximately ± 2%. From this, the stoichiometry factor x can be calculated, which is the ratio between the number of oxygen atoms and silicon atoms.

$$x = \frac{O \ [\text{at./cm}^2]}{Si \ [\text{at./cm}^2]} \tag{2.6}$$

Alternatively, the oxygen content [O] can be used which is the area related density of oxygen atoms to the sum of oxygen atoms and silicon atoms.

$$[O] = \frac{O \ [\text{at./cm}^2]}{Si + O \ [\text{at./cm}^2]} \tag{2.7}$$

Both quantities consider only the number of silicon / oxygen atoms and not the number of atoms of other elements, such as hydrogen, which is also incorporated to a considerable extent: up to 20% in μc-SiO$_x$:H (measured using the hydrogen effusion method). This means that the calculated oxygen content is the ratio of the number of oxygen atoms related to the sum of silicon and oxygen atoms and does not take the incorporated hydrogen or other elements into account. Dr. Bernhard Holländer from PGI-9 at the Forschungszentrum Jülich performed the measurements of the area densities of silicon and oxygen by RBS. To avoid charging effects, the measurements were performed on films deposited on a substrate of mono-crystalline silicon wafers.

2.1.5   The crystalline volume fraction of the films

Raman spectroscopy

Raman spectroscopy was used to estimate the crystalline volume fraction of the material. Raman spectroscopy involves a change in photon frequency. When the film is illuminated, the photons can be reflected, transmitted, or absorbed, and a small fraction of the light is scattered inelastically at phonon modes. These photons are Raman scattered photons. The Raman scattered

photons can gain energy when absorbing a phonon or lose in energy when emitting a phonon, thus preserving the energy and momentum rules, which are

$$\omega_s = \omega_i \pm \omega_{Ph} \tag{2.8}$$

$$\vec{k}_s = \vec{k}_i - \vec{k}_{Ph} \tag{2.9}$$

where ω_i and ω_s are the incoming and scattered photon frequencies, respectively; $\vec{k}_i$ and $\vec{k}_s$ are the incoming and scattered photon wave vectors, respectively; and ω_{Ph} and $\vec{k}_{Ph}$ are phonon frequency and wave vector, respectively. Raman scattering is inefficient when compared to the elastic scattering process, leading to a small measurement signal. This problem can be overcome by using lasers to provide high intensity illumination, allowing the spectra to be measured in few minutes [72,73].
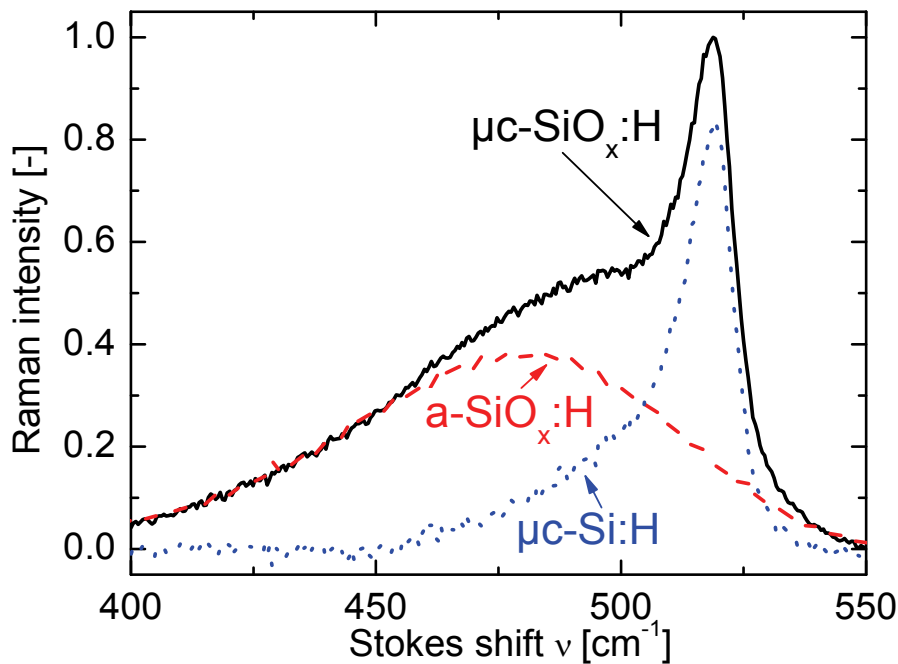
Figure 2.1: The normalized Raman intensity as a function of the Stokes shift for a μc-SiO_x:H layer (solid line). This spectrum of the μc-SiO_x:H layer is deconvoluted into an a-SiO_x:H peak (dashed line) and a μc-Si:H peak (dotted line) to calculate the crystalline volume fraction.

Figure 2.1 shows the deconvolution of a typical Raman spectrum of doped μc-SiO_x:H (solid line). The Raman spectrum for a-SiO_x:H shows a broad peak at around $\nu \approx 480\,\mathrm{cm}^{-1}$ (dashed line) and, for μc-Si:H, a sharp peak at $\nu \approx 520\,\mathrm{cm}^{-1}$ (dotted line). To obtain an estimate for the crystalline volume fraction in the μc-SiO_x:H, we defined the Raman intensity ratio I_c as the ratio of the integrated area $A_{\mu c\text{-Si:H}}$ of the μc-Si:H spectrum (dotted line) to the total peak area $A_{\mu c\text{-SiOx:H}}$ (solid line) [74,75] as

$$I_c = \frac{A_{\mu c\text{-Si:H}}}{A_{\mu c\text{-SiO}_x\text{:H}}} \qquad (2.10).$$

To extract the peak areas, we used the a-SiO$_x$:H reference spectrum (dashed line) which is measured on a sample grown in the amorphous regime with a high oxygen content and thus, can be expected to be completely amorphous. When fitting this a-SiO$_x$:H reference peak (dashed line) to the μc-SiO$_x$:H peak (solid line) between 400 cm^{-1} and 450 cm^{-1}, using an appropriate baseline and a scaling factor, the difference appears as typical peak for highly crystalline μc-Si:H silicon at $\nu \approx 520$ cm^{-1} (dotted line). This typical shape of the μc-Si:H peak ($I_c \gg 90\%$) is broader as compare to mono crystalline silicon and is asymmetric with a wider shoulder on the low wavenumber side, both features are related structural disorder [42,74]. Please note: The intrinsic μc-Si:H absorber layer in solar cells is preferably material with the optimum phase mixture (OPM) [30,31,76] ($I_c \approx 55\%$) and has therefore a more pronounced a-Si:H peak at $\nu \approx 480$ cm^{-1} compare to highly crystalline μc-Si:H. From the resulting peaks, the integrated area of the total μc-SiO$_x$:H peak $A_{\mu c\text{-SiOx:H}}$ and the integrated area of the μc-Si:H peak $A_{\mu c\text{-Si:H}}$ were calculated, to determine the I_c, using equation (2.10). In the following, the problem encountered in the evaluation of the crystalline volume fraction of the material from Raman spectroscopy is described and will be discussed.

(i) The Raman signal from the glass substrate can contribute to the broad a-SiO$_x$:H peak. In some samples, the influence of the glass substrate was evaluated by comparing the Raman spectrum measured in a film on glass with a film deposited on an Ag film. The Ag film covers the substrate and, therefore, effectively reflects the light and eliminates the influence of the glass substrate. This comparison did not show any significant influence of the glass on the Raman spectrum of the μc-SiO$_x$:H.

(ii) The absorption coefficient of the a-SiO$_x$:H phase in the μc-SiO$_x$:H film is not known but can be a factor of 5 lower than the absorption coefficient of the crystalline silicon at the laser wavelength of 488 nm (2.54 eV) used for the Raman spectroscopy (Appendix B). This uncertainty and the unknown Raman cross-sections for these materials, will possibly lead to an overestimation of the crystalline volume fraction when calculating the I_c for layers with higher oxygen contents.

In the following, the Raman intensity ratio I_c is compared to the results obtained by using the X-ray diffraction method and by the evaluation of the dielectric function with the effective medium approach.

X-ray diffraction

To compare the crystalline volume fraction evaluated from the Raman spectrum with a method that does not require a known Raman cross section, some films were measured using X-ray diffraction in grazing incidence configuration (GI-XRD). The GI-XRD method provides direct access to the structure of the material with its components of crystalline Si, a-Si:H and a-SiO$_2$. Florian Köhler from the IEK-5 at the Forschungszentrum Jülich performed the measurements with the GI-XRD method and the evaluation of the data [77]. Prior to the μc-SiO$_x$:H deposition, the glass substrate was covered with a 700 nm ZnO film, to avoid contributions of the glass to the GI-XRD signal. The GI-XRD method determines the crystalline volume fraction with respect to the silicon phase. Therefore, the a-SiO$_2$ phase had to be considered when evaluating the crystalline volume fraction X_c with respect to all phases. Figure 2.2 shows the crystalline volume fraction calculated from the GI-XRD data versus the Raman intensity ratio I_c for the same samples. The deviation between X_c and I_c is within +/- 12% absolute up to an I_c of 35%. A similar deviation was found when comparing X_c and I_c of μc-Si:H without oxygen as the alloying component [77,78]. From the comparison shown in Figure 2.2, one cannot clearly conclude that the crystalline volume fraction I_c evaluated from the Raman spectra is correlated to the X_c up to high crystalline volume fractions (I_c > 35%).
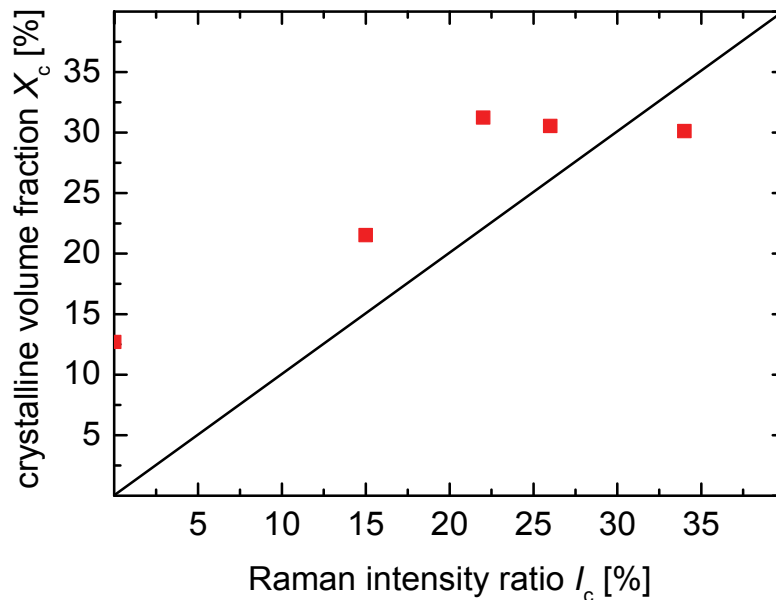
Figure 2.2: The crystalline volume fraction measured by grazing incidence X-Ray diffraction GI-XRD versus the Raman intensity ratio for doped μc-SiO$_x$:H from the present study. The line gives the one to one relationship of both values.

Effective medium approach

Another approach for investigating the crystalline volume fraction determined by Raman spectroscopy is to use I_c as volume fraction in the effective medium approach of Bruggeman

[79], using the Scout program [68], and comparing the resulting optical properties with the measured properties for samples with the same I_c. Scout used the equation derived from Bruggeman's effective medium approach

$$(1-I_c)\frac{\varepsilon_{a-SiO_x:H}-\varepsilon_{\mu c-SiO_x:H}}{\varepsilon_{a-SiO_x:H}+2\varepsilon_{\mu c-SiO_x:H}}+I_c\frac{\varepsilon_{\mu c-Si:H}-\varepsilon_{\mu c-SiO_x:H}}{\varepsilon_{\mu c-Si:H}+2\varepsilon_{\mu c-SiO_x:H}}=0 \qquad (2.11)$$

to calculate the optical properties [79]. $\varepsilon_{\mu c-Si:H}$ is the dielectric function of μc-Si:H with $I_c=80\%$ obtained for samples in the present study without CO_2 admixture (note: a possible post-oxidisation would be [O]=3% in maximum [80] for this kind of process and therefore can be neglected with respect to the observed changes in the dielectric function). $\varepsilon_{a-SiOx:H}$ is the dielectric function of the a-SiO$_x$:H material prepared in the present study with an $I_c=0\%$. The $\varepsilon_{\mu c-SiOx:H}$ is the resulting dielectric function from which the E_{04} was calculated as a function of the Raman intensity ratio I_c. The calculated optical band gap E_{04} was compared to the measured E_{04} obtained from samples prepared in the present study for various Raman intensity ratios I_c (see also Figure 4.12 in section 4.2.5 and the discussion in section 4.4). The calculated and measured optical band gaps E_{04} from two series were compared. (i) The series using a high silane concentration ($SC=0.5\%$) showed good accordance between the calculated and the measured values of the E_{04}. (ii) For the series prepared using a lower silane concentration ($SC=0.2\%$), the calculated and the measured values of the E_{04} describe the same trend, but the deviation between both values for some samples is higher. From these investigations on the Raman intensity ratio, it is also not clear whether the Raman intensity ratio evaluated as described corresponds to the crystalline volume fraction. However, in the present study, we used the Raman intensity ratio as an estimate for the crystalline volume fraction.

2.1.6   The solar cell characterisation

IV-measurements at the sun simulator

The fill factor (*FF*), the short circuit current density (J_{sc}), and the open circuit voltage (V_{oc}) of the solar cells were determined from the *IV*-characteristics. The *IV*-characteristics were measured under illumination provided by a double-source sun simulator [81] from WACOM (WXS-140S-Super) at standard test conditions (class A spectrum, 100 mW/cm², 25°C) [82-84]. The cell area is defined as described in section 2.2.2.

Light soaking

The light soaking of the solar cells was performed at 55°C under open circuit conditions, using metal halide lamps with an intensity of 1000 W/m² in the sample plane and a class B spectrum

[83,84]. The solar cells were continuously exposed to this light source and their solar cell parameters were measured several times during the 1000 h of exposure.

Measurements of the quantum efficiency

The **external quantum efficiency** (*EQE*) of the thin-film solar cells prepared in this thesis was determined with two systems that use different techniques to produce monochromatic light:

(i)   A grating monochromator setup (FWHM of the monochromatic light: $\approx 1 \text{-} 10\,\text{nm}$) measuring in the wavelength range between 300 nm and 1100 nm.

(ii)   An interference-filter setup - which was incorporated into the optical path of a WACOM sun simulator [81] - with 21 interference filters in the wavelength range between 357 nm and 1103 nm (FWHM $\approx 10\,\text{nm}$).

Setup (i) is optimized for small spot measurements and has a much better wavelength resolution (FWHM $= 1 \text{-} 10\,\text{nm}$) compared to the 21 interference filters (measurement points) used in setup (ii). The benefit of setup (ii) is that it allows the *IV*-characteristics and the *EQE* curves to be measured without removing the sample from the set-up, and the illumination area is larger than the substrate area. We used setup (i) for non laser-scribed solar cells on thin substrates (1 mm) and setup (ii) for laser-scribed solar cells on relatively thick glass substrates (3.2 mm). The *EQE* of solar cells measured using setup (ii) had to be laser-scribed because of the large area illuminated by the sun simulator. A large area illumination would otherwise lead to an unwanted current collection in the vicinity of the solar cell, which then results in an undefined cell area. The current collection is pronounced under low illumination conditions, as applied during the *EQE* measurements, compared to AM1.5-G illumination conditions. The large area illumination of the setup (ii) is especially important when using thick glass substrates (3.2 mm). When using a spot smaller than the solar cell area and thick glass substrates, part of the light is guided within the thick substrate out of the contacted cell area and is therefore lost for solar cell's photocurrent generation. When illuminating a larger area, light from the surroundings would also be guided into the cell area, which therefore balances the losses [85]. This means that, if a spot illumination as in the setup (i), is used, the *EQE* for a solar cell on a 3.2 mm thick glass substrate would be lower than for setup (ii). This effect can lead e.g. to an 8% lower current, as determined from the *EQE* measurement of the bottom cell [85]. More details of the solar cell configurations and the solar cell area definition are given in section 2.2.2.

The *EQE* of an a-Si:H top cell in a tandem solar cell was measured using red bias light (OG 695, or 630/870 nm LED-light), and the *EQE* of the bottom cell was measured using blue bias light (BG 7, or 470 nm blue LED-light) [86]. All quantum efficiency measurements were measured at 0 V external bias voltage. To evaluate the current density of the top cell and the bottom cell in the

tandem device ($J_{QE,Top}$, $J_{QE,Bot}$), the quantum efficiency of the individual cells was convoluted with the AM1.5-G solar spectrum [81,83,86].

The **internal quantum efficiency** (*IQE*) was calculated using the equation

$$IQE = \frac{EQE}{1-R} \tag{2.12}.$$

The **reflectance** *R* of the solar cell from the glass side was measured using a UV-VIS-NIR photospectrometer with an attached Ulbricht sphere.

2.1.7 Estimation of the measurement uncertainty

In addition to the scatter of data introduced from the quality of run-to-run reproducibility in sample preparation, we estimated the following measurement errors. The error in electrical conductivity is $\pm 20\%$, dominated by sample geometry, but at least $1 \times 10^{-12} (\Omega cm)^{-1}$, due to the lower limit measurement set-up. The errors for other experimental data depend mainly on the accuracy of the deposition equipment (gas flow 0.05 sccm), or the uncertainties in data evaluation (optical band gap $E_{04} \pm 0.05$ eV, Raman crystallinity $I_c \pm 2.5\%$, oxygen content $[O] \pm 0.020$, and refractive index $n \pm 0.1$). The reflectance *R* and transmittance *T* can be measured with an accuracy of $\pm 2\%$. The error in the solar cell parameters is $\sigma_{Jsc} \pm 3.5\%$ for the short circuit current density J_{sc}, $\pm 2\%$ for the *EQE*, $\sigma_{Voc} \pm 0.5\%$ for the V_{oc}, and $\sigma_{FF} \pm 0.5\%$ for the *FF*. Therefore, the approximate error in the solar cell efficiency η is $\sigma_{\eta} \pm 3.6\%$ as calculated by

$$\sigma_f = \sqrt{\sum_i \left(\frac{\partial f(x)}{\partial x_i} \sigma_i \right)^2} \tag{2.13}$$

from this follows

$$\sigma_{\eta} = \sqrt{(FF \times J_{sc} \times \sigma_{V_{oc}})^2 + (FF \times V_{oc} \times \sigma_{J_{sc}})^2 + (V_{oc} \times J_{sc} \times \sigma_{FF})^2} \tag{2.14}.$$

The deviation between the individual solar cell J_{sc} measurements is much smaller i.e. $\sigma_{Jsc} \pm 1.5\%$ and the absolute error in the J_{sc} is mainly related to the accuracy of the reference solar cell of $\sigma_{Jsc} \pm 2.0\%$ with respect to the AM1.5-G spectrum. Therefore, the run-to-run error e.g. of the solar cell efficiency measurement is $\sigma_{\eta} \pm 1.7\%$ as calculated by (2.14).

2.2   Techniques and methods for preparing the films and the solar cells

The following section describes techniques and processes for the preparation of the films and the solar cells. In addition, it presents the structure, the used substrates, and the contact configuration of the prepared solar cells. It also describes some of the relevant basic properties of the layers used in solar cells.

2.2.1   Plasma enhanced chemical vapour deposition

The plasma enhanced chemical vapour deposition (PECVD) technology was used to deposit the silicon layers of the solar cell. More on PECVD can be found in [39,41,87-89]. It is the standard technology to produce thin-film silicon solar cells in industrial scale volume. Deposition systems for large area solar modules were developed from various suppliers e.g. TEL - Tokyo Electron Ltd., formerly Oerlikon Solar, Applied Materials, ULVAC, Jusung, Anwell, Leybold Optics and some other companies. This technique is also widely used in the flat panel display industry to produce thin film transistors (TFT). Developments in this technology have encouraged the equipment industry to deploy large area deposition systems [4,90]. For example, in 2013, a total annual thin-film silicon solar module production capacity of well over 1 GWp was achieved [90].

For the deposition of silicon layers used in thin-film silicon solar cells, silane (SiH_4) and hydrogen (H_2) were used. To alloy these silicon layers, methane (CH_4) for silicon carbide and carbon dioxide (CO_2) for silicon oxide were added as additional process gases. To dope the p-type material, gas that contains boron (trimethylboron; TMB) or, for n-type doping, gas that contains phosphorus (phosphine; PH_3) was used. In the PECVD process, the gasses were decomposed in a glow discharge process excited by an electrical field in vacuum at a pressure of, typically, 1 mbar. In the present study, an alternating electrical field at radio frequency (RF = 13.56 MHz) or very high frequency (VHF = 94.7 MHz) was used. In the present study VHF was used for the intrinsic µc-Si:H preparation to increase the deposition rate and simultaneously achieve a high material quality [91]. RF was used for doped µc-SiO_x:H since it is easier for up scaling to large areas and RF is also the excitation frequency used in the processes of the industry partners in the projects (Sontor / Sunfilm, Helathis, Fast Track) and a high deposition rate is not highly important for thin layers.

The 6-Chamber deposition system

The PECVD process was performed in a 6-Chamber PECVD deposition system, which was built in 1992 by the Materials-Research-Group (MRG) Company in Denver, USA (Figure 2.3). Because the system comprises 6 chambers, it is possible to prepare nearly all types of layer in a

dedicated chamber (Figure 2.3). This makes it possible to develop new materials e.g. the μc-SiO_x:H p/n-type in one chamber without influencing the reference solar cell process in other chambers. In addition, it allows each chamber to be configured individually for the specific process requirements e.g. electrode distance, excitation frequency, and ranges of mass flow controllers.
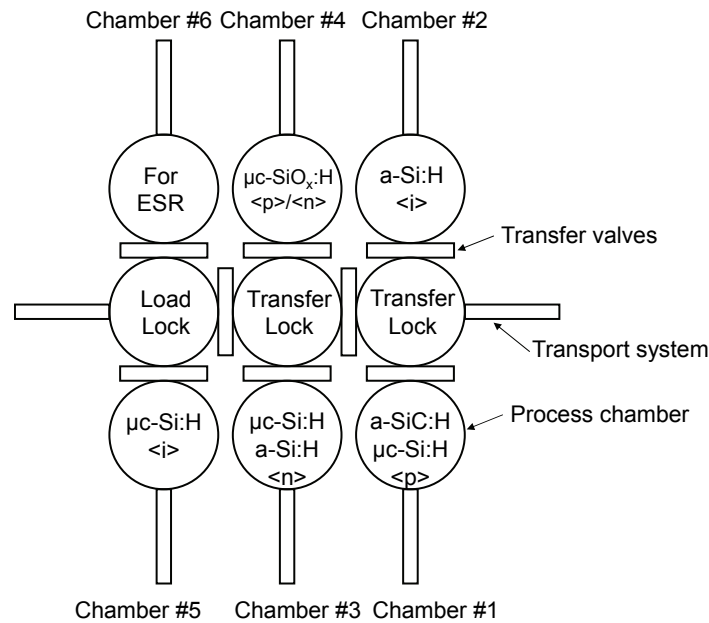

Figure 2.3: A top view sketch of the 6-Chamber PECVD deposition system. The types of layers prepared in the deposition chambers are indicated. The chambers are connected via evacuated transfer locks and load locks to move the substrate, using the transport system, without breaking the vacuum. The transfer valves separate the chambers from each other. The chamber designated for electron spin resonance (ESR) sample preparation was not used for the present study.

Figure 2.4 shows a schematic cross section of one deposition chamber. Further details are described in [92] and [63]. The used plasma power density (W/cm²) is calculated from the forward power P_f and the area calculated from the diameter (14.5 cm) of the counter electrode opposite to the substrate carrier. The substrate carrier is grounded by the rails. The gas flows used in the present study were checked frequently, using the pressure increase method [89], to detect a possible drift of the mass flow controller.
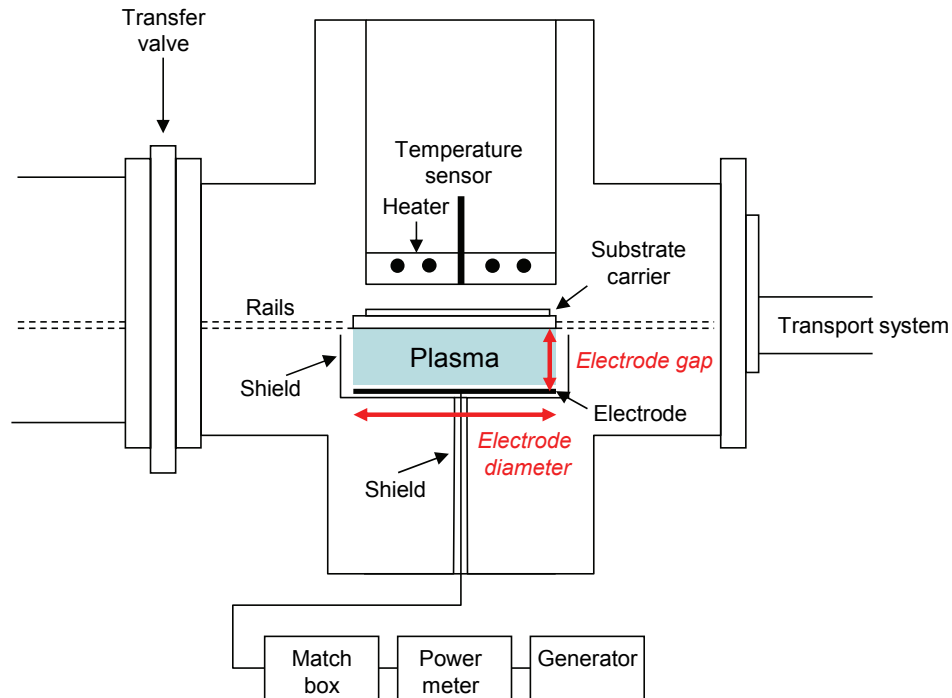
Figure 2.4: A schematic view of one of the plasma enhanced chemical vapour deposition (PECVD) chambers used in the present study for the film and solar cell preparation.

2.2.2   Solar cell device and preparation details

In the following the structure of the tandem solar cell, preparation details of the applied silicon layers, as well as their basic properties are described. Figure 2.5 shows the structure of the a-Si:H/µc-Si:H tandem solar cell with the typical thicknesses of the individual layers. The Figure also indicates the possible applications for doped µc-SiO$_x$:H layers.
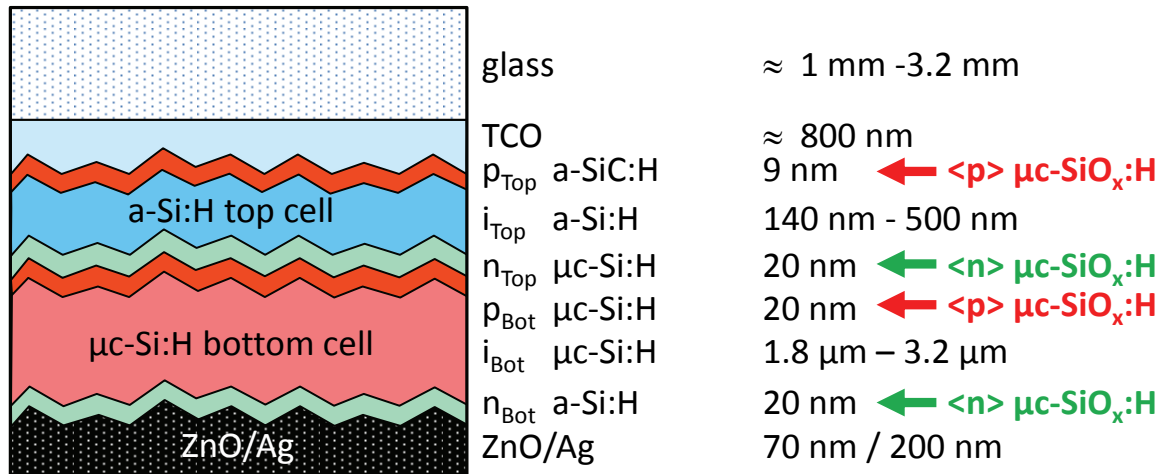
	glass	≈ 1 mm -3.2 mm	
	TCO	≈ 800 nm	
p_{Top}	a-SiC:H	9 nm	← **<p> μc-SiO$_x$:H**
i_{Top}	a-Si:H	140 nm - 500 nm	
n_{Top}	μc-Si:H	20 nm	← **<n> μc-SiO$_x$:H**
p_{Bot}	μc-Si:H	20 nm	← **<p> μc-SiO$_x$:H**
i_{Bot}	μc-Si:H	1.8 μm – 3.2 μm	
n_{Bot}	a-Si:H	20 nm	← **<n> μc-SiO$_x$:H**
	ZnO/Ag	70 nm / 200 nm	

Figure 2.5: A schematic sketch of the a-Si:H/μc-Si:H tandem solar cell. The typical thickness values and layers are also indicated. In addition, the considered applications for the doped μc-SiO$_x$:H layers are indicated as window layer (p_{Top}), intermediate reflector (n_{Top} and/or p_{Bot}), and/or μc-SiO$_x$:H back contact (n_{Bot}).

For solar cells, various kinds of substrates coated with different kinds of transparent conductive oxides (TCO) have been used:

(i)   "Asahi (U)":   SnO$_2$:F coated 1.1 mm thick green glass (Asahi "type U")

(ii)   "Asahi (VU)":   SnO$_2$:F coated 3.2 mm thick white glass, which is glass with a low iron content (Asahi type "VU")

(iii)   "ZnO:Al":   sputtered and subsequently HCl-etched ZnO:Al on 1.1 mm thick glass from Corning type Eagle [93-95]. This substrate was used for μc-Si:H p-i-n single junction solar cells

(iv)   "DT-ZnO:Al":   sputtered and subsequently HCl- and HF-etched ZnO:Al on 3.2 mm thick white glass from Euroglas company [96,97]

The "standard" tandem solar cell in p-i-n/ p-i-n configuration consists of several silicon-based layers, which were all prepared at 185°C substrate temperature. The a-Si:H top cell consists of a ≈ 9 nm thick a-SiC:H p-layer, a 140 nm to 500 nm thick (indicated in chapter 6) a-Si:H i-layer followed by a μc-Si:H n-layer with a thickness of 25 nm. The a-Si:H top cell was followed by the deposition of the μc-Si:H bottom cell. The μc-Si:H p-layer deposited on the n-layer provides an n/p-contact between the cells and was also a nucleation layer for the subsequent μc-Si:H i-layer. The intrinsic μc-Si:H absorber layer has a thickness of 1.8 μm to 3.2 μm (indicated in chapter 6). The n-layer of the μc-Si:H bottom cell is n-type a-Si:H and 20 nm thick. To provide a highly reflective back contact, a ZnO/Ag layer stack is used. The ZnO layer is aluminium (Al) doped and sputtered from a ceramic target with 1 wt.% Al$_2$O$_3$ with a thickness of 70 nm. The Ag layer is also sputtered and has a thickness of 200 nm.

In Figure 2.5, the possible applications for doped µc-SiO$_x$:H layers are indicated:

- as p$_{Top}$: p-layer for the top cell (not in the present study, but in [98-100]),

- as n$_{Top}$/p$_{Bot}$: in part or as a complete n/p-contact which also acts as an intermediate reflector, and

- as n$_{Bot}$: n-layer for the bottom cell, which might also replace the ZnO layer at the back contact/reflector.

In some cases an antireflection foil from the Solarexcel™ company (now a part of DSM Advanced Surfaces) is used on the light-incident side of the glass [101].

Contact configuration of the solar cells

To define the area of the solar cells, two procedures were used: a shadow mask process and a laser scribing process. On one 10×10 cm² substrate, 18 solar cells are defined with an area of 1 cm² (as well as some smaller cells).
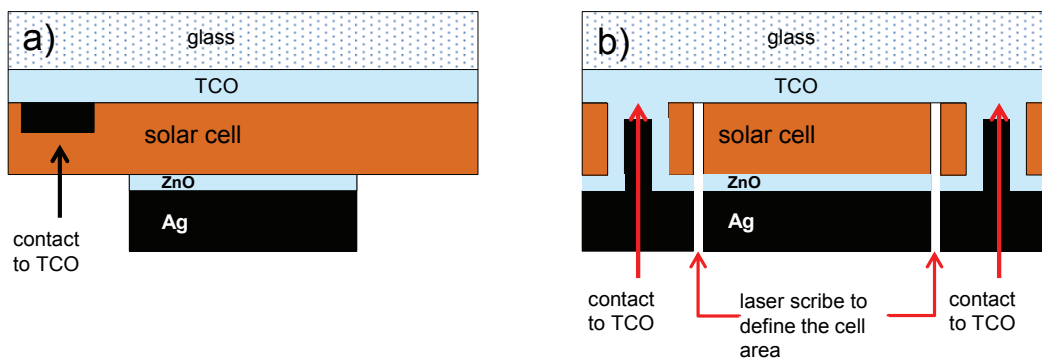

Figure 2.6: A schematic cross section of a small part of the substrate on which the solar cell is located. a) The solar cell area is defined by a shadow mask during the deposition of the Ag back contact and b) the structures are scribed by laser ablation through the glass; therefore, the solar cell area is defined by laser scribing.

Figure 2.6 shows schematic cross sections of a small part of the substrate where one of the solar cells is located. In a), the individual solar cell areas are defined by the back contact. The Ag back contact and the Ag grid contact to the front TCO, were deposited through a shadow mask. When using a ZnO/Ag back reflector, a 70 nm thick ZnO:Al layer was sputtered onto the entire surface of the solar cell. After evaporation of the 700 nm thick Ag layer through the mask, the substrate was dipped in 2% HCl, which removed the ZnO layer at those parts of the substrate where it was not covered by the Ag pads.

In Figure 2.6 b), the individual solar cell areas are defined by laser scribing. After the silicon deposition, the silicon layers were partly removed by laser scribing to create an opening to the front contact of the cell. Subsequently, ZnO/Ag was sputtered on the entire area of the substrate.

This was followed by a second laser-scribing step, which precisely defines the cell area. This step also separates the front and rear electrical contacts.

The contacting configuration shown in Figure 2.6 b) has the following advantages compared to the contacting configuration shown in Figure 2.6 a):

- precise solar cell area definition by laser scribing
- complete electrically isolation of the solar cell layer stack from the surrounding cell
- higher fill factor due to reduced series resistance

2.2.3   Preparation details and some material properties of the silicon layers used in solar cells

Table 2.1 shows the deposition parameters used for the individual layers of the tandem cell and Table 2.2 some optical and electrical properties of these layers. Figure 2.7 shows the absorption coefficient α versus the photon energy E of these layers measured by PDS. The material properties are shown for layers having a thickness of several hundred nanometres and grown on glass substrates. In particular, the doped n-type and p-type layers in the solar cells are considerably thinner, which, in general, has a strong effect on e.g. the electrical conductivity σ and the Raman intensity ratio I_c. However, such thin layers are difficult or impossible to measure accurately and it is therefore general practice to perform the material optimisation and evaluation on "thick" layers. The gases used in the PECVD process were silane (SiH_4), carbon dioxide (CO_2), methane (CH_4), and hydrogen (H_2). For the dopant source, 2% PH_3 in SiH_4 or 1% trimethylboron $B(CH_3)_3$ (TMB) diluted in helium (He) was used. In Table 2.1, the dopant gas flows refer to the PH_3 flow and TMB flow as net flow of dopant gas only (excluding the dilution gas). SiH_4 and H_2 have a purity of 99.9999% (6.0). Other gases, e.g. CH_4, CO_2, and PH_3 have a purity of 5.5, 4.6, and 5.0, respectively.

Table 2.1: Deposition parameters for the individual layers used in the present study unless otherwise stated.

Layer	Plasma power density* [mW/cm²]	Plasma excitation frequency [MHz]	Electrode distance [mm]	Depo. pressure [mbar]	SiH₄ flow [sccm]	H₂ flow [sccm]	CH₄ flow [sccm]	He flow [sccm]	Dopant gas flow [sccm]
p-type									
a-SiC:H	18	13.56	20	1.06	12	110	10	11.8	0.12
μc-Si:H	60<	94.7	20	0.4	1.5	200		2	0.02
intrinsic									
a-Si:H	15	13.56	12	4	10	90			
μc-Si:H	120	94.7	12	1.5	5.2	98			
n-type									
a-Si:H	18	13.56	20	0.67	84				1.2
μc-Si:H	150	13.56	20	4	1	200			0.02

*Electrode area: 167 cm²

Table 2.2: Typical material properties for layers deposited using the deposition parameters shown in Table 2.1.

Layer	σ_{dark} [(Ωcm)⁻¹]	σ_{photo} [(Ωcm)⁻¹]	$\sigma_{photo}/\sigma_{dark}$	E_{04} [eV]	α_{subgap} [cm⁻¹]	I_c [%]	r_d [Å/s]
p-type a-SiC:H	5×10^{-6}			2.05			0.95
p-type μc-Si:H	3			1.98		72	0.6
intrinsic a-Si:H	1×10^{-11}	1×10^{-5}	1×10^{6}	1.91	5.0 @ 1.2 eV		0.82
intrinsic μc-Si:H	5×10^{-8}	1×10^{-5}	2×10^{2}	2.00	1.0 @ 0.7 eV	55	2.7
n-type a-Si:H	5×10^{-2}			1.91			1.5
n-type μc-Si:H	30			1.95		75	0.73

Figure 2.7 shows the absorption coefficient α versus the photon energy E measured by PDS for the layers described in Table 2.1 and Table 2.2. The optical band gap E_{04} and the sub band gap absorption can be determined from the absorption spectra. The sub band gap absorption of a-Si:H and μc-Si:H i-layers is related to the defect density (as described in references [56,57]). **Note:** The sub band gap absorption $E < 1.5$ eV for thin intrinsic a-Si:H layers can be influenced by a defective interface layer between the glass substrate and the silicon layer [102] and by the absorption of the glass substrate [103]. The absorption spectra are also shown as a reference for the developed doped μc-SiO$_x$:H material.
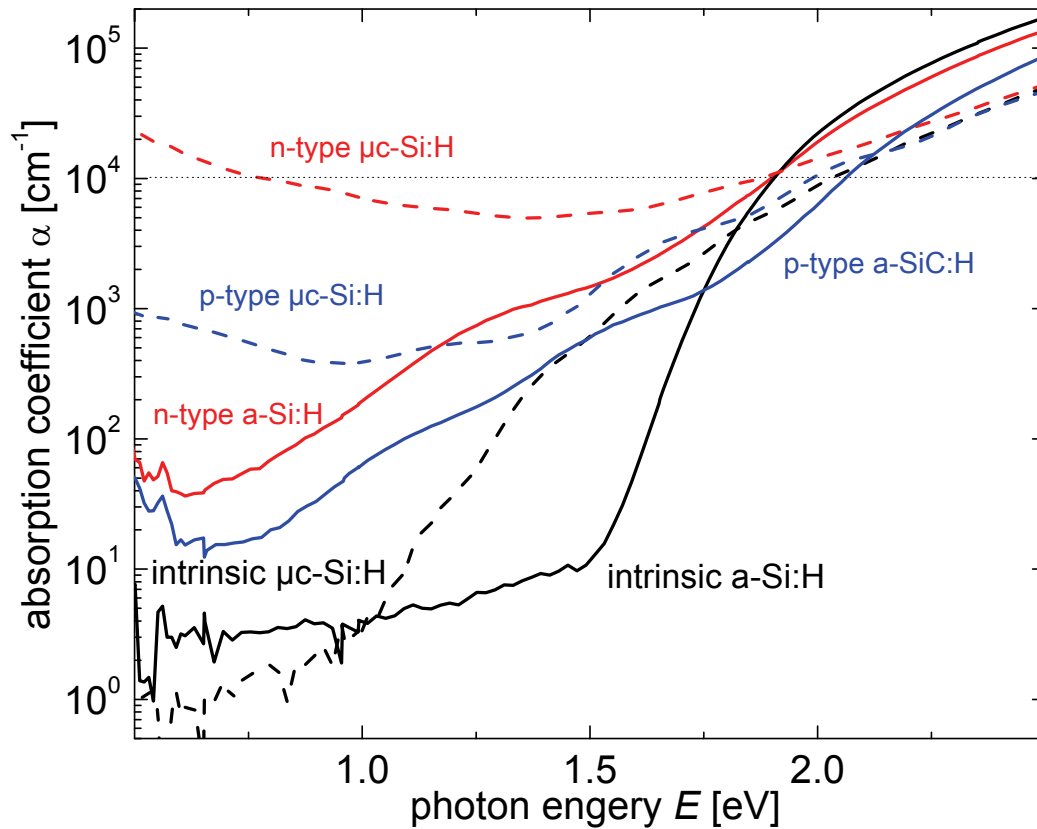
Figure 2.7 The absorption coefficient α measured by PDS versus the photon energy E. The dotted horizontal line indicates the absorption coefficient, which is used as a value to determine the optical band gap E_{04}. The dashed curves represent the microcrystalline layers and the solid curves the amorphous layers. The absorption coefficient spectra are shown in black for the intrinsic layers, in red for the n-layers, and in blue for the p-layers, as also indicated in the graph.

The **a-SiC:H p-layer** is a boron-doped amorphous silicon carbide layer [11], alloyed with carbon to increase the band gap and therefore its transparency. To alloy the silicon carbide layer, CH_4 was added to the PECVD process. The amount of CH_4 admixture is a trade-off between a sufficiently high conductivity and transparency, because the conductivity decreases with increasing optical band gap [11,104]. Using deposition conditions for the p-type a-SiC:H layer as described in Table 2.1, a typical conductivity of $5 \times 10^{-6} (\Omega \text{cm})^{-1}$ at an E_{04} of 2.05 eV was achieved (Table 2.2). In the solar cell, p-type a-SiC:H was directly deposited on the SnO_2:F substrate and was used as the p-layer for single junction a-Si:H solar cells and as the p-layer for the a-Si:H top cell in a-Si:H/μc-Si:H tandem solar cells. The typical thickness of the a-SiC:H p-layer in the solar cell is 9 nm, which is estimated from the deposition rate of a more than 300 nm thick p-layer.

The **μc-Si:H p-layer** is a boron doped microcrystalline silicon layer that is applied as the p-layer for the μc-Si:H bottom cell in the tandem cell and as the p-layer in μc-Si:H single junction solar cells. In the present study, the μc-Si:H p-layer was deposited using an excitation frequency of

94.7 MHz (Table 2.1), to achieve a high crystalline volume fraction as a thin layer. Additional details about the development of this layer are described in [105]. The admixture of TMB to dope the layer deteriorates the crystalline growth; therefore, an additional nucleation layer with reduced SiH_4 flow and TMB flow was used to increase the crystalline volume fraction.

The **intrinsic a-Si:H** absorber layer was prepared at RF, low power, and a silane concentration $SC=SiH_4/(SiH_4+H_2)$ of 10 (Table 2.1). The resulting i-layer has an E_{04} band gap of 1.91 eV and, importantly for the device quality aspects, a photosensitivity of $>10^6$ (Table 2.2Table 2.2). Another quality parameter is the defect density, which is related to the sub band gap absorption [56]. As a measure for the sub band gap absorption of intrinsic a-Si:H, we use the absorption coefficient at a photon energy of 1.2 eV. For an a-Si:H layer with a thickness of 377 nm, an $\alpha(1.2\,eV)$ of $5\,cm^{-1}$ (Table 2.2) was measured. For thicker layers $>1\,\mu m$, the sub band gap absorption coefficient decreases to values below $\alpha(1.2\,eV)=1\,cm^{-1}$ (not shown in Table 2.2 and Figure 2.7). Applied as an i-layer in the a-Si:H top cell an additional buffer layer with a reduced SiH_4 flow at the p/i and the i/n interface was incorporated [104,106,107].

The **intrinsic μc-Si:H** absorber layer was prepared using VHF-PECVD (94.7 MHz) at 1.5 mbar and an electrode gap of 12 mm (Table 2.1). VHF was used to increase the deposition rate and simultaneously improve the material quality [91]. The silane concentration SC was adjusted to achieve optimum phase mixture (OPM) material [30,31,76] with a Raman intensity ratio I_c of 50% to 60% (Table 2.2). This material, with a photo sensitivity of 200, is defined in [31] as device-quality material. As a measure for the sub band gap absorption of intrinsic μc-Si:H, we use the absorption coefficient at a photon energy of 0.7 eV, which is related to the defect density[57]. The sub band gap absorption coefficient has a low value $\alpha(0.7\,eV)=1.0\,cm^{-1}$ (Table 2.2/Figure 2.7) which indicates a low defect density [57]. Previous studies have shown that there is a critical dependence of the film properties on the "substrate" layer [24-29,108,109], especially in the region between a-Si:H and μc-Si:H growth, where the OPM material is prepared. Therefore, attention was paid to a high crystalline volume fraction of the p-layer but also to a highly crystalline nucleation layer during the initial growth of the μc-Si:H i-layer. This nucleation layer was prepared by starting the μc-Si:H i-layer with a reduced silane concentration SC, to avoid an a-Si:H incubation layer at the p/i-interface [108].

The **a-Si:H n-layer** is the other doped layer that builds up the electrical field. It was prepared using SiH_4 and PH_3 at RF and a low plasma power density, as for other amorphous silicon layers described in Table 2.1. No silicon alloying gases were used to increase the optical band gap. The layer's conductivity is $5\times10^{-2}(\Omega cm)^{-1}$ (Table 2.2), which is high enough to provide a sufficient electrical contact to the back contact but low enough to avoid an unwanted "current collection", in case the cell solar cell layer stack is not completely electrically isolated from the surrounding cell [85]. For a highly conductive n-layer (e.g. μc-Si:H n-layer) and a cell area that is only

defined by the area of back reflector, some of the cell current would be collected from the vicinity of the cell and this would lead to an undefined increase in cell area, i.e. higher short circuit current density.

The **µc-Si:H n-layer** was prepared at low silane concentration and higher plasma power densities of $18\,mW/cm^2$ to ensure a microcrystalline growth. It is highly conductive $\sigma = 3 \times 10^2\,(\Omega cm)^{-1}$ and has a high Raman intensity ratio of 75%. These properties are important for the n/p contact between the cells and for promoting the crystalline growth of the subsequent µc-Si:H p-layer in the a-Si:H/µc-Si:H tandem cell. The layer has a high absorption coefficient of $\alpha \approx 5 \times 10^3\,cm^{-1}$ over a wide range of photon energies (Figure 2.7) which leads to an increased parasitic absorption, as compared to amorphous n-layers, in the tandem cell. The deposition parameters for the deposition of n-type µc-Si:H were the starting point for the development of n-type µc-SiO$_x$:H. The parameters for the deposition of doped µc-SiO$_x$:H will be described in the following section in more detail.

2.2.4 The preparation of doped microcrystalline silicon oxide

The following section describes the preparation details for the doped µc-SiO$_x$:H layers used in the present study. The doped µc-SiO$_x$:H layers were all deposited in Chamber #4 of the 6-Chamber PECVD deposition system (Figure 2.3) using an excitation frequency of 13.56 MHz (RF) and a plasma power density of $300\,mW/cm^2$ with respect to the electrode area of $167\,cm^2$. RF was used for doped µc-SiO$_x$:H since it was the excitation frequency used for the processes of the industry partner in the projects (Sontor/Sunfilm, Helathis, Fast Track). The deposition pressure was 4 mbar and the substrate temperature 185°C. For the material investigation, the layers were grown with a thickness between 300 nm and 2 µm (unless otherwise stated). For the material development, various types of substrates were used. All films were deposited on glass substrates from Corning type Eagle. Additionally, for XRD measurements, ZnO coated glass substrates and for RBS measurements, pieces of double side polished crystalline silicon wafer, cleaned with isopropanol, were coated in the same run.

The process gases used were silane (SiH_4), carbon dioxide (CO_2) and hydrogen (H_2). For p-type doping 1% trimethylboron $B(CH_3)_3$ (TMB) in helium (He) were used as dopant gas sources. For n-type doping when requiring a phosphine concentration $PC = (PH_3/(PH_3 + SiH_4)$ of (i) more than 2%, we used a dopant gas source of 5% PH_3 diluted in H_2; and for a PC of (ii) less than or equal 2%, we used a dopant gas source of 2% PH_3 diluted in SiH_4. When referring to the PH_3 flow and TMB flow in the present study, we will mention only the net gas flow of the dopant gas, and will not refer to the dilution gas flow. For example, for a mixture of 5% PH_3 diluted in H_2, if the flow of H_2 is 0.8 sccm, we will give the PH_3 flow as 0.04 sccm. However, the gas flows of the dopant

dilution gas like H_2 or SiH_4 are still taken into account in the calculation of other gas flow parameters, such as the silane concentrations (SC).

In the following definitions of the gas flow parameters, we will use the gas names as synonyms for their gas flow in sccm e.g. SiH_4. As important process parameters for the development of doped μc-SiO_x:H, we consider (i) the "CO_2 to SiH_4 -ratio" named as r_{CO2}, which, for the given deposition conditions, is the main parameter that determines the resulting alloy composition and (ii) the silane concentration SC which strongly affects the crystallinity of the material. The parameter r_{CO2} is frequently used and defined as

$$r_{CO2} = \frac{CO_2}{SiH_4} \qquad (2.15).$$

As an alternative value, the CO_2-concentration is used (see section 4.5). It is defined as

$$CO_2 \text{ - concentration} = \frac{CO_2}{SiH_4 + CO_2} = \frac{r_{CO_2}}{1 + r_{CO_2}} \qquad (2.16).$$

The silane concentration is defined as

$$SC = \frac{SiH_4}{SiH_4 + H_2} \qquad (2.17).$$

At each value of silane concentration (SC) parameter, the CO_2/SiH_4 ratio (r_{CO2}) was varied in one series, called SC-series. While this terminology SC-series is unfortunately a bit misleading, as it does not refer to a variation in the silane concentration (SC) within the series, nevertheless it is necessary owing to the large number of different parameter sets presented in this work, and is, in context to the names of the other series, consistent. The applied silane concentration SC was changed for each "SC-series", by changing the silane flow, or the hydrogen flow, as described in the individual section.

It is important to point out that, within each individual SC-series, the H_2 flow and the SiH_4 was constant, but the CO_2 flow was varied. This means that, in each SC-series, the "true" hydrogen dilution with respect to the $CO_2 + SiH_4$ flow varies considerably. The possible effect of the varying "true" hydrogen dilution on growth and material structure were evaluated by preparing the (S+O)C-series with a constant sum of CO_2 and SiH_4 flow while varying the r_{CO2} within this (S+O)C-series. To describe the $CO_2 + SiH_4$ concentration in hydrogen *(S+O)C,* the following definition is used:

$$(S+O)C = \frac{SiH_4 + CO_2}{SiH_4 + CO_2 + H_2} \tag{2.18}.$$

Figure 2.8 shows the variation of the gas flows for exemplary series to visualise the differences between process gas flows with in SC-series and the (S+O)C-series. The SiH_4 flow and the CO_2 flow are plotted versus the r_{CO2}. In Figure 2.8 a) and Figure 2.8 b), the flows for two SC-series with the respective concentrations $SC=0.2\%$ and $SC=0.1\%$ are shown. In Figure 2.8 c) and Figure 2.8 d), the flows for series with $(S+O)C=0.25\%$ and $(S+O)C=0.5\%$ are shown, respectively. For the (S+O)C-series, the sum of the CO_2 flow and the SiH_4 flow was constant. Consequently, in order to increase the r_{CO2}, the SiH_4 flow is decreased and the CO_2 flow was increased. For SC-series, the SiH_4 flow was constant and only the CO_2 flow was increased, to increase the r_{CO2}. A more detailed but more complex visualisation of the differences between SC-series and (S+O)C-series is given in Appendix C.
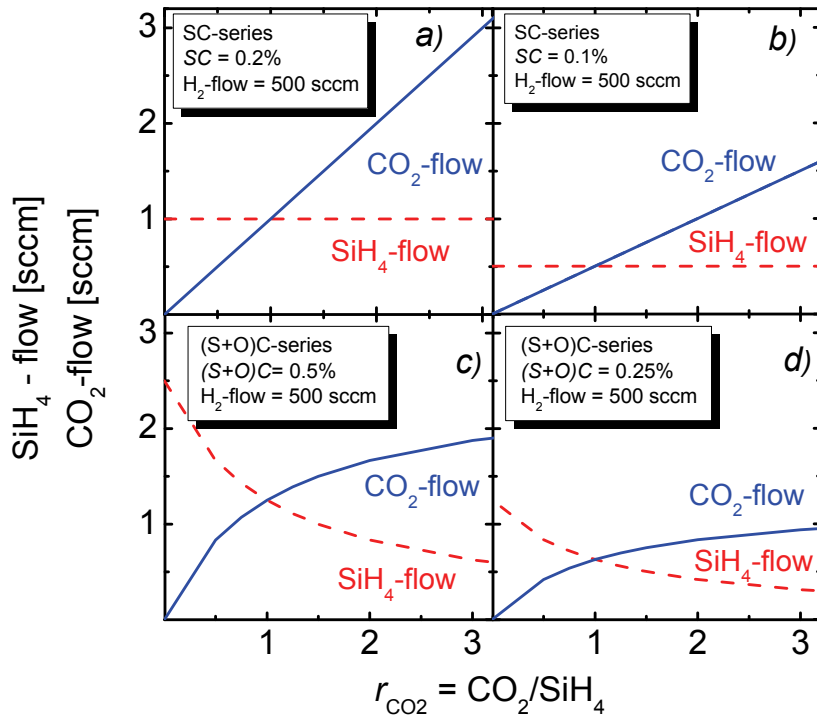

Figure 2.8: The SiH_4 flow and the CO_2 flow versus the CO_2/SiH_4 ratio r_{CO2} as used for exemplary series. a) The flows for an SC-series using a constant silane concentration SC of 0.2% versus the r_{CO2}. b) The flows versus the r_{CO2} also for the SC-series but an SC of 0.1%. c) and d) the corresponding gas flows for (S+O)C-series with a constant sum of $SiH_4 + CO_2$ flow versus the r_{CO2}. c) For an (S+O)C of 0.5% and in d) for an (S+O)C of 0.25%. For all series shown here, a constant hydrogen flow H_2 flow of 500 sccm was used. The dopant gas flows are not shown here for clarity reasons. The dilution gas (SiH_4, H_2) were considered in the calculation of e.g. the silane concentration SC.

2.3   Summary

This chapter describes the techniques to determine the properties of the µc-SiO$_x$:H with a focus on the proposed application as doped layer in thin-film silicon solar cells. These techniques are necessary to understand the interdependence between the deposition conditions, structure/composition and the layer properties. Especially, the evaluation of the crystalline volume fraction was investigated in more detail and different measurement techniques were compared. Additionally, detailed deposition conditions and material properties of the individual silicon layers are presented in this study since they are of basic importance for the understanding of the presented properties of the solar cell devices. For the measurement of the solar cell properties, a cell contact configuration was presented, which addresses the specific issues, when measuring the solar cell properties (e.g. quantum efficiency) for a tandem solar cell with intermediate reflector.

Chapter 3

Background information about silicon oxygen alloys

In this chapter, some background information about the μc-SiO$_x$:H material, which is required for understanding this thesis, is presented. Figure 3.1 shows a model of the silicon dioxide (SiO$_2$) in its crystalline α-quartz structure. The atom coordinates are taken from [110], as shown by [111], using the program Jmol [112]. Each of the four oxygen (O) atoms on one tetrahedral Si-O$_4$ unit is shared with another silicon atom of a surrounding tetrahedral Si-O$_4$ unit. The resulting net chemical formula is SiO$_2$. Amorphous silicon dioxide (a-SiO$_2$) also has a tetrahedral structure in the short range order, but this order is lost in the long range [113].
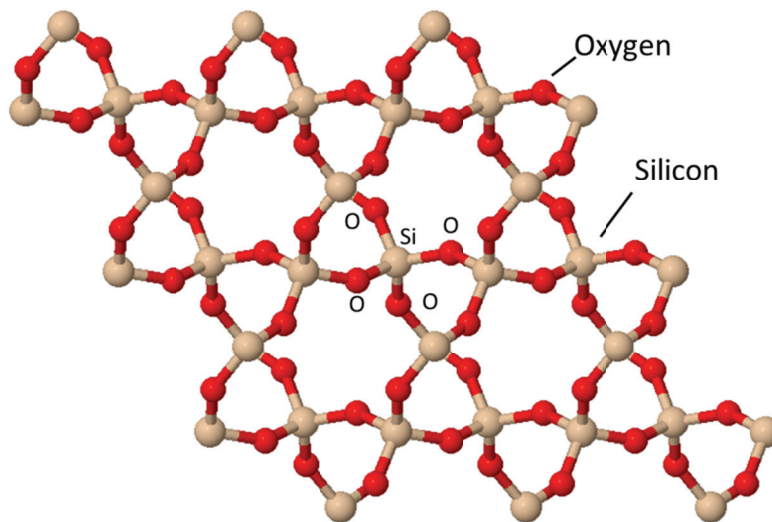
Figure 3.1: A schematic model that illustrates the structure of SiO$_2$ in crystalline α-quartz structure drawn with Jmol [112]. The atom coordinates are taken from [110] as shown by [111]. The silicon atoms are illustrated in white and the oxygen atoms in red. The tetrahedral unit is a central silicon atom bonded to four oxygen atoms.

Hydrogenated amorphous silicon oxide (a-SiO$_x$:H) is assumed to be a material whose stoichiometry factor x is between 0 and 2. a-SiO$_x$:H also contains a considerable amount of hydrogen. However, the stoichiometry factor x in a-SiO$_x$:H describes the ratio between the number of oxygen atoms and silicon atoms $x=$O$/$Si(at.). Alternatively, the oxygen content

[O]$=$O$/$(O$+$Si) is used, where the number of oxygen atoms is related to the sum of silicon atoms and oxygen atoms.

Both quantities are related via the equations (see also Appendix A)

$$[O] = \frac{x}{x+1}$$ (3.1) and,

$$x = \frac{[O]}{1-[O]}$$ (3.2).

This implies that, if the stoichiometry factor *x* varies between 0 and 2, then the oxygen content [O] can vary between 0 and a maximum value of 0.66. Both quantities consider just the number of silicon/oxygen atoms and not the number of atoms of other elements, e.g. hydrogen, which is also incorporated to a considerable amount of up to 20%. This means that the calculated oxygen content is the ratio of the number of oxygen atoms related to the sum of silicon and oxygen atoms and does not take the incorporated hydrogen or other elements into account. However, the oxygen content in the material has a great influence on the structure and the optoelectronic material properties.

There are two commonly used models for the atomic structure of a-SiO$_x$:H: the random bond model (RBM) and the random mixture model (RMM). Both models describe a mixture of silicon and oxygen and agree in the following assumptions [114,115]:

- Each silicon atom is bonded to four other atoms, silicon or oxygen
- Each oxygen atom to bonded to two silicon atoms
- The oxygen atoms are not bonded to another
- The average Si-O bond length is $\approx 1.62\,\text{Å}$
- The average Si-Si bond length is $\approx 2.35\,\text{Å}$
- The average bond angle of Si in the tetrahedral configuration is 109.5°
- The average bond angle in the Si-O-Si configuration is 144°

From these assumptions, one can derive possible tetrahedral units of the a-SiO$_x$:H, as shown in Figure 3.2. Starting from the Si-Si$_4$ (left side), the Si atoms are substituted by oxygen atoms at the tetrahedral edges, one after the other. At the right side, for the Si-O$_4$, all Si atoms, except for the central silicon atom, are all substituted by oxygen atoms, creating a SiO$_2$ structure with an oxygen content of 0.66.
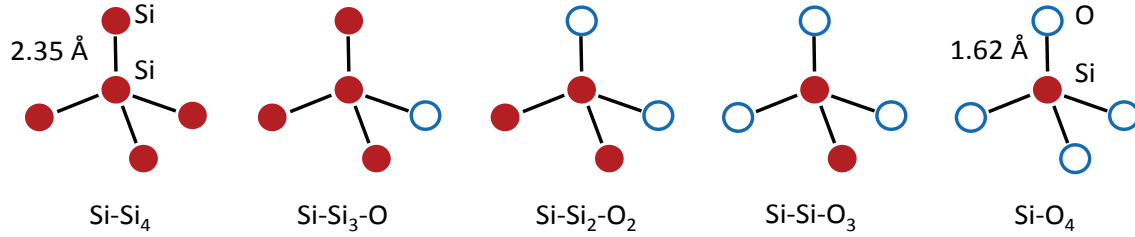
Figure 3.2: The 5 possible tetrahedral units of the a-SiO$_x$:H alloys. From left to right: increasing number of oxygen atoms at the edges of the tetrahedral unit. The filled circles represent the silicon atoms, the empty circles the oxygen atoms.

The random bond model (RBM) is a microscopic model of a-SiO$_x$:H, which considers the probability P of **all** 5 binding configurations Si-Si$_y$-O$_{4-y}$ with y = 0, 1, 2, 3, 4 (P_{Si-O4}, $P_{Si-Si-O3}$, $P_{Si-Si2-O2}$, $P_{Si-Si-O3}$, P_{Si-Si4}). In the RBM, the relative concentrations of the 5 tetrahedral configurations are calculated according to their probability [116]. The relative probabilities P of the binding configurations are given as a function of the stoichiometry factor x [116] as

$$P_y(x) = \frac{4!}{(4-y)!\, y!} \left(\frac{x}{2}\right)^{4-y} \left(1 - \frac{x}{2}\right)^y \qquad (3.3).$$

In contrast to the RBM, the random mixture model (RMM) considers a-SiO$_x$:H as a mixture of oxygen-rich regions and regions of silicon. This means that SiO$_x$ does not exist as a distinct substance, but can be considered as a mixture of Si (Si-Si$_4$) and SiO$_2$ (Si-O$_4$). The RMM assumes that other binding configurations **rarely** exist. This means, for the RMM, the stoichiometry factor x can be converted to the a-SiO$_2$ (Si-O$_4$) fraction in a-SiO$_x$:H by the equation (see also Appendix A)

$$a\text{-}SiO_2 - \text{fraction} = \frac{x}{2} \qquad (3.4).$$

Consequently, only binding configurations with $y=0$ (P_0) and $y=4$ (P_4) are permitted as a function of the stoichiometry factor x. The relative probabilities, which conserve the number of atoms for Si and O, can be described [116] as:

$$P_0(x) = \left(\frac{x}{2}\right) \qquad P_1 = P_2 = P_3 = 0 \qquad P_4(x) = \left(1 - \frac{x}{2}\right) \qquad (3.5)$$

Figure 3.3 shows the relative probabilities of the tetrahedral binding configurations versus the stoichiometry factor x on the lower x-axis and the corresponding oxygen content [O] on the upper x-axis. The probabilities for the RBM model are represented by the solid curves and for the RMM model by the dashed lines. The corresponding binding configurations are labelled in the graph.
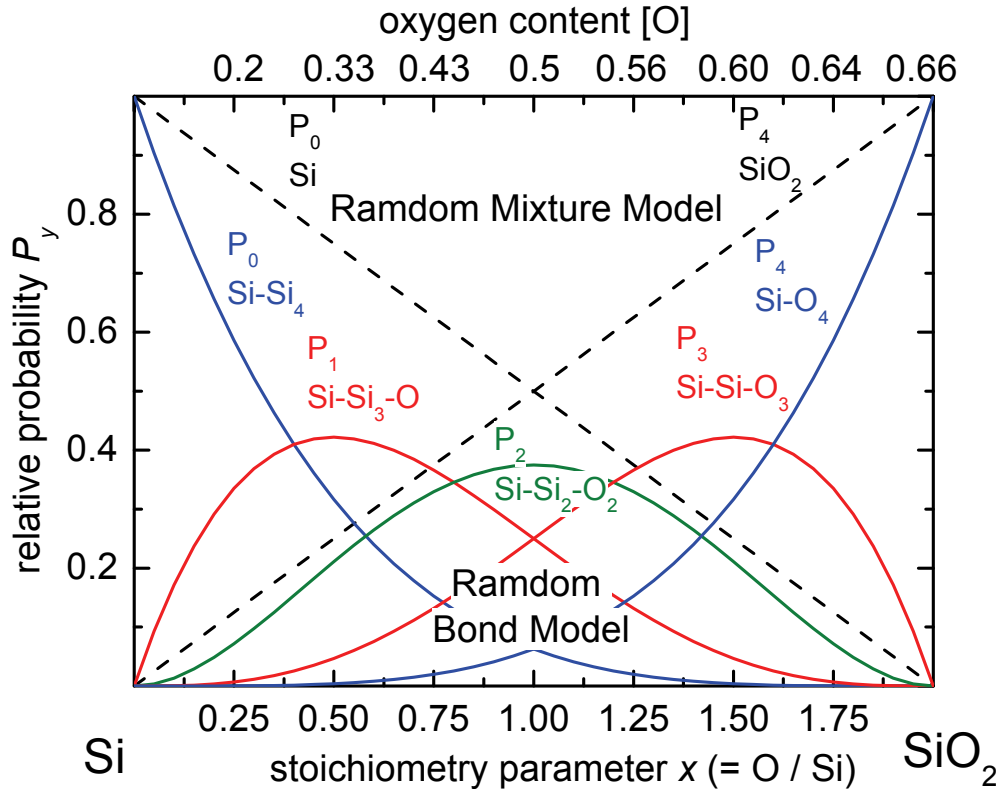
Figure 3.3: The probabilities of the tetrahedral binding configuration versus the stoichiometry factor x on the lower x-axis and the oxygen content [O] on the upper x-axis for the RBM model (solid curves) and for the RMM model (dashed lines) [114,116]. The corresponding binding configurations are labelled in the figure.

Whether the RBM or the RMM describes the structure of the a-SiO$_x$:H better depends on the deposition technique, gases and parameters used for its preparation [62,117-120]. If plasma enhance chemical vapour deposition (PECVD) is used for preparation, the type of process gas as source for the oxygen also has an influence. For example the structure was described by the RBM model when using nitrous oxide (N$_2$O) or oxygen O$_2$ [118-120]. When carbon dioxide (CO$_2$) was used as the process gas, the binding configuration in the material was described by the RMM model [117,121]. Within the RMM model, it is plausible that at the interface between a Si region and a SiO$_2$ region there are also binding configurations other than Si-O$_4$ (P_4) and Si-Si$_4$ (P_0). The fraction of other binding configurations ($P_1 \ldots P_3$) will be small if the Si regions and the SiO$_2$ regions are spatially extended [114]. If the Si regions and the SiO$_2$ regions are not spatially extended, then other binding configurations ($P_1 \ldots P_3$) will be present and both models could be applied to the same material.

Figure 3.4 shows results from infrared spectroscopy that was used to classify material prepared in the present study according to the structural model that better describes the structure of the a-SiO$_x$:H phase. Figure 3.4 shows the wavenumber of the peak position for the Si-O-Si stretching mode ($\nu_{\text{Si-O-Si}}$) versus the oxygen content [O] in the film. For films prepared using CO$_2$ as oxygen source gas, the triangles represent the $\nu_{\text{Si-O-Si}}$ for a-SiO$_x$:H from [62] and the squares represent the $\nu_{\text{Si-O-Si}}$ for μc-SiO$_x$:H from the present study. For films prepared by remote plasma enhanced chemical vapour deposition (RPECVD), using SiH$_4$/N$_2$O/He as process, the circles

represent the $\nu_{Si-O-Si}$ [120]. The dashed line is the calculated $\nu_{Si-O-Si}$ versus the oxygen content, taking theoretical assumptions of the RBM model into account [118]. With these theoretical assumptions, $\nu_{Si-O-Si}$ increases from $\nu_{Si-O-Si}=940$ cm^{-1} to $\nu_{Si-O-Si}=1080$ cm^{-1} with the oxygen content [118], which is in good agreement with experimental data from samples deposited by RPECVD, using $SiH_4/N_2O/He$ as process gas [120]. For these samples, the Si atoms and the O atoms are distributed as proposed by the RBM model. In contrast, the $\nu_{Si-O-Si}$ for films which are prepared using CO_2 as an oxygen source (triangles, squares) does not follow this trend and the $\nu_{Si-O-Si}$ is closer to the $\nu_{Si-O-Si}$ of stoichiometric of $a-SiO_2$ at $\nu_{Si-O-Si}=1080$ cm^{-1} [122]. This indicates that the doped $\mu c-SiO_x:H$ from the present study prepared with CO_2 as oxygen source gas (squares), is most likely better described by the RMM. Consequently, it consists mainly of a mixture of (i) silicon rich regions and (ii) oxygen rich regions. The oxygen rich regions can be considered mainly as $a-SiO_2$ phase [55].
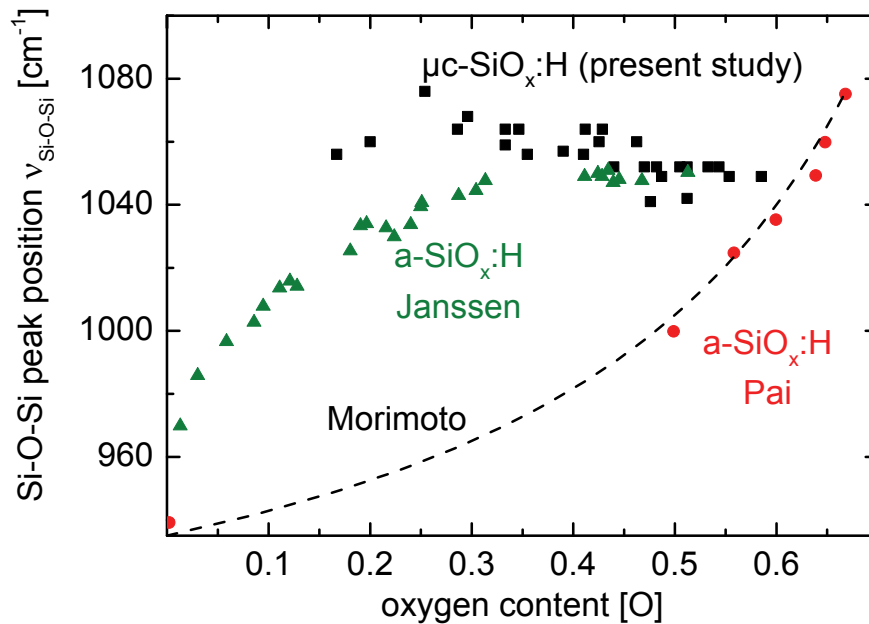

Figure 3.4: The peak position of the Si-O-Si stretching mode versus the oxygen content for various samples. Circles represent the data from Pai [120] for samples using RPECVD and $SiH_4/N_2O/He$ as process gas for the preparation. The triangles represent data from Janssen [62] and squares represent the data from the present study, for samples using CO_2 as the oxygen source for the preparation. The dashed curve represents the calculated the $\nu_{Si-O-Si}$ versus the oxygen content taking theoretical assumptions of the RBM model from Morimoto [118] into account.

This phase separation of the $a-SiO_x:H$ [121] prepared by PECVD using CO_2 as the oxygen source makes it possible to use the advantages of both phases. (i) The $a-SiO_2$ phase has a wide optical band gap [37]. (ii) The doped a-Si:H phase has a higher electrical conductivity [36] than the doped $a-SiO_2$ phase. To further increase the conductivity, a doped microcrystalline silicon ($\mu c-Si:H$) phase can be implemented, for example. Doped $\mu c-Si:H$ has a higher conductivity than doped a-Si:H and can also be prepared by using PECVD. The resulting microcrystalline silicon oxygen alloy $\mu c-SiO_x:H$, was proposed as a phase mixture of (i) $\mu c-Si:H$ and (ii) a-SiO:H [34].

decreasing crystalline volume fraction

several
100 nm

~30-50 nm

stationary
columnar growth

incubation
zone

substrate

crystallites   amorphous regions   voids

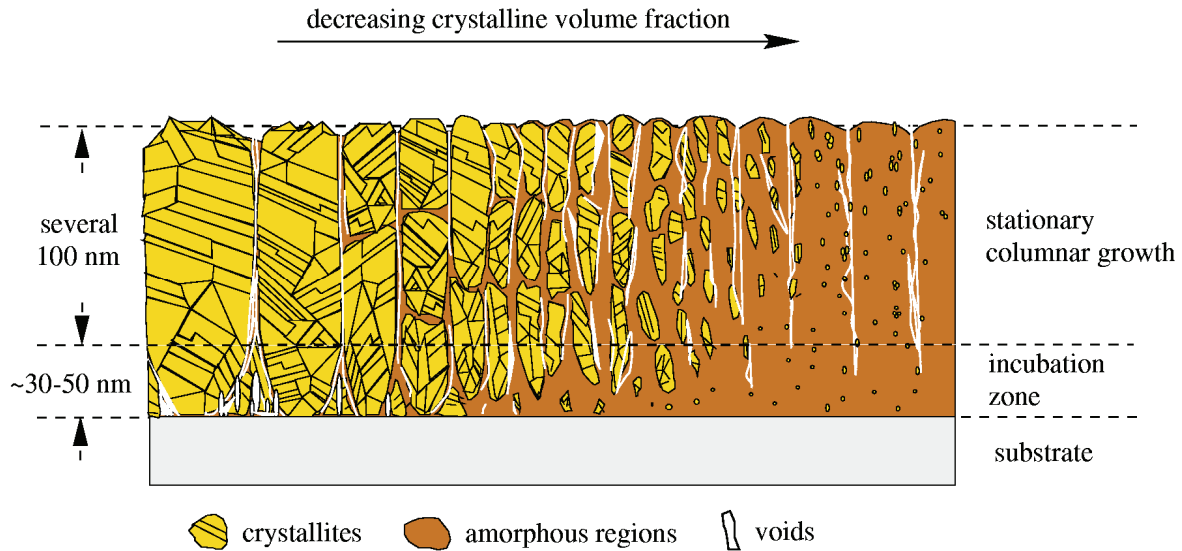*Figure 3.5: A schematic model which illustrates the microstructure of hydrogenated microcrystalline silicon (μc-Si:H) deposited by PECVD on a glass substrate. From the left side to the right side the film structure changes from highly microcrystalline silicon to almost amorphous silicon (a-Si:H). This figure is taken from [123].*

In the following the microcrystalline silicon (μc-Si:H) is introduced and details about the dependence of the structure on the silane concentration are described. Figure 3.5 shows a schematic model that illustrates the microstructure of microcrystalline silicon (μc-Si:H) deposited by PECVD [123]. From the left side to the right side of Figure 3.5, the film structure changes from highly microcrystalline silicon to almost amorphous silicon (a-Si:H). The film structure can be varied by, e.g. the silane concentration in hydrogen [7]. To grow highly microcrystalline silicon the silane concentration has to be decreased [40-42]. Figure 3.5 illustrates a columnar growth of the μc-Si:H [123,124], with elongated crystallites in the direction of growth. These elongated crystallites in the growth direction can be beneficial for the electrical conductivity in the growth direction, which is the desired direction of the current flow through the doped layer in a thin-film silicon solar cell.
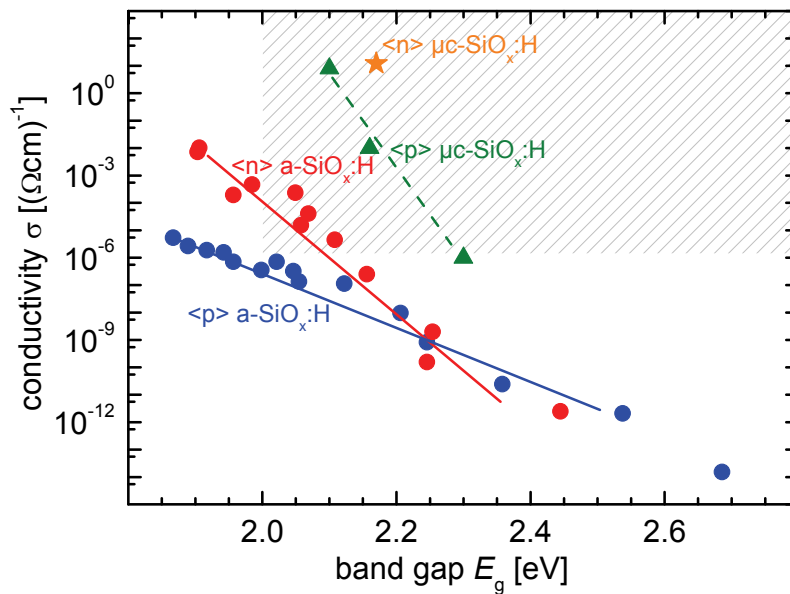
Figure 3.6: The conductivity σ versus the optical band gap for doped a-SiO$_x$:H (circles) [125], for μc-SiO$_x$:H p-type
(triangles) [43] and for μc-SiO$_x$:H n-type (star) [44]. The shaded area shows the combination of (i)
conductivity above the empirical limit for the use of the p-layer in solar cells and (ii) optical band gap as
typically achieved for commonly used p-type a-SiC:H window layers [104]. The conductivity and the
optical band gap where measured on the p-layer deposited as single layer with a thickness of several
hundred nanometres on a glass substrate.

Some optoelectronic properties from previous studies of doped μc-SiO$_x$:H and a-SiO$_x$:H are shown in Figure 3.6. Here, the conductivity σ is plotted against the optical band gap for n/p-type a-SiO$_x$:H (circles) [125], for p-type μc-SiO$_x$:H (triangles) [43], and for n-type μc-SiO$_x$:H (the star) [44]. As shown by [37,125], the optical band gap E_{04} of doped a-SiO$_x$:H can be increased by increasing the oxygen content in the material. The conductivity of the n-type and p-type a-SiO$_x$:H decreases with increasing band gap (circles), similar to the p-type μc-SiO$_x$:H (triangles), due to the lower doping efficiency in a-SiO$_x$:H that is a result of the strong compensation of active dopant configurations by defects [126]. At a given E_{04}, p/n-type a-SiO$_x$:H samples (circles) [125] have a conductivity of 3 to 7 magnitudes lower than the doped μc-SiO$_x$:H samples [34,35,43]. This demonstrates the influence of the doped μc-Si:H phase in the a-SiO$_x$:H material on the conductivity at a given band gap. p-Type window layers for thin-film silicon solar cell applications should have a conductivity of $>10^{-6}(\Omega cm)^{-1}$ when prepared as single layers on glass with a thickness of several hundred nanometres as empirical determined [104]. Note: In solar cells, the p-layers have a thickness of <20 nm. However, such thin layers are difficult or impossible to measure accurately and it is therefore general practice to perform the material optimisation and evaluation on "thick" layers. The shaded area illustrates the targeted combination of conductivity $>10^{-6}(\Omega cm)^{-1}$ and an optical band gap greater than for p-type a-SiC:H with a conductivity in this range [104].

This p-type µc-SiO$_x$:H material can be beneficially used as e.g. the window layer [43] in thin-film silicon solar cells. Despite the absence of information about the refractive index of µc-SiO$_x$:H [43,44] at the beginning of the present study, one can assume that the refractive can be tuned to lower values, analogous to a-SiO$_x$:H [37,127] and therefore is likely to be applicable as intermediate reflector.
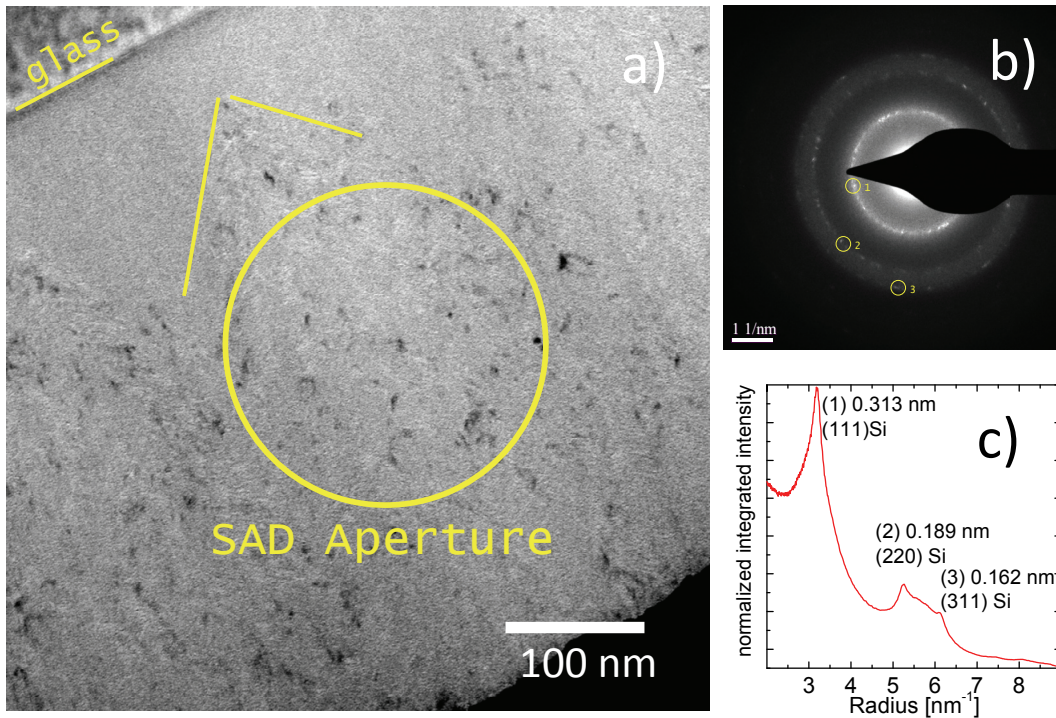

Figure 3.7: a) Cross section transmission electron bright field image, b) selected area diffraction (SAD) pattern and c) radial profile extracted from the SAD pattern of n-type µc-SiO$_x$:H, as an example from the present study. The µc-SiO$_x$:H has a crystalline volume fraction of 22%, as evaluated from the radial profile of the selected area diffraction pattern.

Figure 3.7 a) shows a cross section transmission electron bright field image, b) the selected area diffraction (SAD) pattern and c) the radial profile extracted from the SAD pattern of doped µc-SiO$_x$:H from the present study. The sample shown in Figure 3.7 has an oxygen content of ≈ 0.2, which was measured by Rutherford back scattering (RBS), and a crystalline volume fraction of 22%, as evaluated from the radial profile of the SAD pattern (Figure 3.7 c). The image in Figure 3.7 a) shows the conical growth structures in the z ß zone (indicated for one cone by the set of curves), as already suggested by the model in Figure 3.5. In the incubation zone, the microcrystalline regions are separated by wide a-SiO$_x$:H regions. When measuring the conductivity in the lateral direction for a film thinner than the incubation zone, the large separation of the doped µc-Si:H regions has a strong influence on the conductivity. However, even if the doped microcrystalline silicon regions are separated in the lateral direction, a percolation path through the doped µc-Si:H regions for the current in the perpendicular direction (growth direction) is likely to be present [128-130].

The size and location of the aperture used to obtain the diffraction pattern (SAD Aperture) are also shown in the image. The peak positions in the radial profile of the SAD pattern (Figure 3.7 c) are typical for µc-Si:H, and one can conclude that the microcrystalline phase does not show any peak that could be related to quartz c-SiO_2 and, therefore, that most of the oxygen is present in the a-SiO_x:H phase. Similar results were also reported in previous studies on n-type µc-SiO_x:H [44].

From [34,35,43,44] and this chapter, one can assume that each phase performs different functions: the a-SiO_x:H phase has the required optical properties, while the required electrical properties are provided by the doped microcrystalline silicon phase, as described below.

(i) **The doped amorphous silicon oxide phase (a-SiO_x:H)** could be considered as a mixture of an **a-Si:H fraction** and an **a-SiO_2 fraction** [121]. The a-SiO_x:H phase has a wide optical band gap and a refractive index tuneable to lower values [37]. The wide optical band gap is important to achieve a low parasitic absorption in the solar cell as compared to non-alloyed a-Si:H. A refractive index tuneable to low values is important in order to increase the reflection of the intermediate reflector/back reflector or to reduce the reflection at the window layer.

(ii) **The doped microcrystalline silicon phase** considered as µc-Si:H with a high crystalline volume fraction (crystalline nanoparticles) ensures a sufficient electrical conductivity for a low series resistance of the intermediate reflector, the doped layers, and a low contact resistance to the contacts of the cell. In addition, a microcrystalline phase acts as a nucleation layer and improves growth in subsequent layers [24-29].
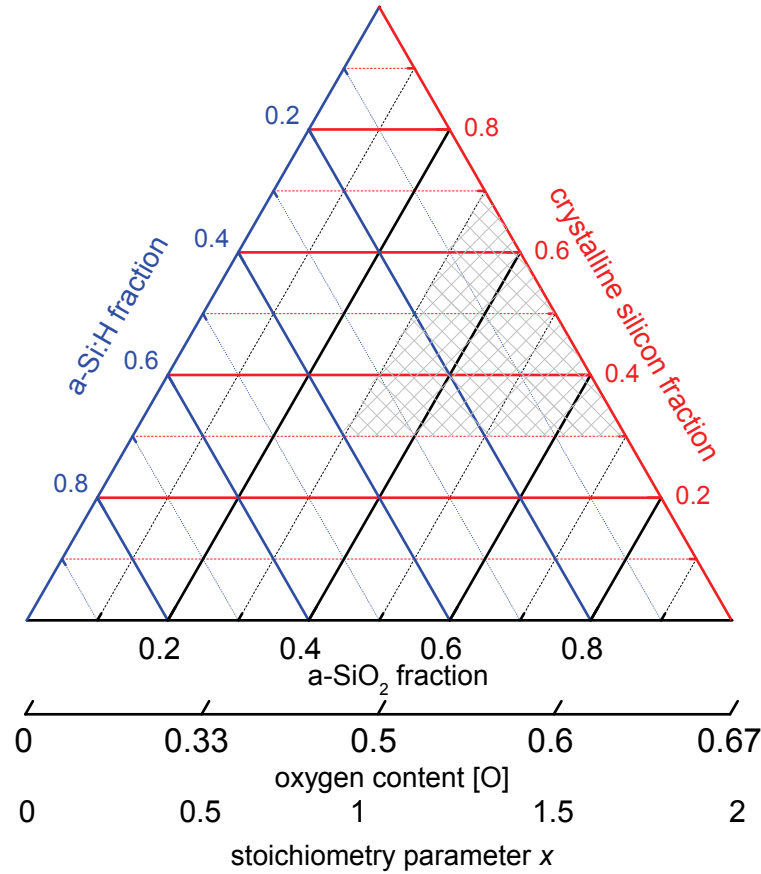
Figure 3.8: For μc-SiO$_x$:H the fractions of amorphous silicon dioxide (a-SiO$_2$), amorphous silicon (a-Si:H) and crystalline silicon are plotted in a ternary diagram. This diagram ensures that the sum of the fractions is one. The shaded triangle indicates the composition that probably results in favourable material properties with a higher transparency for higher oxygen contents.

The amorphous silicon oxide a-SiO$_x$:H is described as material which consists of two fractions the a-Si:H and the oxygen rich a-SiO$_2$ fraction in almost stoichiometric configuration. For clarification, in the present study a-SiO$_x$:H will often be referred to as one phase for simplicity reasons. The crystalline silicon fraction consists of crystalline silicon nanoparticles similar as in microcrystalline silicon with a high crystalline volume fraction.

To visualise the phases compositions Figure 3.8 shows a ternary diagram that summarises possible compositions of μc-SiO$_x$:H. μc-SiO$_x$:H could be thought to consist of three fractions: the crystalline silicon (silicon nanoparticles), the a-Si:H, and the a-SiO$_2$. Based on this assumption, it is plausible that the fractions of the three phases should add up to one. The ternary diagram in Figure 3.8 allows the determination of the unknown fraction when the two other fractions are known and the visualisation of the μc-SiO$_x$:H composition. Parallel to the a-SiO$_2$ fraction axis, the corresponding oxygen content and the stoichiometry factor x are shown. From this axis, one can convert the quantities of the oxygen content to the stoichiometry factor x and

the a-SiO$_2$ fraction. The shaded triangle indicates the composition of the phases, which probably results in favourable material properties for the applications proposed in this thesis. The crystalline silicon fraction is >0.33, which is above the percolation threshold [128,129], and thus ensures a sufficient conductivity, but is low enough to enable a substantial a-SiO$_2$ fraction of >0.3 to achieve a high transparency. Additionally, the μc-SiO$_x$:H with a composition as indicated by the shaded area has a substantial crystallinity to act as a nucleation for an subsequent μc-Si:H layer. A crystalline SiO$_2$ phase is not considered because the diffraction pattern does not indicate that it is present.

In summary, the background information required to understand the work in this thesis has been presented. The structure of a-SiO$_x$:H and parameters for describing the alloy composition were presented, and background information on the various phases of doped μc-SiO$_x$:H was summarised. Finally, the basic concept of the functions of each of the phases in the μc-SiO$_x$:H alloy was explained.

This background information will help to understand the influence of the structure/composition on the optical and electrical properties. The variation of the structure and the composition by adjusting the gas flow parameters will be presented in the following chapter 4.

Chapter 4

Development of doped microcrystalline silicon oxide

Doped microcrystalline silicon oxide (μc-SiO$_x$:H) layers have been prepared by plasma enhanced chemical vapour deposition (PECVD) for use in thin-film silicon solar cells. For this application, the material has to fulfil certain requirements including high transparency, tuneable refractive index together with a sufficient conductivity and, in case the subsequent layer is microcrystalline, it should act as nucleation layer. With a focus on these properties, a detailed variation of the gas flow parameters was performed and their influence on the resulting film properties was analysed. Doped μc-SiO$_x$:H films with a conductivity above 10^{-5} (Ωcm)$^{-1}$ were developed. For these films with a low refractive index of around 1.9, a wide optical band gap above 2.5 eV was achieved. However, also films with a wide range of refractive indices ($2 > n > 3.5$), which are more transparent ($E_{04} > 2.0$ eV) compared to non-alloy silicon films were developed with a conductivity above 10^{-5} (Ωcm)$^{-1}$.

4.1 Introduction

For the use of doped microcrystalline silicon oxide (μc-SiO$_x$:H) applied as a doped layer or as the intermediate reflector in thin-film silicon solar cells, the material has to fulfil certain requirements, which are: high transparency, a refractive index tuneable to low values, and sufficient conductivity (see section 1.3). In addition, the doped μc-SiO$_x$:H layer has to serve as a nucleation layer for the subsequent layer, in case this is microcrystalline. Therefore, the important material parameters are optical band gap (E_{04}), refractive index (n), conductivity (σ), and crystalline fraction (I_c). The aim is to develop doped μc-SiO$_x$:H that is a mixed phase material consisting of an oxygen-rich amorphous silicon oxide (a-SiO$_x$:H) and a doped microcrystalline silicon (μc-Si:H) phase with a high crystalline volume fraction. This phase mixture is intended to improve the optical properties with respect to doped μc-Si:H and the electrical properties with respect to doped a-SiO$_x$:H, in order to achieve a sufficient conductivity

and a high transparency. The present study provides a detailed description of the doped μc-SiO_x:H material development, with a focus on the relationship between the process gas flow parameters and the material properties. The chapter will also report on the relationship between the optoelectronic properties and the material structure/composition. n-Type and p-type doping of the μc-SiO_x:H material was achieved using phosphine (PH_3) and trimethylboron ($B(CH_3)_3$ or TMB), respectively. For use in thin-film silicon solar cells, similar requirements for the properties for both n- and p-type μc-SiO_x:H films have to be fulfilled. Therefore, a very similar systematic approach of the material development and data presentation was used for both types of doping. Details about the process gas flow variations and results for n-type and p-type μc-SiO_x:H are presented in section 4.2 and section 4.3 respectively. A summary of the properties of n-type and p-type μc-SiO_x:H is given in chapter 5.

4.2   Development of n-type microcrystalline silicon oxide

Two types of n-type μc-SiO_x:H sample series were prepared: the silane concentration series (SC-series) and the PH_3-series. For both type of sample series the main parameters e.g. *SC,...* was varied. Within each of the individual sample series, the CO_2 / SiH_4 ratio r_{CO2} was varied by varying the CO_2 flow. A detailed description of the gas flow variations is given below. All other preparation details, that remained identical for all series, such as deposition pressure, etc., have been described previously in section 2.2.4.

4.2.1   Details of the applied process gas flow variations

SC-series

At each value of silane concentration (*SC*) parameter, the CO_2/SiH_4 ratio (r_{CO2}) was varied in one series, called SC-series. While this terminology SC-series is unfortunately a bit misleading, as it does not refer to a variation in the SC concentration within the series, nevertheless it is necessary owing to the large number of different parameter sets presented in this work, and is, in context to the names of the other series, consistent. For all SC-series in the development of n-type μc-SiO_x:H, the silane flow was kept constant at 1 sccm and the phosphine flow was 0.02 sccm. Details about the process gas flows in the individual SC-series are given in Table 4.1. The sample series are named in the first column according to the silane concentration (*SC*) that was used for the particular sample series.

*Table 4.1: The **SC-series** are named in the first column according to the silane concentration SC, which was kept constant within each sample series. The gas flows are shown for each SC-series in the corresponding rows in sccm. The resulting variation in CO_2/SiH_4 ratio r_{CO2} is shown in the last column.*

SC-series *SC*=const.	SiH_4 flow [sccm]	H_2 flow [sccm]	CO_2 flow [sccm]	PH_3 flow [sccm]	r_{CO2} SiH_4/CO_2 ratio
1.0%	1	100	0-3	0.02	0-3
0.5%	1	200	0-3	0.02	0-3
0.2%	1	500	0-7	0.02	0-7
0.1%	1	1000	0-3	0.02	0-3

Figure 4.1 shows, as one example, the process gas flows for the 0.5% SC-series versus the r_{CO2}. To increase the r_{CO2}, the CO_2 flow was increased. In this way, the r_{CO2} was varied between 0 and 3. To obtain the silane concentration for the particular SC-series, the hydrogen flow was varied as indicated by the arrow in Figure 4.1. For example, the 1% SC-series had a hydrogen flow of 100 sccm or the 0.1% SC-series a hydrogen flow of 1000 sccm.
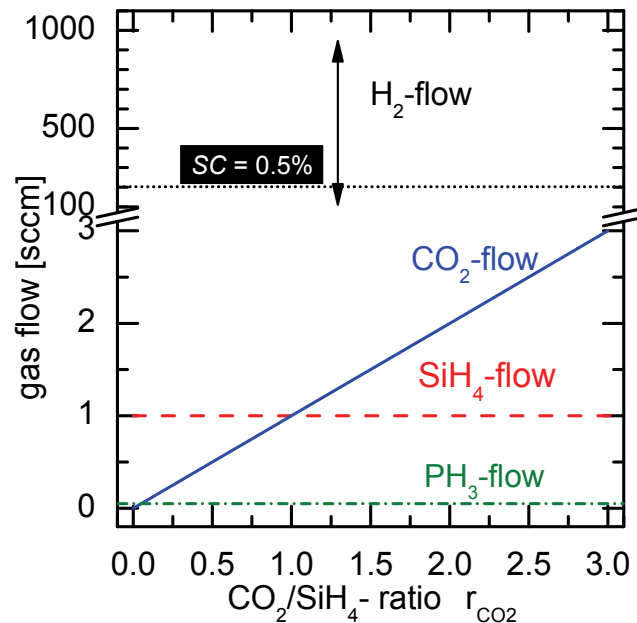

Figure 4.1: The process gas flows versus the CO_2/SiH_4 ratio r_{CO2} shown as an example for the SC-series with a silane concentration of 0.5%. The arrow indicates the process gas flow that was varied between the particular SC-series. The process gases are as indicated on the graph. For details of the process gas flows, see Table 4.1.

PH₃-series

For all PH_3-series in the development of n-type μc-SiO_x:H, the silane flow was kept constant at 1 sccm and the hydrogen flow was 500 sccm, to obtain a 0.2% silane concentration. Details of the pure process gas flows in the individual PH_3-series are given in Table 4.2, the set point values for the mass flow controllers were adjusted accordingly to the used source gas for the phosphine doping that is either 5% PH_3 in H_2 or 2% PH_3 in SiH_4. The sample series are named, in the first column, according to the pure phosphine flow that was used for the particular sample series. In each PH_3-series, the CO_2/SiH_4 ratio was varied.

*Table 4.2: The **PH$_3$-series** are named in the first column by using the pure phosphine flow in sccm, which was kept constant within each sample series. The gas flows in sccm are shown for each sample series in the corresponding rows. The SC in % is shown in the second last column. The resulting variation in CO$_2$/SiH$_4$ ratio r_{CO2} is shown in the last column.*

PH$_3$-series PH$_3$ flow = const.	SiH$_4$ flow [sccm]	H$_2$ flow [sccm]	CO$_2$ flow [sccm]	SC [%]	r_{CO2}
0.00 sccm	1	500	0 - 3	0.2	0 - 3
0.01 sccm	1	500	0 - 3	0.2	0 - 3
0.02 sccm	1	500	0 - 7	0.2	0 - 7
0.04 sccm	1	500	0 - 6	0.2	0 - 6

Figure 4.2 shows, for example, the process gas flows for the 0.04 sccm PH$_3$-series versus the r_{CO2}. To increase the r_{CO2}, the CO$_2$ flow was increased. In this way, the r_{CO2} was varied between 0 and 6. For the particular PH$_3$-series, the phosphine flow was varied as indicated by the arrow in Figure 4.2.
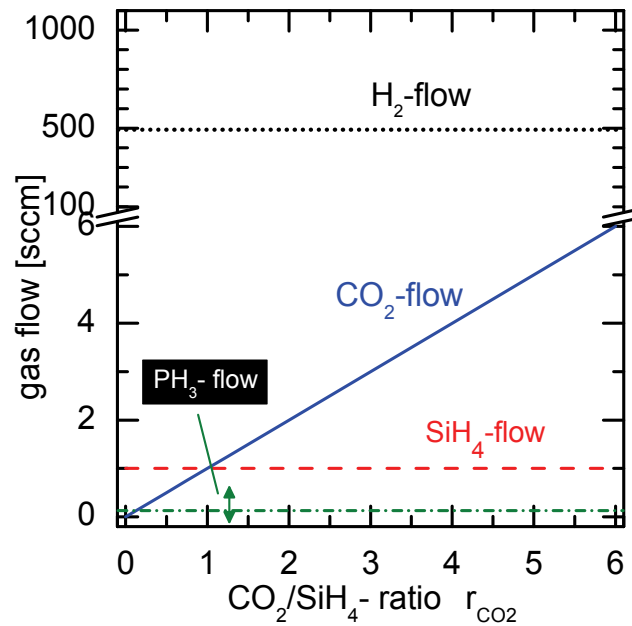

Figure 4.2: The process gas flows versus the CO$_2$/SiH$_4$ ratio r_{CO2} shown as an example for the PH$_3$-series, with a phosphine flow of 0.04 sccm. The arrow indicates the process gas flow that was varied between the particular PH$_3$-series. The process gases are as indicated on the graph. For details of the process gas flows, see Table 4.2.

4.2.2   Deposition rate

The deposition rate r_D of the μc-SiO$_x$:H layers was determined, in order to be able to adjust the layer thickness in the cell. Figure 4.3 shows the deposition rate r_D as a function of the CO$_2$/SiH$_4$ ratio r_{CO2} for different silane concentrations $SC = SiH_4/(H_2 + SiH_4)$ as indicated. The deposition

rate was determined on films with a thickness between 300 nm and 2 µm. To vary *SC*, the hydrogen flow was varied and a silane flow of 1 sccm was used within these series. The deposition rate r_D increases with increasing silane concentration *SC* (indicated by the arrow). To increase the r_{CO2}, the CO_2 flow was increased within an SC-series. The increase in the CO_2 flow has a slightly smaller effect on the deposition rate than the silane concentration *SC*. However, the deposition rate increases with both the *SC* and the r_{CO2}.
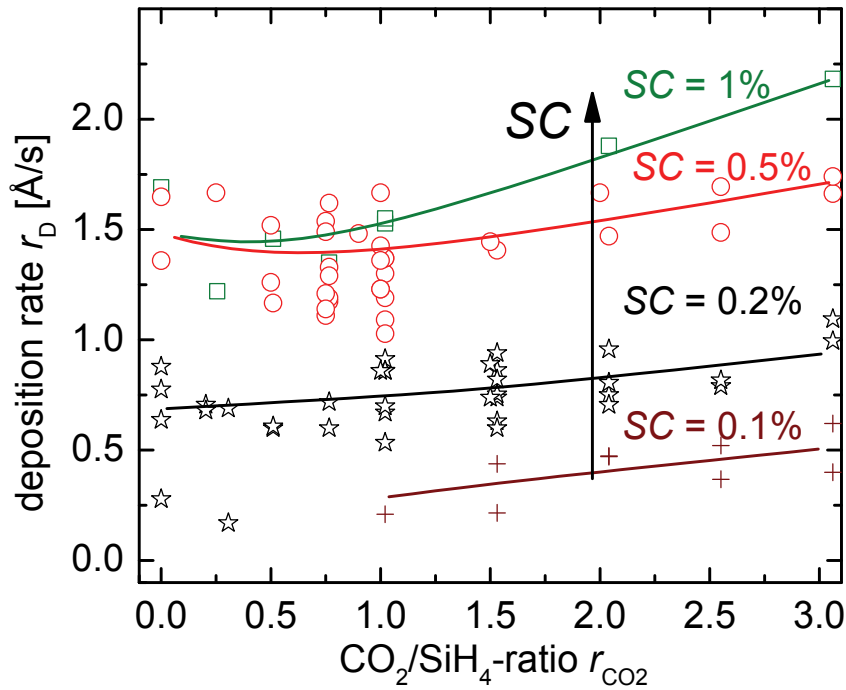
Figure 4.3: *The deposition rate r_D versus the CO_2/SiH_4 ratio r_{CO2}. The silane concentrations SC used for each sample series are indicated. To vary the SC the hydrogen flow was varied. A silane flow of 1 sccm and a phosphine flow of 0.02 sccm were used for all sample series. Thicknesses range from 300 nm to 2 µm, the plasma power density was 300 mW/cm² and the deposition pressure was 4 mbar for all samples. For more details, see chapter 2 and Table 4.1. The curves are guides to the eye.*

4.2.3 Oxygen content

Not surprisingly in amorphous silicon oxide (a-SiO_x:H) films, the optical properties such as refractive index and band gap depend on the oxygen content [36,37,62,125,131]. Therefore, it is of great interest to know the incorporated oxygen content in the microcrystalline material when applying a CO_2 admixture to the plasma. In addition, one can relate the material properties of the doped µc-SiO_x:H from the present study to the material properties of doped a-SiO_x:H from other studies [62,125,131] at a given oxygen content.
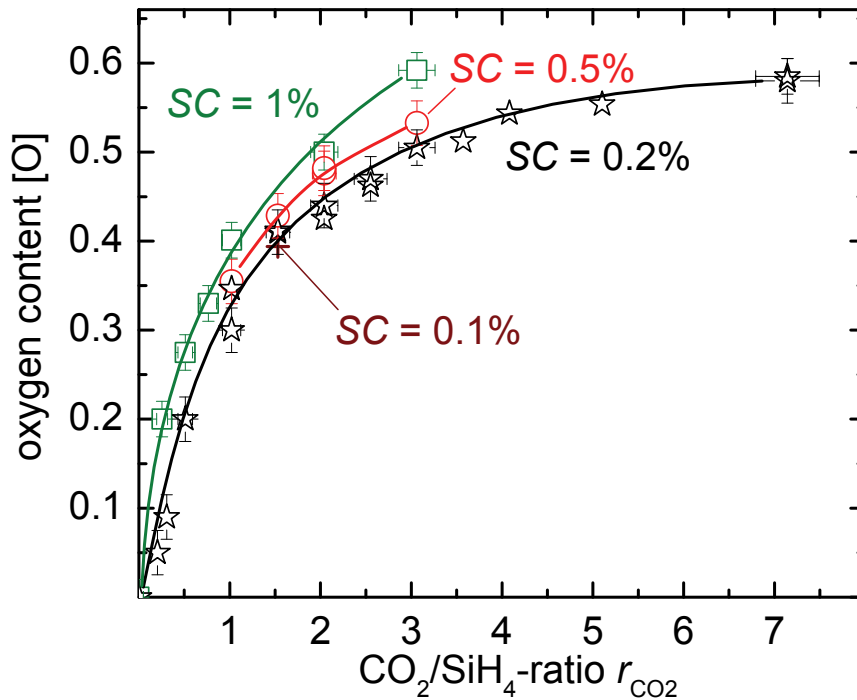
Figure 4.4: The oxygen concentration [O] as a function of the CO_2/SiH_4 ratio r_{CO2}. The silane concentrations SC used for each sample series are indicated on the graph. To vary silane concentration SC, the hydrogen flow was varied and a silane flow of 1 sccm was used for all sample series. The phosphine flow was 0.02 sccm. Thicknesses range from 300 nm to 2 μm, the plasma power density was 300 mW/cm² and the deposition pressure was 4 mbar for all samples. For more details, see chapter 2 and Table 4.1. The curves are guides to the eye.

Figure 4.4 shows the oxygen content [O] in the μc-SiO$_x$:H films, as determined by Rutherford Backscattering Spectroscopy (RBS), versus the CO_2/SiH_4 ratio r_{CO2} for some of the sample series. The oxygen content [O] increases strongly with the r_{CO2} to $[O] \approx 0.4$ at $r_{CO2}=2$. For higher CO_2/SiH_4-ratios, from 2 to 7, the oxygen content increases less steeply to a maximum of 0.6. An oxygen content of 0.66 is the value expected for 100% a-SiO$_2$ (see also Appendix A). The increase of incorporated oxygen with increasing r_{CO2} is observed for all silane concentration series. For higher silane concentrations, slightly higher oxygen contents were observed at a given r_{CO2}. To reach an oxygen content of 0.5, an r_{CO2} of 2 to 3 is needed. This means that, for the used deposition conditions, a 2 to 3 times higher CO_2 flow with respect to the silane flow is necessary to incorporate the same amount of oxygen and silicon in the film. The carbon content in the films is below the detection limit of RBS, which is 2%.

From Figure 4.4 one can conclude that the oxygen content can be adjusted between ≈ 0 and 0.6 by varying the r_{CO2}. The oxygen content depends only very little on the silane concentration at a given r_{CO2}. Thus, for other samples, one can roughly estimate the oxygen content from the r_{CO2}, without measuring by RBS, at least where otherwise similar deposition condition were applied.

4.2.4 Raman intensity ratio and electrical conductivity

Doped microcrystalline silicon is highly conductive, therefore, in the doped μc-SiO_x:H alloy, the crystalline volume fraction should have a strong influence on the conductivity of the alloy. However, the a-SiO_x:H fraction has a low conductivity but a high transparency. This means that, the optical transparency and electrical conductivity will depend on the crystalline volume fraction (Raman intensity ratio I_c) but they are also interrelated in the sense that material with high conductivity (high I_c) will have a low transparency and vice versa. These relationships between deposition conditions (mainly gas flows) and structure (I_c), on the one hand, and electrical and optical properties, on the other hand, will be demonstrated in the following for a number of sample series. We will focus on the Raman intensity ratio I_c and conductivity σ first, before providing results on optical properties in section 4.2.5.

SC-series

Figure 4.5 shows a) the Raman intensity ratio I_c and b) the conductivity versus r_{CO2} for sample series with various silane concentrations. The I_c decreases for all series with increasing CO_2/SiH_4 ratio r_{CO2}. For a given r_{CO2}, an increase in silane concentration from 0.1% up to 1.0%, results in lower values of I_c, as indicated by the arrow. Pronounced scatter is observed for the values of I_c, and σ for different layers deposited under the same nominal gas flows. This scatter can be, for example, the result of the chamber history, because the presented results are on samples prepared during the entire duration of the present study. From Figure 4.5 a), we can conclude that up to an r_{CO2} of 2, and an *SC* of 0.2%, a crystalline fraction is observed. At an r_{CO2} of 2, the μc-SiO_x:H has an oxygen content of 0.44 (Figure 4.4). This means oxygen-rich μc-SiO_x:H material, that still contains a crystallinity volume fraction of the order of 10%, can be prepared when using a low silane concentration ($SC = 0.2\%$).
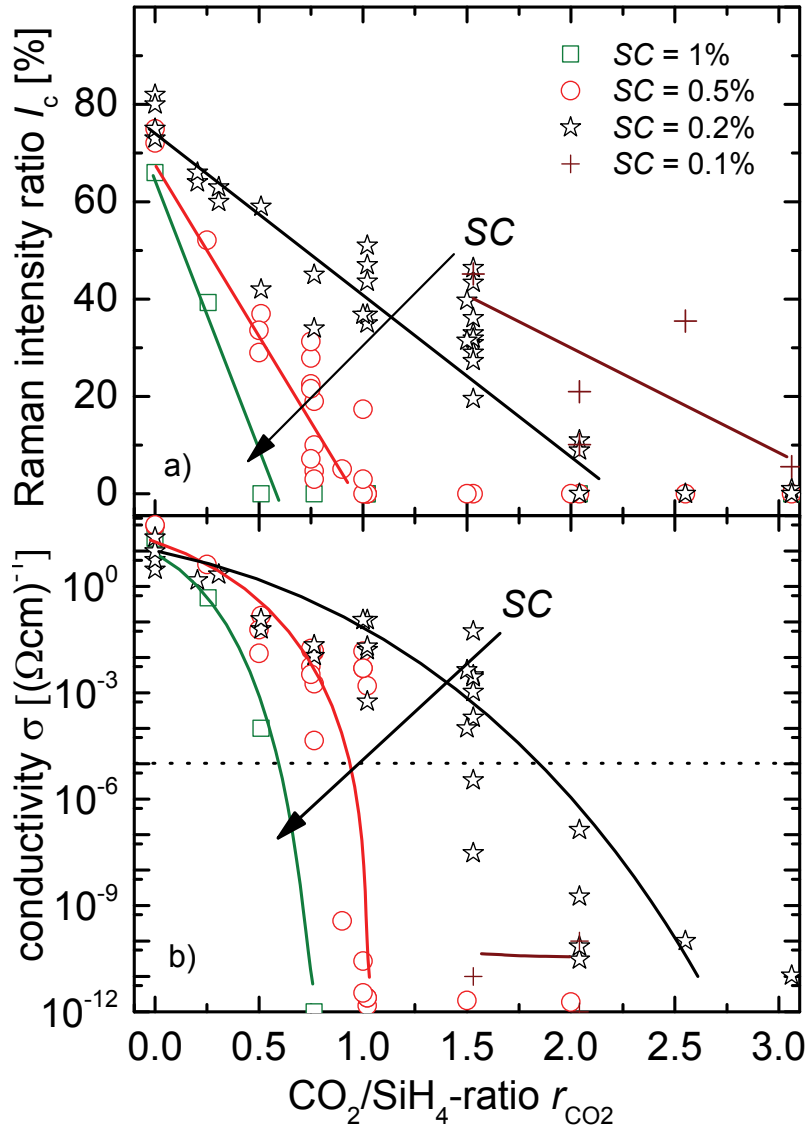
Figure 4.5: a) The Raman intensity ratio I_c and b) the conductivity σ versus the CO_2/SiH_4 ratio r_{CO2}. The lower conductivity limit (σ-(IR)limit) is indicated by the dashed line (see text for details). The used silane concentration SC is indicated on the graph. To vary SC, the hydrogen flow was varied and a silane flow of 1 sccm was used for all series. The phosphine flow was 0.02 sccm. Thicknesses range from 300 nm to 2 μm, the plasma power density was 300 mW/cm² and the deposition pressure was 4 mbar for all samples. For more details, see chapter 2 and Table 4.1. The curves are guides to the eye.

Note: The n-type μc-SiO$_x$:H layer can be used for a variety of applications in thin-film silicon solar cells. For example, in single junction solar cells as the n-layer (see section 6.2), or, if applied in tandem solar cells (see section 6.3), between the a-Si:H top cell and the μc-Si:H bottom cell, as an intermediate reflector. For example when applied as the intermediate reflector, it represents, electrically, an additional series resistance (R_s) between the a-Si:H top and the μc-Si:H bottom cell, which reduces the fill factor (*FF*), and therefore the efficiency (η). To estimate the influence of the intermediate reflector on the *FF,* we added Ohmic *JV*-characteristics of a series resistance R_s that corresponds to the resistance of the intermediate reflector to a measured *JV*-characteristics of a tandem solar cell without intermediate reflector. The results of these calculations are shown in section 6.3. Based on these

calculations, the lowest acceptable conductivity for a 100 nm thick intermediate reflector layer is $10^{-5}(\Omega cm)^{-1}$. This required conductivity σ for the IR layer, the $\sigma(IR)$-limit is indicated by the dotted line in Figure 4.5 b).

The electrical dark conductivity σ was measured for all films in the lateral direction by using co-planar silver contacts. Figure 4.5 b) shows the electrical conductivity σ of the films versus the r_{CO2} for different silane concentrations. A conductivity of $10^{-12}(\Omega cm)^{-1}$ at a film thickness of 500 nm is the detection limit of our conductivity measurement set-up; therefore, conductivities below this value are not shown. For all silane concentration series, the conductivity σ decreases with increasing CO_2/SiH_4 ratio r_{CO2} to less than $10^{-12}(\Omega cm)^{-1}$. When increasing the silane concentration SC from 0.2% up to 1%, the drop in conductivity shifts towards lower CO_2/SiH_4 ratios r_{CO2}, as indicated by the arrow. In other words, to achieve high conductivities at high r_{CO2}, the silane concentration SC has to be reduced. This drop in σ coincides with the decrease of the Raman intensity ratio I_c (Figure 4.5 a). A lower value of I_c results in lower conductivities. However, at the lowest silane concentration SC=0.1%, in spite of high values of I_c, the conductivities are lower.

In Figure 4.6, the dark conductivity σ is plotted versus the Raman intensity ratio I_c for various SC-series. The conductivity increases with increasing I_c. For films with an I_c of close to 0%, the electrical conductivity is between $1 \times 10^{-12}(\Omega cm)^{-1}$ and $1 \times 10^{-3}(\Omega cm)^{-1}$. For the SC-series at $SC = 0.5\%$, the conductivity increases to values above $1 \times 10^{-2}(\Omega cm)^{-1}$, even at Raman intensity ratios of 10%. At a lower silane concentration of 0.2%, a Raman intensity ratio of 40% is needed to achieve a conductivity of $1 \times 10^{-2}(\Omega cm)^{-1}$. For all SC-series with $SC \geq 0.2\%$, the conductivity increases further to $> 10^{1}(\Omega cm)^{-1}$ at $I_c > 60\%$. With an $SC=0.1\%$, in spite of a high Raman intensity ratio of 40%, the conductivities are below $1 \times 10^{-6}(\Omega cm)^{-1}$. At an $I_c=0\%$, (i) for the an SC of 0.2%, a low conductivity of $1 \times 10^{-8}(\Omega cm)^{-1}$ and (ii) for an SC of 0.5%, a higher conductivity of $1 \times 10^{-2}(\Omega cm)^{-1}$, were measured. These conductivities are used as an input parameter for an attempt to model the conductivity versus the I_c, because for these SC-series having these conductivities at $I_c=0\%$ have a relevant number of samples and measurements available over the full range of I_c. The Raman intensity ratio I_c was used as an estimate for the crystalline volume fraction (see section 2.1.5).
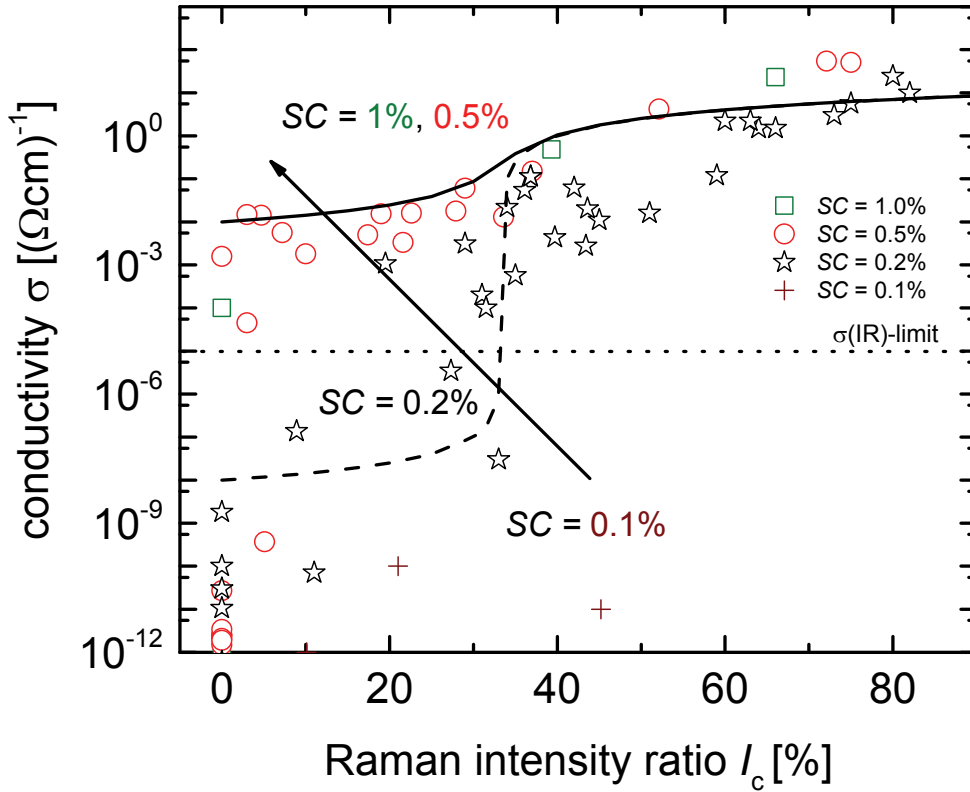
Figure 4.6: The conductivity σ versus the Raman intensity ratio I_c. The silane concentrations SC are indicated in the legend and on the graph. To vary SC, the hydrogen flow was varied and a silane flow of 1 sccm was used for all series. The phosphine flow is 0.02 sccm. Thicknesses range from 300 nm to 2 μm, the plasma power density was 300 mW/cm² and the deposition pressure was 4 mbar for all samples. For more details, see chapter 2 and Table 4.1. The lower conductivity limit (σ-(IR)limit) for use as the intermediate reflector is indicated (dotted line). The $\sigma_{\mu c\text{-}SiOx:H}$ as a function of I_c, calculated from Bruggeman's EMT, is shown for a highly conductive amorphous phase $\sigma_{a\text{-}SiOx:H} = 10^{-2}\,(\Omega cm)^{-1}$ as a solid curve and for a low conductive amorphous phase $\sigma_{a\text{-}SiOx:H} = 10^{-8}\,(\Omega cm)^{-1}$ as a dashed curve. The arrow is indicating the increase in SC.

In an attempt to model the conductivity of the doped μc-SiO$_x$:H alloy on the basis of the conductivity of the individual material components (μc-Si:H & a-SiO$_x$:H), the dependency between the conductivity and the crystalline volume fraction I_c is calculated using Bruggeman's effective medium theory (EMT) model [130]. In this EMT model, two phases are considered: a highly conductive and highly crystalline μc-Si:H phase and a doped a-SiO$_x$:H phase. The equation following from this model is

$$0 = I_c \frac{\sigma_{\mu c-Si:H} - \sigma_{\mu c-SiOx:H}}{\sigma_{\mu c-Si:H} + 2\sigma_{\mu c-SiOx:H}} + \left(1 - I_c\right)\frac{\sigma_{a-SiOx:H} - \sigma_{\mu c-SiOx:H}}{\sigma_{a-SiOx:H} + 2\sigma_{\mu c-SiOx:H}} \tag{4.1},$$

where $\sigma_{\mu c\text{-}SiOx:H}$, as a function of I_c, has a quadratic solution whose positive solution is

$$\sigma_{\mu c-SiOx:H}(I_c) = \frac{1}{4}\left(a + \sqrt{a^2 + 8\sigma_{\mu c-Si:H}\sigma_{a-SiOx:H}}\right)$$ (4.2),

in which

$$a = (2 - 3I_c)\sigma_{a-SiOx:H} + (3I_c - 1)\sigma_{\mu c-Si:H}$$ [130] (4.3).

$\sigma_{\mu c-Si:H}$ is the conductivity for the doped μc-Si:H phase. $\sigma_{\mu c-Si:H}$ is assumed to be $10\,(\Omega cm)^{-1}$, which is the conductivity for highly n-type doped μc-Si:H with $I_c = 80\%$ from the present study. For the a-SiO$_x$:H phase, two cases are assumed: (i) low conductivity of $\sigma_{a-SiOx:H} = 1 \times 10^{-8}\,(\Omega cm)^{-1}$ for the SC-series using an *SC* of 0.2% and (ii) a higher conductivity of $\sigma_{a-SiOx:H} = 1 \times 10^{-2}\,(\Omega cm)^{-1}$ for the SC-series using an *SC* of 0.5%. Figure 4.6 shows the $\sigma_{\mu c-SiOx:H}$ as a function of I_c calculated for an a-SiO$_x$:H phase with a (i) low conductivity as a dashed curve and for an amorphous phase with higher (ii) conductivity as a solid curve. For $I_c < 33\%$, the $\sigma_{\mu c-SiOx:H}$ is predominantly determined by the assumed conductivity of the a-SiO$_x$:H phase. For $I_c < 33\%$, the solid graph is in reasonable agreement with the SC-series using an *SC* of 0.5% and the dashed graph with the SC-series using an *SC* of 0.2%. The $\sigma_{\mu c-SiOx:H}$ at $I_c > 40\%$ for both cases are similarly independent of the assumed conductivity of the a-SiO$_x$:H phase.
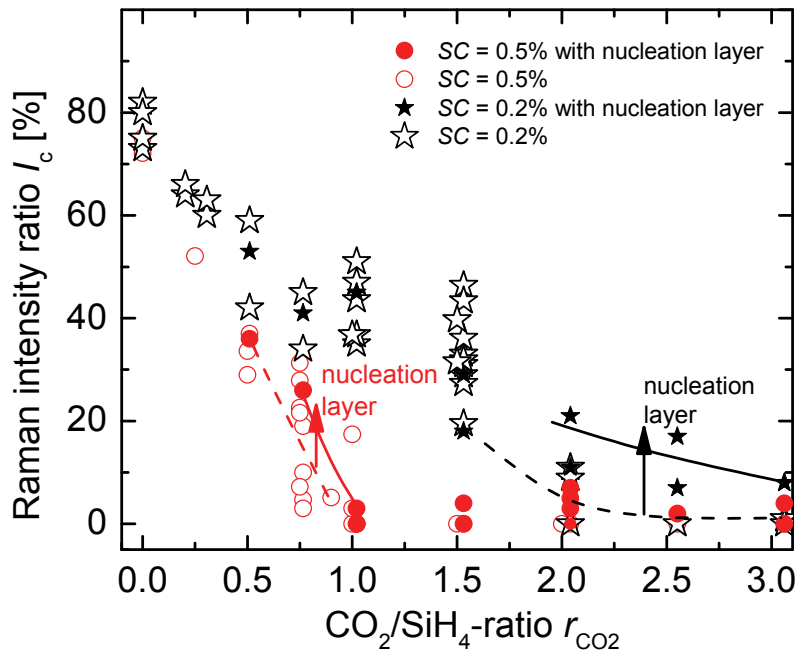
Figure 4.7: The Raman intensity ratio I_c as a function of the CO_2/SiH_4 ratio r_{CO2} for layers with a nucleation layer (filled symbols) and without nucleation layer (open symbols). The dashed curves are guides to the eye for the films without a nucleation layer. The solid curves are guides to the eye for the films with a nucleation layer. The silane concentration SC used is indicated in the legend. To vary SC, the hydrogen flow was varied and a silane flow of 1 sccm was used for all series. The phosphine flow is 0.02 sccm. Thicknesses range from 300 nm to 2 μm, the plasma power density was 300 mW/cm² and the deposition pressure was 4 mbar for all samples. For more details, see chapter 2 and Table 4.1.

To simulate the situation of the growth of μc-SiO$_x$:H layers (e.g. intermediate reflector) on crystalline layers in solar cells, and to enable a crystalline nucleation/reduced incubation zone, doped μc-SiO$_x$:H layers were also grown on highly crystalline nucleation layers. A 30 nm thick highly crystalline μc-Si:H n-layer was deposited as a nucleation layer on the glass substrate before the μc-SiO$_x$:H layer was deposited. The deposition conditions for the nucleation layer are as for μc-Si:H n-layer in Table 2.1 [63]. Figure 4.7 shows the Raman intensity ratio I_c versus the CO_2/SiH_4 ratio r_{CO2} for films with and without a nucleation layer prepared using different silane concentrations (0.2% and 0.5%). For the series with SC=0.5% between an r_{CO2} of 0.5 and 1, a slight increase in I_c is visible. For the 0.2% silane concentration series between an r_{CO2} of 2 and 3, the increase in I_c is more pronounced. This means that, in some cases, the Raman intensity ratio I_c also depends on whether or not a nucleation layer is used. The μc-SiO$_x$:H layers were grown with a sufficient thickness between 300 nm and 2 μm (unless otherwise stated) to reduce an influence of the fluctuations within incubation zone on the I_c.

PH$_3$-series

The previously shown SC-series were prepared to show the influence of the silane concentration and the r_{CO2} on the Raman intensity ratio and the conductivity. For these SC-series, the phosphine flow was kept constant at 0.02 sccm. The PH$_3$-series were prepared to investigate the

influence of the phosphine flow on the Raman intensity ratio and the conductivity when varying the r_{CO2}. It is of particular interest, because the phosphine flow is constant within a particular series but the $SiH_4 + CO_2$ gas flow increases with r_{CO2}. Consequently, the concentration of phosphine in the gas phase with respect to $SiH_4 + CO_2$ decreases with increasing r_{CO2}. In order to investigate this influence, the phosphine flow was varied for these particular series and the Raman intensity ratio and conductivity were measured. The silane concentration was 0.2% for all series. Figure 4.8 shows a) the Raman intensity ratio I_c and b) the conductivity σ versus the CO_2 / SiH_4 ratio r_{CO2} for various PH_3-series. The results for a phosphine flow of 0.02 sccm have been already provided in Figure 4.5 and are presented here for reference.
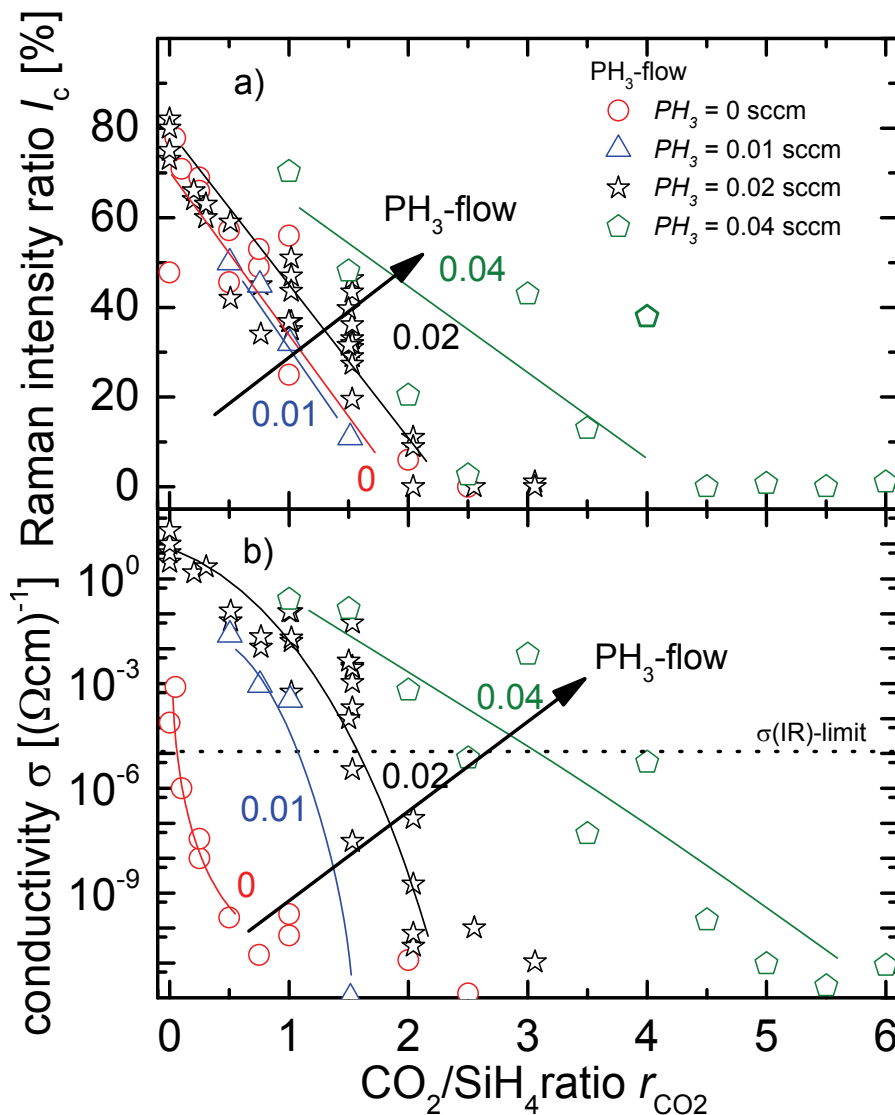

Figure 4.8: a) The Raman intensity ratio I_c and b) the conductivity σ versus the CO_2 / SiH_4 ratio r_{CO2}. The phosphine flows are indicated in sccm. All layers were prepared using a silane concentration of 0.2%. The lower conductivity limit (σ-(IR)limit) for use as an intermediate reflector is indicated (dashed line). Thicknesses range from 300 nm to 2 μm, the plasma power density was 300 mW/cm² and the deposition pressure was 4 mbar for all samples. For more details, see Table 4.2 and chapter 2.

For $0\,\mathrm{sccm}$ and $0.01\,\mathrm{sccm}$ phosphine flow, the decrease in I_c with increasing r_{CO2} is similar. With a further increase in phosphine flow ($0.02\,\mathrm{sccm}$ & $0.04\,\mathrm{sccm}$), the Raman intensity ratio increases at a given r_{CO2}. For all series, the conductivity (Figure 4.8 b) decreases with increasing r_{CO2}. With increasing phosphine flow, the μc-SiO$_x$:H films have higher conductivities at a given r_{CO2}. On the one hand, the higher conductivity σ can be related to the higher dopant concentration, and on the other hand, to the higher I_c at a given r_{CO2}. From Figure 4.8 one can conclude that, for n-type μc-SiO$_x$:H the I_c and σ can be increased at a given r_{CO2} by increasing the PH$_3$ flow.

4.2.5   Optical properties

This section presents the optical properties of n-type μc-SiO$_x$:H films, e.g. the absorption coefficient spectra, optical band gap, and refractive index. In addition, it shows the dependency between the optical properties and the process gas flow parameters. It also gives the relationship between the oxygen content, crystalline volume fraction, and optical properties.

Optical absorption

Figure 4.9 shows the absorption coefficient α measured by photothermal deflection spectroscopy (PDS) plotted versus the photon energy from $0.5\,\mathrm{eV}$ to $3.1\,\mathrm{eV}$ for layers prepared at various r_{CO2}, as indicated in the figure. All layers were prepared using a silane concentration of 0.2% and a phosphine flow of $0.02\,\mathrm{sccm}$.
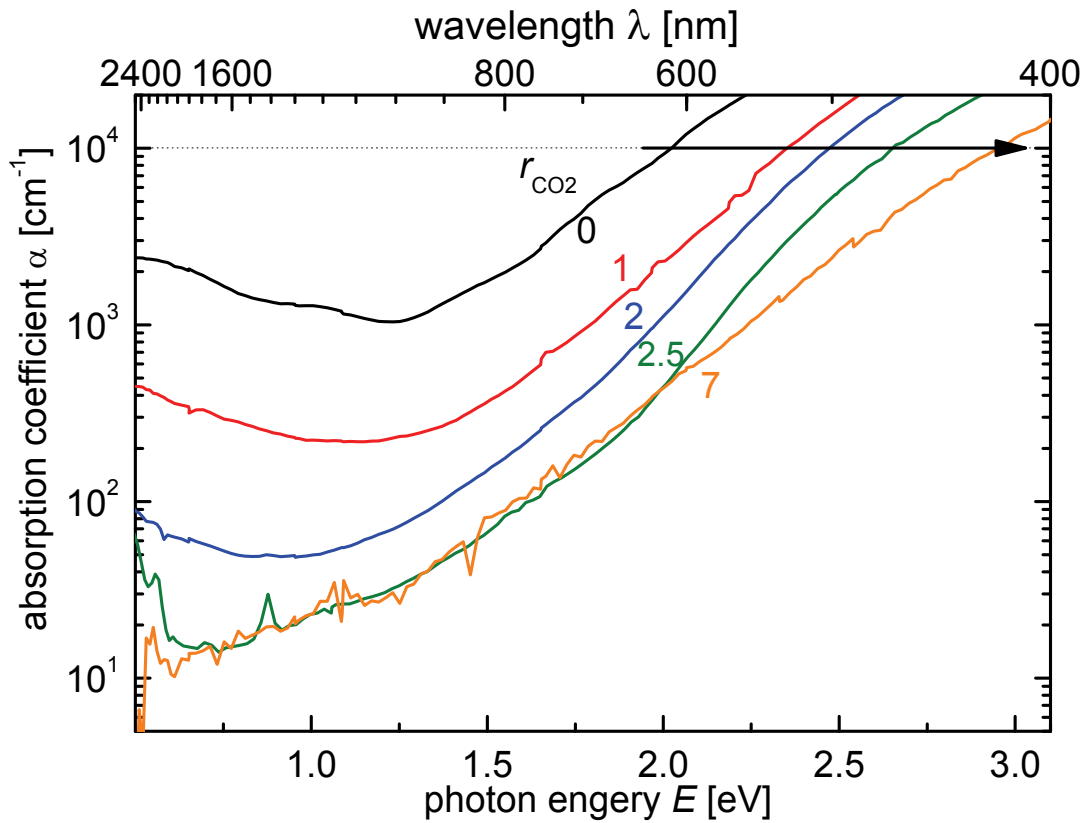
Figure 4.9 The absorption coefficient α measured by PDS versus the photon energy E on the lower x-axis and the wavelength λ on the upper x-axis. The material was prepared at 0.2% silane concentration, a phosphine flow of 0.02 sccm and a CO_2/SiH_4 ratio r_{CO2} as indicated on the graphs. Thicknesses range from 430 nm to 935 nm, the plasma power density was 300 mW/cm² and the deposition pressure was 4 mbar for all samples. For more details, see chapter 2 and Table 4.1. The straight dotted line indicates the absorption, which is used as a value to determine the optical band gap E_{04}.

As described in section 2.1.3, the optical band gap E_{04} is determined by the photon energy value at which an optical absorption coefficient α of 10^4 cm^{-1} is obtained (dotted line). The E_{04} increases from 2 eV to 2.95 eV when the CO_2/SiH_4 ratio r_{CO2} increases from 0 to 7. The crystalline volume fraction decreases for the films from I_c=80% at r_{CO2}=0 to I_c=0% at $r_{CO2} \geq 2.5$ (Figure 4.5 a).

An E_{04} optical band gap of 2 eV can be attributed to highly crystalline doped µc-Si:H (I_c=80%), when determining the E_{04} from the absorption coefficient spectra as in the present study. This is a different quantity to the commonly stated value of 1.1 eV for the band gap E_g of µc-Si:H. A graph of the absorption as a function of photon energy for a number of materials is given in Appendix B.

However, the absorption coefficient spectra show that the absorption edge is shifted to higher photon energies with increasing r_{CO2}. In the sub band gap range (photon energies below 1.1 eV), the absorption coefficient decreases with increasing r_{CO2}. One reason for this decrease is the reduced free carrier absorption, which occurs for several reasons; with an increasing r_{CO2}, dopants are strongly compensated by defects, the phosphorus is no longer incorporated as a

dopant in the a-SiO$_x$:H phase or the reduced phosphine concentration with respect to the SiH$_4$+CO$_2$ flow.

Figure 4.10 shows the optical band gap E_{04} versus a) the CO$_2$/SiH$_4$ ratio r_{CO2} and b) the oxygen content [O] for various SC-series (details see Table 4.1). Note that, the oxygen content was measured by RBS in only some of the samples shown in a) and consequently cannot be shown in b).
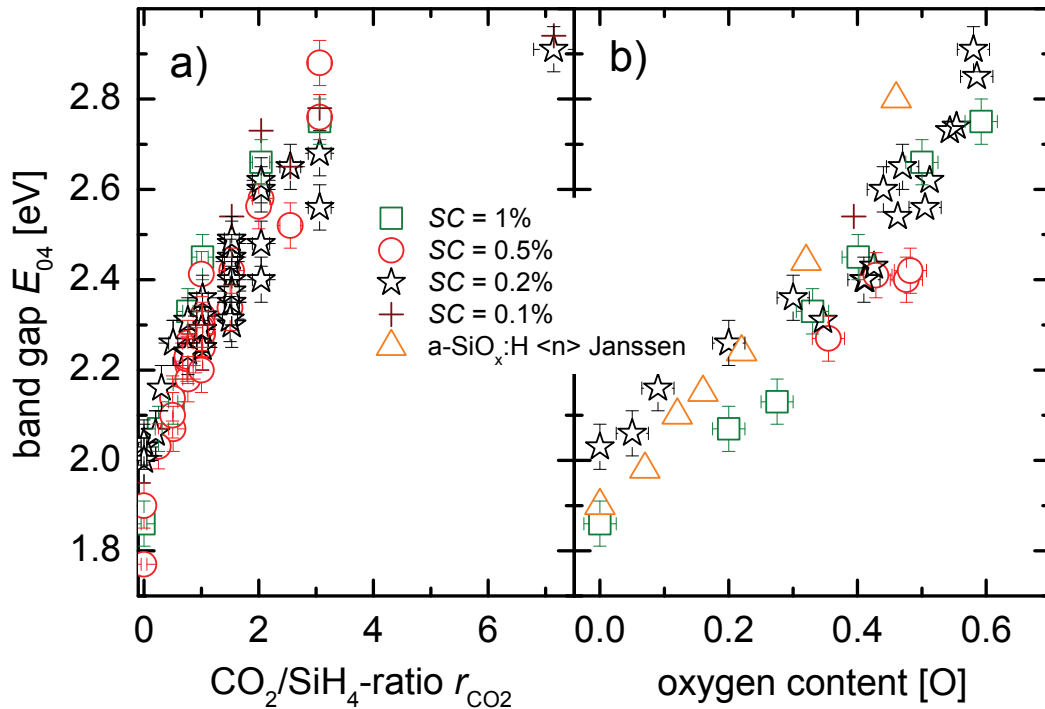

Figure 4.10 The optical band gap E_{04} versus a) the r_{CO2} and b) the oxygen content [O]. The silane concentrations SC, are indicated in the legend. To vary the SC the hydrogen flow was varied and a silane flow of 1 sccm and a phosphine flow of 0.02 sccm was used for all series. Thicknesses range from 300 nm to 2 μm, the plasma power density was 300 mW/cm² and the deposition pressure was 4 mbar for all samples. For more details, see chapter 2 and Table 4.1. Results for amorphous silicon oxide films (n-type a-SiO$_x$:H) from the literature [131], labelled "Janssen" are shown for comparison.

The optical band gap increases with increasing r_{CO2} and oxygen content [O]. It covers a range from below 1.8 eV up to a value of 2.95 eV. For all silane concentration series, a similar increase of the E_{04} with increasing r_{CO2} is observed. In addition, the E_{04} versus the oxygen content [O] for n-type a-SiO$_x$:H [131] is shown. The E_{04} dependency on the oxygen content for n-type microcrystalline silicon oxide (μc-SiO$_x$:H) and for amorphous silicon oxide (a-SiO$_x$:H) is similar. This similarity is found despite the microcrystalline silicon (μc-Si:H) phase in the μc-SiO$_x$:H material. From these findings, one can conclude that the E_{04} of the n-type μc-SiO$_x$:H is mainly determined by the oxygen content in the material, which, in turn, is strongly influenced by the r_{CO2}.

Refractive index

The refractive index is an important material property because it partly determines the reflection of the layers within the solar cells.
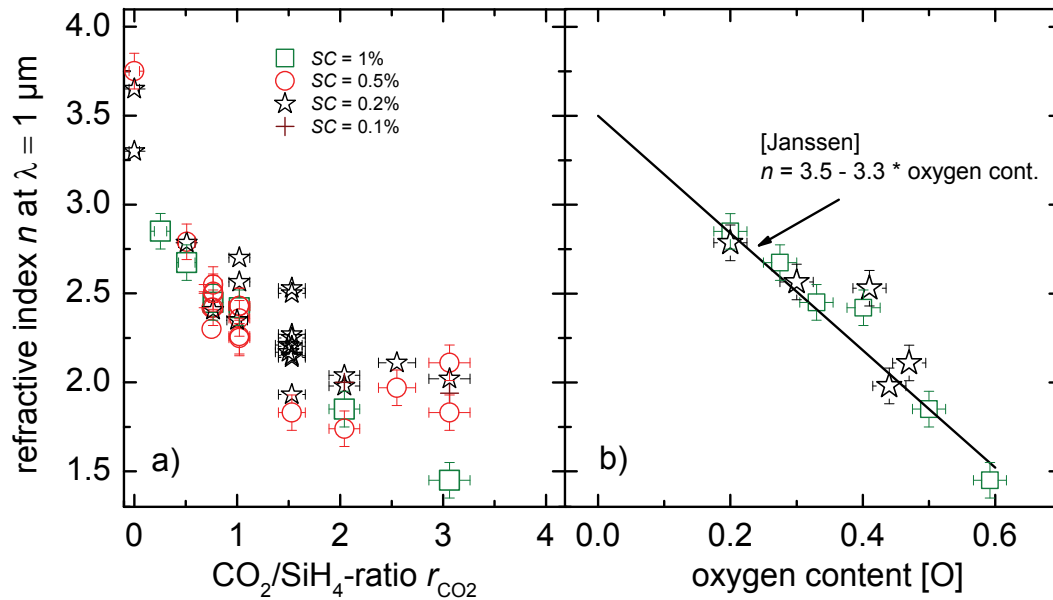

Figure 4.11: The refractive index n versus a) the CO_2/SiH_4 ratio r_{CO2} and b) oxygen content [O]. The silane concentrations SC are indicated in the legend. To vary SC, the hydrogen flow was varied and a silane flow of 1 sccm and a phosphine flow of 0.02 sccm were used for all series (details see Table 4.1). The line in b) is calculated by the function as indicated. Thicknesses range from 300 nm to 2 μm, the plasma power density was 300 mW/cm² and the deposition pressure was 4 mbar for all samples. For more details, see chapter 2 and Table 4.1. The function is taken from the literature [131], labelled "Janssen", for amorphous silicon oxide films (n-type a-SiO$_x$:H) and is shown for comparison.

Figure 4.11 shows, for n-type μc-SiO$_x$:H, the refractive index versus a) the gas flow parameter and b) the oxygen content for various SC-series as indicated in the legend. For details of the process gas flows, see Table 4.1. The refractive index is calculated as described in section 2.1.3. When the r_{CO2} increases from 0 to 3, the refractive index decreases from 3.8 to 1.5; i.e. the value of a-SiO$_2$. Please note that the oxygen content was measured by RBS in some of the samples shown in a), and consequently cannot be shown in b). The refractive index decreases with increasing oxygen content. This decrease is similar for all silane concentrations. The decrease follows the function that was suggested for undoped a-SiO$_x$:H films [131]. One can summarize that the refractive index n of the material can be varied using appropriate gas mixtures for the μc-SiO$_x$:H preparation, down to values of a-SiO$_2$. The relationship between the refractive index and the oxygen content for n-type μc-SiO$_x$:H is similar to that for undoped a-SiO$_x$:H, despite the microcrystalline fraction in μc-SiO$_x$:H.

Optical band gap E_{04} versus Raman intensity ratio

Information about the link between optical properties and crystalline volume fraction is provided in Figure 4.12. This figure depicts the optical band gap E_{04} versus the Raman intensity ratio I_c for several silane concentrations series. In each SC-series, the r_{CO2} was varied. For more details of the process gas flows, see Table 4.1.

Based on these results, the samples are classified into the categories a-Si:H, a-SiO$_x$:H, µc-Si:H and µc-SiO$_x$:H as indicated in Figure 4.12. At $I_c=0\%$, we find a wide range of values for the E_{04} optical band gap, between 2.1 eV to 2.95 eV, depending on the oxygen content (not shown). n-Type **a-Si:H** without CO_2 admixture typically has an E_{04} of 1.91 eV (Figure 2.7). For higher E_{04}, at $I_c=0\%$ the amorphous silicon is alloyed with oxygen; therefore, the material is classified as **a-SiO$_x$:H**. Above an I_c of 70%, the material is classified as **µc-Si:H**. An E_{04} optical band gap close to 2 eV can be attributed to this n-type µc-Si:H without CO_2 admixture. Between the two extreme cases, from $I_c=0\%$ to $I_c=70\%$, material which was prepared using a CO_2 admixture, is classified as **µc-SiO$_x$:H**. This µc-SiO$_x$:H is composed of two phases, a highly crystalline µc-Si:H phase and an a-SiO$_x$:H phase.

This phase composition results, for example, at an I_c of 35% and an E_{04} of up to 2.65 eV, which corresponds to a material with a substantial crystalline volume fraction and high transparency. Between an I_c of 10% and 70%, the E_{04} at a given I_c apparently depends on the *SC* that was used. For example, at a given I_c around 35%, the band gap increases with decreasing silane concentration. For SC>0.5%, an $E_{04}=2.1$ eV; for *SC*=0.2%, an $E_{04}\approx2.35$ eV; and for *SC*=0.1%, an E_{04} of up to 2.65 eV was measured. However, this E_{04} increase is not directly related to the decrease in *SC* but rather to the used r_{CO2} for samples having the same Raman intensity ratio I_c (see Figure 4.5) i.e. when using lower silane concentrations, more CO_2 can be added, resulting in the same I_c and a higher E_{04}.
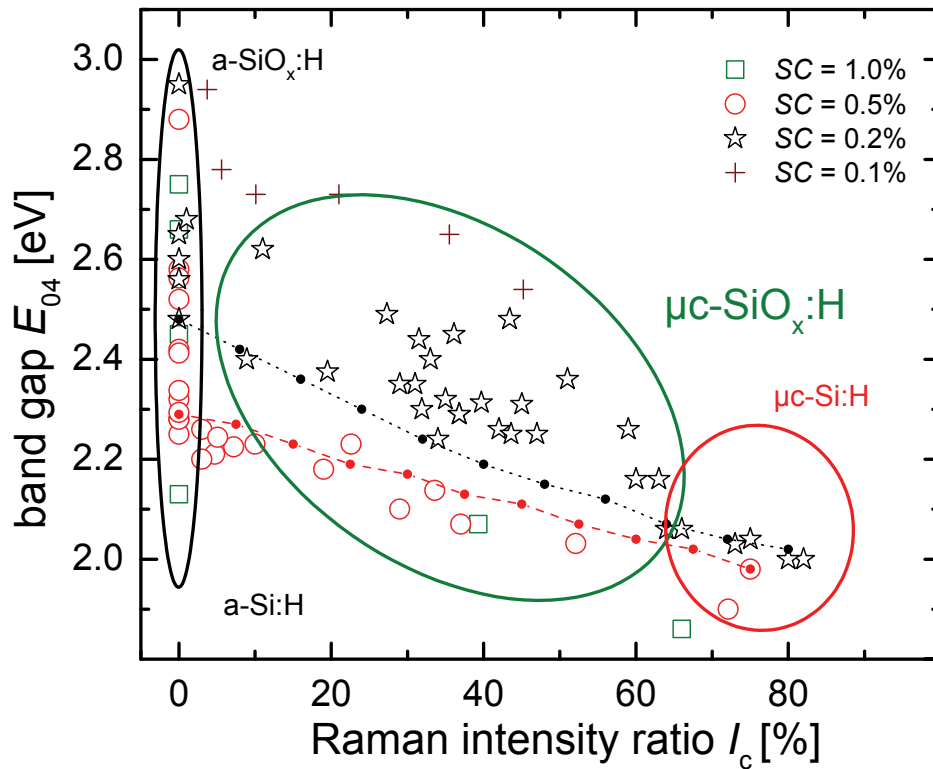
Figure 4.12: The band gap (E_{04}) versus the Raman intensity ratio (I_c). The applied silane concentrations SC are indicated in the legend. To vary SC, the hydrogen flow was varied and a silane flow of 1 sccm was used for all series. The phosphine flow was 0.02 sccm. Thicknesses range from 300 nm to 2 µm, the plasma power density was 300 mW/cm² and the deposition pressure was 4 mbar for all samples. For more details, see chapter 2 and Table 4.1. For more details of the process gas flows, see Table 4.1. The material classification into the categories of a-Si:H, a-SiO$_x$:H, µc-Si:H and µc-SiO$_x$:H is indicated. The dotted curve represents the values calculated from the effective medium model (EMT) of Bruggeman, using the dielectric function of the 0.2% SC-series, and the dashed curve for the 0.5% SC-series.

To investigate the origin of the increase in E_{04} with decreasing SC at a given I_c in more detail, we calculated the E_{04} versus the crystalline volume fraction. For this, we used the optical properties of highly crystalline µc-Si:H samples and various a-SiO$_x$:H samples prepared in the particular series. We calculated the optical properties by using the effective medium theorie (EMT) model of Bruggeman [79], as described in section 2.1.4. The equation is derived from the Bruggeman EMT as

$$(1-I_c)\frac{\varepsilon_{a-SiO_x:H} - \varepsilon_{\mu c-SiO_x:H}}{\varepsilon_{a-SiO_x:H} + 2\varepsilon_{\mu c-SiO_x:H}} + I_c\frac{\varepsilon_{\mu c-Si:H} - \varepsilon_{\mu c-SiO_x:H}}{\varepsilon_{\mu c-Si:H} + 2\varepsilon_{\mu c-SiO_x:H}} = 0 \tag{4.4}.$$

The dielectric function ε of both phases, the a-SiO$_x$:H phase ($\varepsilon_{a-SiOx:H}$) and highly crystalline µc-Si:H ($\varepsilon_{\mu c-Si:H}$) phase, was used to calculate the $\varepsilon_{\mu c-SiOx:H}$ and the E_{04} of the µc-SiO$_x$:H phase mixture as a function of I_c. The $\varepsilon_{\mu c-Si:H}$ was determined from the optical properties α and n of µc-Si:H samples with $I_c \approx 80\%$ and without CO_2 admixture. To determine the $\varepsilon_{a-SiOx:H}$ for the

a-SiO$_x$:H phase, the optical properties (α, n) of samples with an I_c=0% were used. Two sets of α, n for the $\varepsilon_{\text{a-SiOx:H}}$ were used: (i) from an a-SiO$_x$:H sample prepared at an SC of 0.5%, for the dashed curve, and (ii) from an a-SiO$_x$:H sample prepared at an SC of 0.2%, for the dotted curve. The a-SiO$_x$:H samples of both SC-series were selected with the aim that these samples have optical properties similar to those of the a-SiO$_x$:H phase in the respective μc-SiO$_x$:H material of the particular SC-series. We used the $\varepsilon_{\text{a-SiOx:H}}$ (i) for the 0.5% SC-series from a sample with an r_{CO2} of 1 and (ii) for the 0.2% SC-series from a sample with an r_{CO2} of 2. Both r_{CO2} are the lowest values within the respective SC-series, which results in completely amorphous growth (I_c=0%) (see Figure 4.5 a). For lower values of r_{CO2} in the respective SC-series, an I_c>0%, was measured. From $\varepsilon_{\mu\text{c-SiOx:H}}$ the α and n were calculated within Scout (section 2.1.3 [68]) and the E_{04} was determined from the photon energy at which α=10^4 cm^{-1}.

The calculated E_{04} from the EMT for the series using an SC=0.5% (dashed curve) is in good agreement with the measured E_{04} for this series. The calculated E_{04} for the series using an SC=0.2% (dotted curve) is lower than the measured E_{04} for this series. However, the calculated E_{04} band gap determined for the SC=0.2% series is higher than for the SC=0.5% series at a given I_c. This increase is in agreement with the experimental results. The higher E_{04} for the SC-series=0.2% at a given I_c can be attributed to the higher band gap of the a-SiO$_x$:H phase. This is possible because, when using a lower silane concentration, one can apply a higher r_{CO2}, which yields in a higher band gap (Figure 4.12), and obtain the same I_c (Figure 4.5 a).

4.2.6   Electrical conductivity vs. refractive index and optical band gap

The relationship between optical and electrical properties is the most relevant interdependence in the development of the n-type μc-SiO$_x$:H as a doped layer for thin-film silicon solar cells. Figure 4.13 shows the conductivity versus a) the refractive index and b) the optical band gap as an overview for the suitability of the silicon oxide for various applications in thin-film silicon solar cells. For use as an n-type layer or as an intermediate reflector in thin-film silicon solar cells, a wide optical band gap E_{04}, and a tuneable refractive index n at a sufficient conductivity σ are desired. The shaded areas in Figure 4.13 indicate the properties with σ>10^{-5} (Ωcm)$^{-1}$ which is above the σ-(IR)limit, E_{04}>2.0 eV which is higher than for non-alloyed n-layers, and n<3.5 which is lower than for non-alloyed n-layers.
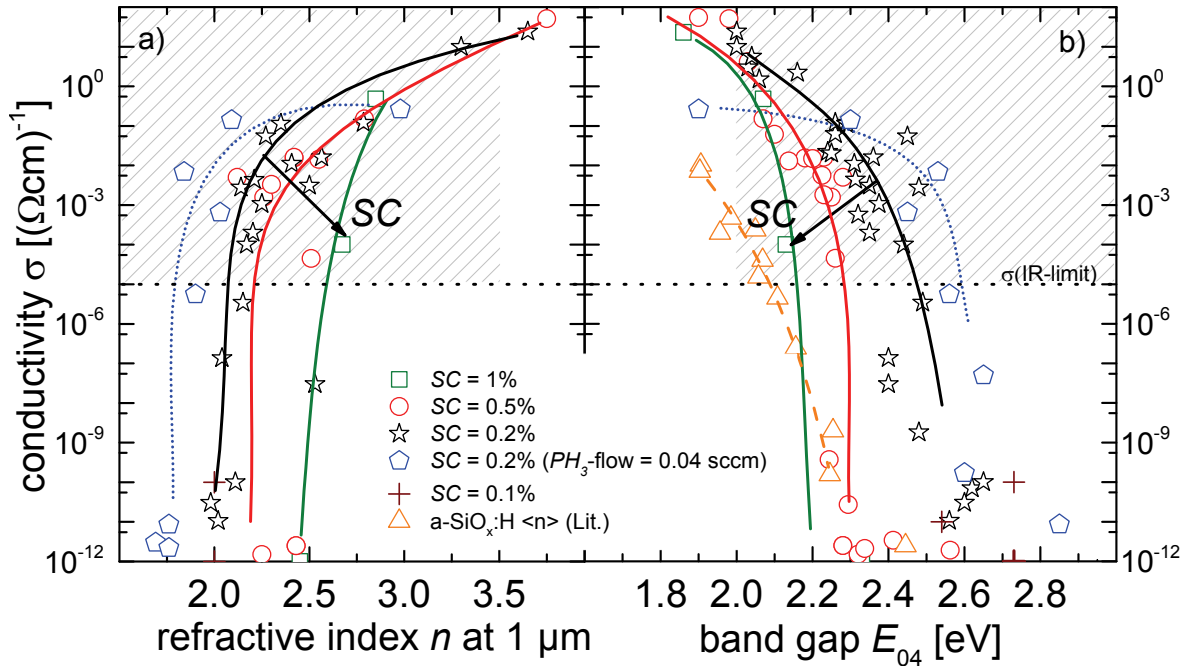
Figure 4.13: The electrical conductivity σ for μc-SiO$_x$:H films with different silane concentrations versus a) the refractive index n and b) the band gap E$_{04}$. The silane concentrations SC are indicated in the legend. All series were prepared using a phosphine flow of 0.02 sccm except where otherwise stated. To vary SC, the hydrogen flow was varied and a silane flow of 1 sccm was used for all series. In both graphs, the calculated lower conductivity σ-(IR)limit for use as an intermediate reflector is indicated as a dotted line. The E$_{04}$ of n-type amorphous silicon oxide films (a-SiO$_x$:H) from the literature [125,131] is shown for comparison. The dashed curve is a guide to the eye for the literature values, the dotted curve for the series using a phosphine flow of 0.04 sccm, and the solid curves for the SC-series using a phosphine flow of 0.02 sccm. Thicknesses range from 300 nm to 2 μm, the plasma power density was 300 mW/cm² and the deposition pressure was 4 mbar for all samples. For more details, see chapter 2.

Figure 4.13 shows the results from samples for various silane concentrations from 0.1% to 1%, as indicated in the legend and described in Table 4.1. To vary the silane concentration *SC*, the hydrogen flow was varied. All series were prepared using a phosphine flow of 0.02 sccm except where otherwise stated. The E_{04} band gap of amorphous silicon oxide films (n-type a-SiO$_x$:H) from the literature [125,131] is shown for comparison.

Several findings are evident in Figure 4.13:

- n-type μc-SiO$_x$:H films prepared with a lower *SC* show higher conductivities at a given *n* and E_{04}. In other words, the E_{04} band gap can be increased and the refractive index *n* decreased for a given conductivity when using a lower *SC*.

- n-type μc-SiO$_x$:H films with a larger E_{04} band gap (>2.0 eV), compared to films without oxygen incorporation (Figure 2.7), can be prepared with a broad range of refractive indices from 1.84 to 3.5 and conductivities above the σ-(IR)limit (1×10^{-5} (Ωcm)$^{-1}$).

- The n-type μc-SiO$_x$:H films with the lowest refractive index of 1.84, the highest band gap of 2.53 eV and conductivities above the σ-(IR)limit (7×10^{-3} (Ωcm)$^{-1}$) were prepared within the series using a higher phosphine flow of 0.04 sccm.

- At a given E_{04}, n-type a-SiO$_x$:H samples (triangles) [125,131] have a conductivity, of 3 to 7 orders of magnitude lower compared to the n-type μc-SiO$_x$:H samples.

From this figure, one can conclude that the introduction of a doped microcrystalline phase in the n-type a-SiO$_x$:H leads to a highly transparent films with sufficient conductivity and a refractive index that is tuneable over a wide range. These properties enable many applications in thin-film silicon solar cells. For example, the low refractive index provides a distinct refractive index step to the a-Si:H i-layer ($n \approx 3.8$) of the top cell, which leads to reflection of the light back into the top cell. This means that the material has considerable potential to serve as a highly transparent n-type intermediate reflector layer. In addition, one can choose a material with a refractive index (1.84 to 3.5) tailored for the proposed application with a sufficient conductivity ($>10^{-5}\,(\Omega\mathrm{cm})^{-1}$) and higher transparency ($E_{04}>2.0\,\mathrm{eV}$), compared to n-type a-Si:H or μc-Si:H.

4.3 Development of p-type microcrystalline silicon oxide

For the application of p-type μc-SiO$_x$:H films in thin-film silicon solar cells, their material properties have to fulfil requirements similar to those for n-type μc-SiO$_x$:H films. Therefore, a very similar systematic to that for the n-type μc-SiO$_x$:H is used to describe the material development and, consequently, the presentation of the results for the p-type μc-SiO$_x$:H is similar. The reader will be referred frequently to the corresponding chapter for n-type μc-SiO$_x$:H (section 4.2). A summary of the properties of n-type and p-type μc-SiO$_x$:H is given in chapter 5.

4.3.1 Details of the applied process gas flow variations

Several types of sample series such as SC-series, (S+O)C-series and TMB-series were prepared within the development of p-type μc-SiO$_x$:H. For each type of sample series the main parameters e.g. *SC, (S+O)C,...* was varied, and for these main parameters the CO_2/SiH_4 ratio r_{CO2} was varied. A detailed description of the gas flow variations will be given in the following. All other preparation details, such as deposition pressure, etc., that remain identical for all series, have been described previously in section 2.2.4. The μc-SiO$_x$:H layers were grown with a sufficient thickness between 300 nm and 2 μm (unless otherwise stated) to reduce an influence of the fluctuations within incubation zone.

SC-series

At each value of silane concentration (*SC*) parameter, the CO_2/SiH_4 ratio (r_{CO2}) was varied in one series, called SC-series. While this terminology SC-series is unfortunately a bit misleading, as it does not refer to a variation in the silane concentration *SC* within the series, it is necessary owing to the large number of different parameter sets presented in this work, and is, in context to the names of the other series, consistent. Table 4.3 shows details of the gas flow variations for the various SC-series. The sample series are named in the first column according to the silane concentration $SC = SiH_4/(SiH_4 + H_2)$ that was used for the particular sample series. To obtain an *SC* between 0.1% and 0.4%, the silane flow was varied between 0.5 sccm and 2 sccm and a hydrogen flow of 500 sccm was used. Because the SiH_4 mass flow controller reaches its lower limit with reasonable accuracy at 0.5 sccm, it is necessary to increase the hydrogen flow to 1000 sccm (SC-series indicated with *) to be able to further reduce the silane concentration *SC* to 0.05%. For the 0.1% SC-series, both hydrogen flows (500 sccm and 1000 sccm) were applied, to make it possible to compare SC-series with the same *SC* but a varied hydrogen flow. A further reduction in the silane concentration *SC,* compared to the n-type material, is needed to be able to prepare material with a crystalline volume fraction. For all series, a flow of 0.5 sccm of 1% TMB in He was used, resulting in a net TMB flow of 0.005 sccm as the dopant source.

*Table 4.3: The **SC-series** are named in the first column according to the silane concentration SC, which was kept constant within each sample series. The gas flows are shown for each SC-series in the corresponding rows in sccm. The resulting variation in CO_2/SiH_4 ratio r_{CO2} is shown in the last column.*

SC-series SC=const.	SiH_4 flow [sccm]	H_2 flow [sccm]	CO_2 flow [sccm]	TMB flow [sccm]	He flow [sccm]	r_{CO2} SiH_4/CO_2-ratio
0.4%	2	**500**	0-4	0.005	0.5	0-2
0.2%	1	**500**	0-3	0.005	0.5	0-3
0.1%	0.5	**500**	0-2	0.005	0.5	0-4
0.1%*	1	**1000**	0-6	0.005	0.5	0-6
0.05%*	0.5	**1000**	0-6	0.005	0.5	0-12

Figure 4.14 shows, as one example, the process gas flows for the 0.2% SC-series versus the r_{CO2}. To increase the r_{CO2}, the CO_2 flow was increased. In this way, the r_{CO2} was varied between 0 and 3. To set the silane concentration to the desired value of *SC*, the hydrogen flow or the silane flow was varied, as indicated by the arrows in Figure 4.1. It is important to note that, to increase the r_{CO2}, more CO_2 was added, which resulted in an increase in the total amount of $SiH_4 + CO_2$ flow.
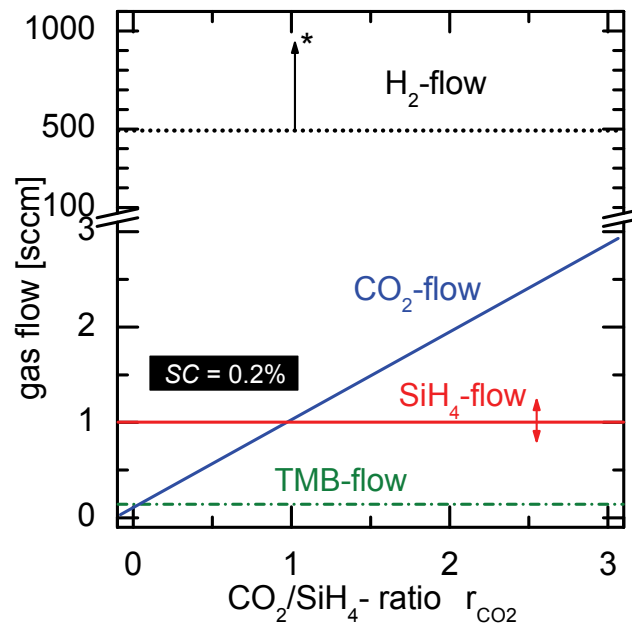
Figure 4.14: The process gas flows versus the CO_2/SiH_4 ratio r_{CO2}, shown, as an example, for the SC-series with a silane concentration of 0.2%. The arrows indicate the process gas flows that were varied between the particular SC-series. The process gases are as indicated in the graph. For details of the process gas flows, see Table 4.3.

(S+O)C-series

The (S+O)C-series were prepared to apply a constant amount of $SiH_4 + CO_2$ gas flow when varying the CO_2/SiH_4 ratio r_{CO2}. To increase the r_{CO2}, the SiH_4 flow was decreased and the CO_2 flow was increased. This leads to a constant $SiH_4 + CO_2$ flow with respect to the hydrogen flow

within one series. Details of the process gas flows in the individual SC-series are given in Table 4.4. The sample series are named in the first column according to the $(S+O)C=(SiH_4+CO_2)/(SiH_4+CO_2+H_2)$ concentration that was used for the particular sample series. Two (S+O)C-series were prepared, one using an $(S+O)C$ of 0.5% and the other an $(S+O)C$ of 0.25%. For the particular series, the TMB flow is proportional to the SiH_4+CO_2 gas flow.

*Table 4.4: The **(S+O)C-series** are named in the first column according to the sum of silane and carbon dioxide concentration with respect to the hydrogen flow (S+O)C, which was kept constant within each series. The gas flows are shown for each sample series in the corresponding rows in sccm. The resulting variation in CO_2/SiH_4 ratio r_{CO2} is shown in the last column.*

(S+O)C-series (S+O)C=const.	SiH4 flow [sccm]	H2 flow [sccm]	CO2 flow [sccm]	TMB flow [sccm]	He flow [sccm]	r_{CO2} SiH_4/CO_2-ratio
0.5%	0.36 - 2.5	500	0 - 2.14	0.006	0.5	0 - 6
0.25%	0.18 - 1.25	500	0 - 1.07	0.003	0.5	0 - 6

Figure 4.15 shows, as one example, the process gas flows versus the r_{CO2} for the 0.25% (S+O)C-series. The (S+O)C-series were prepared to apply a constant amount of process gas when varying the r_{CO2} within each sample series. Consequently, to increase the r_{CO2}, the SiH_4 flow was decreased from 1.25 sccm to 0.18 sccm and the CO_2 flow increased from 0 sccm to 1.07 sccm.
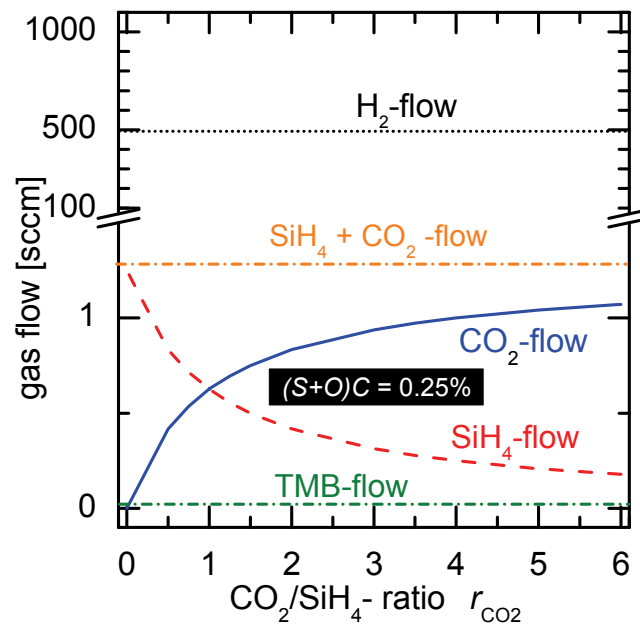
Figure 4.15: The process gas flows versus the CO_2/SiH_4 ratio r_{CO2} shown as an example for the (S+O)C-series of 0.25%. The process gases are as indicated on the graph. For details of the process gas flows, see Table 4.4.

TMB-series

To investigate the influence of the TMB flow, several sample series were prepared. Details of the process gas flows in the individual TMB-series are given in Table 4.5. The sample series are named, in the first column, after the TMB flow that was used for the particular sample series. For all series, a gas mixture of 1% TMB diluted in He was used. The net flow in sccm is shown as TMB flow. For example, a 0.5 sccm flow of 1% TMB in He results in a net TMB flow of 0.005 sccm. Two sets of sample series were performed with two silane concentrations ($SC=0.1\%$ and $SC=0.2\%$). For both silane concentrations, several TMB flows, from 0.005 sccm to 0.02 sccm, were applied. For the particular TMB-series, the CO_2 flow was increased in order to increase the r_{CO2}, while the SC and the TMB flow was kept constant.

*Table 4.5: The **TMB-series** are named, in the first column, according to the TMB flow in sccm, which was kept constant within each sample series. The gas flows in sccm are shown for each sample series in the corresponding rows. The SC is shown in the next to last column. The resulting variation in CO_2/SiH_4 ratio r_{CO2} is shown in the last column.*

TMB-series TMB flow=const.	SiH_4 flow [sccm]	H_2 flow [sccm]	CO_2 flow [sccm]	He flow [sccm]	SC [%]	r_{CO2} SiH_4/CO_2-ratio
0.0025 sccm	0.5	500	0 - 1.5	0.25	**0.1**	0 - 3
0.005 sccm	0.5	500	0 - 1.5	0.5	**0.1**	0 - 3
0.01 sccm	0.5	500	0 - 1.5	1	**0.1**	0 - 3
0.02 sccm	0.5	500	0 - 1.5	2	**0.1**	0 - 3
0.0025 sccm	1	500	0 - 3	0.25	**0.2**	0 - 3
0.005 sccm	1	500	0 - 3	0.5	**0.2**	0 - 3
0.01 sccm	1	500	0 - 3	1	**0.2**	0 - 3
0.02 sccm	1	500	0 - 3	2	**0.2**	0 - 3

Figure 4.16 shows, as one example, the process gas flows for the TMB=0.01 sccm sample series at SC=0.2% versus the r_{CO2}. To increase the r_{CO2}, the CO_2 flow was increased from 0 sccm to 3 sccm. In this way, the r_{CO2} was varied between 0 and 3. For the particular sample series, the TMB flow was varied as indicated by the arrow in Figure 4.16.
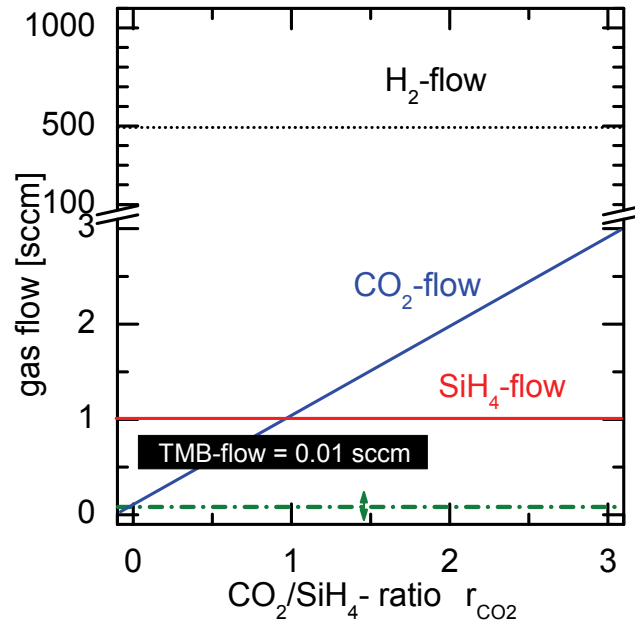
Figure 4.16: The process gas flows versus the CO_2/SiH_4 ratio r_{CO2}, shown as an example for the TMB-series with a phosphine flow of 0.01 sccm and an SC = 0.2%. The arrow indicates the process gas flow that was varied between the individual TMB-series. The process gases are as indicated on the graph. For details of the process gas flows, see Table 4.5.

4.3.2   Oxygen content

As has been previously shown for the n-type $\mu c\text{-SiO}_x$:H in Section 4.2.3, the optical properties of p-type $\mu c\text{-SiO}_x$:H are strongly determined by the oxygen content in the film, and play an important role for applications in thin-film silicon solar cells. Therefore, it is also important to determine incorporated oxygen in the p-type $\mu c\text{-SiO}_x$:H material and its dependency on the r_{CO2}. Figure 4.17 shows the oxygen content measured by RBS versus the r_{CO2} for $\mu c\text{-SiO}_x$:H p-type films for different series, as described in Table 4.3 and Table 4.4.
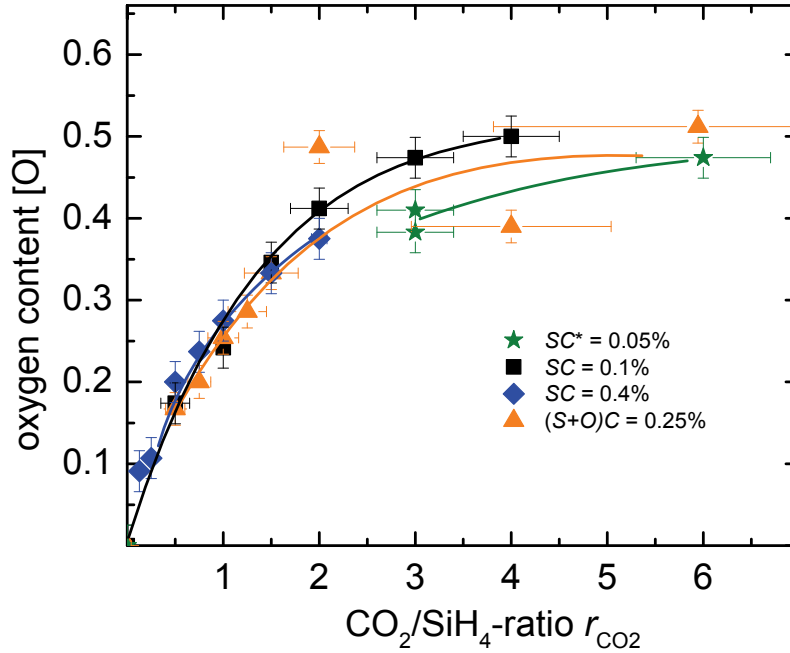
Figure 4.17: The oxygen content [O] versus the CO_2/SiH_4 ratio r_{CO2}. For the SC-series with constant SC, and for the (S+O)C-series with constant SiH_4+CO_2 flow, the concentrations are shown in the legend. For the series marked with *, a higher hydrogen flow of 1000 sccm was applied. The gas flows are described in Table 4.3 and Table 4.4. Thicknesses range from 300 nm to 2 μm (except for the (S+O)C-series from 200 nm to 2 μm), the plasma power density was 300 mW/cm² and the deposition pressure was 4 mbar for all samples. For more details, see chapter 2. The curves are guides to the eye.

Figure 4.17 shows the oxygen content versus the CO_2/SiH_4 ratio r_{CO2} with an *SC* of 0.05%* (stars), *SC* of 0.1% (squares), *(S+O)C* of 0.25% (trinagles) and *SC* of 0.4% (diamonds). The oxygen content increases up to an r_{CO2} of 2 from 0 to 0.4, and, for higher r_{CO2}, further to 0.51. It is remarkable that at a given r_{CO2} of 1 for *SC*=0.1% (squares) and *SC*=0.4% (diamonds), despite a change by a factor of 4 in CO_2 flow, the oxygen content is similar. In addition Figure 4.17 shows that the oxygen content increases for the (S+O)C-series (triangles) in a similar way as in in the *SC*-series. As a result of the similarity between the increase of the oxygen content with CO_2 to SiH_4 ratio (r_{CO2}) for the SC-series and for the (S+O)C-series, it can be concluded that the determining parameter for the amount of oxygen incorporated in the p-type μc-SiO$_x$:H is the r_{CO2}, but not the absolute flow of CO_2. This is valid for an increase in the SiH_4+CO_2 flow, as in the SC-series, or a constant SiH_4+CO_2 gas flow, as in the (S+O)C-series. For an $r_{CO2}>2$ the r_{CO2} value has a large uncertainty that originates in larger relative variations in the SiH_4 flow at the lower flow limit of the SiH_4 mass flow controller. The carbon content in the films is below the detection limit of RBS, which is 2% [70].

4.3.3 Raman intensity ratio and electrical conductivity

In this section, the relationships between deposition conditions (mainly the gas flows) and structure (I_c), on the one hand, and the structure and electrical and optical properties, on the other hand, will be shown in the following for a several sample series. We will focus on the Raman

intensity ratio I_c and conductivity σ first, before presenting results on optical properties in section 4.3.4.

SC-series

Figure 4.18 shows a) the Raman intensity ratio I_c, and b) the conductivity σ for p-type μc-SiO$_x$:H films versus the CO$_2$/SiH$_4$ ratio r_{CO2} for the SC-series (0.05% (stars), 0.1% (squares), 0.2% (circles), and 0.4% (diamonds)). A hydrogen flow of 1000 sccm was used for the SC-series, using 0.05% (filled stars) and 0.1% (filled squares). A net TMB flow of 0.005 sccm as the dopant source was used for all series shown in Figure 4.18. For more details of the gas flows, see Table 4.3. As in section 4.2, the required conductivity for the IR layer, the σ(IR)-limit, is indicated by the dotted line in Figure 4.18 b).

The Raman intensity ratio I_c and the conductivity σ decrease with increasing r_{CO2} for all series. As for n-type μc-SiO$_x$:H, it is desired to prepare material containing a doped μc-Si:H fraction at a high CO$_2$/SiH$_4$ ratio r_{CO2}. Therefore, we examine Figure 4.18 a) with a focus on the maximum r_{CO2} at which a Raman intensity ratio $>0\%$ was measured for each sample series. With increasing *SC*, the maximum r_{CO2} that still resulted in microcrystalline growth decreases from $r_{CO2}<2$ for the SC=0.1% (squares) to $r_{CO2}<0.25$ for the *SC*=0.4% (diamonds). In other words, at higher silane concentrations, the r_{CO2} should not be chosen too high to achieve crystalline growth. When using a low *SC* of 0.05% (stars), a high r_{CO2} of 6 (not shown in the graph) still results in a microcrystalline growth. The *SC*=0.1% series with a hydrogen flow of 1000 sccm (full squares) and 500 sccm (open squares) show a similar decrease in I_c versus the r_{CO2}, despite a difference in the SiH$_4$+H$_2$ flow and CO$_2$ flow.
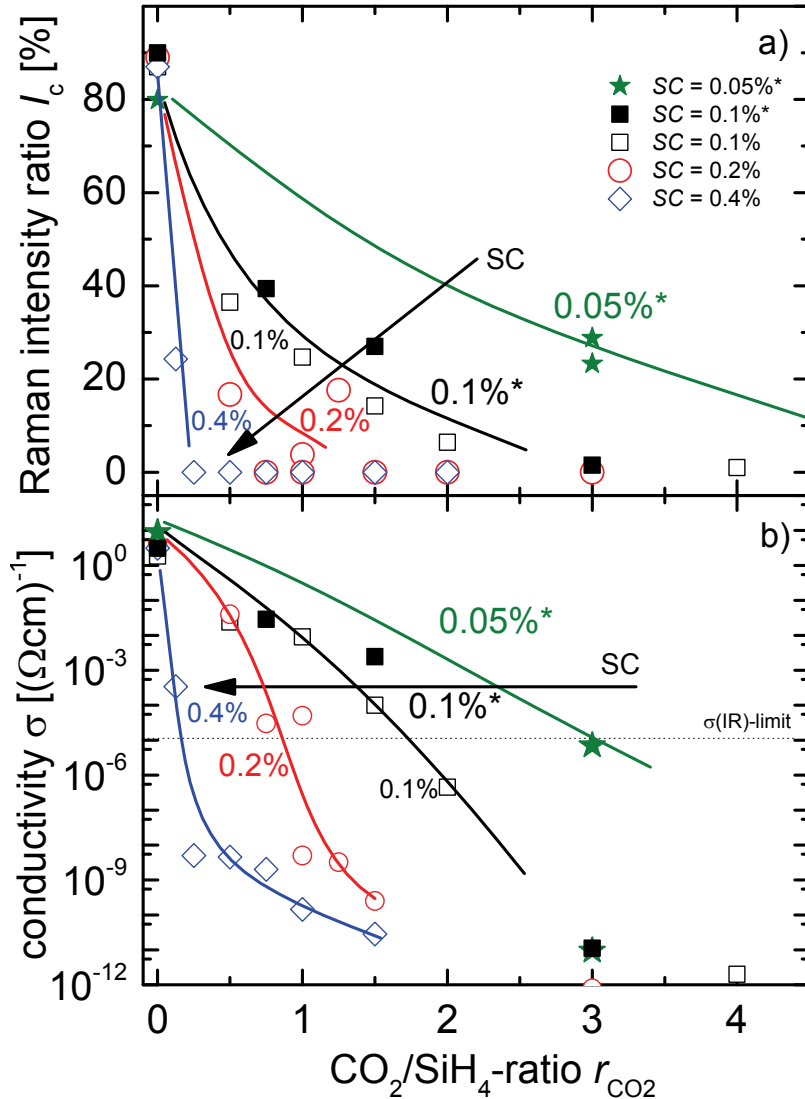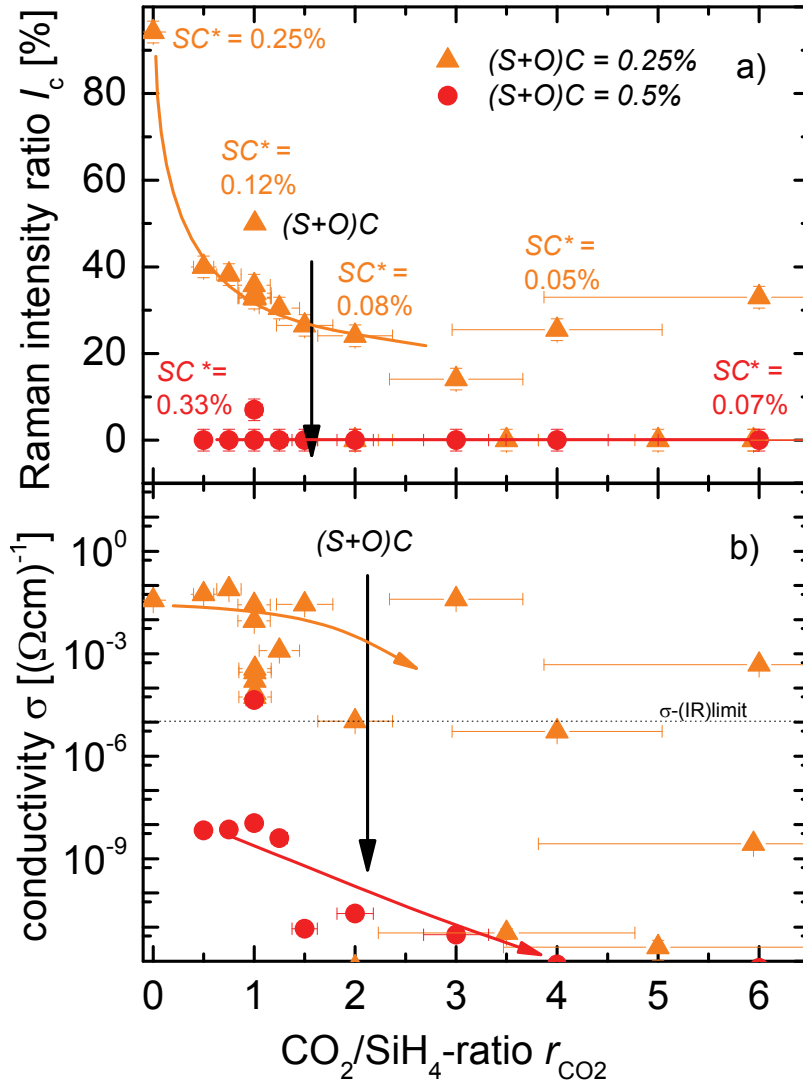
*Figure 4.18: a) The Raman intensity ratio I_c and b) the conductivity σ versus the CO_2/SiH_4 ratio r_{CO2}. The silane concentration SC is shown in %. For the SC-series indicated by the *, a H_2 flow of 1000 sccm and, for the other series H_2, a flow of 500 sccm was used. For all series, a TMB flow of 0.005 sccm was applied. The gas flows are described in Table 4.3. The lower conductivity limit (σ(IR)-limit) is indicated as a dotted line. Thicknesses range from 300 nm to 2 µm, the plasma power density was 300 mW/cm² and the deposition pressure was 4 mbar for all samples. For more details, see chapter 2. The curves are guides to the eye.*

Figure 4.18 b) shows the dark conductivity σ of the films versus the r_{CO2}. The conductivity σ decreases with increasing r_{CO2} for all series. The conductivity falls below the σ(IR)-limit of 1×10^{-5} at higher r_{CO2} when the *SC* decreases. Within the 0.4% SC-series (diamonds), this σ(IR)-limit is reached at an r_{CO2} of 0.25 and, for the 0.05% SC-series (stars), at an r_{CO2} of 3. The conductivities of both 0.1% SC-series using different hydrogen flows (squares) show the similar dependency versus the r_{CO2}.

This means that one can use higher r_{CO2} when decreasing the silane concentration and still obtain conductivities above the σ(IR)-limit. The relationship between the r_{CO2} and optical properties such as the E_{04} band gap will be shown in section 4.3.4.

(S+O)C-series

Figure 4.19 shows a) the Raman intensity ratio I_c and b) the conductivity σ versus the r_{CO2} for two (S+O)C-series, with $(S+O)=0.25\%$ (triangles) and $(S+O)=0.5\%$ (circles). Details of the process gas flows in the individual (S+O)C-series are given in Table 4.4.

Figure 4.19: a) The Raman intensity ratio I_c and b) the conductivity σ versus the CO_2/SiH_4 ratio r_{CO2}. Both series were prepared with constant $SiH_4 + CO_2$ gas flow and a hydrogen gas flow of 500 sccm. The (S+O)C is shown in the legend in %. The SC* values indicated on the graph are calculated from the specific gas flow values for better comparison to the SC-series. The TMB flow for the 0.25% and 0.5% (S+O)C-series was 0.003 sccm and 0.006 sccm, respectively. The gas flows are also described in Table 4.4. Thicknesses range from 300 nm to 2 μm (except for the 0.25% (S+O)C-series from 200 nm to 2 μm), the plasma power density was 300 mW/cm² and the deposition pressure was 4 mbar for all samples. For more details, see chapter 2. The lower conductivity limit (σ-(IR)limit) is indicated as a dotted line. The curves are guides to the eye.

For the series using an *(S+O)C* of 0.5% (circles), the conductivity σ is low and the Raman intensity ratio $I_c \approx 0\%$ for all r_{CO2}. The low I_c and σ can be attributed to the high $SiH_4 + CO_2$ flow. For the series using an *(S+C)O* of 0.25% (triangles), the Raman intensity ratio and the

conductivity are higher. The higher I_c and σ can be attributed to the reduced amount of $SiH_4 + CO_2$ or increased hydrogen dilution. The Raman intensity ratio I_c and the conductivity σ decrease with increasing r_{CO2}. However, even for high $r_{CO2} \approx 6$, a Raman intensity ratio $> 20\%$ and a conductivity $> 10^{-5} (\Omega cm)^{-1}$ was measured. This is associated with the decrease in silane concentration SC (as labelled) when increasing the r_{CO2}. The decrease in SC has the opposite effect on I_c and σ than the increase in CO_2 flow has, which is demonstrated in Figure 4.18. For an $r_{CO2} > 2$, I_c- and σ-values show much scatter, which can be related to uncertainties in r_{CO2} that originate in variations in the SiH_4 flow at the lower flow limit of the mass flow controller.

TMB-series

It is known that methane, which is dissociated to CH_3 [132,133] and boron compounds [134] hinder the crystalline growth during the deposition of p-type μc-Si:H with PECVD. Trimethylboron $B(CH_3)_3$ (TMB) contains boron and 3 CH_3 groups; therefore, it is likely that TMB also hinders the microcrystalline growth when depositing p-type μc-SiO$_x$:H. The effect of the boron compounds on the growth could be due to the fact that doping with boron moves the Fermi level of the μc-Si:H to the valence band, therefore influences the desorption of the hydrogen on the growing surface, which leads to a lower surface mobility of the Si and therefore a reduced crystalline volume fraction [135,136]. To evaluate the effect of the TMB flow on the p-type μc-SiO$_x$:H properties, several TMB-series with varying r_{CO2} were prepared. Details of the process gas flows in the individual TMB-series are given in Table 4.5. Figure 4.20 shows a) the Raman intensity ratio I_c and b) the conductivity σ versus r_{CO2} for various TMB-series, as indicated in the legend.

The I_c decreases for all TMB-series with increasing CO_2/SiH_4 ratio r_{CO2}. For a given r_{CO2}, an increase in TMB flow from 0.0025 sccm up to 0.02 sccm results in lower values of I_c, as indicated by the arrow. In other words: with increasing TMB flow the maximum possible r_{CO2} which that still results in a crystalline growth is reduced. From this trend, one can conclude that the TMB flow strongly hinders the microcrystalline growth for p-type μc-SiO$_x$:H.

For a given r_{CO2}, an increase in SC from $SC = 0.1\%$ (open symbols, dashed curves) to $SC = 0.2\%$ (full symbols, solid curves), but at the same TMB flow, results in a lower I_c, as indicated by the dashed arrows. This was already shown in Figure 4.18 a), but in Figure 4.20 a), the influence of the SC for various TMB flows can be directly compared.
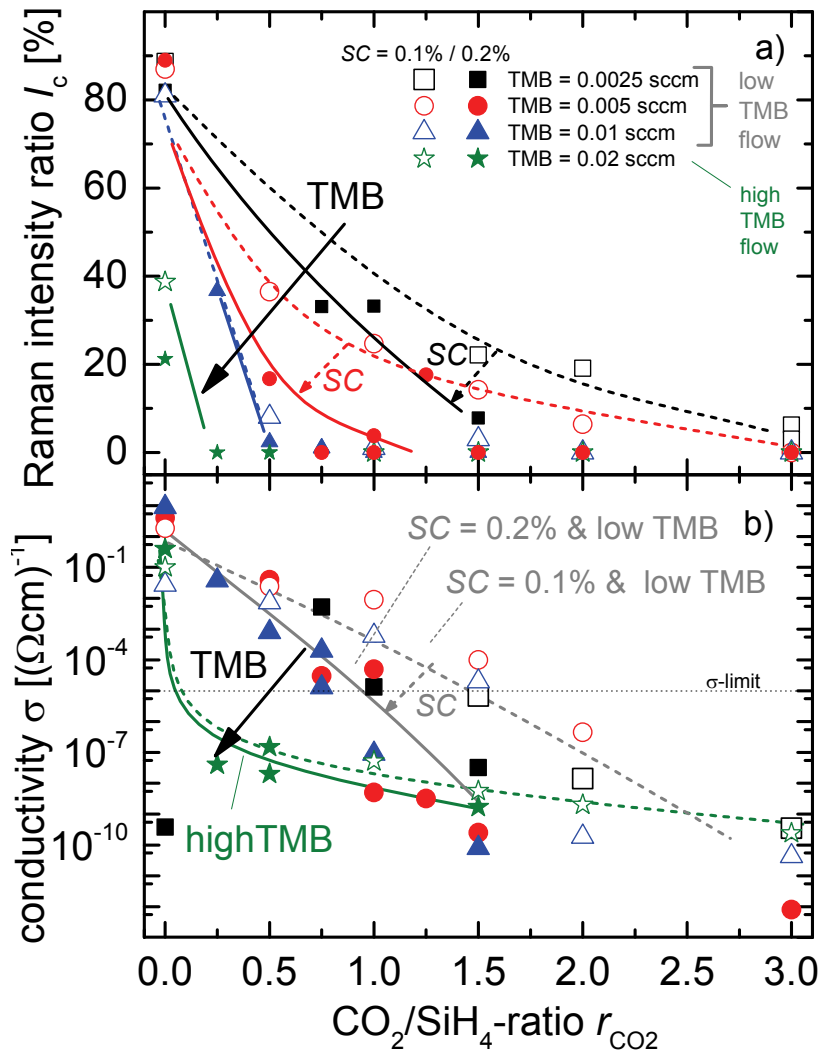
Figure 4.20: a) The Raman intensity ratio I_c and b) the conductivity σ versus the CO_2/SiH_4 ratio r_{CO2}. The silane concentrations SC with respect to the hydrogen flow in % and the TMB flow in sccm are indicated in the legend. The gas flows of these TMB-series are described in more detail in Table 4.5. The open symbols indicate the layers deposited using an SC = 0.1% and the full symbols the layers using an SC = 0.2%. The dashed curves are guides to the eye for SC = 0.1% and the solid curves for SC = 0.2% for the individual TMB flow series. In b) the conductivities for the series using low TMB flow < 0.02 sccm follow a trend that depends on the used SC, as indicated by the grey curves as guides to the eye. Thicknesses range from 300 nm to 2 μm, the plasma power density was 300 mW/cm² and the deposition pressure was 4 mbar for all samples. For more details, see chapter 2. The lower conductivity limit (σ-(IR)limit) is indicated by the dotted line.

Figure 4.20 b) shows that the conductivity σ decreases for all TMB-series with increasing CO_2/SiH_4 ratio r_{CO2}. Counter intuitively, at a given r_{CO2}, a high TMB flow of 0.02 sccm results in a lower conductivity, compared to the series using a lower TMB flow of ≤ 0.01 sccm, which is indicated by the arrow. At low TMB flows (≤ 0.01 sccm) and a given r_{CO2}, an increase in SC from SC=0.1% (open symbols, dashed curves) to SC=0.2% (full symbols, solid curves) results in a lower conductivity, as indicated by the dashed arrow. This means that, for low TMB flows

of ≤ 0.01 sccm, a higher conductivity at a given r_{CO2} was achieved when using a lower silane concentration and the TMB flow has a reduced influence.

From Figure 4.20 one can conclude that the I_c and σ for a given $r_{CO2} > 0$ are sensitive to the TMB flow. The Raman intensity ratio for a given r_{CO2} depends on the TMB flow and the *SC*. For TMB flows of ≤ 0.01 sccm, the conductivity at a given r_{CO2} depends mainly on the *SC*. This means that, below a certain threshold of the TMB flow (≤ 0.01 sccm), the silane concentration has a stronger influence on the conductivity than the TMB flow.

Conductivity versus Raman intensity ratio

In Figure 4.21, the conductivity σ versus the Raman intensity ratio I_c for all p-type μc-SiO$_x$:H samples presented in the present study are summarized. For samples with Raman intensity ratios of 0%, or slightly above, a large range of conductivities was measured. The conductivity for this completely amorphous a-SiO$_x$:H material ranges from $1 \times 10^{-13} (\Omega\text{cm})^{-1}$ to $3 \times 10^{-5} (\Omega\text{cm})^{-1}$. This is due to the fact that, for material without a crystalline silicon fraction which is p-type a-SiO$_x$:H, the conductivity varies strongly, depending on its oxygen content (not shown). This can be attributed to the inefficient dopant activation [62] in a-SiO$_x$:H. To achieve higher conductivities, a doped highly crystalline μc-Si:H phase is needed. In μc-Si:H the dopant activation of boron is close to unity [62,105,137]. A conductivity of up to $9 (\Omega\text{cm})^{-1}$ is achieved for highly crystalline material ($I_c = 80\%$). However, already for Raman intensity ratios of 10%, the conductivity increases to values above $1 \times 10^{-3} (\Omega\text{cm})^{-1}$. At high crystalline volume fractions, the oxygen-rich a-SiO$_x$:H phase is replaced by the crystalline silicon fraction, which is unfavourable for the transparency, as will be shown in the next section.
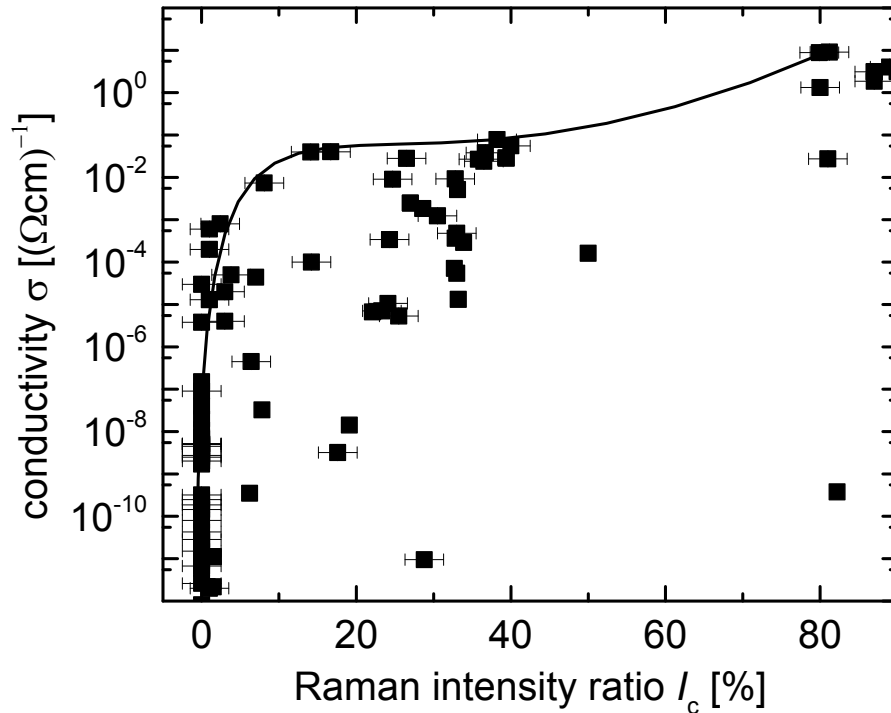
Figure 4.21: The conductivity σ versus the Raman intensity ratio I_c for all p-type samples. The curve follows the maximum conductivities at a given I_c. Thicknesses range from 200 nm and 2 μm, the plasma power density was 300 mW/cm² and the deposition pressure was 4 mbar for all samples. For more details, see chapter 2.

4.3.4   Optical Properties

This section presents the optical properties of p-type μc-SiO$_x$:H films, i.e. the absorption coefficient spectra, optical band gap, and refractive index. In addition, it shows the dependency between the optical properties and the process gas flow parameters. It also describes the relationship between the oxygen content, crystalline volume fraction, and optical properties. This section presents the data on p-type μc-SiO$_x$:H films in a systematic manner, similar to that for n-type μc-SiO$_x$:H.

Optical Absorption

Figure 4.22 shows the absorption coefficient α measured by photothermal deflection spectroscopy (PDS) versus the photon energy E from 0.5 eV to 2.5 eV for layers deposited using an *SC* of 0.2%, a TMB flow of 0.005 sccm, and various r_{CO2}, as indicated on the graph. As described in section 2.1.3, the optical band gap E_{04} is determined by the photon energy value at which an optical absorption coefficient α of 10^4 cm^{-1} is obtained.
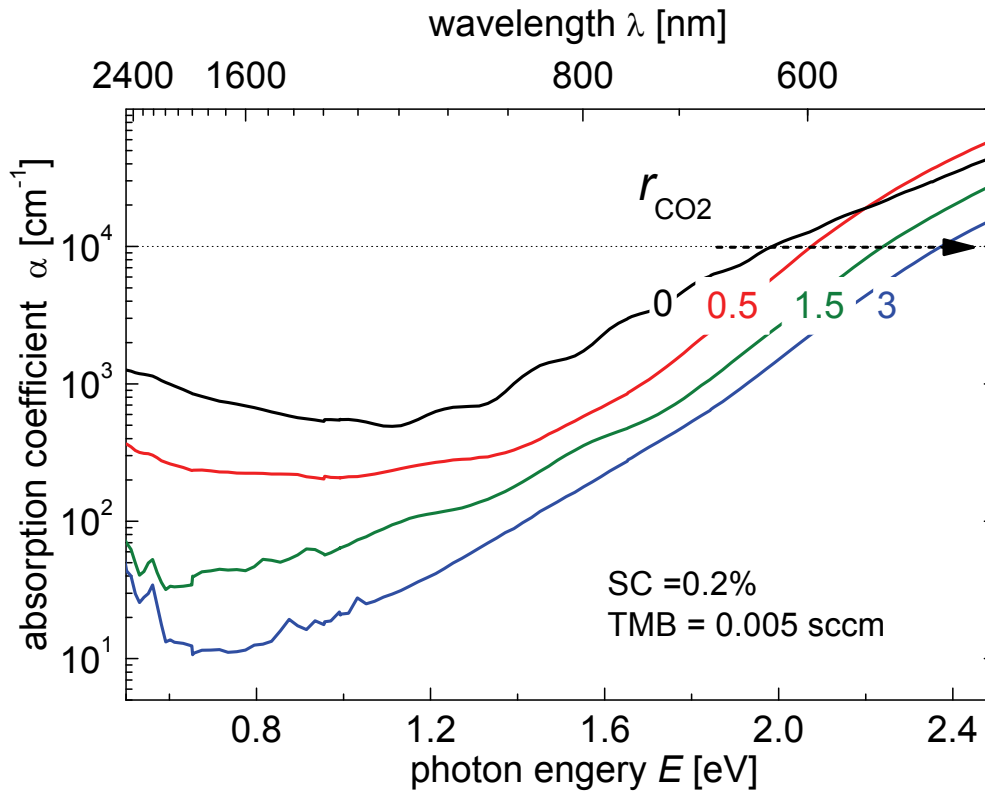
Figure 4.22: The absorption coefficient α measured by PDS versus the photon energy E on the lower x-axis and the wavelength λ on the upper x-axis. The material was prepared at 0.2% silane concentration and various CO_2/SiH_4 ratio r_{CO2} as indicated on the graph. A TMB flow of 0.005 sccm was applied. For details of the process gas flows, see Table 4.3. Thicknesses range from 470 nm to 752 nm, the plasma power density was 300 mW/cm² and the deposition pressure was 4 mbar for all samples. For more details, see chapter 2. The dotted line indicates the absorption coefficient, which is used as a value to determine the optical band gap E_{04}.

This E_{04} increases from 1.97 eV to 2.37 eV with increasing r_{CO2} from 0 to 3 as indicated by the arrow. However, the absorption coefficient spectra show that the absorption edge is shifted to higher photon energies with increasing r_{CO2}. In the sub band gap, at photon energies of below 1.1 eV, the absorption coefficient decreases with increasing r_{CO2}, which is also a consequence of less free carrier absorption, due to strong compensation of dopants by defects or because boron is not incorporated as a dopant in the a-SiO_x:H phase with high oxygen content. The observed trends for p-type μc-SiO_x:H films are similar to those for n-type μc-SiO_x:H films.
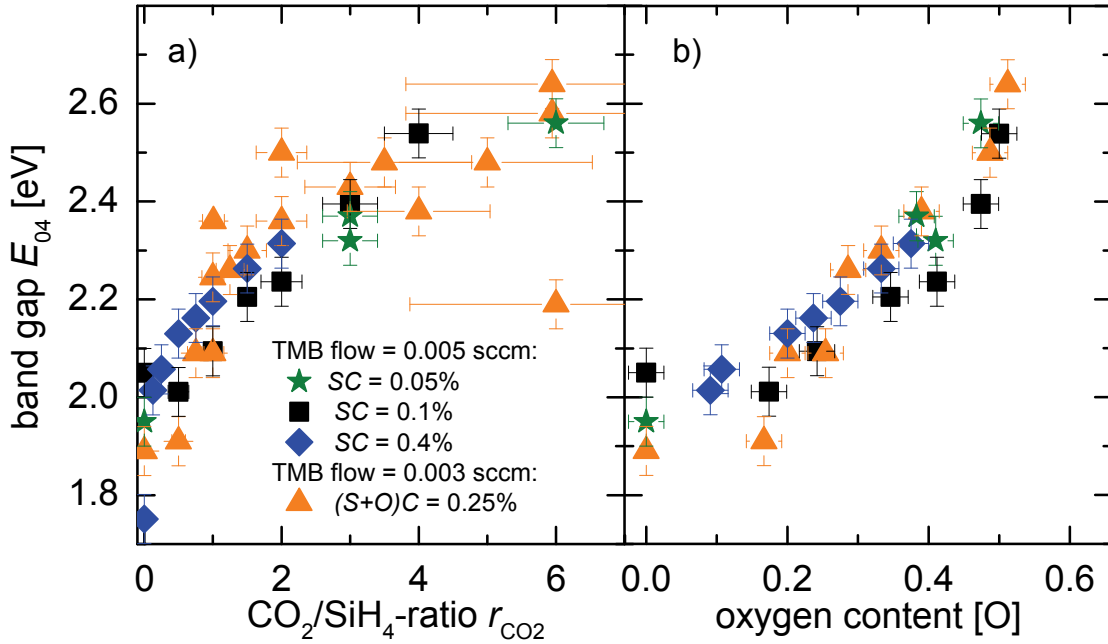
Figure 4.23: The band gap E_{04} versus a) the r_{CO2} and b) the oxygen content for SC-series and (S+O)C-series. For various SC-series with constant silane concentration and for the series with constant $SiH_4 + CO_2$ flow the (S+O)C-series is indicated in the legend. The TMB flow for the SC-series is 0.005 sccm, and for (S+O)C-series, 0.003 sccm. Details of the gas flow parameters are shown in Table 4.3 and Table 4.4. Thicknesses range from 300 nm to 2 µm (except for the (S+O)C-series from 200 nm to 2 µm), the plasma power density was 300 mW/cm² and the deposition pressure was 4 mbar for all samples. For more details, see chapter 2.

Figure 4.23 shows the E_{04} versus a) the r_{CO2} and versus b) the oxygen content for various SC-series and one (S+O)C-series, as indicated in the legend. For details of the gas flows, see Table 4.3 and Table 4.4. The E_{04} increases from around 1.9 eV to more than 2.6 eV with increasing r_{CO2} and oxygen content for both types of series, with some scatter in E_{04}. However, for all silane concentrations, a similar trend of the E_{04} on the r_{CO2} and the oxygen content is observed, despite the previously discussed differences in the properties, such as I_c and σ. From the figure, one can conclude that the E_{04} depends predominantly on the oxygen content, which is strongly influenced by the r_{CO2}, similar to the n-type µc-SiO$_x$:H.

Refractive index

Figure 4.24 shows the refractive index a) versus the r_{CO2} and b) versus the oxygen content for various SC-series and one (S+O)C-series, as indicated in the legend. For details of the process gas flows see Table 4.3 and Table 4.4.
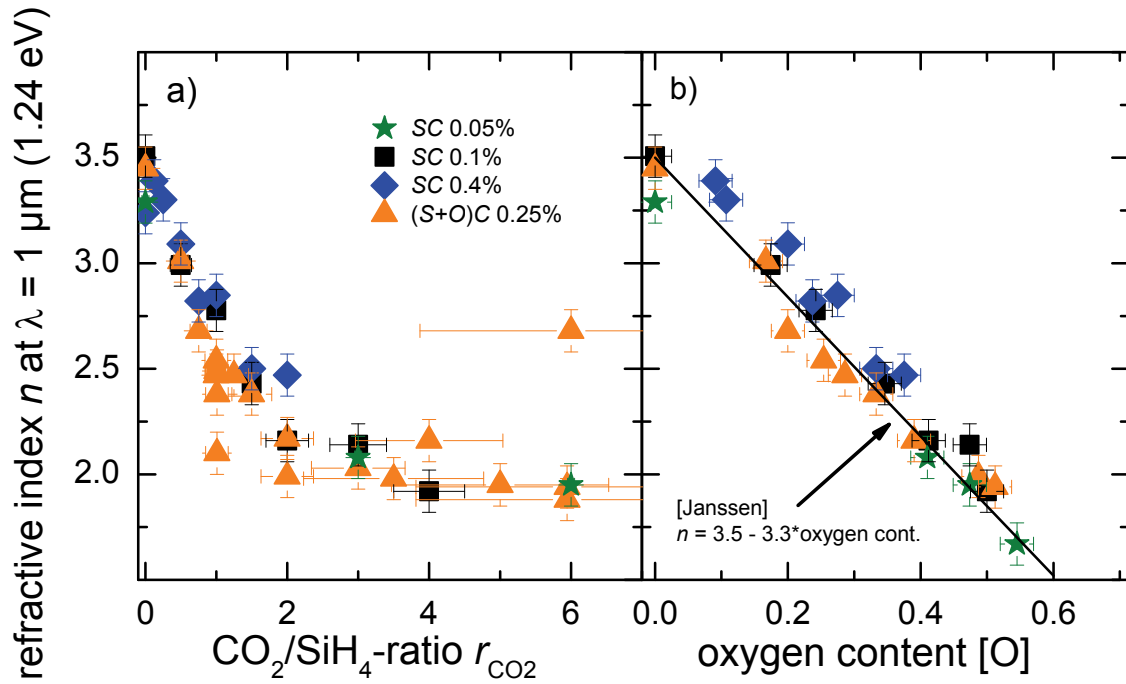
Figure 4.24: The refractive index n versus a) the CO_2/SiH_4 ratio r_{CO2} and b) the oxygen content [O] for various SC-series and for one (S+O)C series. The SC and the (S+O)C are shown in the legend in %. The TMB flow for the SC-series is 0.005 sccm, and for the (S+O)C-series, 0.003 sccm. Details of the gas flow parameters are shown in Table 4.3 and Table 4.4. Thicknesses range from 300 nm to 2 μm (except for the (S+O)C-series from 200 nm to 2 μm), the plasma power density was 300 mW/cm² and the deposition pressure was 4 mbar for all samples. For more details, see chapter 2. The line in b) is calculated by the function as indicated. The function is taken from the literature [131], labelled "Janssen", for amorphous silicon oxide films (n-type a-SiO$_x$:H) and is shown for comparison.

The refractive index decreases strongly from 3.9 to 2 with increasing r_{CO2} from 0 to 2. To reduce the refractive index to 1.8, the r_{CO2} has to be further increased to 6. For all series, the refractive index has a similar dependency on the r_{CO2}. Please note that, the oxygen content was measured by RBS in only some of the samples in a) and, consequently, cannot be shown in b). The refractive index decreases almost linearly from 3.5 at [O]≈0, finally reaching an *n* of 1.67 at an oxygen content of 0.55. As for n-type μc-SiO$_x$:H (Figure 4.11), the decrease in refractive index with the oxygen content follows the function that was proposed for a-SiO$_x$:H films [131]. From this, one can conclude that the oxygen content has a similar influence on the refractive index in μc-SiO$_x$:H as in a-SiO$_x$:H. Like for n-type μc-SiO$_x$:H, one can summarize that the material's refractive index can be varied by the r_{CO2}.
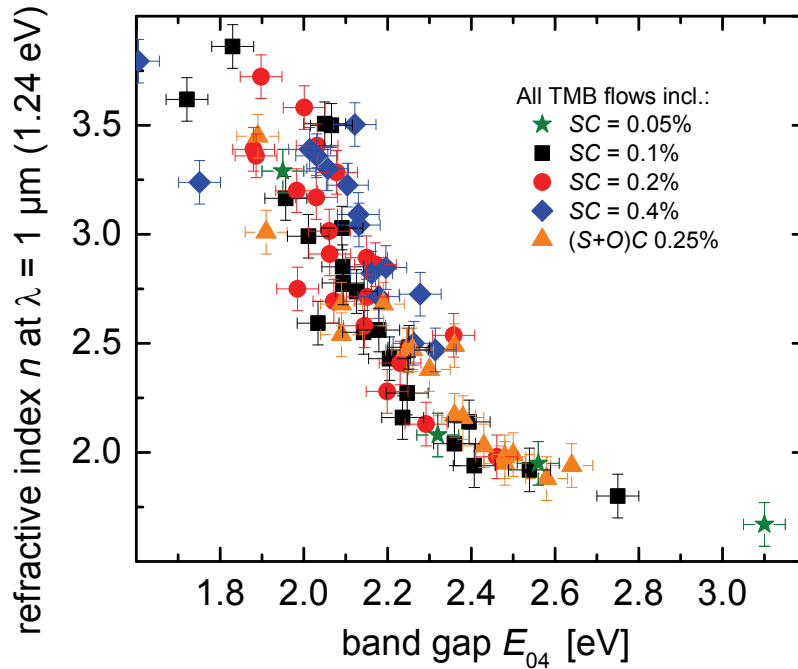
Figure 4.25: The refractive index n versus the band gap E_{04} for the SC-series and for one (S+O)C-series, as indicated in the legend. The results are from samples prepared using various TMB flows and r_{CO2}. Thicknesses range from 300 nm to 2 μm (except for the (S+O)C-series from 200 nm to 2 μm), the plasma power density was 300 mW/cm² and the deposition pressure was 4 mbar for all samples. For more details, see chapter 2.

Figure 4.25 shows the dependency between the band gap E_{04} and the refractive index n for p-type μc-SiO$_x$:H films prepared using various r_{CO2} and TMB-flows. The *SC* and the *(S+O)C* are indicated in the legend. With increasing band gap, from 1.6 eV to 3.1 eV, the refractive index decreases from 3.8 to 1.67. This represents a decrease of n with increasing band gap, as suggested by Moss [138], but it is not in quantitative agreement with the Moss formula (see Appendix F). This disagreement is most likely related to the fact that the μc-SiO$_x$:H is a phase mixture. In addition, the refractive index n and the optical band gap E_{04} are given for different photon energies, the refractive index is given for a wavelength of 1 μm (1.24 eV), and the E_{04} band gap is the photon energy at which an absorption coefficient of 10^4 cm^{-1} is obtained. Therefore, variations in the dispersion function will have an influence on the relationship between n and E_{04}, which could partly explain the scatter. However, the general trend of decreasing refractive index with increasing optical band gap E_{04} is clearly visible. This trend is also commonly encountered in other materials. This relationship leads to less transparent films at higher refractive indices, compared to films with lower refractive indices. However it is possible to prepare p-type μc-SiO$_x$:H films, which have a higher optical band gap than films which are non-alloyed e.g. μc-Si:H or a-Si:H, over a wide range of refractive indices from 1.9 to 3.7 with a sufficient conductivity (see section 4.3.5).

Optical properties versus Raman intensity ratio

The dependencies between oxygen content, optical properties, and deposition parameters were presented in previous figures for p-type µc-SiO$_x$:H. Figure 4.26 shows the E_{04} versus the Raman intensity ratio I_c for p-type layers prepared using various r_{CO2} and TMB flows. This figure can help to identify a material's suitability as e.g. a transparent nucleation layer for a subsequent µc-Si:H i-layer of the bottom cell, which means a high Raman intensity ratio (see Figure 6.8) and, simultaneously, a high E_{04}. As already shown for n-type µc-SiO$_x$:H (Figure 4.12), this figure helps also to classify the p-type material into the categories a-Si:H, a-SiO$_x$:H, µc-Si:H, and µc-SiO$_x$:H. The *SC* and the *(S+O)C* are indicated in the legend and results of various TMB flows are included.
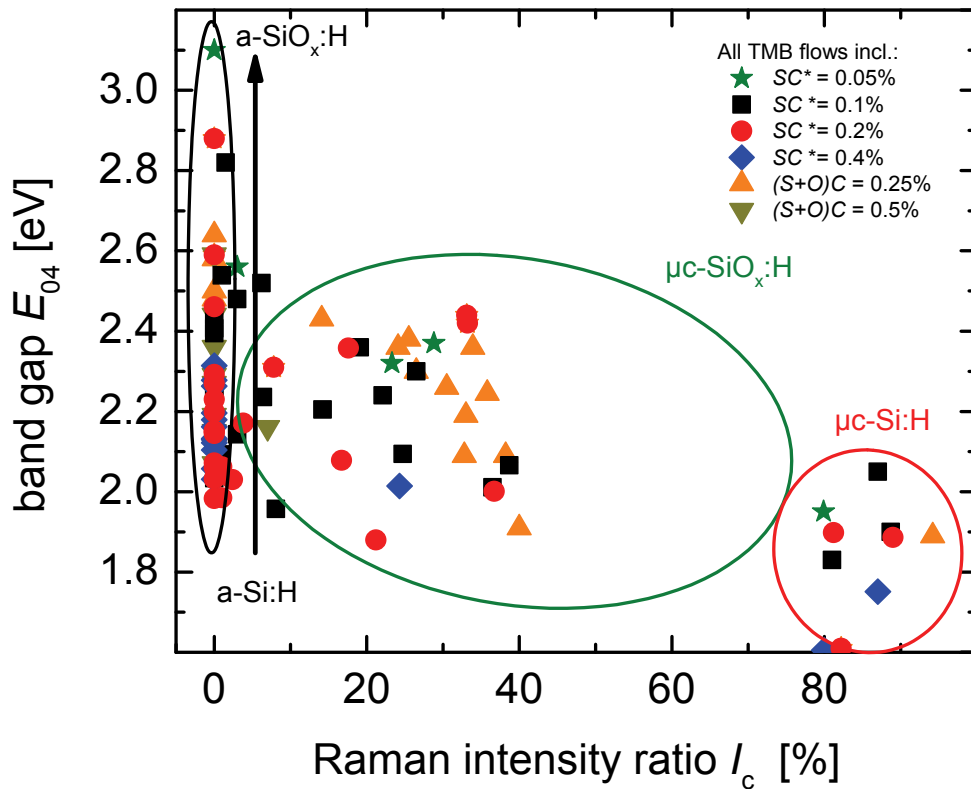
Figure 4.26: The band gap E_{04} versus the Raman intensity ratio I_c. For the series with constant silane concentration the SC and for the series with constant SiH_4+CO_2 flow the (S+O)C is shown in the legend. Thicknesses range from 300 nm to 2 µm (except for the (S+O)C-series from 200 nm to 2 µm), the plasma power density was 300 mW/cm² and the deposition pressure was 4 mbar for all samples. For more details, see chapter 2. All TMB flows are included. The material is classified into categories such as a-Si:H, a-SiO$_x$:H, µc-Si:H and µc-SiO$_x$:H as indicated.

Figure 4.26 shows, for amorphous material (I_c=0%), a wide range of band gaps E_{04} (1.9 eV to 3.1 eV). This material with an E_{04} of around 1.9 eV, is classified as a-Si:H and with an E_{04} of around 3.1 eV as a-SiO$_x$:H. At high Raman intensity ratios >70%, the material is here classified as µc-Si:H. In µc-Si:H the oxygen-rich, a-SiO$_x$:H phase is replaced by the crystalline silicon fraction, which results in a low E_{04} of 1.9 eV. Between the two extreme cases, from I_c=0% to

$I_c = 80\%$, a phase mixture is present that contains an amorphous silicon oxide phase and a microcrystalline silicon phase. This p-type $\mu c\text{-SiO}_x$:H material has a wide band gap of up to 2.46 eV at a Raman intensity ratio of 40%. Both properties are favourable for application as a highly transparent nucleation layer for a subsequently deposited $\mu c\text{-Si}$:H layer. Within the series from the present study no p-type $\mu c\text{-SiO}_x$:H films with an I_c between 40% and 75% were prepared which is the result of a strong decrease of the I_c for already low CO_2 to SiH_4 ratios (r_{CO2}) (see section 4.3.3).

4.3.5   Electrical conductivity vs. optical band gap and refractive index

For p-type $\mu c\text{-SiO}_x$:H, as for the n-type $\mu c\text{-SiO}_x$:H, the relationship between optical and electrical properties is the most relevant aspect in its development as a doped layer for thin-film silicon solar cells. A plot of conductivity versus refractive index n as in Figure 4.27 a) and versus the optical band gap (E_{04}) as in Figure 4.27 b) can serve as basis to assess its suitability for the proposed applications. For use as p-type window layer or as an intermediate reflector in thin-film silicon solar cells, a wide optical band gap E_{04}, and a tuneable refractive index n at a sufficient conductivity σ are desired. The shaded areas in Figure 4.27 indicate the properties with $\sigma > 10^{-5}(\Omega\text{cm})^{-1}$ which is above the σ-(IR)limit, $E_{04} > 2.0$ eV which is higher than for non-alloyed p-layers, and $n < 3.5$ which is lower than for non-alloyed n-layers. The solid curves are a guide to the eye for the SC-series with varied r_{CO2}. The dotted curves are a guide to the eye for the series of samples in which the flow of $SiH_4 + CO_2$ was constant and r_{CO2} was varied. The TMB flow within the (S+O)C-series is 0.003 sccm, similar to the TMB flow of 0.005 sccm within the SC-series. For more details of the gas flows, see Table 4.3 and Table 4.4.
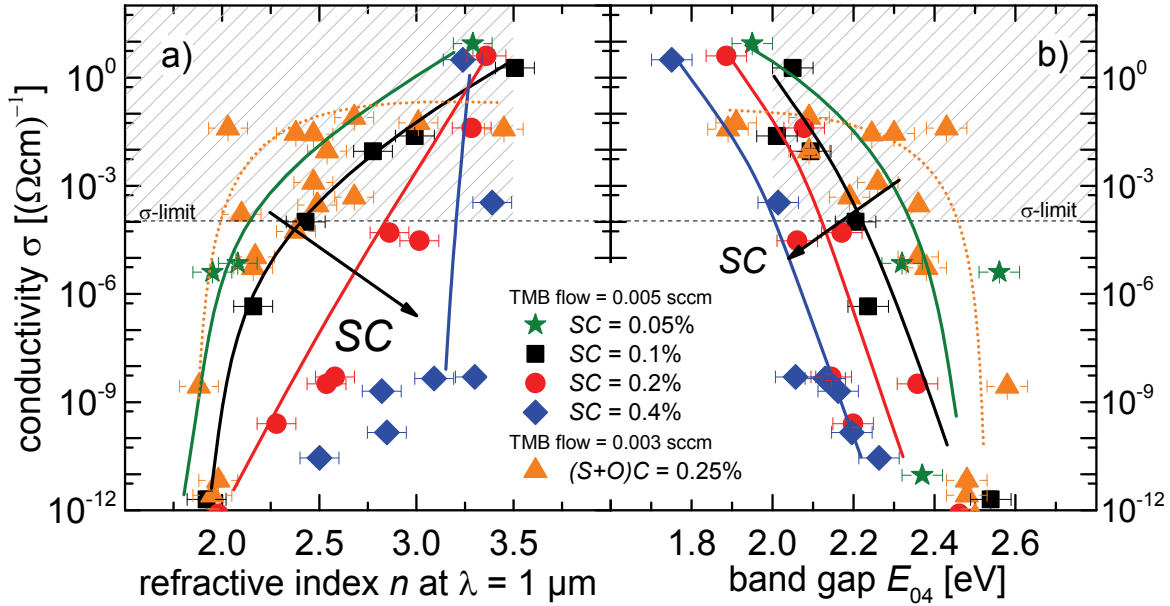
Figure 4.27: The electrical conductivity σ versus a) the refractive index n and b) the optical band gap E_{04} for p-type μc-SiO_x:H films. For the series with constant silane concentration the SC, and for the series with constant $SiH_4 + CO_2$ flow, the (S+O)C are shown in the legend in %. The TMB flow for the SC-series is 0.005 sccm and for the (S+O)C-series 0.003 sccm. Thicknesses range from 300 nm to 2 μm (except for the (S+O)C-series from 200 nm to 2 μm), the plasma power density was 300 mW/cm² and the deposition pressure was 4 mbar for all samples. For more details, see chapter 2. The lower conductivity limit (σ-(IR)limit) is indicated as dashed line. The dotted curves are guides to the eye for the (S+O)C-series and the solid curves are guides to the eye for SC-series.

For all sample series, the conductivity decreases with increasing optical band gap E_{04} and decreasing refractive index n. However, compared to non-alloyed p-type amorphous or microcrystalline silicon, which has an E_{04} of 2.0 eV and an n of ≈ 3.5, material with a conductivity above the critical limit (σ-(IR)limit$=1 \times 10^{-6} (\Omega cm)^{-1}$) can be obtained at higher E_{04} and lower n.

Several findings are evident in Figure 4.27:

- p-type μc-SiO_x:H films prepared with a lower *SC* show higher conductivities at a given n and E_{04}. In other words, the E_{04} band gap can be increased and the refractive index n decreased for a given conductivity when using a lower *SC* and appropriate r_{CO2}.

- p-type μc-SiO_x:H films with a wider E_{04} band gap (>2.0 eV), compared to films without oxygen incorporation (Figure 2.7), and a broad range of refractive indices from 1.9 to 3.5 and conductivities above the σ-(IR)limit ($1 \times 10^{-5} (\Omega cm)^{-1}$) can be prepared.

- p-type μc-SiO_x:H films with the lowest refractive index of 1.94, the highest band gap of 2.56 eV and conductivities above the σ-(IR)limit ($4 \times 10^{-6} (\Omega cm)^{-1}$) were prepared within the series using a low *SC* of 0.05%.

From this figure, one can conclude that p-type μc-SiO_x:H can be prepared with the similar favourable properties as n-type μc-SiO_x:H if appropriate deposition conditions are used.

4.4   Discussion of n- and p-type μc-SiO$_x$:H

As described in the introduction, doped μc-SiO$_x$ material has to fulfil a number of requirements related to its electronic and optical properties for the applications to thin-film silicon solar cells. The investigated doped μc-SiO$_x$:H material shows a high transparency, sufficient conductivity, and significant crystallinity. Because of the relationship between the refractive index and the optical band gap, the refractive index cannot be tuned independently. However, the refractive index can be tuned over a wide range for films that have a higher optical band gap than in the case of non-alloyed a-Si:H or μc-Si:H. This can be achieved because of the material's phases: a doped highly crystalline μc-Si:H phase and an a-SiO$_x$:H phase. The relationships between (i) the structure (I_c), dopant gas flow and electrical conductivity (σ), (ii) the composition [O] and the optical properties (E_{04}, n), and (iii) the gas flow parameters and growth will be discussed in the following.

The relationship between the structure, dopant gas flow, and electrical conductivity:

In the following, the influence of the crystalline volume fraction and the dopant gas flow on the electrical conductivity of μc-SiO$_x$:H will be discussed. The doped crystalline volume fraction has a strong influence on the conductivity. According to the percolation theory, a crystalline volume fraction threshold from which the conductivity increases significantly is expected, but e.g. in Figure 4.6, for n-type μc-SiO$_x$:H, or in Figure 4.21, for p-type μc-SiO$_x$:H, no obvious threshold can be identified. The percolation threshold is strongly influenced by the direction of the current flow through the doped μc-SiO$_x$:H film and by the geometry of the conductive inclusions, which are in the present case the doped silicon crystals. If, for example, one compares in growth direction elongated inclusions with spherical inclusions [139]: (i) On the one hand, the percolation would occur at much lower crystalline volume fractions for the elongated inclusions when used as doped layer in solar cells since the current flow is in this case in growth direction through the layer. (ii) On the other hand, the percolation would occur at higher crystalline volume fractions for the elongated inclusions when considering the current flow during conductivity measurements with co-planar contacts since the current flow is in this case in lateral direction through the film. However, some indications for a percolation threshold for n-type μc-SiO$_x$:H (Figure 4.6) are present and are elaborated in the following. The percolation threshold from the effective medium theory (EMT), using Bruggeman's model, is expected at $I_c \approx 33\%$ for spherical conductive inclusions in a less conducting matrix for three dimensions [130].

Bruggeman's EMT predicts that, below the percolation threshold $I_c \leq 33\%$, the conductivity is strongly determined by the conductivity of the matrix material, which is in μc-SiO$_x$:H the a-SiO$_x$:H phase conductivity ($\sigma_{\text{a-SiOx:H}}$). Some indications that support this prediction emerge from a comparison of the measured conductivity of the various SC-series for $I_c \leq 33\%$ with the calculated conductivity, using the formula derived from the EMT (Figure 4.6). If the doped a-SiO$_x$:H phase is more conductive ($\sigma_{\text{a-SiOx:H}} = 10^{-2} (\Omega\text{cm})^{-1}$), the percolation threshold is less

pronounced, which is the case for the $SC=0.5\%$ series. If the doped a-SiO$_x$:H phase is less conductive ($\sigma_{\text{a-SiOx:H}}=10^{-8}(\Omega\text{cm})^{-1}$), the percolation threshold is more pronounced, as is seen for the $SC=0.2\%$ series (see also Appendix G). The difference in $\sigma_{\text{a-SiOx:H}}$ can be related to the smaller band gap of the a-SiO$_x$:H phase for the SC-series with $SC=0.5\%$ compared to the SC-series with the $SC=0.2\%$ (Figure 4.12). These findings suggest a percolation threshold of n-type μc-SiO$_x$:H if the amorphous phase is less conductive. If the doped a-SiO$_x$:H is more conductive, the percolation threshold is less pronounced, as also predicted by Bruggeman's EMT.

For $I_c \geq 33\%$, the difference in conductivity between the different SC-series at a given I_c becomes smaller with increasing I_c. At an I_c of 80% (Figure 4.6), the conductivities reach typical conductivities for doped μc-Si:H. The difference between the predicted conductivity from the EMT and the measured conductivity for low SC$\leq$0.5% from $I_c=33\%$ to $I_c=80\%$ can be explained by considering the poor material quality of μc-Si:H phase, caused by the low silane concentration ($SC\leq0.5\%$). This is in accordance with frequently observed results that a too low silane concentration in the process gas might deteriorate the electrical properties of the material. This is possibly a result of a too high etching contribution during the growth and, therefore, poor defect and grain boundary passivation. This results in low doping efficiency or a disruption of the current path by e.g. grain boundaries [39].

In the following for n-type μc-SiO$_x$:H the influence of the phosphine flow on the conductivity is discussed. With increasing the phosphine concentration, the conductivity of the material increases (Figure 4.8 b) at a given O content. The increase in conductivity can be related to (i) a higher dopant concentration and, therefore, a higher free carrier concentration in the μc-Si:H phase or (ii) a larger crystalline volume fraction. Doped μc-Si:H has a higher free carrier concentration compared to a-SiO$_x$:H, because of its better doping efficiency. The increase in conductivity at a given O concentration for lower phosphine flow (PH$_3$=0.01 sccm) compared to no phosphine flow (PH$_3$=0 sccm) (Figure 4.8 a) can be clearly attributed to the increase in free carriers, since the crystalline volume fractions for both PH$_3$-series are similar at a given CO_2/SiH_4 ratio r_{CO2} (Figure 4.8 b). For higher phosphine flows >0.01 sccm, the crystalline volume fraction at a given CO_2/SiH_4 ratio is increased (Figure 4.8 a). Therefore, some of the increase in conductivity with phosphine flow can also be attributed to the increase in the crystalline volume fraction. An increase of the crystalline volume fraction with increasing phosphine flow (Figure 4.8 b) has also been reported in literature for μc-Si:H [140]. From this, one can conclude that an increased phosphine flow increases the conductivity, and the increase in conductivity can be attributed to a higher doping of the μc-Si:H phase and to an increase in crystalline volume fraction.

For p-type μc-SiO$_x$:H, the doping source gas is TMB in He, which has the opposite influence on the crystalline volume fraction at a given r_{CO2}, compared to the admixture of phosphine. In the present study, the He flow has most likely a minor effect on the material properties because (i) a

strong contribution on crystalline growth or the composition is not expected since a noble gas is less reactive with the surface of the growing film and (ii) a strong influence on the plasma is not expected since the He concentration is low. Figure 4.20 a) shows that the crystalline volume fraction is very sensitive to an increase in TMB in He flow. This means that the TMB admixture hinders crystal growth. A TMB flow of 0.02 sccm results in a low conductivity (Figure 4.20). For a TMB flow ≤0.01 sccm, the conductivity depends on the SC at a given r_{CO2}. For low silane concentrations, higher conductivities are achieved. This can be related to the increase in crystalline volume fraction with decreasing SC.

In the thin-film silicon solar cells, the doped layers have to conduct the current in the growth direction between the cells or to the contact e.g. the back contact. Therefore, the conductivity in the growth direction is more relevant for this application, but the conductivity of the films was measured lateral to the substrate in planar direction. The conductivity in the lateral direction and the growth direction could be different. There are many possibilities for an anisotropic conductivity. For example if the shape of the silicon crystals is elongated in growth direction instead of spherical. Alternatively, if, for example, there were spatially separated highly conductive crystalline columns in the growth direction, the conductivity in this direction would be most likely higher than in the lateral direction. For μc-Si:H, a columnar growth is expected, as shown by cross-section TEM images [42] and the image of one of the n-type μc-SiO$_x$:H shown in Figure 3.7. This image also shows a conical growth of the crystalline volume fraction within the first 100 nm. This could have the additional effect that the lateral conductivity would have a dependency related to the layer thickness, since the crystalline volume fraction changes with thickness. From a thickness series of doped n-type μc-SiO$_x$:H we know that above a layer thickness of 300 nm the increase in crystalline volume fraction (I_c) and conductivity (σ) (see Appendix H) with thickness is reduced. Therefore, in the present study, only layers with a thickness of more than 300 nm were considered to reduce the influence of the conical growth and of a nucleation layer (unless otherwise stated).

In addition, in the solar cell, an underlying μc-Si:H layer might act as a nucleation layer, and support the crystalline growth in the first tens of nanometres of the film and, therefore, the conductivity. This would not be visible in these investigations, because the conductivity was measured on layers with a thickness greater than 300 nm (unless otherwise stated). These effects on the conductivity will be visible when implementing the developed doped μc-SiO$_x$:H layers in solar cells. However, the results on conductivity versus the gas flow parameters can still be used as a general trend. It is most probable that, when applying the doped μc-SiO$_x$:H material as a thin layer to thin-film silicon solar cells, the gas flow parameter at which a sufficient conductivity for a certain application is achieved, will shift in one or the other direction. This means, in case of a growth on an amorphous layer, the nucleation would take longer, but on a microcrystalline silicon layer, there is an almost immediate microcrystalline growth.

The relationship between the composition and optical band gap / refractive index:

The optical properties such as optical band gap E_{04} and the refractive index n of the μc-SiO$_x$:H films are strongly determined by the oxygen content. The oxygen content can be varied by the CO_2/SiH_4 ratio r_{CO2}. It is valid for both n- and for p-type μc-SiO$_x$:H films. The E_{04} increases and the refractive index decreases with increasing the r_{CO2}. A general trend of a decreasing refractive index with E_{04} is clearly visible (Figure 4.25). This reduces the tuneability of the refractive index at a high band gap, e.g. at $n=3$, the E_{04} is reduced to 2.2 eV (Figure 4.25). However, the refractive index can be tuned over a wide range for films that have a higher optical band gap, such as non-alloyed a-Si:H or μc-Si:H. A similar dependency between the optical properties (E_{04}, n) and the oxygen content was found for μc-SiO$_x$:H, as was also found in a-SiO$_x$:H [131]. From these findings, one can conclude that the E_{04} and n are mainly determined by the oxygen content in the material. The μc-Si:H has, in comparison to oxygen-rich a-SiO$_x$:H, a relatively low E_{04} of 2 eV. Therefore, the transparency will be reduced when the crystalline volume fraction increases (Figure 4.12 and Figure 4.26).

The E_{04} calculated from the EMT for the series using an $SC=0.5\%$ is in good agreement with the experimental data (Figure 4.12). The deviation is higher between the experimental and the calculated E_{04} for the series using an $SC=0.2\%$. This deviation from the EMT for lower SC of 0.2% can be caused by a higher E_{04} for the a-SiO$_x$:H phase, as assumed for the EMT calculation, or by an overestimation of the crystalline volume fraction when measuring the Raman intensity ratio. The overestimation of the crystalline volume fraction when using the Raman intensity ratio can be the result of a different Raman cross-sections for the given excitation wavelength for the oxygen-rich amorphous phase and the microcrystalline silicon phase as described in section 2.1.4. Therefore, the measured Raman intensity ratio may not be simply proportional to the crystalline volume fraction.

Influence of the gas flow parameters on the growth

Properties such as the refractive index, transparency, and conductivity of doped μc-SiO$_x$:H material depend strongly on the oxygen content and the crystalline volume fraction. The oxygen content depends on the CO_2/SiH_4 ratio r_{CO2} and the crystalline volume fraction on the silane concentration SC. The influence of other deposition parameters, such as pressure and plasma power density, on the growth are shown in [141] and [142], respectively. In the following, the influence of the gas flow parameters on the growth of μc-SiO$_x$:H is discussed.

To reach an oxygen content [O] of 0.5, an r_{CO2} of 2 to 3 is required. This means that, for the used deposition conditions, a 2 to 3 times higher CO_2 flow with respect to the silane flow is necessary to incorporate the same amount of oxygen and silicon ([O]=0.5) into the film. This can be partly explained by a higher dissociation energy for CO-O (532 kJ/mol), compared to SiH$_3$-H (335 kJ/mol) [143]. The CO molecules do not contribute to the growth because they are is highly stable, due to their dissociation energy of 1075 kJ/mol for C-O [143]. This is also the reason for the relatively low carbon content (<2%) in the films, which is below the detection limit of RBS

for n-type as for p-type μc-SiO_x:H films. For p-type μc-SiO_x:H films the carbon content is low in spite of the CH_3 as a potential carbon source from the TMB. The crystalline volume fraction is reduced when CO_2 is added to the process gas to increase the oxygen content.

The crystalline volume fraction I_c can be increased by using low silane concentrations. At low SC and with a CO_2 admixture, μc-SiO_x:H films containing both a μc-Si:H phase and an oxygen rich a-SiO_x:H phase can be prepared. By doing this, the a-Si:H fraction, which has a low E_{04} and relatively low conductivity, can be reduced. This can be explained by preferential etching, due to the hydrogen plasma with higher etching rates for a-Si:H and lower etching rates for μc-Si:H and a-SiO_2 [144-148]. When using very low silane concentrations of 0.1%, the conductivity is reduced, despite a high crystalline volume fraction that might be attributed to a defect-rich μc-Si:H phase in this case, as a result of a too strong etching contribution during the growth process (Figure 4.6). On the other hand, at higher silane concentrations ($SC \geq 0.5\%$) high conductivities $> 10^{-2} (\Omega cm)^{-1}$ (Figure 4.6), even for low Raman intensity ratios $< 30\%$, are observed, suggesting a high quality and highly conductive current path through the doped a-Si:H phase. For these layers, the E_{04} is reduced because of their narrow band gap amorphous fraction (Figure 4.12).

In most of the prepared series (e.g. SC-series), the CO_2 flow was increased in order to increase the CO_2 / SiH_4 ratio r_{CO2}; for these, the amount of $SiH_4 + CO_2$ was increased within a series. To separate the effect of the CO_2 admixture and the increased amount of $SiH_4 + CO_2$ gas on the material properties, the (S+O)C-series in which the $SiH_4 + CO_2$ gas flow remained constant and the r_{CO2} was varied, was prepared. For this (S+O)C-series, using an *(S+O)C* of 0.25%, a decrease in the Raman intensity ratio and in conductivity with increasing r_{CO2} was shown (Figure 4.19). This decrease is similar to that for the SC-series (Figure 4.18). This means that the CO_2 admixture hinders the crystalline growth in the (S+O)C-series in a similar way as in the SC-series. In the present study this was demonstrated for p-type μc-SiO_x:H but for n-type similar results were achieved but not shown.

4.5   Conclusion

In the present study, p-type and n-type μc-SiO$_x$:H films were developed and investigated with respect to the desired properties for application to thin-film solar cells. The desired properties are an adaptable refractive index at a sufficient conductivity and a high transparency.

The present study elaborates that the p-type and n-type μc-SiO$_x$:H films reach the desired properties due to the phase separation between the doped μc-Si:H phase and the a-SiO$_x$:H phase. The optoelectronic functionality of the phases can be derived from the presented results as follows: (i) a high crystalline volume fraction increases the conductivity and (ii) an a-SiO$_x$:H fraction with a high oxygen content increases the band gap and decreases the refractive index. A high oxygen content in the a-SiO$_x$:H phase and a sufficient crystalline volume fraction requires a low a-Si:H volume fraction.

The determining gas flow parameters to influence the composition and the structure of the p-type and n-type μc-SiO$_x$:H are the CO_2 to SiH_4 ratio for the oxygen content and the silane concentration in hydrogen to reach a sufficient microcrystalline growth. For p-type doping the TMB flow hinders the microcrystalline growth and for n-type doping the PH_3 flow seems to support the microcrystalline growth. Further guidelines to prepare μc-SiO$_x$:H and an overview of both p- and n-type μc-SiO$_x$:H.will be presented in chapter 5.

During the time span of the present study, the low refractive index of doped μc-SiO$_x$:H, which is especially important for application as an reflector in thin-film silicon solar cells, has initiated material research with a focus on the optoelectronic properties [98,99,139,141,142,149-152].

From the results of the present study one can expect further improvement of the optoelectronic properties such as a higher transparency and a lower refractive index at a sufficient conductivity for n-type μc-SiO$_x$:H using a higher PH_3 flow, or for p-type μc-SiO$_x$:H for a finer tuned TMB flow. Using other dopant gases for p-type μc-SiO$_x$:H, for example diborane (B_2H_6) or boron trifluoride BF_3 might also reduce the deteriorating effect of the TMB $B(CH_3)_3$ in He on the microcrystalline growth. Additionally, using a very high plasma excitation frequency VHF might also help to support the microcrystalline growth in doped μc-SiO$_x$:H.

Chapter 5

A summary of p-type and n-type microcrystalline silicon oxide

The dependencies between the gas flow parameters, the material composition, and the optical properties for both p- and n-type μc-SiO$_x$:H are summarized. μc-SiO$_x$:H can be proposed as composed of three phases: a-Si:H, highly crystalline μc-Si:H and a-SiO$_2$. The fractions of the three phases can be illustrated in a ternary diagram. In the ternary diagram, phase compositions with preferable material properties were identified. For the optical and electrical properties, which are relevant for the proposed applications in thin-film silicon solar cells, a survey graph is shown. Guiding principles for the development of doped μc-SiO$_x$:H for application in thin-film silicon solar cells are presented.

The requirements on the doped μc-SiO$_x$:H material properties for application as the intermediate/back reflector or as the window layer in thin-film silicon solar cells are manifold. To fulfil these requirements, the versatility of the doped μc-SiO$_x$:H is used. The properties of the doped μc-SiO$_x$:H can be widely adjusted by changing its composition. This leads to a rather complex material system that is influenced by the crystalline volume fraction and the oxygen content of doped μc-SiO$_x$:H, compared to amorphous alloys e.g. (a-SiO$_x$:H) or microcrystalline silicon (μc-Si:H), where either the alloy content or the crystalline fraction has an influence.

Therefore, this chapter provides an overview and presents some figures to evaluate the dependencies between the composition of the doped μc-SiO$_x$:H and the relevant properties for its use as doped layer in thin-film silicon solar cells. It also helps to evaluate to which extent a likely favourable composition of only highly crystalline μc-Si:H (high conductivity) and a-SiO$_2$ (high transparency) is present. From this, one can find useful options for the further development of doped μc-SiO$_x$:H. Additionally, some guiding principles for the development of doped μc-SiO$_x$:H for application in thin-film silicon solar cells are presented.

5.1   Results

A wide band gap and a reduced refractive index (compared to silicon) are desired properties for doped layers in thin-film silicon solar cells. More precisely, a refractive index value between Si and TCO as window layer and a low refractive index for the application as reflector is the desired range. Details of the properties for the individual series of doped μc-SiO$_x$:H are described in chapter 4. In the following a general relationship between the oxygen content and the optical properties of both the n-type and p-type μc-SiO$_x$:H material will be presented. Figure 5.1 shows the band gap E_{04} and the refractive index n versus the oxygen content [O], measured by RBS, for n-type (circles) and p-type (squares) μc-SiO$_x$:H films prepared in the present study. The measured optical properties (E_{04}, n) are strongly determined by the oxygen content for both n-type and p-type μc-SiO$_x$:H. The band gap E_{04} (full symbols) increases and the refractive index n (open symbols) decreases with increasing oxygen content, albeit with some scatter. The measured E_{04} and n can be reasonably fitted as a function of the oxygen content, despite variations in other material properties, e.g. the crystalline volume fraction. These functions are shown for the refractive index to $n = 3.5 - 3.3 \times [O]$ as dashed line and for the band gap to $E_{04} = 1.97 + 0.62 \times [O]/(1-[O])$ as solid curve. From these functions, one can roughly estimate the optical properties (E_{04}, n), which can be expected for given oxygen content in the films within the present study.
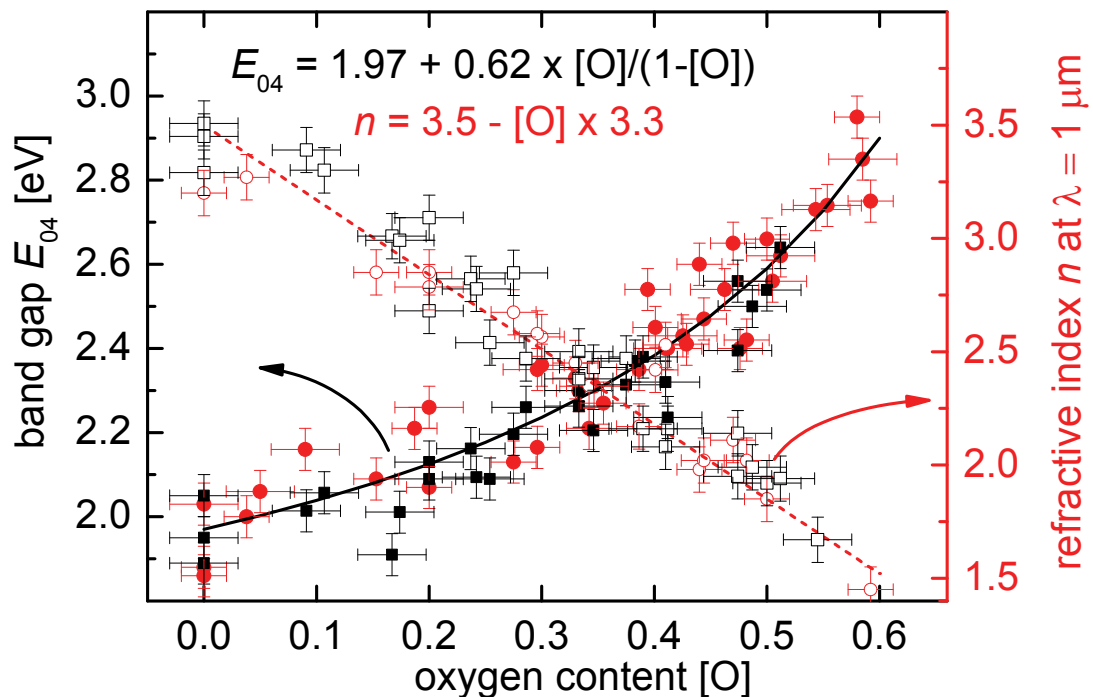
Figure 5.1: The band gap E_{04} (full symbols) and the refractive index (open symbols) versus the oxygen content [O] for all p-type (squares) and n-type (circles) μc-SiO$_x$:H films regardless of their crystalline volume fraction, measured by RBS. The lines are fitted as function of the oxygen content to the refractive index (dashed line) and to the E_{04} band gap (solid curve).

Figure 5.2 shows the oxygen contents determined by RBS for all films versus the CO_2-concentration and versus the equivalent CO_2/SiH_4 ratio r_{CO2} used for the film preparation. The CO_2-concentration is calculated from the r_{CO2} by using the equation (see also Appendix D):

$$CO_2 \text{ - conc.} [\%] = \frac{CO_2}{SiH_4 + CO_2} \times 100 = \frac{r_{CO_2}}{1 + r_{CO_2}} \times 100 \qquad (5.1).$$

For n-type (circles) and p-type (squares) $\mu c\text{-}SiO_x\text{:}H$ films the oxygen content is proportional to the CO_2 concentration. The data is fitted by linear regression (solid line):

$$O - content = \frac{CO_2 \text{ - conc.} [\%]}{100} \times 0.624 \qquad (5.2).$$

As already noted, it is seen that this relationship is a reasonable fit, despite some scatter, for all samples, independent of other material properties such as the crystalline volume fraction. The 0.624 is the fitting parameter. The physical meaning of the value of this parameter was considered to be outside the scope of the present study. For n-type $\mu c\text{-}SiO_x\text{:}H$, a slight offset in the O-content is visible for a CO_2-concentration $>30\%$ compared to p-type material. From Figure 5.1, one can approximately calculate the dependency between the oxygen content, measured using RBS, and the optical properties (E_{04}, n). From Figure 5.2, one can derive the dependence of the oxygen content on the gas flow parameter CO_2-concentration. Therefore, using these dependencies, one can estimate the band gap E_{04} and the refractive index n from the r_{CO2} or the respective CO_2 concentration, without measuring the oxygen content for both n-type and p-type $\mu c\text{-}SiO_x\text{:}H$ layers in the present study.
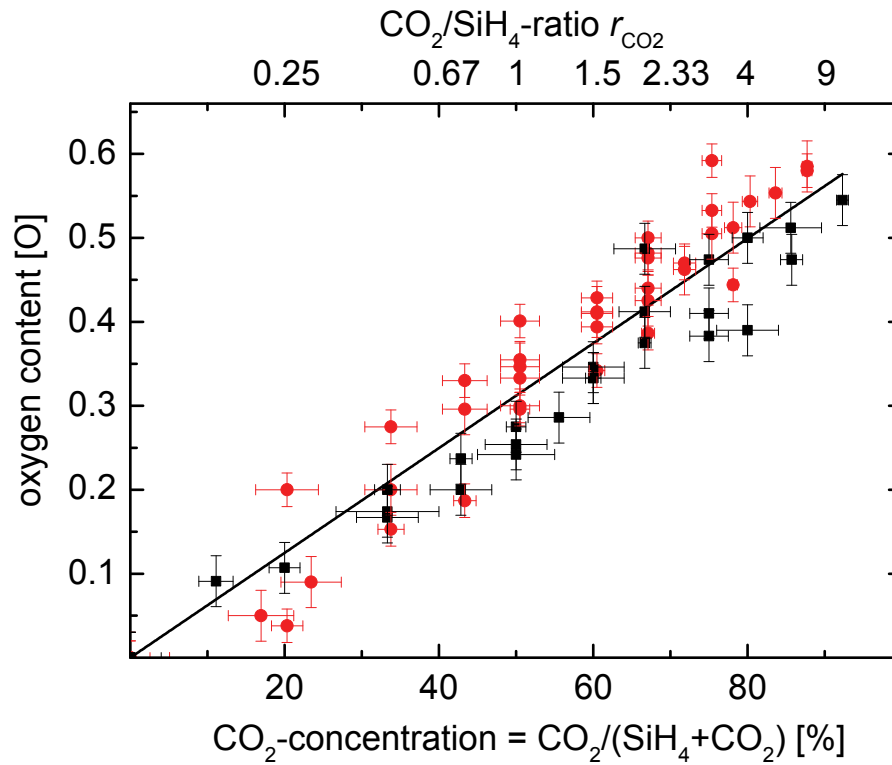
Figure 5.2: The oxygen content [O] versus the CO_2/SiH_4 ratio r_{CO2} and the corresponding CO_2-concentration for n-type (circles) and p-type (squares) µc-SiO$_x$:H films. The linear regression (solid line) is fitted to the data of the oxygen content [O] versus the CO_2 concentration for both types of samples. The CO_2 concentration is defined as $CO_2/(CO_2+SiH_4)$.

The ternary diagram in Figure 5.3 allows visualizing the composition of µc-SiO$_x$:H. µc-SiO$_x$:H can be thought of as a composite of three phases: the highly crystalline µc-Si:H, the a-Si:H and the a-SiO$_2$, whose sum of volume fractions has to be equal to one. Please note: Voids are not taken into account since they most likely do not require a volume of more than 3% [80].
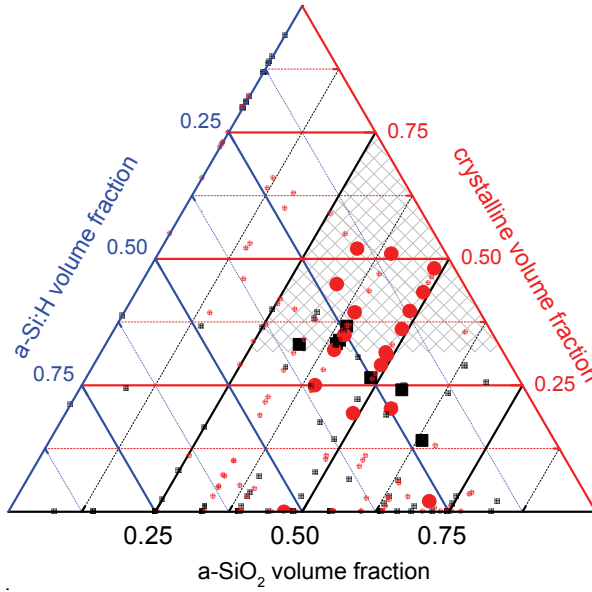
Figure 5.3: For n-type (circles) and p-type μc-SiO$_x$:H (squares) films, the volume fractions of the amorphous silicon dioxide (a-SiO$_2$), amorphous silicon (a-Si:H), and crystalline silicon (highly crystalline μc-Si:H) phases are shown in a ternary diagram. The bold symbols represent the volume fractions of films with an E$_{04}$ above 2.3 eV and a conductivity $\geq 10^{-5}$ (Ωcm)$^{-1}$. The faint, smaller symbols represent the volume fractions of films that have E$_{04}$ below 2.3 eV or a conductivity $< 10^{-5}$ (Ωcm)$^{-1}$. The black squares represent the p-type and red circles represent the n-type μc-SiO$_x$:H films. The composition of the films is calculated on the basis of the dependency shown in Figure 5.2 and the Raman intensity ratio. The shaded triangle indicates the composition of the films that is likely to result in favourable material properties.

To determine the volume fractions of the phases the following assumptions were used:

For the **crystalline volume fraction** (right red axis), the Raman intensity ratio I_c was used. The **a-SiO$_2$ volume fraction** (lower black axis) was calculated from the a-SiO$_2$ fraction, assuming a density of 2.27×10^{22} [SiO$_2$]/cm³ for pure a-SiO$_2$ and a density of 5×10^{22} [Si]/cm³ for pure silicon (see Appendix E). To calculate the a-SiO$_2$ fraction from the oxygen content, we used equation (3.2) and (3.4) (see also Appendix A). Because the oxygen content was not measured for all samples shown in this graph, we used the dependency presented in Figure 5.2 to calculate the oxygen content. The **a-Si:H volume fraction** (left blue axis) was calculated as **a-Si:H volume fraction** = 1- crystalline volume fraction -   a-SiO$_2$ volume fraction. Please note: Voids are not taken into account since they most likely do not require a volume of more than 3% [80].

The results presented in Figure 5.3 for p-type material (squares) and for n-type (circles) are shown as small faint symbols. The bold symbols represent the results for the p-type (bold squares) and n-type (bold circles) layers with E_{04} above 2.3 eV and a conductivity σ of more than 10^{-5} (Ωcm)$^{-1}$. $E_{04} > 2.3$ eV and $\sigma \geq 10^{-5}$ (Ωcm)$^{-1}$ were selected as particularly appropriate for use thin-film silicon solar cells.

The shaded triangle indicates the phase compositions that are likely to result in favourable material properties for application in thin-film silicon solar cells. For this triangle, the crystalline volume fraction is > 0.33, which is above the percolation threshold, as stated in literature

[128,129], ensuring a sufficient conductivity, but low enough to enable an a-SiO$_2$ volume fraction >0.2 to achieve a high transparency. Additionally, this µc-SiO$_x$:H composite has a substantial (>20%) crystalline volume fraction that can act as a nucleation layer for a subsequent µc-Si:H layer. Additionally one can expect an improved the nucleation on a silicon oxide surface as compared to non-alloyed a-Si:H [25,26]. Most of the samples with appropriate properties are within the shaded triangle.

From the ternary diagram in Figure 5.3, one can approximately roughly determine the composition of µc-SiO$_x$:H required to achieve material that is highly transparent and has sufficient conductivity.
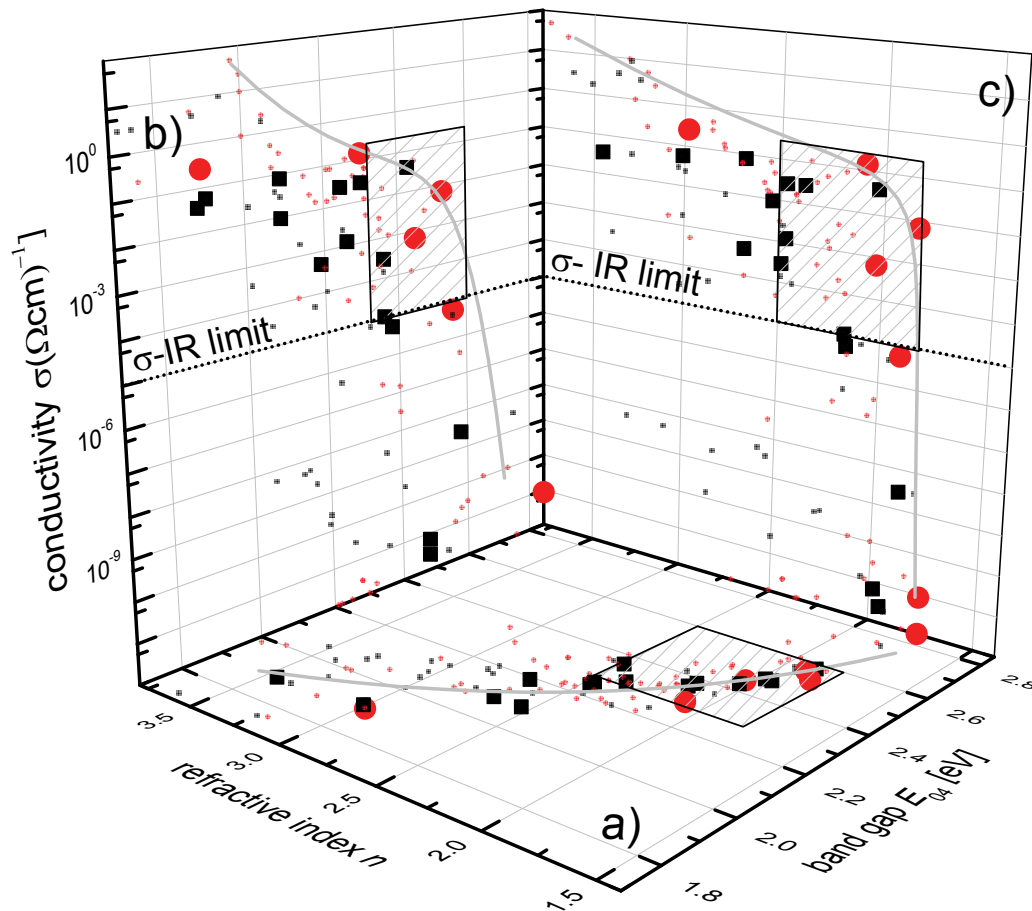
Figure 5.4: a) The refractive index n versus the band gap E$_{04}$. The electrical conductivity σ versus b) the band gap E$_{04}$ and c) the refractive index n. As an example, results for the (S+O)C = 0.25% p-type series (bold black squares) and for n-type PH$_3$ = 0.04 sccm n-type series (bold red circles)are shown. The curve in a) is a guide to the eye, in b) and c) the curves indicate the highest values for the respective property. The results from other series for p-type (black squares) and for n-type (red circles) materials are shown as small faint symbols. The film properties which, favourable for use in thin-film silicon solar cells, such as a band gap > 2.3 eV, a conductivity above σ-IR limit and a refractive indices between 1.8 and 2.5, are indicated by the shaded windows.

For the application of doped µc-SiO$_x$:H in thin-film silicon solar cells, material properties such as the refractive index *n*, optical band gap E$_{04}$ and conductivity σ are important properties. To find a favourable combination of these properties, one can use a survey graph, as shown in

Figure 5.4. Figure 5.4 shows a) the refractive index versus the E_{04} band gap and the conductivity σ versus b) the band gap E_{04} and c) the refractive index n. As an example, the results for the *(S+O)C=0.25%* p-type series (bold black squares) and for n-type $PH_3=0.04$ sccm n-type series (bold red circles) are shown. The results from other series for p-type (black squares) and for n-type (red circles) materials are shown as small faint symbols. The film properties that are favourable for use in thin-film silicon solar cells, such as a band gap >2.3 eV, a conductivity above $10^{-5} (\Omega cm)^{-1}$ and possible refractive indices between 1.8 and 2.5, are indicated by the shaded windows in parts a), b), and c). This figure summarizes the relevant material properties for application as the doped layer in thin-film silicon solar cells.

For the development of doped μc-SiO_x:H for application in thin-film silicon solar cells, one can draw some guiding principles from the experience with the material development in the present study as follows:

1.   Use the recipe of your n-type μc-Si:H, but replace half of the silane by CO_2 (CO_2/SiH_4 ratio = 1 is a good starting point)

2.   Use a higher plasma power density than for your n-type μc-Si:H layer (depends strongly on the system and the recipe)

3.   If no film is deposited, or if the deposition rate is low (very inhomogeneous thickness): $\Rightarrow$ More SiH_4 or less H_2

4.   What can you do, if the layer properties are not in the desired range?

      σ: $>1 \times 10^{-5} (\Omega cm)^{-1}$
      E_{04}: >2.3 eV
      I_c: $>33\%$

      Amorphous, low transparency and low conductivity:
      $\Rightarrow$ More H_2 / less SiH_4 and less CO_2
      Crystalline, high transparency and low conductivity:
      $\Rightarrow$ Less H_2 / more SiH_4, more phosphine (n-type), less TMB (p-type) (if possible)
      Amorphous, low transparency and sufficient conductivity:
      $\Rightarrow$ More CO_2 and more H_2, or less SiH_4
      Crystalline, low transparency und sufficient conductivity:
      $\Rightarrow$ More CO_2
      Amorphous, high transparency and low conductivity:
      $\Rightarrow$ Less CO_2 and less SiH_4, or more H_2, or more PH_3 (n-type), and less TMB (p-type) (if possible)

Crystalline, low transparency und low conductivity:

$\Rightarrow$ More CO_2 and more PH_3 (n-type), less TMB (p-type)

Amorphous, high transparency and sufficient conductivity:

$\Rightarrow$ More H_2

Chapter 6

Thin-film silicon solar cells with doped μc-SiO$_x$:H layers

In this chapter, the application of the doped microcrystalline silicon oxide (μc-SiO$_x$:H) layers in various types of thin-film silicon solar cells (a-Si:H single junction, μc-Si:H single junction and a-Si:H/μc-Si:H tandem junction) will be demonstrated. The n-type μc-SiO$_x$:H was used as the n-layer for a-Si:H solar cells. For μc-Si:H single junction solar cells, the application as the p-type window layer and as the n-layer is presented. The application of doped μc-SiO$_x$:H layers in a-Si:H/μc-Si:H tandem solar cells as the n/p contact between both cells i.e. as an intermediate reflector and as the n-layer of the μc-Si:H bottom cell is demonstrated.

6.1   Introduction

In the present study, p-type and n-type microcrystalline silicon oxide (μc-SiO$_x$:H) layers with advantageous material properties for application to thin-film silicon solar cells were developed (chapter 4 and chapter 5). A higher transparency, compared to films that are not alloyed, and an adaptable refractive index combined with sufficient conductivity enables the application of the doped μc-SiO$_x$:H layers in thin-film silicon solar cells. Prepared with a low refractive index, doped μc-SiO$_x$:H layers are promising for use as intermediate reflectors in a-Si:H/μc-Si:H tandem solar cells.

Chapter 6 shows the application of the doped μc-SiO$_x$:H layers in various types of thin-film silicon solar cells. In single junction solar cells, the solar cell parameters and external quantum efficiency *EQE* can be directly related to the influence of the doped μc-SiO$_x$:H layers. However, in the tandem solar cells, there are additional influences due to more complex effects (e.g. current matching). Therefore, the applications of doped μc-SiO$_x$:H layers in single junctions solar cells are shown in section 6.2.

Section 6.2.1 describes the application of doped μc-SiO$_x$:H in a-Si:H single junction solar cells deposited on SnO$_2$ substrates (Asahi (VU)). p-Type μc-SiO$_x$:H layers were not used as the window layer because they cannot be directly applied on SnO$_2$:F substrates; exposing SnO$_2$:F substrates to a highly hydrogen-diluted plasma, as used for the deposition of μc-SiO$_x$:H, would result in an oxygen-depleted surface of the SnO$_2$:F. This reduced surface layer contains a thin layer of Sn and SnO which reduces the transmission [153]. Nevertheless, the application of μc-SiO$_x$:H as the n-layer in a-Si:H single junction solar cells is demonstrated.

Section 6.2.2 describes the impact of μc-SiO$_x$:H p- and n-layers on the external quantum efficiency *EQE* and the solar cell parameters in μc-Si:H p-i-n solar cells deposited on ZnO:Al. In contrast to the SnO$_2$ the ZnO:Al TCO can be used in combination with highly hydrogen-diluted plasma, as used for the deposition of μc-SiO$_x$:H [154,155].

Finally, section 6.3 describes the results for the application of p-type and n-type μc-SiO$_x$:H layers as intermediate reflector and n-layer of the bottom in a-Si:H/μc-Si:H tandem solar cells cell. The tandem devices were prepared on various substrates, as indicated in the individual sections.

6.2   Single junction solar cells

6.2.1   a-Si:H single junction solar cells

Figure 6.1 shows a schematic sketch of an a-Si:H single junction solar cell. a-Si:H single junction solar cells with an a-Si:H or μc-Si:H n-layers as indicated in the text were used as the reference. For the a-Si:H single junction solar cells with a μc-SiO$_x$:H n-layer, a 5 nm thick n-type μc-Si:H layer was deposited prior to act as nucleation layer for the μc-SiO$_x$:H layer. The thickness of the complete n-layer is 25 nm for all cells. For the μc-SiO$_x$:H n-layer deposition, the following gas flows were applied (in absolute values): 1 sccm SiH$_4$ flow, 0.02 sccm PH$_3$ flow, 0.75 sccm CO$_2$ flow and 200 sccm H$_2$ flow. When depositing such a μc-SiO$_x$:H n-layer as thick layer on glass it has a crystalline volume fraction I_c of $\approx 20\%$, a conductivity of $\approx 10^{-2}$ (Ωcm)$^{-1}$, an $E_{04} \approx 2.25$ eV and a refractive index of ≈ 2.5, as shown in chapter 4. The solar cells were prepared on 10×10 cm² SnO$_2$:F substrates (Asahi (VU)), each contains several 1×1 cm² laser-scribed solar cells. Further preparation details are described in section 2.2.
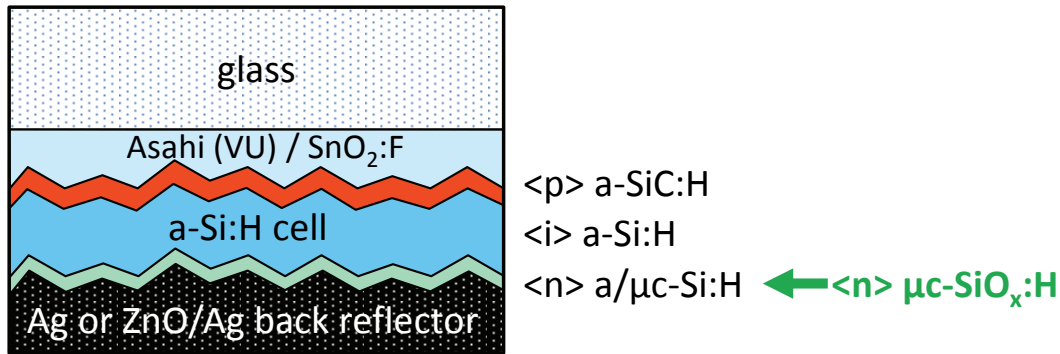
Figure 6.1: A schematic sketch of the a-Si:H single junction solar cell. The solar cells have an a-SiC:H p-layer and an a-Si:H i-layer. Different types of n-layers and the back reflectors were used as stated in the text. a-Si:H, μc-Si:H or μc-SiO$_x$:H layers were used as n-layer an. As back reflector, a ZnO/Ag or an Ag back reflector was used.

μc-SiO$_x$:H n-type material has, compared to a-Si:H or μc-Si:H n-layers, advantageous properties for use as the n-layer in a-Si:H single junction solar cells. The improved transparency can reduce the parasitic absorption in the n-layer. Additionally, the reduced refractive index can improve the reflection or reduce the parasitic absorption at the back reflector [150,156-158]. To distinguish between the influence of the improved transparency and the reduced refractive index, different n-layers (a-Si:H and μc-SiO$_x$:H) and back reflectors (ZnO and ZnO/Ag) were applied to a-Si:H single junction solar cells and their external quantum efficiencies were compared. In addition, the solar cell parameters of a-Si:H solar cells using a μc-SiO$_x$:H n-layer were compared with those of solar cells with a μc-Si:H n-layer in the initial state and after 1000 h light soaking. For this comparison, a-Si:H i-layers with different thickness were studied, in order to separate the influence of an increase in J_{sc} and i-layer thickness.

The *EQE* for a-Si:H single junction solar cells with μc-SiO$_x$:H as the n-layer

Figure 6.2 shows external quantum efficiencies *EQE*s versus the wavelength for a-Si:H single junction solar cells with μc-SiO$_x$:H (solid lines) and a-Si:H n-layers (dashed lines). Ag back reflectors (blue lines) and ZnO/Ag back reflectors (red lines) were applied on both types of n-layers. The ZnO layer is aluminium (Al) doped and sputtered from a ceramic target with 1 at.% Al with a thickness of 70 nm. Please note: The ZnO layer has, apart from its optical function, additional functions as e.g. adhesion layer, diffusion barrier, etc.. The subsequently sputtered Ag layer has a thickness of 200 nm. The a-Si:H i-layer thickness is 340 nm for these solar cells.
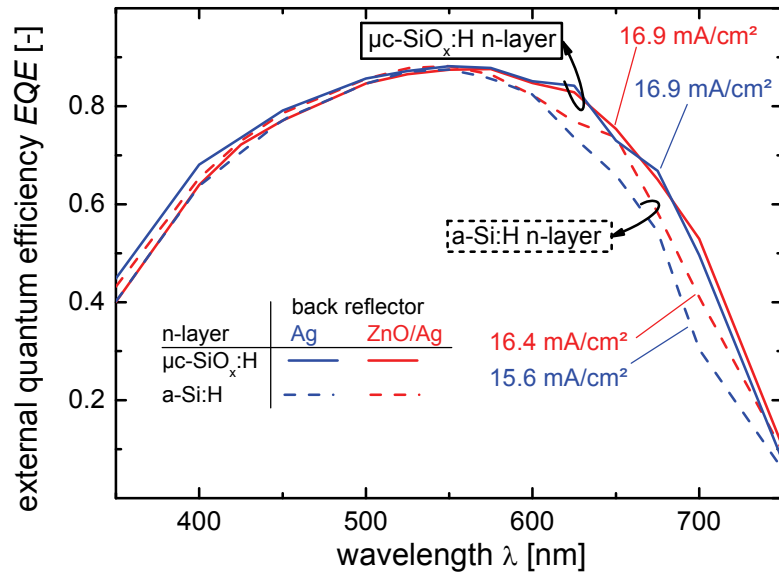
Figure 6.2: The external quantum efficiency EQE versus the wavelength of the a-Si:H p-i-n solar cells with μc-SiOx:H n-layer (solid) and a-Si:H n-layers (dashed) as indicated. All n-layers have a thickness of 25 nm. The applied back reflectors are Ag (blue) and ZnO/Ag (red). The corresponding current densities J_{QE} calculated from the EQE are shown in the graph. All cells have a size of 1 ×1 cm² and the EQEs were measured at 0 V bias voltage.

As a reference, *EQE*s for solar cells having an a-Si:H n-layer with an Ag back reflector (blue dashed) and a ZnO/Ag back reflector (red dashed) are used, resulting in a J_{QE} of 15.6 mA/cm² and 16.4 mA/cm², respectively. When implementing an n-type μc-SiOx:H layer, a J_{QE} of 16.9 mA/cm² for both solar cells with an Ag-back reflector and a ZnO/Ag-back reflector was achieved. For all solar cells, the gain in J_{QE} is due to an increase in *EQE* in the wavelengths range between 550 nm and 750 nm. This can be a consequence of reduced parasitic absorption in the n-layer, which, in turn, could be related to: (i) its improved transparency, or (ii) by reduced parasitic absorption or improved reflection at the Ag-back reflector. (ii) would be related to the reduced refractive index of the n-type μc-SiOx:H layer which similar as the refractive index of the ZnO interlayer ($n \approx 2$) but lower as compared to n-type a-Si:H layer [150,156-159]. In the following, the *EQE*s of the individual cells are compared and the origin of the difference is discussed.

I.   When comparing the *EQE*s of the cells having a ZnO/Ag-back reflector (red) with an a-Si:H n-layer (red/dashed) and a μc-SiOx:H n-layer (red/solid), the gain in J_{QE} is 0.5 mA/cm² (16.4 mA/cm² to 16.9 mA/cm²). Here, only the n-layer was substituted; therefore, the gain can soley be attributed to a reduced parasitic absorption of the μc-SiOx:H n-layer since the ZnO acts as a low refractive index inter layer which.

II.   When comparing the *EQE*s of solar cells having an a-Si:H n-layers (dashed) with an Ag-back reflector (dashed/blue) and a ZnO/Ag-back reflector (dashed/red), the gain in J_{QE} is 0.8 mA/cm² (15.6 mA/cm² to 16.4 mA/cm²). This can be related to a reduced parasitic absorption at the back reflector, due to the use of a ZnO interlayer between the n-layer and

the Ag-back reflector. This is most probably caused by the lower refractive index of the ZnO, compared to the a-Si:H n-layer [156-158].

III.   When comparing the *EQE*s of the solar cells having an Ag-back reflector (blue) with an a-Si:H n-layer (blue/dashed) and a μc-SiO$_x$:H n-layer (blue/solid), the gain in J_{QE} is even high: 1.3 mA/cm² (15.6 mA/cm² to 16.9 mA/cm²). This indicates that in this case, the gain is due to a reduced parasitic absorption in both the n-layer and at the back reflector. This is most probably caused by the lower refractive index and the higher transparency of the n-type μc-SiO$_x$:H [150,156-159].

Based on the above discussion, one can conclude that the μc-SiO$_x$:H n-layer has a lower parasitic absorption than the a-Si:H n-layer. When using the combination of a μc-SiO$_x$:H n-layer and an Ag-back reflector, the μc-SiO$_x$:H n-layer also reduces the parasitic absorption at the back reflector in a similar way as the ZnO interlayer. It is remarkable that the μc-SiO$_x$:H n-layer has an effect on the *EQE* similar to that of ZnO at the Ag back reflector which is most likely related to the similar low refractive index values of the ZnO and the μc-SiO$_x$:H.

Apart from the influence on the *EQE* the fill factor *FF* for the solar cell with μc-SiO$_x$:H n-layer and Ag back contact is below 30% and has a "s-shape". For the other described solar cells the *FF* is above 70%. The low *FF* of solar cells as a result of a combination of μc-SiO$_x$:H n-layer and Ag back reflector was observed occasionally but not investigated in detail. The V_{oc} is between of 892 mV and 908mV for all cells. More details on the influence of the μc-SiO$_x$:H n-layer on the *FF* and V_{oc} will be addressed in the next section for cells with an ZnO/Ag-back reflector.

<u>Solar cell parameters in the initial state and after light soaking for a-Si:H single junction solar cells with μc-SiO$_x$:H n-layers compared to μc-Si:H n-layers</u>

a-Si:H single junction solar cells with μc-SiO$_x$:H n-layers and with μc-Si:H n-layers were investigated in the initial state and after 1000 h light soaking. For both type of n-layers, solar cells with different a-Si:H i-layer thickness were prepared, to compare solar cells with both type of n-layers but the same short circuit current density J_{sc}. The i-layer thickness was varied by adjusting the deposition time and verified with a step profiler (see section 2.1.1). Further preparation details are described in chapter 4. For these solar cells, ZnO/Ag back reflectors were used. Figure 6.3 a) - d) shows the initial solar cell parameters and Figure 6.3 e) - h) the solar cell parameters after 1000 h light soaking versus the i-layer thickness.
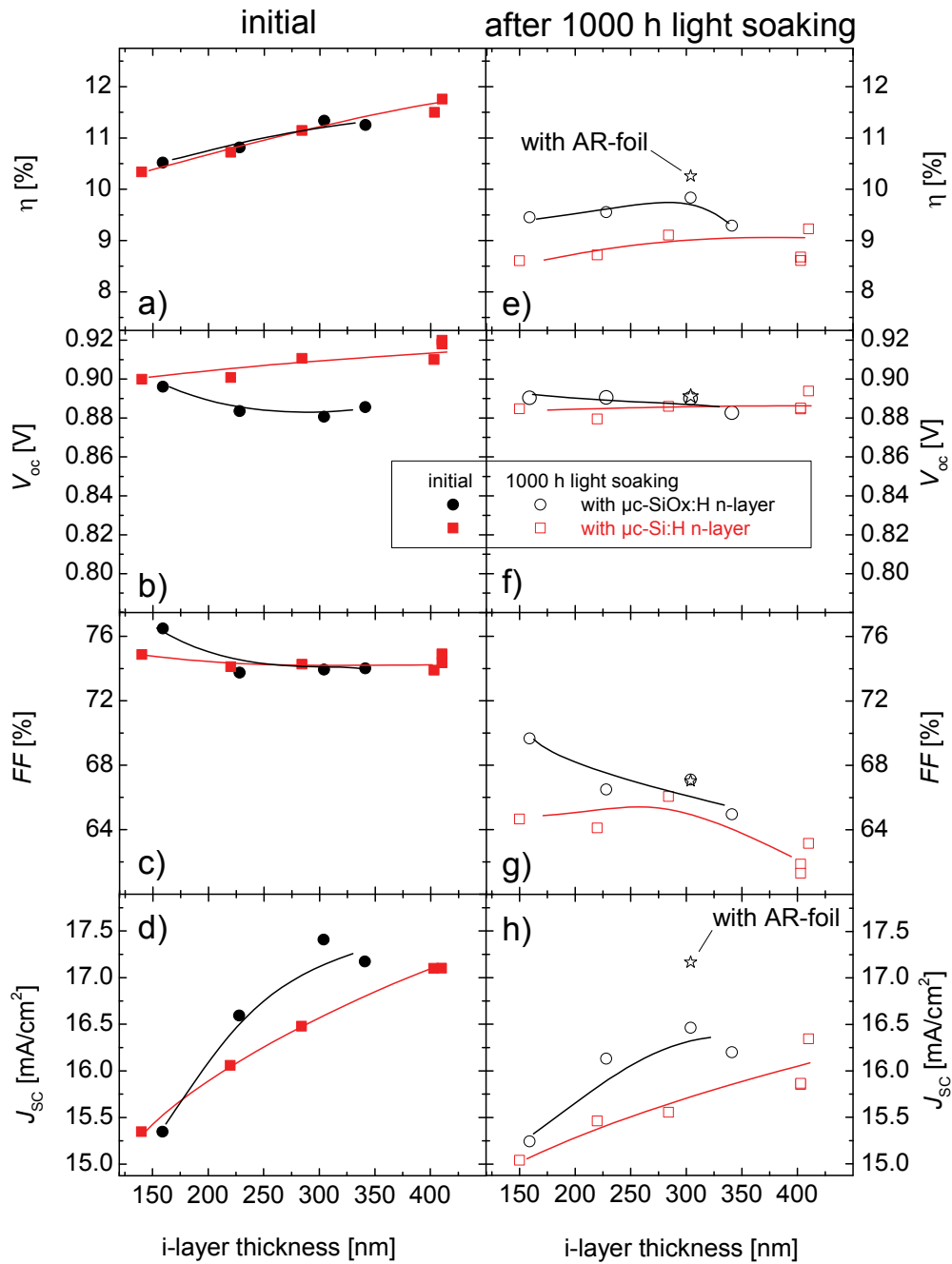
Figure 6.3: The solar cell parameters in the initial state: a) efficiency η, b) open circuit voltage V_{oc}, c) fill factor FF and d) short circuit current density J_{sc} versus the a-Si:H i-layer thickness. The solar cell parameters after 1000 h light soaking: e) efficiency η, f) open circuit voltage V_{oc}, g) fill factor FF and h) short circuit current density J_{sc} versus the a-Si:H i-layer thickness. The circles show the solar cell parameters for the solar cells using a µc-SiO$_x$:H n-layer and the squares for the solar cells with a µc-Si:H n-layer. The stars represent the parameters for the solar cell with an AR-foil (for details see text). The full symbols show the solar cell parameters in the initial state and the open symbols after 1000 h light soaking.

The efficiency η in the initial state (Figure 6.3 a) increases with i-layer thickness to more than 11% for both types of n-layers. This increase is attributed to the increase in short circuit current density J_{sc} (Figure 6.3 d) to more than 17 mA/cm². At a similar thickness of 300 nm, the solar cells with a µc-SiO$_x$:H n-layer (circles) have a 0.9 mA/cm² higher J_{sc}, but also a 30 mV lower

open circuit voltage V_{oc} (Figure 6.3 b), compared to the solar cells with a μc-Si:H n-layer (squares).

The solar cell parameters after 1000 h light soaking versus the i-layer thickness are shown for both series in Figure 6.3 e) - h) as open symbols. For the solar cells with a μc-Si:H n-layers (open squares) and a μc-SiO$_x$:H n-layer (open circles), the efficiency reaches a maximum of 9.22% and 9.84%, respectively. These efficiencies were reached at a J_{sc} of 16.3 mA/cm² for both types of n-layers, but at different i-layer thickness. Using a μc-SiO$_x$:H n-layer at 304 nm i-layer thickness, and using a μc-Si:H n-layer at 410 nm i-layer thickness. The thinner i-layer results in a higher fill factor FF after light soaking. The V_{oc} is similar for both series after light soaking. From this, one can conclude that, when using a μc-SiO$_x$:H n-layer, thinner i-layers can be used to achieve the same J_{sc}, yielding a reduced degradation. When applying an antireflection foil (AR) on the light-incident side of the glass from the Solarexcel™ company, now a part of DSM Advanced Surfaces [101] to this solar cell, a maximum efficiency of 10.26% (open star) was measured after 1000 h light soaking.

6.2.2   μc-Si:H single junction solar cells

Figure 6.4 shows a schematic sketch of a μc-Si:H solar cell. The p-layer and n-layer were replaced by p-type and n-type μc-SiO$_x$:H layers, respectively, as indicated. This section will show the influence of the doped μc-SiO$_x$:H layers applied to μc-Si:H p-i-n solar cells on the solar cell parameters and the *EQE*.
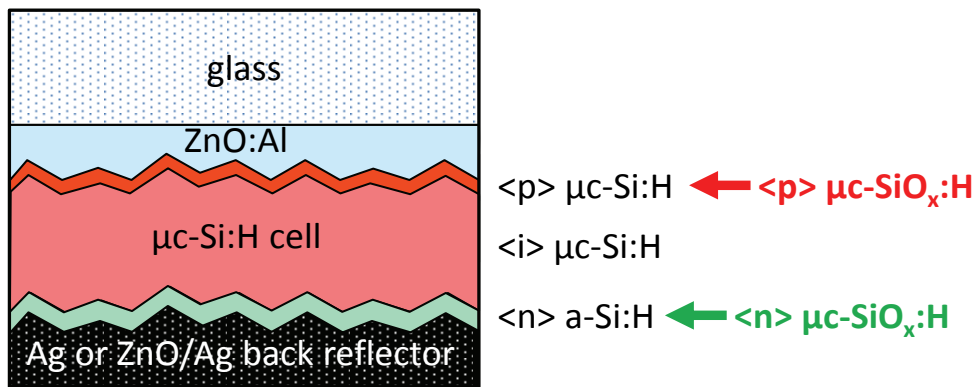
Figure 6.4: A schematic sketch of the μc-Si:H single junction solar cell. The solar cells have a p-type μc-SiO$_x$:H window layer or/and an n-type μc-SiO$_x$:H back contact, as described in the figures and the text.

p-type μc-SiO$_x$:H applied to μc-Si:H p-i-n solar cells

μc-SiO$_x$:H p-layers, as varied in the (S+O)C-series (see Table 4.4) with an *(S+O)C*=0.25%, were applied to μc-Si:H p-i-n solar cells. In the (S+O)C-series, the refractive index can be tuned over a wide range from 3.5 to 2 resulting in an E_{04} between 1.9 eV and 2.43 eV and a conductivity above 10^{-5} $(\Omega cm)^{-1}$, as shown in Figure 4.27. The optical properties were varied by varying the CO$_2$/SiH$_4$ ratio r_{CO2} from 0 to 6 and keeping the sum of SiH$_4$+CO$_2$ flow constant.

Figure 6.5 shows the external quantum efficiency (*EQE*) versus the wavelength and Figure 6.6 shows the photovoltaic parameters of these solar cell series versus the r_{CO2}. The thickness of the p-layer was adjusted to 15 nm by setting the deposition times according to the deposition rates evaluated in the material studies. The solar cells were prepared on HCl etched ZnO:Al, and have a 1 μm thick μc-Si:H i-layer, an a-Si:H n-layer and an Ag layer as an back reflector without ZnO:Al interlayer. Details of the layer preparation and the properties of the silicon layers are described in chapter 4.
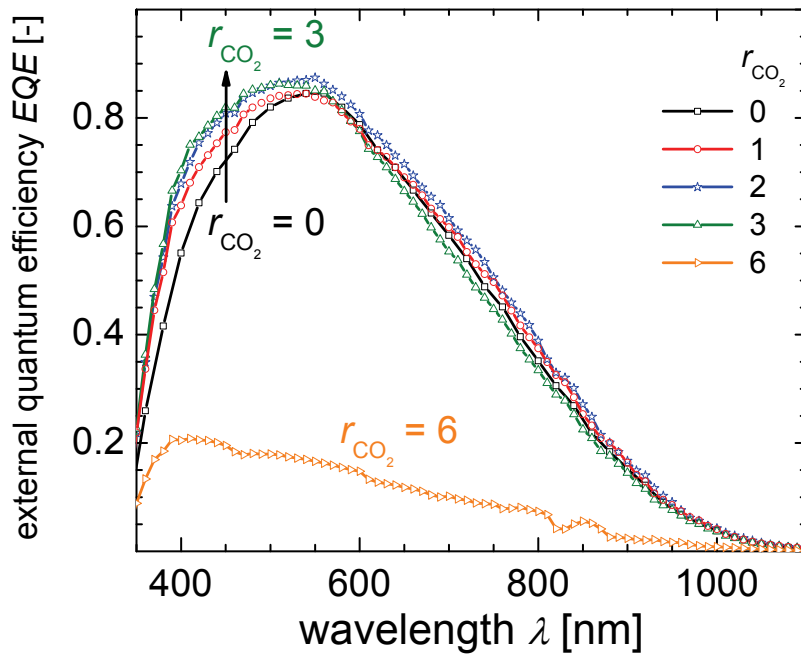
Figure 6.5: The quantum efficiency EQE versus the wavelength of the μc-Si:H p-i-n solar cells with μc-SiO$_x$:H p-layers. The CO$_2$/SiH$_4$-ratios r$_{CO2}$ during the deposition of the p-layer are indicated on the graph and in the legend. The thickness of the p-layer is 15 nm. The back reflector/contact is an Ag layer, the n-layer is n-type a-Si:H, and the i-layer thickness is 1 μm. All cells have a size of 1×1 cm² and the EQEs were measured at 0 V bias voltage.

Figure 6.5 shows an increase in *EQE* in the wavelength range from 350 nm up to 600 nm with increasing r_{CO2} from 0 to 3. At a wavelength of 450 nm, an increase in *EQE* of absolute 0.1 is obtained. For an r_{CO2} of up to 3, the external quantum efficiency in the long wavelength region ($\lambda > 750$ nm) is typical for this kind of μc-Si:H solar cell (1 μm thickness, Ag back reflector), which indicates that the i-layer has a sufficient crystalline volume fraction that enables light absorption for $\lambda > 750$ nm. For $r_{CO2} = 6$, the *EQE* is strongly reduced over the complete spectrum, which can be caused by the low crystalline volume fraction of the μc-Si:H i-layer, due to insufficient nucleation on the p-layer [26] or the reduced carrier collection caused by the high resistance of the p-layer.
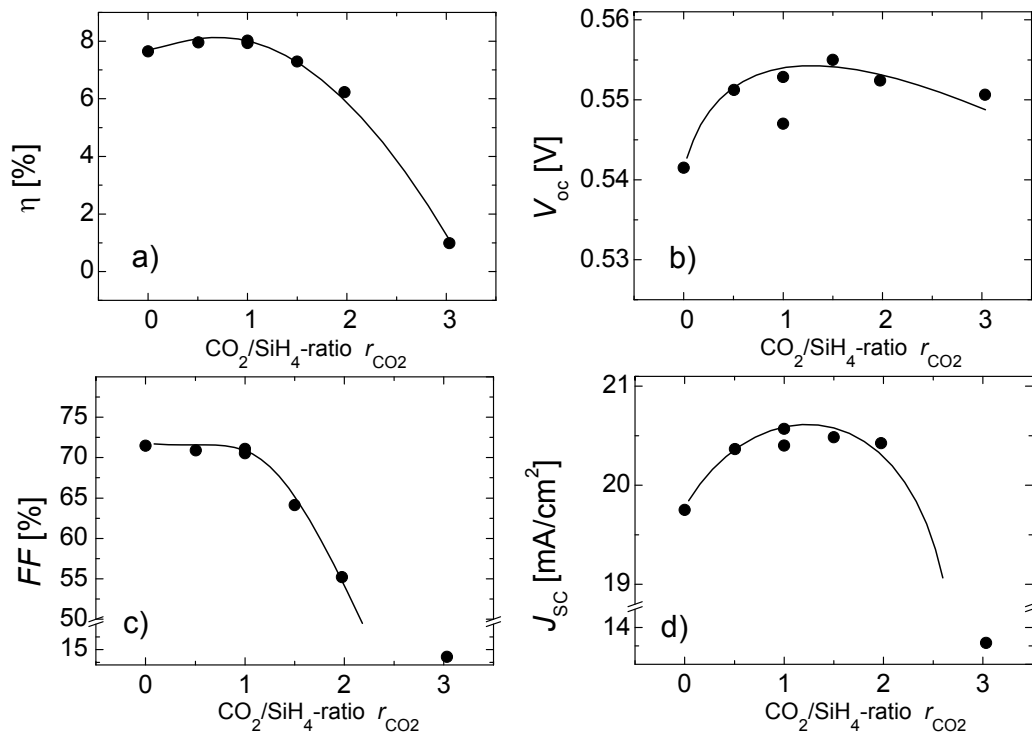
Figure 6.6: The solar cell parameters: a) efficiency η, b) open circuit voltage V_{oc}, c) fill factor FF and d) short circuit current density J_{sc} versus the CO_2/SiH_4 ratio r_{CO2} during the deposition of the p-layer. The thickness of the p-layer is set at 15 nm. The back reflector is an Ag layer and the i-layer thickness is 1μm.

Figure 6.6 shows a) the efficiency η, b) the fill factor *FF*, c) the open circuit voltage V_{oc} and d) the short circuit current density J_{sc} versus the CO_2/SiH_4 ratio r_{CO2} during p-layer preparation. The solar cell parameters are measured on the solar cells whose *EQEs* were presented in Figure 6.5 and structural and electrical properties of the μc-SiO$_x$:H material were shown in Figure 4.19 and Figure 4.27. From an r_{CO2} of 0 to 1, a slight increase in J_{sc} can be observed. The increase in J_{sc}, in combination with a V_{oc} above 0.55 V and a *FF* above 70%, results in an efficiency above 8% at an r_{CO2} of 1. Above an r_{CO2} of 1.5, the *FF* is still 64%, but drops sharply for higher r_{CO2} values. Please note: At an r_{CO2} of 3 the J_{sc} is below 14 mA/cm² which differs from Figure 6.5 This discrepancy is most likely related to the "s-shape" of the *JV* curve which leads to a significant dependency of the *EQE* on the light intensity. However, the $V_{oc} > 0.55$ V, *FF* > 70% and the increase in J_{sc} demonstrate that the μc-SiO$_x$:H, as the p-layer in μc-Si:H p-i-n solar cells, can build up the electric field, has a sufficient conductivity, acts as a nucleation layer for the subsequent μc-Si:H i-layer, and improves the external quantum efficiency.

The increased *EQE* up to a wavelength of 550 nm can be related to a reduced reflection out of the cells and/or a reduced parasitic absorption in the p-layer. A colour change from the glass side of the cells, which is visible to the naked eye (not shown) when applying a μc-SiO$_x$:H p-layer, provides the first indication of a difference in reflection, compared to solar cells with a standard μc-Si:H p-layers. The change in reflection is most likely caused by a reduction in the refractive index of the μc-SiO$_x$:H p-layer (Figure 4.24). However, a major part of the improvement in

EQE, can be related to the increased optical band gap E_{04} (see Figure 4.23) and therefore a reduced parasitic absorption of the μc-SiO$_x$:H p-layer. This is the case since the reflection is lower compare to the parasitic absorption up to a wavelength of 550 nm (see Figure 1.3). Reflectance measurements of these cells were not performed; therefore, the two effects cannot be separated in more detail.

However, the $V_{oc} > 0.55$ V, $FF > 70\%$ and the increase in J_{sc} demonstrate that the μc-SiO$_x$:H can be used beneficially as the p-layer in μc-Si:H p-i-n solar cells.

Doped μc-SiO$_x$:H as the p-layer and the n-layer in μc-Si:H p-i-n solar cells

In the following, the p- and n-layers were replaced by doped μc-SiO$_x$:H layers in p-i-n solar cells with a μc-Si:H i-layer (Table 6.1). These μc-Si:H p-i-n solar cells were deposited on a HCl-etched ZnO:Al substrate, with a 1 μm thick μc-Si:H i-layer and a ZnO/Ag back reflector. Details of the preparation and the properties of the silicon layers are described in chapter 4. The p-type μc-SiO$_x$:H layer was prepared using an r_{CO2} of 1 and an *(S+O)C* of 0.25%. Further preparation details are shown in Table 4.4. The μc-SiO$_x$:H n-layer was prepared using the same recipe as for the n-type μc-SiO$_x$:H layer used for the a-Si:H p-i-n solar cell.

Table 6.1: Solar cell parameters of μc-Si:H p-i-n solar cells using different types of doped layers. Non-alloyed silicon or μc-SiO$_x$:H layers were used as the p- and n-layer. The p-layer and n-layer marked with an * are the doped silicon layers usually used for μc-Si:H p-i-n solar cells.

	p-layer	n-layer	η [%]	FF [%]	V_{oc} [V]	J_{sc} [mA/cm²]	*Line style in Figure 6.7*
A	μc-Si:H*	a-Si:H*	8.6	69	0.534	23.4	dashed
B	μc-Si:H*	μc-SiO$_x$:H	9.6	72	0.536	24.8	solid
C	μc-SiO$_x$:H	μc-SiO$_x$:H	8.9	69	0.509	25.4	dotted

Table 6.1 describes the type of the n- and p-layers of the solar cells and shows the corresponding solar cell parameters.

When the a-Si:H n-layer of a solar cell "A" is replaced by a μc-SiO$_x$:H n-layer as used in solar cell "B", the J_{sc} is increased to 24.8 mA/cm², which is 1.4 mA/cm² higher, compared to solar cell "A". The solar cells "A" and "B" have a similar V_{oc} and *FF*. Therefore, the use of a μc-SiO$_x$:H n-layer in solar cell "B" results in an η of 9.5%.

When replacing the p-layer as well as the n-layer with μc-SiO$_x$:H layers as in solar cell "C" the J_{sc} increases by 0.8 mA/cm² to 25.4 mA/cm², compared to Solar cell "B". The V_{oc} is reduced to 509 mV and the *FF* to 69%, resulting in η = 8.9%.

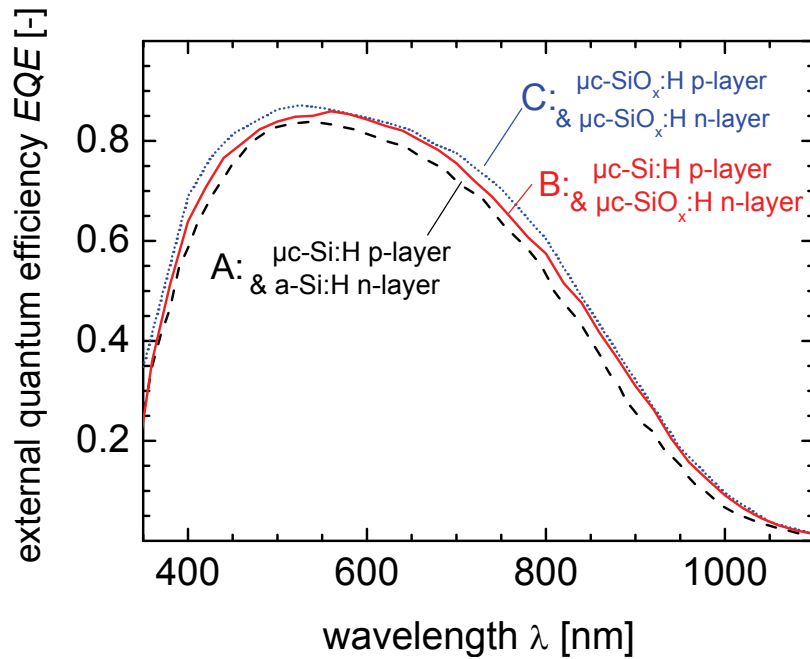*Figure 6.7: The quantum efficiency EQE of the μc-Si:H p-i-n solar cell versus the wavelength with different types of p- and n-layers, as indicated in the graph. All solar cells have an i-layer thickness of approx. 1 μm. The back reflector is ZnO/Ag layer stack. All cells have a size of 1 ×1 cm² and the EQEs were measured at 0 V bias voltage.*

Figure 6.7 shows the *EQE* of the three cells. As a reference, the *EQE* of a μc-Si:H p-i-n solar cell "A" (dashed line), with the normally used μc-Si:H p-layer and a-Si:H n-layer, is shown. When comparing the *EQE* of this solar cell "A" (dashed line) with the μc-Si:H p-i-n solar cell "B" that has a μc-SiO$_x$:H n-layer (dotted line), the gain in the wavelength range between 500 nm and 1050 nm is significant and leads to the increase in J_{sc} of 1.4 mA/cm². When applying a p-type μc-SiO$_x$:H as the window layer and a μc-SiO$_x$:H n-layer (dotted line) to the μc-Si:H p-i-n solar cell "C", a gain in *EQE,* compared to solar cell "B", was achieved, in particular up to a wavelength of 550 nm and between 650 nm and 800 nm. This gain leads to a J_{sc} of 25.4 mA/cm², which is 2 mA/cm² higher, compared to the solar cell "A" that has the normally used μc-Si:H p-layer and a-Si:H n-layer.

The results from Table 6.1 and Figure 6.7 suggest that using n-type μc-SiO$_x$:H as the n-layer in μc-Si:H p-i-n solar cells can reduce the parasitic absorption without deteriorating other solar cell parameters of the solar cell. p-Type μc-SiO$_x$:H, as a window layer, can further increase the short wavelength response of the μc-Si:H p-i-n solar cells, which is probably due to a reduced reflection of the light and/or a reduced parasitic absorption. However, the μc-SiO$_x$:H p-layer does not lead to a higher efficiency in this combination because of an reduction of V_{oc} and *FF* which can possibly adjusted by an adapted i-layer recipe.

6.3   a-Si:H/μc-Si:H tandem solar cells

The application of doped μc-SiO$_x$:H layers in a-Si:H/μc-Si:H tandem solar cells as the n/p contact between both cells i.e. as the intermediate reflector and as the n-layer of the μc-Si:H bottom cell is demonstrated. To find appropriate deposition conditions, the process gas flows for the deposition of the n-type μc-SiO$_x$:H intermediate reflector were varied and the fill factor and the external quantum efficiency of the tandem solar cell are shown. A possible reduction of the a-Si:H top cell thickness when using an intermediate reflector while keeping the J_{sc} constant is presented. Further on, this section will show results of tandem solar cells deposited on different TCOs such as SnO$_{2:}$F and double textured DT-ZnO:Al [96,97,160].

6.3.1   Device structure

The device structures of the a-Si:H/μc-Si:H tandem solar cells with p-type and n-type μc-SiO$_x$:H material is shown in Figure 6.8. The possible positions for doped μc-SiO$_x$:H layers are named in Figure 6.8 as p$_{Top}$ for the p-layer of the top cell (not demonstrated in the present study), n$_{Top}$ and p$_{Bot}$ as the n/p-contact, which also acts as the intermediate reflector, and as n$_{Bot}$ i.e. the n-layer for the bottom cell. More preparation details are described in chapter 2.
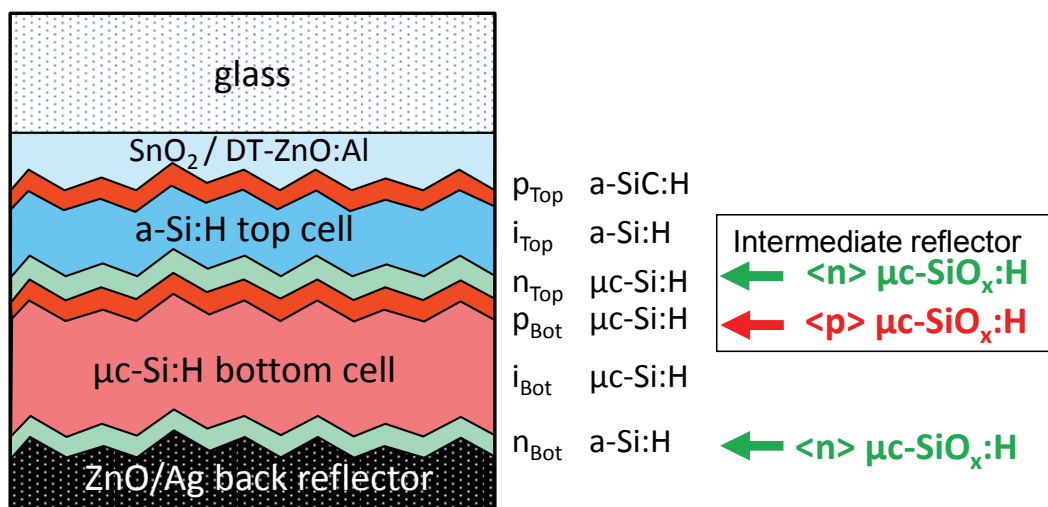
Figure 6.8: A schematic sketch of the a-Si:H/μc-Si:H tandem solar cell. The possible positions for the doped μc-SiO$_x$:H layers in tandem cells are p$_{Top}$ as a μc-SiO$_x$:H window layer, n$_{Top}$ and p$_{Bot}$ as the intermediate reflector and n$_{Bot}$ as the μc-SiO$_x$:H n-layer.

6.3.2   Requirements for doped μc-SiO$_x$:H for application in thin-film silicon solar cells

For applications in thin-film silicon solar cells, such as in the intermediate reflector, the window layer and the back contact, the required or beneficial optical material properties for the doped μc-SiO$_x$:H layer are a wide optical band gap E_{04} > 2.0 eV, to reduce parasitic absorption, and

adaptable refractive index, preferably between 1.5 and 3, but in any case below 3.8. The possibility to tailor the refractive index to the needs of the specific application is especially important, because, for a window layer (p_{Top}), a suitable refractive index. For example an $n \approx 2.76$ is needed to reduce the reflection between TCO ($n \approx 2$) and silicon ($n \approx 3.8$) ($n_{\text{window layer}} = (n_{TCO} \times n_{Si})^{0.5}$). For application as an intermediate reflector (n_{Top}/p_{Bot}), a low refractive index n is needed to increase the refractive index contrast to the silicon layer, which leads to a reflection of the light back into the a-Si:H top cell. Additionally, the reduced refractive index can improve the reflection and/or reduces the parasitic absorption of the back reflector (n_{Bot}) [150,156-158]. Table 6.2 summarizes the most important required layer properties, which will be described in the following.

Table 6.2: Required or beneficial layer properties for the indicated applications. The indicated applications are sketched in Figure 6.8. The limits of the conductivity in growth direction and in lateral direction *were calculated as described in the text. The * indicate that the limit of the conductivity for these layers was not estimated.*

	E_{04} [eV]	n	σ lower limit $[(\Omega cm)^{-1}]$ in growth direction	σ upper limit $[(\Omega cm)^{-1}]$ in lateral direction	*Further requirements*
p_{Top}	>2.0	≈2.76**	2×10^{-6}	2×10^{-1}	(i) good low-ohmic TCO/p_{Top} contact; (ii) growth compatible with TCO
n_{Top}	>2.0	1.5 - 3 <<3.8	1×10^{-5}	*	(iii) nucleation layer for p_{Bot}-layer; (iv) tunnel recombination junction (TRJ) with p_{Bot}-layer
p_{Bot}	>2.0	1.5 - 3 <<3.8	1×10^{-5}	*	(v) nucleation layer for i_{Bot}-layer; (vi) TRJ with n_{Top}-layer
n_{Bot}	>2.0	1.5 - 3 <<3.8	2×10^{-6}	∞	(vii) good low-ohmic n_{Bot}/BR contact;

**as anti-reflection window layer between TCO ($n \approx 2$) and Si ($n \approx 3.8$) $\Rightarrow n_{\text{window layer}} = (n_{TCO} \times n_{Si})^{0.5}$

Besides the optical properties, the limits of the required electrical conductivity are also listed in Table 6.2. These conductivities are important in order to achieve a low series resistance (R_s) and a high shunt resistance (R_{sh}), to avoid a reduced fill factor (*FF*) and, consequently, a reduced solar cell efficiency (η). The lower limit refers to the lower limit in growth direction and the upper limit in lateral direction. Consequently, there is no upper limit in growth direction and no lower limit in lateral direction.

Figure 6.9 a) shows the results of connecting a series resistance R_s in series to the tandem cell to estimate the influence of the intermediate reflector on the *FF*. The voltage drop over a series resistance R_s is added numerically as Ohmic *JV*-characteristics (dashed lines) to a *JV*-characteristics of an illuminated tandem solar cell without intermediate reflector (dotted line). The resulting *JV*-characteristics is shown as a solid line in Figure 6.9 a).

Figure 6.9 b) shows the results of connecting a shunt resistance R_{sh} in parallel to the tandem cell. The current leakage through the shunt resistance, as Ohmic *JV*-characteristics, is shown as dashed line and the *JV*-characteristics of an illuminated tandem solar cell as a dotted line. The resulting *JV*-characteristics is shown as a solid line in Figure 6.9 b).
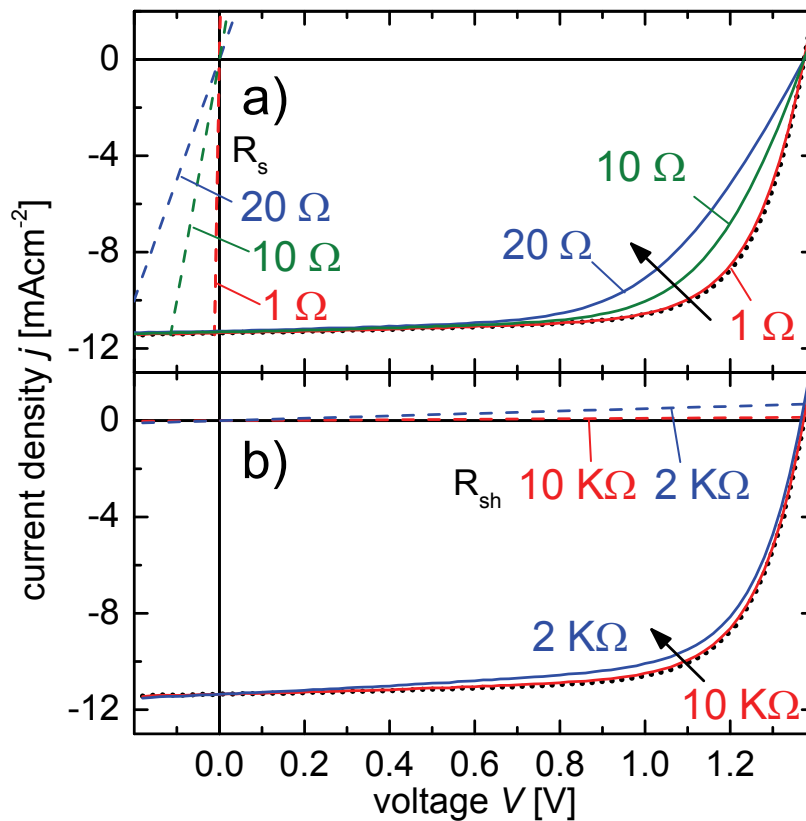
Figure 6.9: JV-characteristics of a tandem solar cell (dotted lines) and the Ohmic JV-characteristics of the resistance (dashed lines) illustrating the influence of a) series and b) shunt resistances on the JV-characteristics. The Ohmic JV-characteristics of the resistances are added numerically to the JV-characteristics of the solar cell. The resulting JV-characteristics of the tandem solar cell are represented by solid lines. The values for the additional resistances are labelled in the graph. A corresponding simplified equivalent circuit is shown in Figure 6.11.

Figure 6.11 a) shows the results of these calculations by plotting the *FF* versus the additional R_s. For an additional series resistor of 1   , a decrease in *FF* of approx. 1%-point was calculated. When increasing this series resistance, to 10   , a drop in *FF* of approx. 7%-points is expected. A maximum of 1%-point decrease in *FF* was taken as a reasonable value; therefore, the highest acceptable additional series resistance is 1   This additional series resistance would be reached when using, for instance, an intermediate reflector with a thickness of 100 nm and a conductivity of $10^{-5} (\Omega cm)^{-1}$. This conductivity value ($10^{-5} (\Omega cm)^{-1}$) is defined as a lower

acceptable conductivity limit for the intermediate reflector layer (σ-(IR)limit). For window layers or back contacts, which are typically thinner (15 nm - 25 nm), the σ-limit is accordingly lower at $\approx 2 \times 10^{-6} \, (\Omega \text{cm})^{-1}$.

Correspondingly, the calculation of the influence of the R_s on the FF the influence of the reduced R_{sh} is shown in Figure 6.9 b). The minimum acceptable shunt resistance R_{sh} (10 kΩ) between the front TCO of neighbouring cell stripes when interconnecting them to a module was estimated (Figure 6.11 b) [161]. A reduction of the shunt resistance to 10 kΩ would lead to a decrease in FF of approx. 1%-point. A maximum of 1%-point decreases in FF was taken as reasonable value. This additional shunt resistance would be the result of a high conductivity ($>0.2 \, (\Omega \text{cm})^{-1}$) in the lateral direction, e.g. of the window layer (p_{Top}), when interconnecting the cell stripes to a module assuming a scribe width of 30 µm between the cell stripes in a module and a window layer (p_{Top}) thickness of 15 nm (see Figure 6.10). The results of the module interconnection are not shown in the present study.
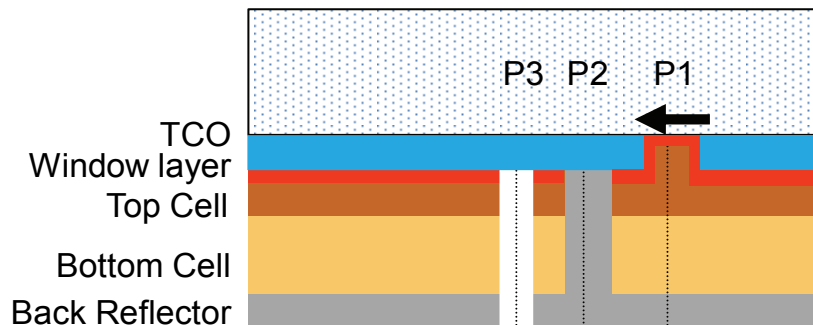
Figure 6.10: A schematic cross section of the interconnection of two cell stripes. The cell stripe can be shunted because of a highly conductive window layer. The arrow is indicating current flow through a highly conductive window layer.

Additionally, a low lateral conductivity avoids a shunting of the bottom cell by the intermediate reflector as described in section 1.3 (Figure 1.5). Furthermore a low lateral conductivity of the doped layers can also help to reduce the influence of cracks in the absorber layers on the cell's shunt resistance [6], due to shunt-quenching [162,163].

It is important to note that the additional series resistance R_s will be determined by the conductivity of the doped µc-SiO$_x$:H film in the growth direction. When interconnecting the cells stripes to a module, the shunt resistance R_{sh}, due to a p-type µc-SiO$_x$:H window layer (p_{Top}), will be determined by the conductivity of the p-layer in the lateral direction.
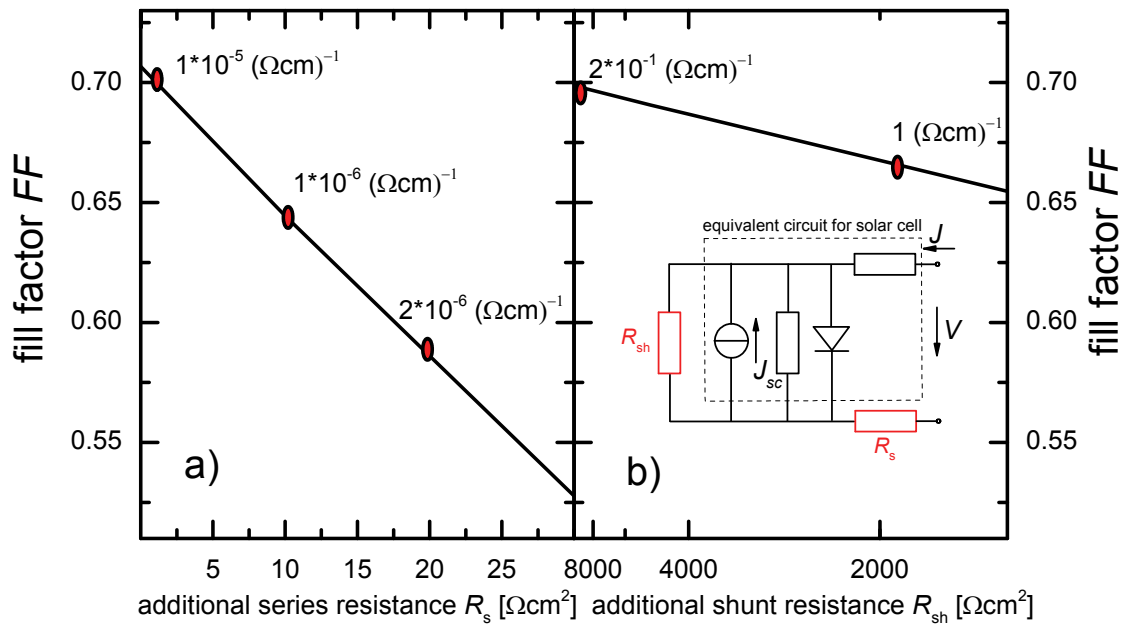
Figure 6.11: The fill factor FF versus a) the additional series resistance R_s and b) the additional shunt resistance R_{sh} as shown in Figure 6.9. The conductivities for the intermediate reflector layer labelled in a) are calculated assuming 100 nm thick intermediate reflectors. The conductivities for the window layer (p_{Top}) labelled in b) are calculated assuming a scribe width of 30 μm between the cell stripes in a module and a window layer (p_{Top}) thickness of 15 nm. A corresponding simplified equivalent circuit of the solar cell and the added series resistor and shunt resistor is also shown.

Further requirements when applying doped μc-SiOx:H layers to a-Si:H/μc-Si:H tandem solar cells are listed in Table 6.2. A p-type a-SiC:H as the window layer for the a-Si:H top cell (p_{Top}) is known to result in an insufficient electrical contact to the ZnO:Al [154], which is most likely related to n-type doping of the ZnO:Al. A solution for the (i) ZnO/p_{Top} contact issue, for example, by using the p-type μc-SiOx:H as the contact layer to achieve a good low-ohmic contact, is shown in [98,99]. For the SnO₂:F/p interface, e.g. a plasma that has a high hydrogen dilution, as used for the p-type μc-SiOx:H deposition, reduces the SnO₂ transparency [153]. Therefore, the deposition conditions have to be (ii) growth compatible with the underlying TCO. Moreover, if the subsequent layer, growing on the doped μc-SiOx:H, is also microcrystalline, then its (iii, v) function as a nucleation layer is desired [108]. Additionally, a (iv, vi) good electrical tunnel recombination junction between the n-layer and the p-layer at the n/p contact is required for a low electrical resistance [164]. Finally, (vii) a good low-Ohmic contact to the back reflector has to be provided.

6.3.3 The deposition conditions for the intermediate reflector

In the following section, the influence of the deposition conditions of the n-type μc-SiOx:H (n_{Top}) intermediate reflector (IR) on the *FF* and the external quantum efficiency (*EQE*) of the tandem cell is evaluated. The a-Si:H/μc-Si:H tandem solar cells were prepared on SnO₂:F substrates of Asahi type U, as described in chapter 2. For these tandem solar cells, the absorber layer thickness

for the a-Si:H top cell and the µc-Si:H bottom cell are 250 nm and 1.8 µm, respectively. The 70 nm thick $\mu c\text{-SiO}_x\text{:H}$ n-type (n_{Top}) intermediate reflector is placed between the 5 nm thick µc-Si:H n-layer of the a-Si:H top cell and the subsequent µc-Si:H p-layer layer of the µc-Si:H bottom cell. The 5 nm thick n-type µc-Si:H layer was prepared to be highly crystalline so that it can support the nucleation of the $\mu c\text{-SiO}_x\text{:H}$ n-type layer which is regarding its crystalline volume fraction critical on the nature of the previously deposited layer [165]. For the reference tandem solar cells without an intermediate reflector, a 25 nm thick µc-Si:H n-layer was used as n_{Top}.

The deposition conditions for the n-type $\mu c\text{-SiO}_x\text{:H}$ intermediate reflector (n_{Top}) were varied as for the SC-series in the development of n-type $\mu c\text{-SiO}_x\text{:H}$ films (section 4.2). For most series, a silane flow of 1 sccm and a phosphine flow of 0.02 sccm were used. Except for the SC-series $SC=0.4\%$, here a higher SiH_4 flow of 2 sccm, a PH_3 flow of 0.04 sccm and a H_2 flow of 500 sccm was used. To adjust the silane concentration for the other SC-series, the hydrogen flow was e.g. 200 sccm for the 0.5% SC-series. For the $SC=0.4\%$ series, the material properties are not presented, for the sake of clarity, in section 4.2, but the films were prepared and the optoelectronic properties measured. Within each individual series, the CO_2/SiH_4 ratio r_{CO2} was increased by increasing the CO_2 flow.
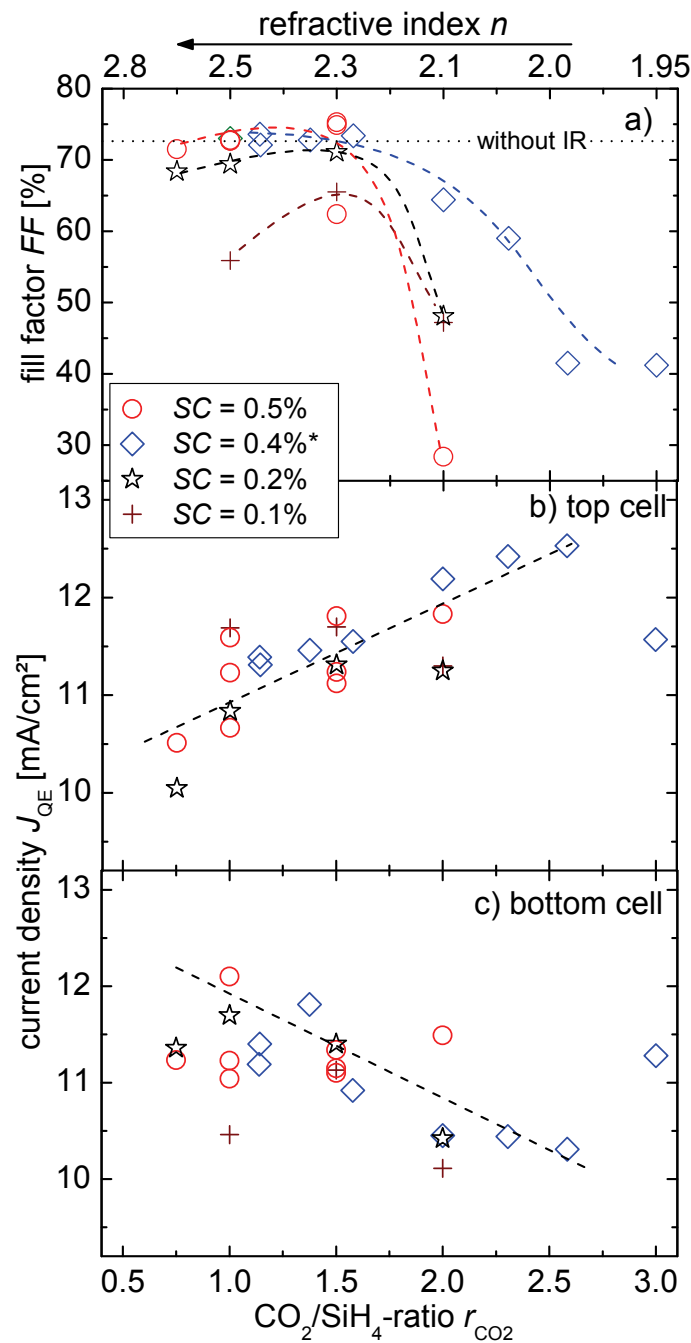
*Figure 6.12: a) The fill factor, the current density calculated from the quantum efficiency of b) the a-Si:H top solar cell and c) of the μc-Si:H bottom cell versus the r_{CO2} used for the μc-SiO$_x$:H n-type intermediate reflector applied in tandem solar cells. The silane concentrations SC are indicated in the legend. The SiH$_4$ flow is 1 sccm and 2 sccm for the SC-series marked with *. For more details on the gas flows, see Table 4.1. The dotted line represents the fill factor of a tandem solar cell without an intermediate reflector. a) the dashed lines are a guide to the eye for the individual SC-series. b) and c): the dashed lines are showing the common trend. A rough estimation for the refractive indices, taken for films on glass, for the n-type μc-SiOx:H intermediate reflector are indicated at the top of the graph, as (section 4.2, Figure 4.11).*

Figure 6.12 a) shows the *FF* versus the r_{CO2} for different intermediate reflector deposition conditions. A *FF* of 72% that is similar to the *FF* of tandem solar cells without μc-SiO$_x$:H intermediate reflector (IR) serves as a reference and is indicated by a dotted line. For tandem solar cells with an intermediate reflector prepared at an $r_{CO2} \leq 1.5$ and a hydrogen dilution down

to $SC=0.2\%$, the FF remains at a high value. For higher r_{CO2}, the FF decreases considerably. At a silane concentration SC of 0.1%, the FF is well below the reference for all r_{CO2}.

For n-type μc-SiO$_x$:H films prepared at an $SC=0.5\%$ and r_{CO2} of 1.5 a low conductivity of $<10^{-12}(\Omega cm)^{-1}$ was measured lateral, when deposited on a glass substrate (Figure 4.5 b). If the film would have the such conductivity of $10^{-12}(\Omega cm)^{-1}$ as intermediate layer also in growth direction in the solar cell it should result in a strong increase in the series resistance and thus in a low FF. Remarkably, the solar cell with an intermediate reflector deposited using the aforementioned deposition conditions ($SC=0.5\%$ and $r_{CO2}=1.5$) has a FF of $>72\%$. The high FF for this solar cell might be attributed to (i) the increased crystalline volume fraction introduced by the n-type μc-Si:H nucleation layer for the growth of the μc-SiO$_x$:H IR or (ii) a higher conductivity in the growth direction than in the lateral direction due to elongated μc-Si:H structures in growth direction [139,149]. For an $SC=0.2\%$ the FF decreases for $r_{CO2}>1.5$. The decrease in FF at an r_{CO2} of 1.5 approximately coincides with the decrease of the conductivity below the σ-(IR)limit, as calculated in section 4.2.4 (Figure 4.5 b).

Figure 6.12 show b) the J_{QE} of the a-Si:H top cell ($J_{QE,Top}$), and c) the J_{QE} of the μc-Si:H bottom cell ($J_{QE,Bot}$), versus the r_{CO2} for different SC-series, as indicated in the legend. The current density J_{QE} of the a-Si:H top cell and the μc-Si:H bottom cell were calculated from quantum efficiency spectra measurements, as described in section 2.1.6. Intermediate reflectors using a silane concentration of 1% were not applied, due to their low transparency at the required conductivities.

In general, the J_{QE} of the top cell increases with increasing r_{CO2} of the applied intermediate reflectors. The J_{QE} for the top cell obtained in these series is 12.5 mA/cm² for an intermediate reflector prepared at an $r_{CO2}=2.5$ and an $SC=0.4\%$. Simultaneously, the J_{QE} of the μc-Si:H bottom cell decreases with increasing r_{CO2} by approximately the same amount. A constant sum of $J_{QE,Top}$ and $J_{QE,Bot}$ is observed over wide range of r_{CO2} for the μc-SiO$_x$:H n-type intermediate reflector prepared with silane concentrations of 0.2% and 0.5%. One can conclude that the n-type μc-SiO$_x$:H intermediate reflector works without a significant decrease in the sum of $J_{QE,Top}$ and $J_{QE,Bot}$ over a wide range of deposition conditions.

The refractive index of the n-type μc-SiO$_x$:H films, determined for films on glass in section 4.2 and shown in Figure 4.11, is indicated at the top of the graph in Figure 6.12. The refractive index of the n-type μc-SiO$_x$:H films decreases with increasing r_{CO2}. Therefore, the refractive index difference to the adjacent silicon layers increases. This increase in refractive index difference leads to an increase in reflection at the n-type μc-SiO$_x$:H intermediate reflector back into the a-Si:H top cell. This reflected light can be absorbed by the a-Si:H top cell, which therefore can lead to an increase in the J_{QE} of the a-Si:H top cell.

From this figure, one can conclude that, the top cell J_{QE} increases and the bottom cell J_{QE} decreases with increasing r_{CO2}. However, for an $r_{CO2}>1.5$ the FF decreases strongly for the used preparation conditions. Therefore, there is a trade-off between the amount of current transfer to

the top cell and a decrease of *FF*. Both effects can be related to the layer properties: the *FF* decreases for layers with a lower conductivity and the top cell J_{QE} increases with decreasing refractive index *n*. However, below a refractive index of 2.25, the low conductivity of the μc-SiO$_x$:H intermediate reflector leads to a reduction of the fill factor of the tandem solar cell.

6.3.4   Possible reduction of the a-Si:H top cell thickness

One possibility to reduce the light-induced degradation of the a-Si:H top cell is to reduce the i-layer thickness. However, a thin i-layer leads to the delivery of a low current [13-16]. By introducing an n-type μc-SiO$_x$:H intermediate reflector (IR), the current of the a-Si:H top cell can be increased. Therefore, an a-Si:H top cell thickness reduction is possible while maintaining its current density. For the cells presented so far, the thickness of the component cells is constant and the deposition conditions for the intermediate reflector were varied. In the following, the thickness of the a-Si:H top cell was varied while the thickness of the μc-Si:H bottom was kept constant at 1.8 μm. A 55 nm thick n-type μc-SiO$_x$:H intermediate reflector was implemented using a silane concentration of 0.2% and an r_{CO2} of 1.5 with a refractive index of 2.25. For comparison, a series of tandem cells without an intermediate reflector was prepared with a variation in the a-Si:H top cell thickness and a constant 1.8 μm thick bottom cell. The a-Si:H/μc-Si:H tandem solar cells were prepared on SnO$_2$:F substrates from Asahi (U), as described in section 2.2.2. The current density J_{QE} of the a-Si:H top cell and the μc-Si:H bottom cell were calculated from quantum efficiency spectra measurements, as described in section 2.1.6.
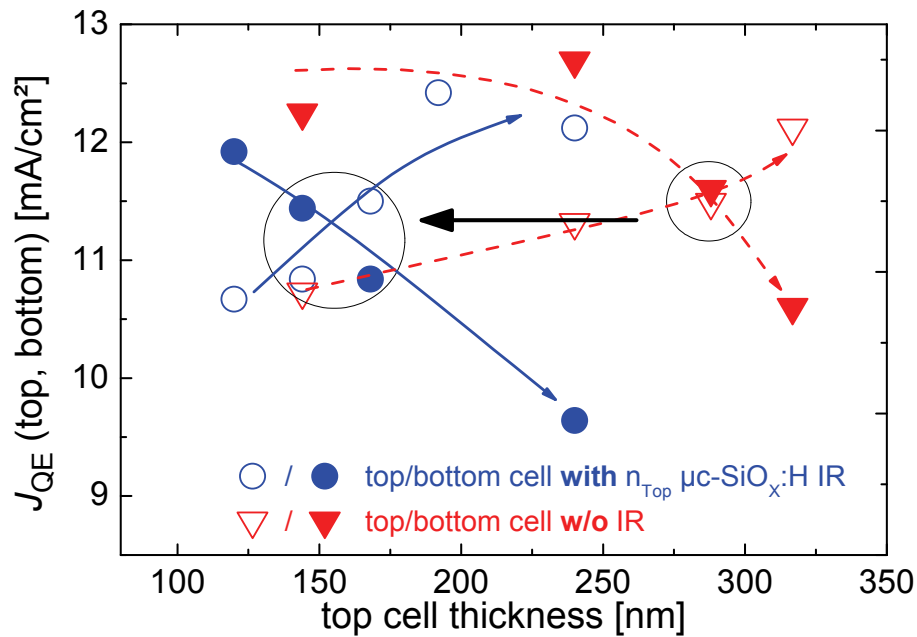
Figure 6.13: The current densities calculated from the quantum efficiency for a-Si:H top cells (open symbols) $J_{QE,Top}$ and bottom cells (full symbols) $J_{QE,Bot}$ versus the top cell thickness. The thickness of the µc-Si:H bottom cell is the same for all cells. The circles show the J_{QE} of the cells with µc-SiO$_x$:H n_{Top} as the intermediate reflector (IR), the triangles the J_{QE} of the cells without IR. The dashed curves are a guide to the eye for the cells without IR and the solid curves are for the cells with µc-SiO$_x$:H n-type IR (n_{Top}). The arrow indicates the possible thickness reduction when using an n-type µc-SiO$_x$:H intermediate reflector (n_{Top}) for this particular device.

Figure 6.13 shows the J_{QE} of the a-Si:H top cell ($J_{QE,Top}$) and of the µc-Si:H bottom cell ($J_{QE,Bot}$) versus the top cell thickness. For both cell configurations, with and without IR, the $J_{QE,Top}$ increases with the top cell's thickness, while the $J_{QE,Bot}$ decreases. For these tandem solar cells, with a bottom cell thickness of 1.8 µm and without IR, a top cell thickness of 290 nm is needed to achieve a J_{QE} current matching between the individual cells. For the tandem solar cells with IR that have the same bottom cell thickness, a top cell thickness of only 150 nm is sufficient to meet the current matching requirement. This demonstrates a way of achieving current matching for thinner top cells at a similar tandem cell short circuit current density of ≈ 11.5 mA/cm² by using this n-type µc-SiO$_x$:H IR (n_{Top}). The increase of the $J_{QE,Top}$ is the consequence of the light reflected back into a-Si:H top cell by the IR. In conclusion, a µc-SiO$_x$:H n-layer of the a-Si:H top cell (n_{Top}) as the intermediate reflector leads to an effective current transfer from the bottom cell to the top cell. For a typical bottom cell i-layer thickness of 1.8 µm, the top cell i-layer thickness can be reduced from 290 nm to 140 nm. For this exemplary device, the possible thickness reduction of the top cell i-layer thickness is around 40%. For a direct comparison, stability experiments on tandem solar cells with reduced top cell thickness are under way.

6.3.5   p-type and n-type μc-SiO$_x$:H applied to tandem solar cells

This section demonstrates the application of doped μc-SiO$_x$:H layers in a-Si:H/μc-Si:H tandem solar cells as the n/p contact between the two cells i.e. as the intermediate reflector and as the n-layer of the μc-Si:H bottom cell. Some properties and preparation details of the doped μc-SiO$_x$:H films used in this section are shown in Table 6.3.

Table 6.3: The preparation conditions such as silane concentration SC and the CO_2/SiH_4 ratio r_{CO2} are shown for the μc-SiO$_x$:H layers as labelled in this section ($n_{Top,1}/n_{Top,2}/p_{Bot}/n_{Bot}$). Additionally, properties such as the optical band gap (E_{04}), refractive index (n) and conductivity (σ) are shown.

layer	SC [%]	r_{CO2}	E_{04} [eV]	n	σ [(Ωcm)$^{-1}$]	Also used in
n$_{TOP,1}$	0.2	1.5	2.35	2.25	$\approx 10^{-3}$	6.3.4 (Tandem)
n$_{TOP,2}$	0.5	0.75	2.25	2.5	$\approx 10^{-2}$	6.2.1 (a-Si:H SJ)
p$_{Bot}$	0.126	1	2.25	2.5	$\approx 10^{-3}$	6.2.2 (μc-Si:H SJ)
n$_{Bot}$	0.5	0.75	2.25	2.5	$\approx 10^{-2}$	6.2.2 (μc-Si:H SJ)

The influence of the various doped μc-SiO$_x$:H layers on the quantum efficiency and the reflectance of the tandem cells is shown in this section. All cells have a size of $1 \times 1\,cm^2$ and the results are from the best cell of a substrate. The external quantum efficiencies (*EQE*s) were measured at 0 V external bias voltage. 0 V external bias voltage in a tandem cell results in a negative bias voltage for the measured top/bottom cell that is a result of the supplied voltage from the other light biased bottom/top cell. Occasionally, to verify the effect of the negative bias voltage, the tandem cells were measured with a positive bias voltage with a value of the expected voltage from the light biased cell but strong bias voltage dependence of the *EQE* was not observed. The low bias voltage dependence and similar fill factors of the cells indicate a similar collection probability in the investigated cells.

The section then shows results of the developed tandem solar cells deposited on SnO$_2$:F and DT-ZnO:Al [96,97,160] TCOs. The n- and p-type μc-SiO$_x$:H layers that were applied in the order of the deposition sequence replaced the conventionally used doped layers in a-Si:H/μc-Si:H tandem solar cells. All tandem solar cells have an a-Si:H top cell thickness of 340 nm and a μc-Si:H bottom cell thickness of 3.2 μm. As the substrate, Asahi (VU) or DT-ZnO:Al, as described in section 2.2.2, was used.
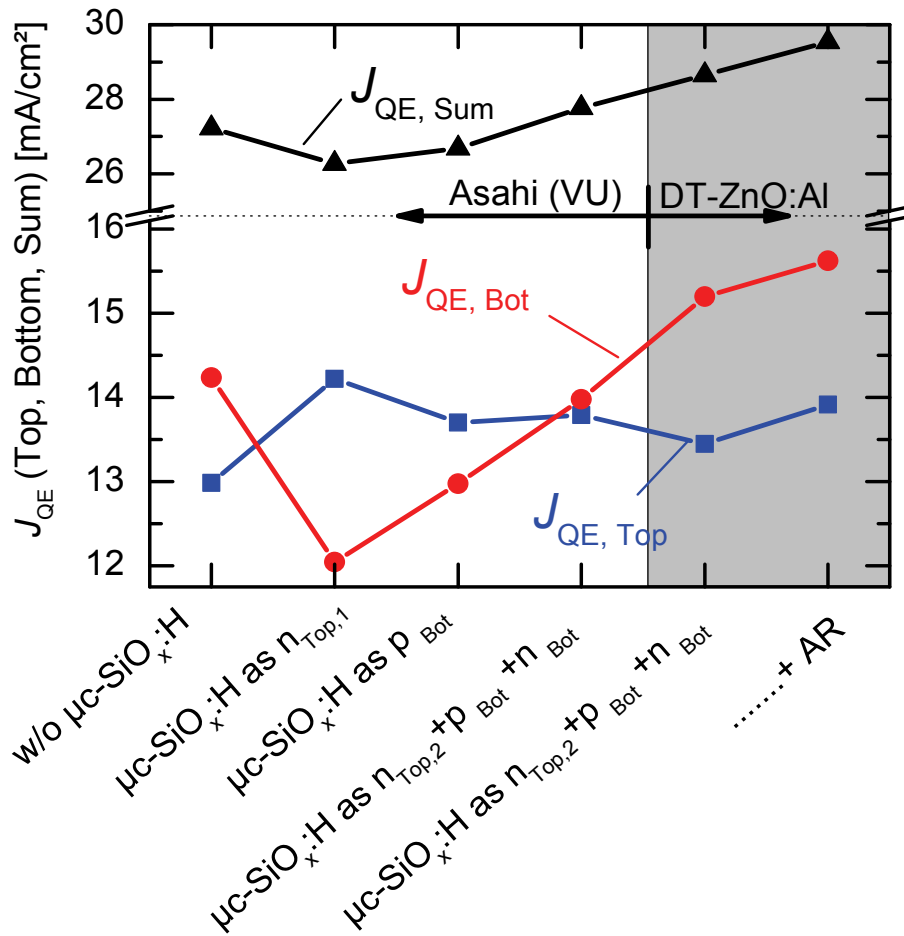
Figure 6.14: Current densities calculated from the quantum efficiency for $J_{QE,Top}$ of a top cells are indicated by the blue squares, $J_{QE,Bot}$ of bottom cells by the red circles, and sum $J_{QE,Sum}$ by the black triangles. The doped µc-SiOx:H layers replaced non-alloyed doped silicon layers and the usage of the antireflection foil (AR) are described along the x-axis of the graph. The positions where µc-SiOx:H layers are used are indicated by n_{Top}, p_{Bot}, and n_{Bot}, as sketched in Figure 6.8. The properties and preparation conditions of the doped µc-SiOx:H layers ($n_{Top,1}/n_{Top,2}/p_{Bot}/n_{Bot}$) are shown in Table 6.3. The grey area represents solar cells deposited on DT-ZnO:Al. As anti-reflection on the glass side, a foil from Solar Excel® was applied as indicated by the AR. All cells have a size of $1 \times 1 \, cm^2$ and the results are from the best cell of a substrate. The lines are guides to the eye.

Figure 6.14 shows the $J_{QE,Top}$, $J_{QE,Bot}$ and the sum of both cells ($J_{QE,Sum}$) of the tandem solar cells with doped µc-SiOx:H layers replacing other layers, as indicated at the x-axis. The substrates used for the cells are indicated in the Figure. Figure 6.15 and Figure 6.16 show the *EQE, IQE* and *R* spectra of the cells, as indicated on the graph. For clarity, the spectra of the solar cells are distributed over two figures. Figure 6.15 and Figure 6.16 show the *EQE* of the a-Si:H top cell in the wavelength range between 350 nm and 750 nm, of the µc-Si:H bottom cell in the wavelength range between 500 nm and 1100 nm, and the sum of both EQE_{Sum}. The internal quantum efficiency *IQE* was determined from the equation $IQE = EQE_{Sum}/(1-R)$, where the reflectance *R* is shown in Figure 6.15 a) and Figure 6.16 b) versus the wavelength (λ).
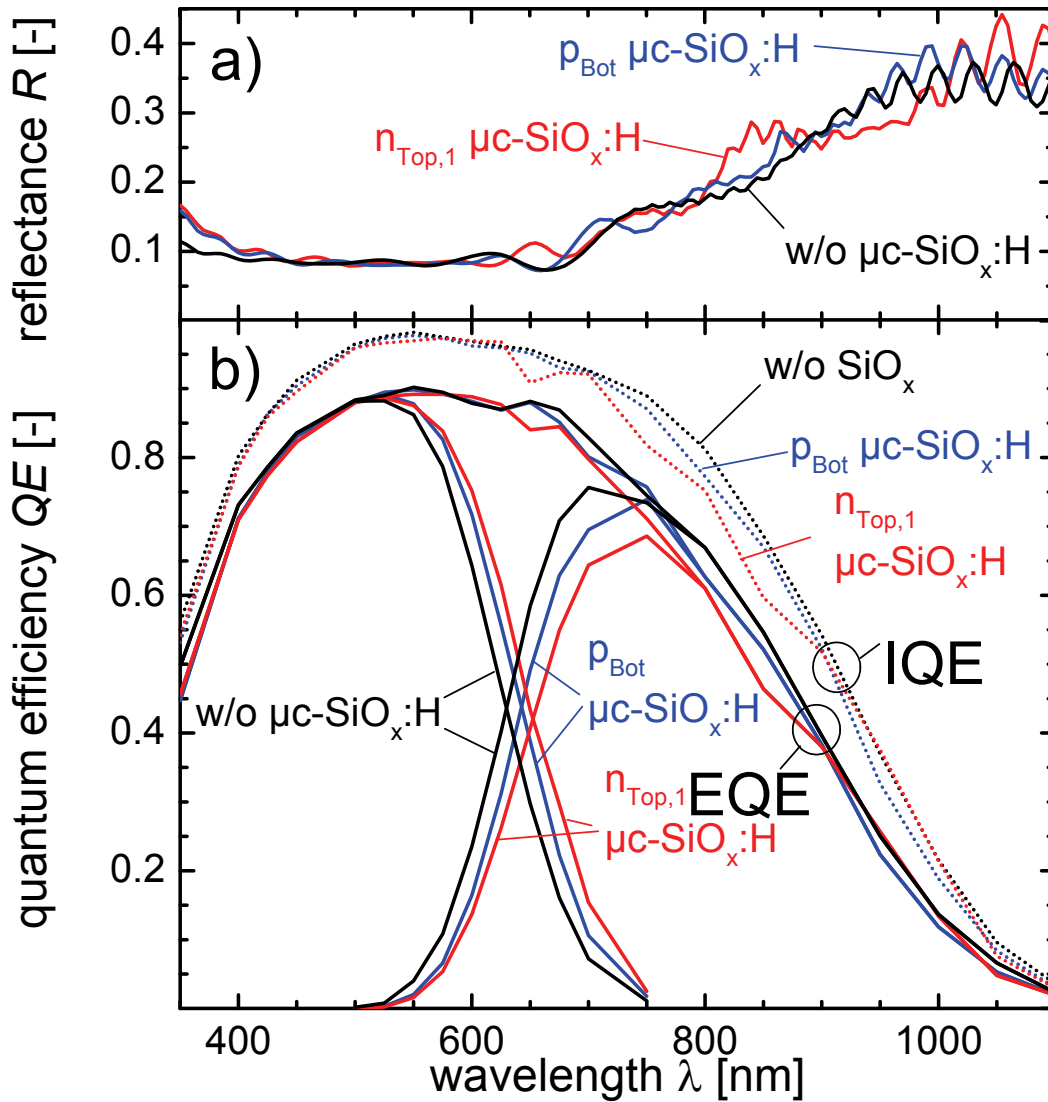
Figure 6.15: a) the reflectance R of the a-Si:H/µc-Si:H tandem cell. b) the external quantum efficiency EQE for the a-Si:H top cell, the µc-Si:H bottom cell, the sum of both cell EQE (solid lines) and the internal quantum efficiency IQE (dotted line) for the tandem cells versus the wavelength. The results are shown for tandem cells without µc-SiO$_x$:H layers and for tandem cells with µc-SiO$_x$:H layers implemented as an n$_{Top,1}$ layer and a p$_{Bot}$ layer, as is indicated on the graph. For all solar cells, Asahi (VU) was used as substrate and no anti-reflection was used. All cells have a size of 1 ×1 cm² and the EQEs were measured at 0 V external bias voltage.

Figure 6.14/Figure 6.15 show, for the standard tandem cell without (w/o) intermediate reflector "w/o µc-SiO$_x$:H" layers, a $J_{QE,Top}$ of 13 mA/cm² and a $J_{QE,Bot}$ of 14.2 mA/cm². The top cell is therefore the current limiting cell in the device. For the tandem cell which has "µc-SiO$_x$:H as n$_{Top,1}$" with a refractive index of 2.25 (see also Table 6.3) and a thickness of 55 nm as the intermediate reflector, the $J_{QE,Top}$ increases to 14.2 mA/cm² and the $J_{QE,Bot}$ decreased to 12.1 mA/cm² (Figure 6.14). The increase of the $J_{QE,Top}$ by 1.2 mA/cm², due to the n$_{Top,1}$ as the intermediate reflector, demonstrates the current transfer from the bottom cell to the top cell, even for a thick tandem device, although only a smaller amount of the light reaches the intermediate reflector, compared to tandem cells with thinner a-Si:H top cells. Using the "µc-SiO$_x$:H as n$_{Top,1}$" IR, the $J_{QE,Sum}$ is reduced by 1 mA/cm². This decrease is mainly caused by the increase in

parasitic absorption, which is visible as the difference between the *IQE* spectra of the cell w/o IR and with $n_{Top,1}$ μc-SiO$_x$:H IR in the wavelength range between 650 nm and 900 nm (Figure 6.15 b). From this difference between the *IQE* spectra, it is not possible to distinguish in which layer the additional parasitic absorption occurs: in the intermediate reflector, in p_{Top} or in the TCO. Just a part of the reduction in the bottom cell EQE_{Bot} can be clearly assigned to the increase in reflectance between 800 nm and 900 nm (Figure 6.15 a). In this case the reflected light neither reaches the μc-Si:H bottom cell, because it is reflected by the intermediate reflector, which is in front of it, nor is it absorbed by the a-Si:H top cell, because it has an energy below the band gap of a-Si:H.

The tandem cell that is shown in Figure 6.14 as "μc-SiO$_x$:H as p_{Bot}" uses a μc-SiO$_x$:H p-layer for the μc-Si:H bottom cell (p_{Bot}) that has a slightly higher refractive index of 2.5 (see also Table 6.3) and a lower thickness of 40 nm, compared to the previously described solar cell with "μc-SiO$_x$:H as $n_{Top,1}$". With respect to the latter tandem cell, the $J_{QE,Top}$ decreases by 0.5 mA/cm² and $J_{QE,Bot}$ increases by 0.9 mA/cm². The smaller current transfer and therefore the decrease in $J_{QE,Top}$ is most probably the result of the higher refractive index $n=2.5$ of the used p-type μc-SiO$_x$:H intermediate reflector, which leads to a lower reflectivity, caused by the smaller refractive index contrast. The increase in $J_{QE,Bot}$ can be attributed to the reduced parasitic absorption, visible from the gain in the *IQE* between $\lambda=600$ nm and $\lambda=900$ nm (Figure 6.15 b), and reduced reflectance of the solar cell R for λ between 800 nm and 900 nm.

From Figure 6.15 and Figure 6.14, it can be concluded that, by adjusting the refractive index of the intermediate reflector, one can vary the amount of transferred current to the top cell. This is shown by the differences in *EQE* and R between tandem cell using the $n_{Top,1}$ IR with a refractive index of 2.25 and the p_{Bot} IR with a refractive index of 2.5. This higher refractive index leads to a reduced parasitic absorption (Figure 6.15 b) and a decreased reflectance out of the cell with a photon energy below the band gap of the a-Si:H top cell (Figure 6.15 a). Additionally, this demonstrates that the p-layer of the bottom cell can also act as an intermediate reflector.
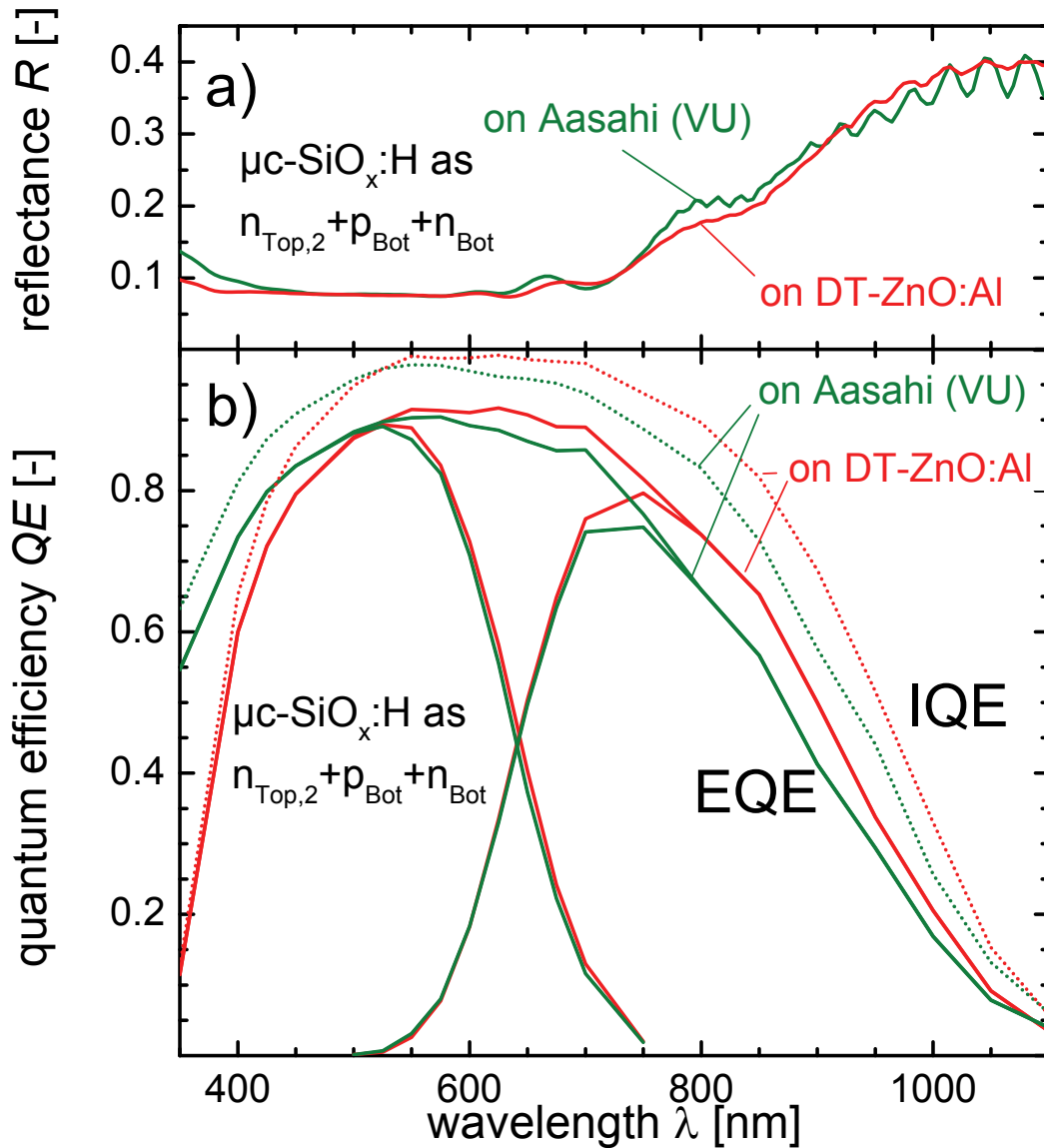
Figure 6.16: a) the reflectance R of the a-Si:H/μc-Si:H tandem cell. b) the external quantum efficiency EQE for the a-Si:H top cell, the μc-Si:H bottom cell, the sum of both cell EQE (solid lines), and the internal quantum efficiency IQE (dotted line), and for the tandem cells versus the wavelength. The results are shown for tandem cells with μc-SiOx:H layers implemented as $n_{Top,2}$, p_{Bot} and n_{Bot} layer grown on Asahi (VU) substrates and on DT-ZnO:Al substrates. All cells have a size of 1 ×1 cm² and the EQEs were measured at 0 V external bias voltage.

The tandem cells that is indicated as "$n_{Top,2}+p_{Bot}+n_{Bot}$" in Figure 6.14 and Figure 6.16 uses doped μc-SiOx:H for the n-layer and p-layer between the cells with a total thickness of 55 nm and as the n-layer of the bottom cell with a thickness of 25 nm. The μc-SiOx:H n-layer of the a-Si:H top cell ($n_{Top,2}$) and the μc-SiOx:H p-layer for the μc-Si:H bottom cell (p_{Bot}) have a refractive index of 2.5 (see also Table 6.3). The same μc-SiOx:H n-layer as used in the μc-Si:H p-i-n solar cells (see section 6.2.2), with a refractive index of ≈ 2.5, was also used in the μc-Si:H bottom cell (n_{Bot}). This combination of doped μc-SiOx:H layers for the $n_{Top,2}$, p_{Bot} and n_{Bot} yields a $J_{QE,Top}$ of 13.8 mA/cm² and a $J_{QE,Bot}$ of 14.0 mA/cm², which corresponds to a gain of 1.5 mA/cm² in $J_{QE,Sum}$ and an almost fulfilled current matching requirement between the a-Si:H top cell and the μc-Si:H bottom cell, compared to the cell that has only a μc-SiOx:H $n_{Top,1}$. The gain in $J_{QE,Sum}$ is caused

by the reduced parasitic absorption, because the reflectance R is similar as for the previously shown cells in Figure 6.15 b, and the EQE_{sum} increases for wavelengths above 550 nm. The reduced parasitic absorption was achieved through the use of highly transparent doped silicon layers. The fulfilled current matching requirements are achieved due to the appropriate refractive index and thickness of the intermediate reflector for this device configuration. This tandem solar cell ($n_{Top,2}$, p_{Bot} and n_{Bot}) has an initial efficiency of 12.9%, FF of 71.4%, V_{oc} of 1.31 V and J_{sc} of 13.8 mA/cm².

Using an anti-reflection foil (AR) on the front side of the glass (from the company Solarexcel™ company, now a part of DSM Advanced Surfaces) [101] for cells in this series (EQE not shown), a J_{sc} of 14.1 mA/cm² was achieved ($J_{QE,Top}$=14.1 mA/cm², $J_{QE,Bot}$=14.3 mA/cm²), resulting in an initial η of 13.5% (Table 6.4). The highest solar cell efficiencies in the initial state and after 1000 h light soaking achieved in the series are shown in Table 6.4. From these results, one can conclude that the benefits of doped μc-SiO$_x$:H applied as intermediate reflector and back contact of the bottom cell are cumulative. For a direct comparison, stability experiments on tandem solar cells without intermediate reflector are under way.

The light trapping, the in-coupling of the light, the parasitic absorption and, therefore, the generated current depends strongly on the TCO that is used, especially if the surface texture is different than for the DT-ZnO:Al and Asahi (VU) [96,97,151]. To investigate the influence of the different TCOs on the EQE and reflectance, the same layer stack as for the solar cell on Asahi (VU) TCO was prepared on the DT-ZnO:Al TCO. The "$n_{Top,2}$+p_{Bot}+n_{Bot}" a-Si:H/μc-Si:H tandem solar cell was prepared for this comparison. Here, as for the cell on Asahi (VU), an a-SiC:H p-layer is used as the window layer for the a-Si:H top cell (p_{Top}), which is known to result in an insufficient electrical contact between the p-layer and the ZnO:Al [154]. Therefore, the V_{oc} is only 1.28 V and the FF is 62.7%, but using the same p-layer provides the highest degree of comparability in terms of the EQE and reflectance. Solving the ZnO/p contact issue, for example, by using p-type μc-SiO$_x$:H as the contact layer, is reported in [98,99].

For this tandem cell, using μc-SiO$_x$:H as "$n_{Top,2}$+p_{Bot}+n_{Bot}" layers grown on DT-ZnO:Al, the $J_{QE,Top}$ is slightly lower (Figure 6.14) compared to this cell grown on Asahi (VU) TCO, due to the lower EQE for λ<500 nm (Figure 6.16 b). Since the reflectance of the solar cell is the similar for both cells (Figure 6.16 a) for λ<500 nm, we can conclude that the reduction in EQE of the top cell is due to a higher parasitic absorption in this wavelength range. Most probably, this increase in parasitic absorption is related to the smaller band gap of the DT-ZnO:Al, compared to the Asahi (VU) SnO$_2$:F [166]. The $J_{QE,Bot}$ is 15.2 mA/cm² for the cell grown on the DT-ZnO:Al substrate (Figure 6.14), which is 1.2 mA/cm² higher than for the same cell on the Asahi (VU) TCO. For λ>500 nm, the reflectance is also similar for both cells, but the EQE is higher for the cell on DT-ZnO:Al (Figure 6.16); therefore, the gain in EQE can be attributed to a lower parasitic absorption of the TCO in this wavelength range (λ>500 nm). An IQE above 98% in the wavelength between 550 nm and 700 nm, and a $J_{QE,Sum}$=28.6 mA/cm² demonstrates the low

parasitic absorption of the doped $\mu c\text{-}SiO_x$:H layers and the DT-ZnO:Al substrate. Using the AR-foil from the Solarexcel™ company on this device further increased the $J_{QE,Sum}$ to 29.5 mA/cm² with $J_{QE,Top}=13.9$ mA/cm² and $J_{QE,Bot}=15.6$ mA/cm² (Figure 6.14).

Table 6.4: Solar cell parameters of best achieved device performances using doped μc-SiO$_x$:H layers in different solar cell structures on Asahi (VU).

Type of solar cells	η [%]	*FF* [%]	V_{OC} [V]	J_{SC} [mA/cm²]
a-Si:H p-i-n, initial	11.3	74.3	0.891	17.1
….after 1000 h light soaking (LS)	9.8	67.1	0.890	16.5
….with AR, after 1000 h LS	10.3	67.0	0.891	17.2
μc-Si:H p-i-n (1 μm), initial	9.6	72.0	0.536	24.8
a-Si:H/μc-Si:H tandem with AR, initial	13.5	71.7	1.333	14.1
….after 1000 h light soaking	11.8	64.7	1.336	13.6

6.4   Conclusion

Doped µc-SiO$_x$:H films were developed with respect to the desired properties for application to thin-film solar cells. The desired properties are an adaptable refractive index at a sufficient conductivity and a high transparency. These doped µc-SiO$_x$:H layers were used to replace the conventionally used non-alloyed silicon layers (µc-Si:H or a-Si:H). When applied to solar cells, these layers increased the cell performance by reducing the parasitic absorption and for top cell limited tandem cells by transferring the current generation in the top cell. Doped µc-SiO$_x$:H layers with lower refractive indices applied as intermediate reflector, transfer more current from the bottom cell to the top cell. Due to the adaptable refractive index, the µc-SiO$_x$:H intermediate reflector can be tailored to the particular a-Si:H/µc-Si:H tandem solar cell with respect to current matching and reduced reflection of the solar cell. Due to the high transparency of the µc-SiO$_x$:H layers, as compared to non-alloyed silicon layers, the parasitic absorption can be decreased considerably. n-Type µc-SiO$_x$:H applied as n-layer has a similar effect on the *EQE* as the ZnO at the Ag back reflector.

Further improvement in optoelectronic properties in terms of higher transparency and lower refractive index at a sufficient conductivity can be expected at high SiH$_4$/CO$_2$ ratios and a higher PH$_3$ flow for n-type µc-SiO$_x$:H or a more finely tuned TMB flow for p-type µc-SiO$_x$:H. Making use of the wide adaptability of the refractive index, doped µc-SiO$_x$:H might also be appropriate for use in Bragg reflectors, which are more wavelength selective.

During the time span of the present study, the benefits of doped µc-SiO$_x$:H layers, especially the flexibility and favourable properties for application in thin-film silicon solar cells, has initiated further research.

Doped µc-SiO$_x$:H as the window layer in a-Si:H solar cells improves the solar cell efficiency. A µc-SiO$_x$:H window layer improves the in-coupling of the light caused by the refractive index, which is between that of silicon and ZnO. Additionally, p-type µc-SiO$_x$:H provides a good electrical contact between the p-layer and the ZnO substrate [98-100]. As shown in the present study, n-type µc-SiO$_x$:H applied as the n-layer in a-Si:H single junction solar cells has shown its capabilities to act as a back reflector, improving both the short circuit current density [150,156] and the fill factor [162].

In addition it was recently reported elsewhere that µc-SiO$_x$:H has also proven to be beneficial for use the µc-Si:H solar cells [167], not only improving the J_{sc} when used as the n-layer [168,169] or as the p/i buffer layer [170], but also improving the V_{oc} and *FF* of the µc-Si:H cell [47,163,170].

n- an p-type µc-SiO$_x$:H used as an intermediate reflector (IR) for a-Si:H/µc-Si:H tandem solar cells increased the current of the a-Si:H top cell in the tandem solar cell [149,152,171-173] by a
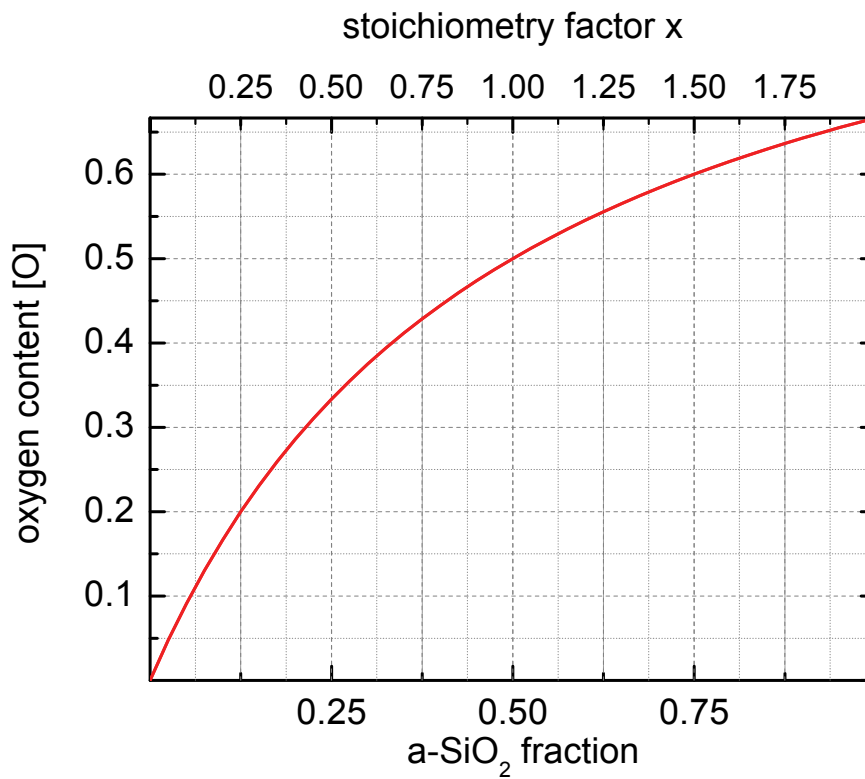
similar amount of more than 1 mA/cm², as in the present study. We achieved a stabilized efficiency of 11.8% in an a-Si:H/μc-Si:H tandem cell with anti-reflection foil.

Furthermore doped μc-SiO$_x$:H layers were also applied by other groups to a-Si:H/μc-Si:H/μc-Si:H triple junction solar cells and improved the stabilized efficiencies to 13.6% [174] and 13.4% [151]. a-Si:H/a-SiGe:H/μc-Si:H [175] triple junction solar cells with doped μc-SiO$_x$:H layers showed initial efficiencies of more than 16%. Using doped μc-SiO$_x$:H layers in a-Si:H/μc-Si:H solar modules produced by AMAT showed stabilized efficiencies of 10.1% [98] and by the Oerlikon Solar (now TEL-Tokyo Electron Ltd.) of 12.24% [176] in the Gen 5 format.

Appendix

A   The oxygen content versus the a-SiO$_2$ fraction and the stoichiometry factor x

The oxygen content versus the a-SiO$_2$ fraction (lower axis), which is the ratio between SiO$_2$ and SiO$_2$+Si, and the stoichiometry factor x (upper axis), which is the ratio between O atoms and Si atoms

$$[O] = \frac{O}{Si + O} = \frac{x}{x+1} = \frac{2 \times a\text{-}SiO_2 frac.}{(2 \times a\text{-}SiO_2 frac.) + 1} \qquad (0.1).$$

B   The absorption coefficient spectra for a-SiO$_2$, c-Si, a-SiO$_x$:H, a-Si:H, μc-SiO$_x$:H, and μc-Si:H
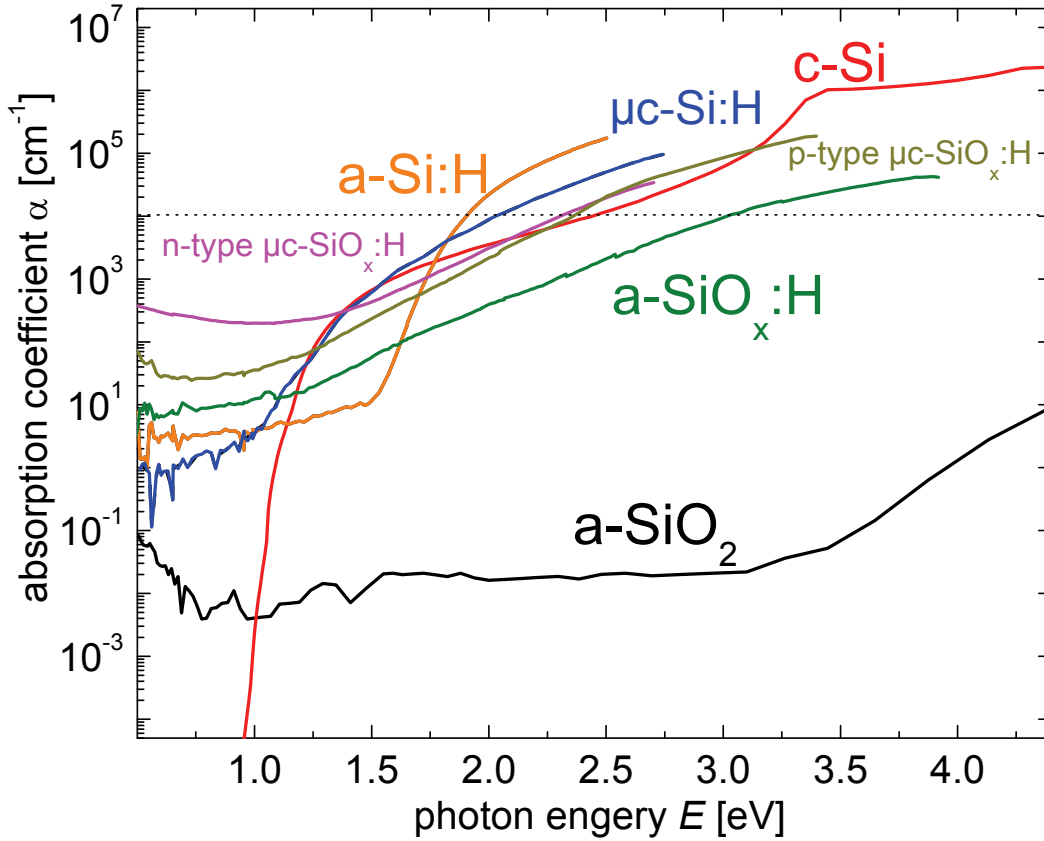

Absorption coefficient of a-SiO$_2$ [177], c-Si [53] and as an example from the present study n-type a-SiO$_x$:H, p/n-type μc-SiO$_x$:H, i-type a-Si:H and i-type μc-Si:H versus the photon energy E. The straight dotted line indicates the absorption, which is used as a value to determine the E_{04} optical band gap.

C   A guide to the gas flows for some of the deposition series
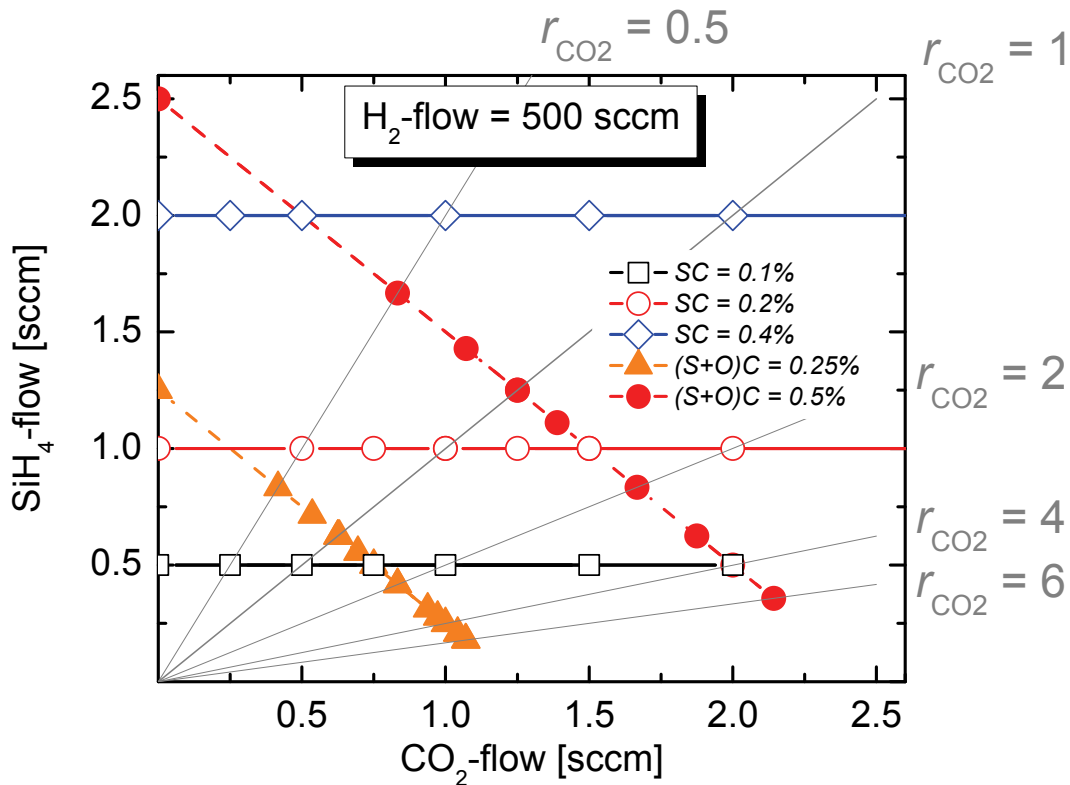
The SiH_4 flow versus the CO_2 flow for various deposition series is shown. The type of series, such as SC-series or (S+O)C-series, are indicated in the legend. The symbols indicate the gas flows for some series that were prepared during the development of doped μc-SiO_x:H. The thin lines represent the gas flows of SiH_4 and CO_2 for the r_{CO2} values that are indicated at the right and the upper side of the figure. All parameters are shown for a hydrogen flow of 500 sccm.
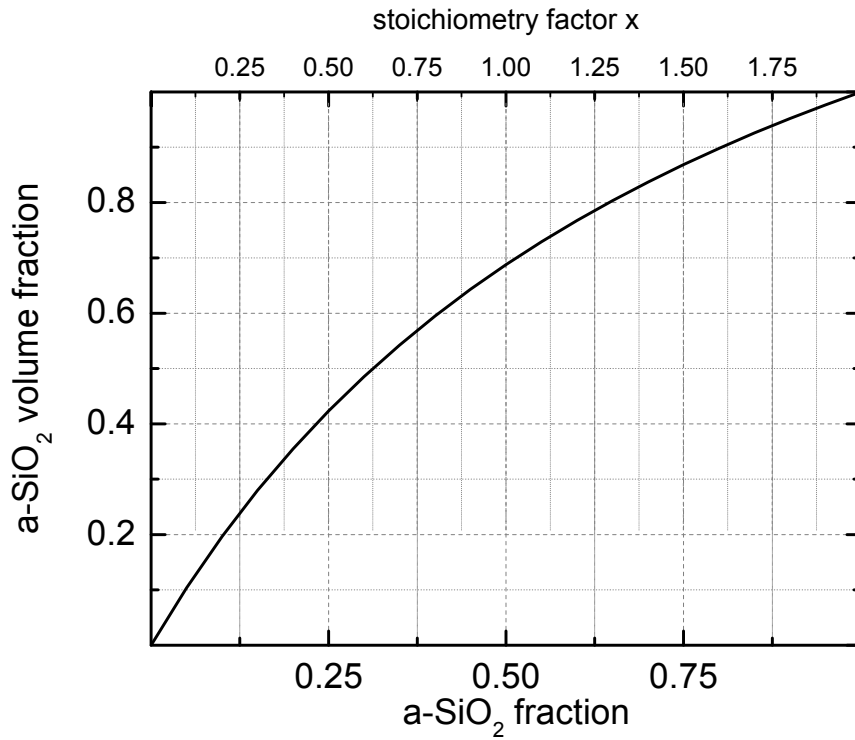
D   The dependency between the CO_2-concentration and the r_{CO2}
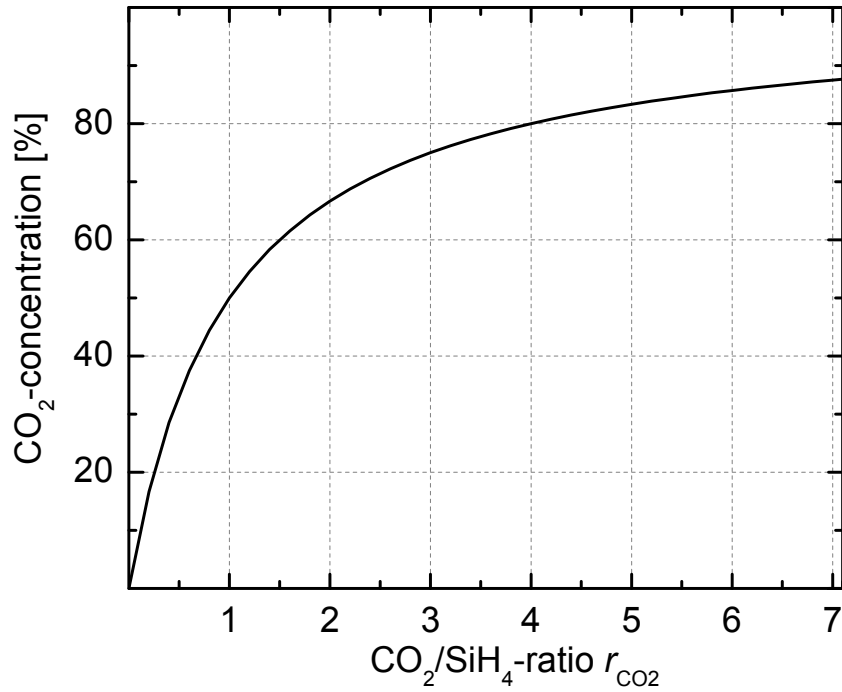
The figure shows the dependency between the CO_2 concentration and the r_{CO2} calculated by

$$CO_2 \text{ - conc.}[\%](r_{CO_2}) = \frac{CO_2}{SiH_4 + CO_2} \times 100 = \frac{r_{CO_2}}{1 + r_{CO_2}} \times 100 \tag{0.2}.$$

E   The a-SiO$_2$:H volume fraction versus a-SiO$_2$:H fraction

The a-SiO$_2$ volume fraction versus a-SiO$_2$ fraction and stoichiometry factor. The a-SiO$_2$ volume fraction, which is the ratio between a-SiO$_2$ volume and the total volume, was calculated from the a-SiO$_2$ fraction, which is the ratio between SiO$_2$ and SiO$_2$+Si, assuming
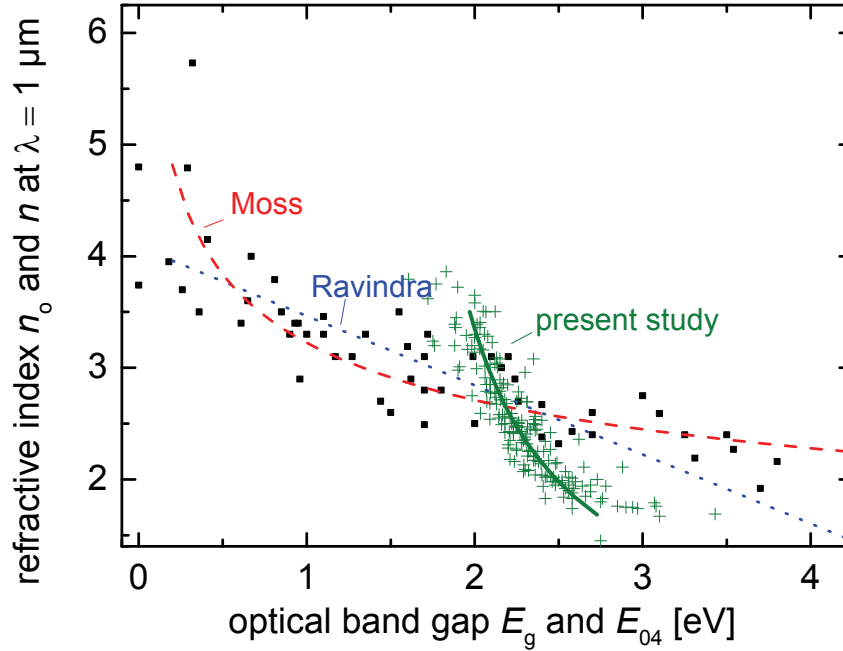
$$\rho_{SiO_2} = 2.27 \times 10^{22} [SiO_2]/cm^{-3} \tag{0.3}$$

$$\rho_{Si} = 5 \times 10^{22} [Si]/cm^{-3} \tag{0.4}$$

$$a\text{-}SiO_2 vol.\,frac. = \frac{\dfrac{a\text{-}SiO_2 frac.}{\rho_{SiO_2}}}{\dfrac{a\text{-}SiO_2 frac.}{\rho_{SiO_2}} + \dfrac{Si\,frac.}{\rho_{Si}}} \tag{0.5}$$

where ρ_{SiO2} is the density of SiO$_2$ per volume and ρ_{Si} is the density of Si per volume. The stoichiometry factor is calculated from the a-SiO$_2$ fraction$=x/2$ (see also Appendix A or equation (3.4)).

# F   The refractive index versus the optical band gap

The refractive index n_0 versus the optical band gap E_g and the function derived from the empirical functions of Moss (dashed) and Ravindra (dotted) [138]. The experimental data (squares) are also taken from [138]. Additionally, the refractive index n at $\lambda = 1\,\mu m$ versus the E_{04} band gap from the present study (crosses) are shown. The solid line describes the function derived from the relations derived in Figure 5.1.

$$n = 3.5 - [O] \times 3.3 \tag{0.6}$$

$$E_{04} = 1.97 - 0.62 \times \frac{[O]}{1-[O]} \tag{0.7}$$

$$n = 3.5 - 3.3 \times \frac{E_{04} - 1.97}{E_{04} - 1.35} \tag{0.8}$$

G   Percolation threshold in doped μc-SiO$_x$:H
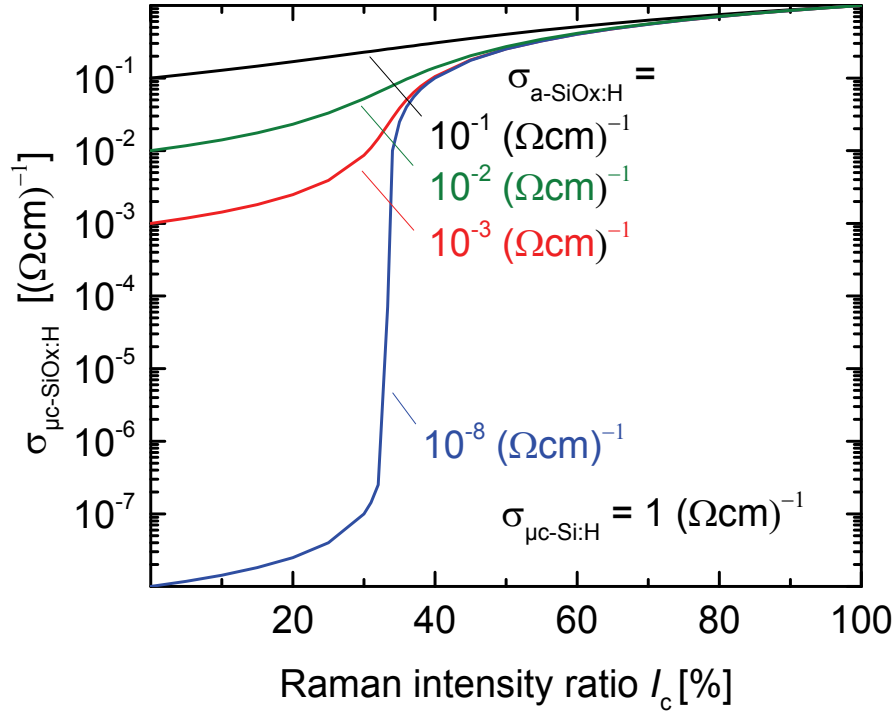
The calculated conductivity of the doped μc-SiO$_x$:H material ($\sigma_{\mu c\text{-}SiOx:H}$) versus the crystalline volume fraction I_c. As a simple approach, the conductivity of the doped highly crystalline μc-Si:H phase is assumed to be $1\,(\Omega cm)^{-1}$. The conductivity of the doped a-SiO$_x$:H phase ($\sigma_{a\text{-}SiOx:H}$) is set to various values as labelled on the graph. In an attempt to model the conductivity of the doped μc-SiO$_x$:H alloy on the basis of the conductivity of the individual material component (μc-Si:H & a-SiO$_x$:H), the dependency between the conductivity and the I_c is calculated using the equation derived from the Bruggeman's EMT model [130]. In the EMT model two phases are considered: a highly conductive and doped highly crystalline μc-Si:H phase $\sigma_{\mu c\text{-}Si:H} = 1\,(\Omega cm)^{-1}$ and doped a-SiO$_x$:H phase with a low conductivity (as indicated on the graph in $\sigma_{a\text{-}SiOx:H} = 10^{-x}\,(\Omega cm)^{-1}$). The equation following from this model is

$$0 = I_c \frac{\sigma_{\mu c\text{-}Si:H} - \sigma_{\mu c\text{-}SiOx:H}}{\sigma_{\mu c\text{-}Si:H} + 2\sigma_{\mu c\text{-}SiOx:H}} + \left(1 - I_c\right)\frac{\sigma_{a\text{-}SiOx:H} - \sigma_{\mu c\text{-}SiOx:H}}{\sigma_{a\text{-}SiOx:H} + 2\sigma_{\mu c\text{-}SiOx:H}} \qquad (0.9),$$

where $\sigma_{\mu c\text{-}SiOx:H}$ as a function of I_c has a quadratic solution whose positive solution is

$$\sigma_{\mu c\text{-}SiOx:H}(I_c) = \frac{1}{4}\left(a + \sqrt{a^2 + 8\sigma_{\mu c\text{-}Si:H}\sigma_{a\text{-}SiOx:H}}\right) \qquad (0.10),$$

in which

$$a = (2 - 3I_c)\sigma_{a-SiOx:H} + (3I_c - 1)\sigma_{\mu c-Si:H} \qquad\qquad [130]\ (0.11).$$

$\sigma_{\mu c\text{-}Si:H}$ is the conductivity for the doped highly crystalline µc-Si:H phase. Various cases for the conductivity of the doped a-SiO$_x$:H phase ($\sigma_{a\text{-}SiOx:H}$) are assumed (from $10^{-1}(\Omega cm)^{-1}$ to $10^{-8}(\Omega cm)^{-1}$). For lower $\sigma_{a\text{-}SiOx:H}$, the increase of the calculated conductivity of the doped µc-SiO$_x$:H material ($\sigma_{\mu c\text{-}SiOx:H}$) at $I_c = 33\%$ is more pronounced, compare to higher $\sigma_{a\text{-}SiOx:H}$. The percolation threshold appears at the volume fraction of the highly conductive phase (embedded in a material with a much lower conductivity) at which the conductivity increases strongly.

H   The conductivity versus the thickness
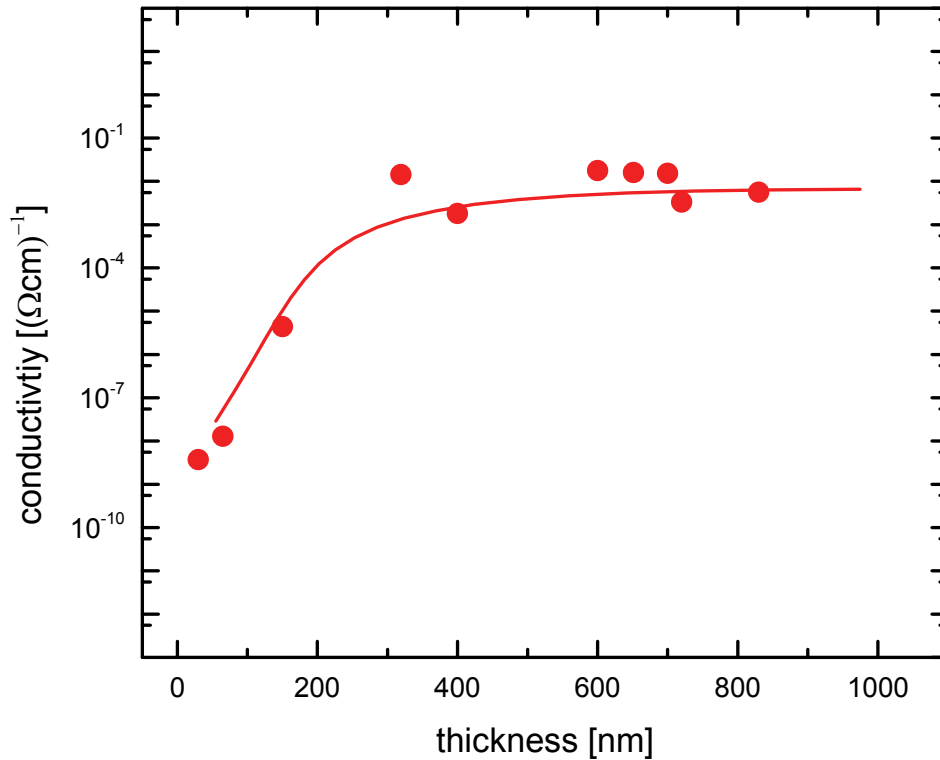
The conductivity of the n-type μc-SiO$_x$:H material ($\sigma_{\mu c\text{-SiOx:H}}$) versus the thickness. All films were grown using a plasma power density of 300 mW/cm² and a deposition pressure of 4 mbar. For all samples the H$_2$ flow was 200 sccm, the PH$_3$ flow was 0.02 sccm, the CO$_2$ was 0.75 sccm and the SiH$_4$ flow was 1 sccm. These gas flows result in an SC of 0.5% and an r_{CO2} of 0.75. For more details, see chapter 2. The conductivity increases from $4 \times 10^{-9}\,(\Omega\text{cm})^{-1}$ to $10^{-2}\,(\Omega\text{cm})^{-1}$ at 300 nm with increasing thickness. Above 300 nm the conductivity is between $10^{-3}\,(\Omega\text{cm})^{-1}$ and $10^{-2}\,(\Omega\text{cm})^{-1}$.

References

[1]   G. Masson, S. Orlandi, M. Rekinger, Global Market Outlook: For Photovoltaics 2014-2018, European Photovoltaic Industry Association (EPIA) (2014) 16-46.

[2]   E.A. Alsema, Emissions of PV Systems, Prog. Photovoltaics Res. Appl. 25 (2000) 17-25.

[3]   M. Raugei, P. Fullana-i-Palmer, V. Fthenakis, The energy return on energy investment (EROI) of photovoltaics: Methodology and comparisons with fossil fuel life cycles, Energy Policy 45 (2012) 576-582.

[4]   R.E.I. Schropp, Large-Area Thin-Film Silicon: Synergy between Displays and Solar Cells, Jpn. J. Appl. Phys. 51 (2012) 03CA07-1 - 03CA07-5.

[5]   M. Faraji, S. Gokhale, S.M. Choudhari, M.G. Takwale, S. V. Ghaisas, High mobility hydrogenated and oxygenated microcrystalline silicon as a photosensitive material in photovoltaic applications, Appl. Phys. Lett. 60 (1992) 3289-3291.

[6]   J. Meier, R. Flückiger, H. Keppner, A. Shah, Complete microcrystalline p-i-n solar cell-Crystalline or amorphous cell behavior?, Appl. Phys. Lett. 65 (1994) 860-862.

[7]   O. Vetterl, F. Finger, R. Carius, P. Hapke, L. Houben, O. Kluth, et al., Intrinsic microcrystalline silicon: A new material for photovoltaics, Sol. Energy Mater. Sol. Cells 62 (2000) 97-108.

[8]   J. Meier, P. Torres, R. Platz, S. Dubail, U. Kroll, J.A. Selvan, et al., On the Way Towards High Efficiency Thin-Film Silicon Solar Cells by the Micromorph Concept, Mater. Res. Soc. Symp. Proc. 420 (1996) 3-14.

[9]   A. V. Shah, M. Vaněček, J. Meier, F. Meillaud, J. Guillet, D. Fischer, et al., Basic efficiency limits, recent experimental results and novel light-trapping schemes in a-Si:H, μc-Si:H and "micromorph tandem" solar cells, J. Non. Cryst. Solids 338-340 (2004) 639-645.

[10]   K. Ding, T. Kirchartz, B.E. Pieters, C. Ulbrich, A.M. Ermes, S. Schicho, et al., Characterization and simulation of a-Si:H/μc-Si:H tandem solar cells, Sol. Energy Mater. Sol. Cells 95 (2011) 3318-3327.

[11]   F. Materials, H. City, H. Tauri, T. Matsuyama, S. Okamoto, H. Dohjoh, et al., High-Quality p-Type a-SiC Films Obtained by Using a New Doping Gas of $B(CH_3)_3$, Jpn. J. Appl. Phys. 28 (1989) 2436-2440.

[12]   J. Springer, A. Poruba, L. Müllerova, M. Vaněček, O. Kluth, B. Rech, Absorption loss at nano rough silver back reflector of thin-film silicon solar cells, J. Appl. Phys. 95 (2004) 1427-1429.

[13]   S. Tsuda, N. Nakamura, K. Wanatabe, T. Takahama, H. Nishiwaki, M. Ohnishi, et al., Light-Induced Instability Of Amorphous Silicon Photovoltaic Cells, Sol. Cells 9 (1983) 25-36.

[14]   B. Rech, H. Wagner, Potential of amorphous silicon for solar cells, Appl. Phys. A69 (1999) 155-167.

[15]   S. Schicho, D. Hrunski, R. van Aubel, A. Gordijn, High potential of thin (<1 μm) a-Si:H/μc-Si:H tandem solar cells, Prog. Photovoltaics Res. Appl. 18 (2010) 83-89.

[16]   T. Repmann, Stapelsolarzellen aus amorphem und mikrokristallinem Silizium, Rheinisch-Westfälische Technische Hochschule Aachen, Germany, (2003).

[17]   D. Fischer, S. Dubai, N. Pellaton, A.J.A. Selvan, R. Platz, C. Hof, et al., The micromorph solar cell: extending an a-Si:H technology towards thin film crystallline silicon, Proc. 25th IEEE Photovolt. Spec. Conf., Washington D. C., USA, (1996) 1053-1056.

[18]   K. Yamamoto, A. Nakajima, M. Yoshimi, T. Sawada, S. Fukuda, T. Suezaki, Novel hybrid thin film silicon solar cell and module, Proc. 3rd World Conf. Photovolt. Sol. Energy Convers., Osaka, Japan, (2003) 2789-2792.

[19]   K. Yamamoto, A. Nakajima, M. Yoshimi, T. Sawada, S. Fukuda, T. Suezaki, et al., A thin-film silicon solar cell and module, Prog. Photovoltaics Res. Appl. 13 (2005) 489-494.

[20]   J. Springer, Optical Model for Thin Film Silicon Solar Cells, Charles University, Prague, Czech Republic, (2004).

[21]   K. Yamamoto, A. Nakajima, M. Yoshimi, T. Sawada, S. Fukuda, T. Suezaki, et al., A high efficiency thin film silicon solar cell and module, Sol. Energy 77 (2004) 939-949.

[22]   R. Platz, N.P. Vaucher, D. Fischer, J. Meier, A. Shah, Improved Tandem Cell Performance Through Enhanced Top Cell Currents, Proc. 26th Eur. Photovolt. Sol. Energy Conf. IEEE Photovolt. Spec. Conf., Annaheim, USA, (1997) 691-694.

[23]   J. Meier, J. Spitznagel, S. Fay, C. Bucher, U. Graf, U. Kroll, et al., Enhanced Light-Trapping for Micromorph Tandem Solar Cells, Proc. 29th IEEE Photovolt. Spec. Conf., New Orleans, USA, (2002) 1118-1121.

[24]   C.C. Tsai, G.B. Anderson, R. Anderson, Growth of Amorphous, Microcrystalline, and Epitaxial Silicon in Low Temperature Plasma Deposition, Mater. Res. Soc. Symp. Proc. 192 (1990) 475-480.

[25]   R. Collins, J. Koh, A. Ferlauto, P. Rovira, Real time analysis of amorphous and microcrystalline silicon film growth by multichannel ellipsometry, Thin Solid Films 364 (2000) 129-137.

[26]   A. Lambertz, F. Finger, R. Carius, Silicon solar cells and material near the transition from microcrystalline to amorphous growth, Proc. 3rd World Conf. Photovolt. Sol. Energy Convers., Osaka, Japan, (2003) 1804-1807.

[27] O. Vetterl, M. Huelsbeck, J. Wolff, R. Carius, F. Finger, Preparation of microcrystalline silicon seed-layers with defined structural properties, Thin Solid Films 427 (2003) 46-50.

[28] P. Roca i Cabarrocas, N. Layadi, T. Heitz, B. Drévillon, I. Solomon, Substrate selectivity in the formation of microcrystalline silicon: Mechanisms and technological consequences, Appl. Phys. Lett. 66 (1995) 3609-3611.

[29] T. Fujibayashi, M. Kondo, Roles of microcrystalline silicon p layer as seed, window, and doping layers for microcrystalline silicon p-i-n solar cells, J. Appl. Phys. 99 (2006) 043703-1 - 043703-4.

[30] Y. Mai, S. Klein, R. Carius, J. Wolff, A. Lambertz, F. Finger, et al., Microcrystalline silicon solar cells deposited at high rates, J. Appl. Phys. 97 (2005) 114913-1 - 114913-12.

[31] O. Vetterl, A. Gross, T. Jana, S. Ray, A. Lambertz, R. Carius, et al., Changes in electric and optical properties of intrinsic microcrystalline silicon upon variation of the structural composition, J. Non. Cryst. Solids 299 (2002) 772-777.

[32] T. Chen, Y. Huang, A. Lambertz, D. Yang, R. Carius, F. Finger, et al., The Anti-Reflection Effect of Microcrystalline Silicon Carbide Window Layers in High Efficiency Silicon Thin Film Solar Cells, Proc. 24th Eur. Photovolt. Sol. Energy Conf. Exhib., Hamburg, Germany, (2009) 2638-2640.

[33] K. Yamamoto, A. Nakajima, M. Yoshimi, T. Sawada, S. Fukuda, T. Suezaki, High Efficiency Thin Film Silicon Hybrid Cell and Module With Newly Developed Innovative Interlayer, Proc. 4th World Conf. Photovolt. Sol. Energy Conversion, Hawaii, USA, (2006) 1489-1492.

[34] P. Sichanugrist, T. Yoshida, Y. Ichikawa, H. Sakai, Amorphous silicon oxide with microcrystalline Si phase, J. Non. Cryst. Solids 164-166 (1993) 1081-1084.

[35] S. Fujikake, H. Ohta, P. Sichanugrist, M. Ohsawa, Y. Ichikawa, H. Sakai, a-SiO:H Films and their Application to Solar Cells, Optoelectron. Technol. 9 (1994) 379-390.

[36] K. Haga, K. Yamamoto, M. Kumano, H. Wanatabe, Wide Optical-Gap a-Si:O:H Films Prepared from SiH_4-CO_2 Gas Mixture, Jpn. J. Appl. Phys. 25 (1986) L39-L41.

[37] K. Haga, H. Watanabe, Optical properties of plasma-deposited silicon-oxygen alloy films, Jpn. J. Appl. Phys. 29 (1990) 636-639.

[38] Y. Ichikawa, S. Fujikake, H. Ohta, T. Sasaki, H. Sakai, 12% two-stacked a-Si: H tandem cells with a new p-layer structure, Conf. Rec. 22nd IEEE Photovolt. Spec. Conf., Las Vegas, USA, (1991) 1296-1301.

[39] A.V. Shah (ed.), Thin-Film Silicon Solar Cells, EPFL Press, Lausanne, Switzerland, (2010).

[40] A. Matsuda, Formation kinetics and control of microcrystallite in μc-Si:H from glow discharge plasma, J. Non. Cryst. Solids 59-60 (1983) 767-774.

[41]   R.E.I. Schropp, M. Zeman, Amorphous and Microcrystalline Silicon Solar Cells: Modeling, Materials and Device Technology, Kluwer Academic Publishers, Boston/Dordrecht/London, (1998) 9-39.

[42]   L. Houben, M. Luysberg, P. Hapke, R. Carius, F. Finger, H. Wagner, Structural properties of microcrystalline silicon in the transition from highly crystalline to amorphous growth, Philos. Mag. A77 (1998) 1447-1460.

[43]   P. Sichanugrist, T. Sasaki, A. Asano, Y. Ichikawa, H. Sakai, Amorphous silicon oxide and its application to metal/n-i-p/ITO type a-Si solar cells, Sol. Energy Mater. Sol. Cells 34 (1994) 415-422.

[44]   A. Sarker, C. Banerjee, A.K. Barua, Preparation and characterization of n-type microcrystalline hydrogenated silicon oxide film, J. Phys. 35 (2002) 1205-1209.

[45]   A.K. Barua, A. Sarker, A.K. Bandyopadhyay, D. Das, S. Ray, Improvement in the conversion efficiency of single and double junction a-Si solar cells by using high quality p-SiO:H window layer and seed layer/thin n-µc-Si:H bilayer, Proc. 28th IEEE Photovolt. Spec. Conf. (2000) 829-832.

[46]   A. Sarker, C. Banerjee, S.C. Saha, A.K. Barua, Fabrication of Large Area Integrated Double Junction a-Si Solar Modules by using P-type and N-type Hydrogenated Silicon Oxide Films, Tech. Dig. Int. PVSEC-14, Bankok, Thailand, (2004) 98-99.

[47]   N. Pingate, D. Yotsaksri, P. Sichanugrist, Microcrystalline SiO and its Application to Solar Cell, Proc. 4th World Conf. Photovolt. Sol. Energy Conversion, Waikoloa, Hawaii, USA (2006) 1507-1508.

[48]   F. Finger, R. Carius, T. Dylla, S. Klein, S. Okur, Stability of microcrystalline silicon for thin film solar cell applications, IEEE Proc. Circuits, Devices Syst. 150 (2003) 300-308.

[49]   D.M. Goldie, Properties of Amorphous Silicon and its Alloys, T. Searle (Ed.), INSPEC, London, United Kingdom, (1998) 191-198.

[50]   W. Beyer, Hydrogen Incorporation in Amorphous Silicon and Processes of Its Release, D. Adler, H. Fritzsche (Eds.), Tetrahedrally-Bonded Amorph. Semicond., Springer US, (1985) 129-146.

[51]   B. Aker, Charge transfer from adsorbates to the bulk in a-Si:H, Philos. Mag. Part B55 (1987) 313-340.

[52]   W.B. Jackson, N.M. Amer, A.C. Boccara, D. Fournier, Photothermal deflection spectroscopy and detection, Appl. Opt. 20 (1981) 1333-1344.

[53]   M.A. Green, M. Keevers, Optical properties of intrinsic silicon at 300 K, Prog. Photovoltaics Res. Appl. 3 (1995) 189-192.

[54]   J. Tauc, R. Grigorovici, A. Vancu, Optical Properties and Electronic Structure of Amorphous Germanium, Phys. Status Solidi B15 (1966) 627-637.

[55] G.D. Cody, A comparison of the optical absorption edge of crystalline and amorphous silicon, Proc. 2nd Int. Work. Phys. Appl. Amour. Semicond., Turin, Italy, (1988) 1-16.

[56] W.B. Jackson, N.M. Amer, Direct measurement of gap-state absorption in hydrogenated amorphous silicon by photothermal defection spectroscopy, Phys. Rev. B25 (1982) 5559-5562.

[57] S. Klein, F. Finger, R. Carius, T. Dylla, J. Klomfaß, Relationship between the optical absorption and the density of deep gap states in microcrystalline silicon, J. Appl. Phys. 102 (2007) 103501-1 - 103501-5.

[58] M. Stutzmann, Handbook on semiconductors Vol.3 (a&b), North-Holland, Amsterdam, The Netherlands, (1994).

[59] R.M. Dawson, Y.M. Li, M. Gunes, D. Heller, S. Nag, R.W. Collins, et al., Optical prperties of hydrogenated amorphous silicon, silicon-germanium and silicon-carbon thin films, Mater. Res. Soc. Symp. Proc. 258 (1992) 595-600.

[60] Y. Hishikawa, N. Nakamura, S. Tsuda, S. Nakando, Y. Kishi, Y. Kuwano, Interference-Free Determination of the Optical Absorption Coefficient and the Optical Gap of Amorphous Silicon Films, Jpn. J. Appl. Phys. 30 (1991) 1008-1014.

[61] B.S. Richards, A. Lambertz, A.B. Sproul, Determination of the optical properties of non-uniformly thick non-hydrogenated sputtered silicon thin films on glass, Thin Solid Films 460 (2004) 247-255.

[62] R. Janssen, Strukturelle und elektronische Eigenschaften amorpher Silizium-Suboxide, Technische Universität München, Germany, (2000).

[63] T. Grundler, Silicon Oxide as an Intermediate Reflector in Silicon Thin Film Solar Cells, Rheinisch-Westfälische Technische Hochschule Aachen, Germany, (2009).

[64] S. Wemple, M. DiDomenico Jr., Behavior of the electronic dielectric constant in covalent and ionic materials, Phys. Rev. B3 (1971) 1338-1351.

[65] S. Wemple, Refractive-Index behavior of Amorphous Semiconductors and Glasses, Phys. Rev. B7 (1973) 3767-3777.

[66] W. v. Sellmeier, Zur Erklärung der abnormen Farbenfolge im Spectrum einiger Substanzen, Ann. Phys. 143 (1871) 272-282.

[67] S.K. O'Leary, S.R. Johnson, P.K. Lim, The relationship between the distribution of electronic states and the optical absorption spectrum of an amorphous semiconductor: An empirical analysis, J. Appl. Phys. 82 (1997) 3334-3340.

[68] M. Theiss, Scout 2.9900, (2008).

[69] M.J. van den Boogaard, Microvoids and hydrogen diffusion in hydrogenated silicon, Utrecht University, Netherlands, (1992).

[70] B. Holländer, H. Heer, M. Wagener, H. Halling, S. Mantl, B. Holl, New high-precision 5-axes RBS/channeling goniometer for ion beam analysis of 150 mm wafers, Nucl. Instruments Methods Phys. Res. Sect. B Beam Interact. with Mater. Atoms 161-163 (2000) 227-230.

[71] W.K. Chu, J.W. Mayer, M.A. Nicolet, Backscattering Spectroscopy, Acad. Press, New York, USA, (1978).

[72] P. Hapke, VHF-Plasmaabscheidung von mikrokristllinem Silizium (μc-Si:H): Einfluß der Plasmaanregungsfrequenz auf die strukturellen und elektrischen Eigenschaften, Rheinisch-Westfälischen Technischen Hochschule Aachen, Germany, (1995).

[73] S. Perkowitz, Optical Characterisation of Semicontuctors: Infrared, Raman and Photoluminescence Spectroscopy, Academic Press Limited, Lodon, United Kingdom, (1993).

[74] C. Smit, R.A.C.M.M. van Swaaij, H. Donker, A.M.H.N. Petit, W.M.M. Kessels, M.C.M. van de Sanden, Determining the material structure of microcrystalline silicon from Raman spectra, J. Appl. Phys. 94 (2003) 3582-3587.

[75] R. Tsu, Critical volume fraction of crystallinity for conductivity percolation in phosphorus-doped Si:F:H alloys, Appl. Phys. Lett. 40 (1982) 534-535.

[76] O. Vetterl, P. Hapke, O. Kluth, A. Lambertz, S. Wieder, B. Rech, et al., Intrinsic Microcrystalline Silicon for Solar Cells, Solid State Phenom. 67-68 (1999) 101-106.

[77] F. Köhler, Zur Mikrostruktur siliziumbasierter Dünnschichten für die Photovoltaik, Rheinisch-Westfälischen Technischen Hochschule Aachen, Germany, (2012).

[78] S. Klein, Microcrystalline Silicon Prepared by Hot Wire CVD: Preparation and Characterisation of Material and Solar Cells, Technische Universität München, Germany, (2004).

[79] D.A.G. Bruggeman, Berechnung verschiedener physikalischer Konstanten von heterogenen Substanzen, Ann. Phys. 5 (1935) 636-664.

[80] S. Michard, M. Meier, U. Zastrow, O. Astakhov, F. Finger, Investigation of porosity and atmospheric gas diffusion in microcrystalline silicon fabricated at high growth rates, Can. J. Phys. 92 (2014) 774-777.

[81] T. Kirchartz, K. Ding, U. Rau, Fundamental Electrical Characterization of Thin-Film Solar Cells, Adv. Charact. Tech. Thin Film Sol. Cells, Wiley-VCH Verlag GmbH & Co. KG, (2011) 33-60.

[82] IEC 60904-1 Photovoltaic devices - Part 1: Measurement of photovoltaic current-voltage characteristics, (2006).

[83] IEC 60904-3 Photovoltaic devices - Part 3: Measurement principles for terrestrial photovoltaic (PV) solar devices with reference spectral irradiance data, (2008).

[84]   IEC 60904-9 Photovoltaic devices - Part 9: Solar simulator performance requirements, (2007).

[85]   W. Reetz, T. Kirchartz, A. Lambertz, J. Hüpkes, A. Gerber, Current-Voltage and Spectral Response Based Characterization of Thin Film Silicon Solar Cells - Investigation of Primary Error Sources, 24th Eur. Photovolt. Sol. Energy Conf., Hamburg, Germany, (2009) 2784-2788.

[86]   W. Reetz, H. Stiebig, T. Brammer, Spectral Response of stacked solar cells based on a-Si:H, Proc. 2nd ISEC-Europe Sol. Congr. Eurosun 98, Portoroz, Slovenia, (1998) 1-7.

[87]   B. Chapman, Glow Discharge Processes: Sputtering and Plasma Etching, John Wiley & Sons LTD, New York, USA, (1980).

[88]   W. Luft, Y.S. Tsuo, Hydrogenated Amorphous Silicon Alloy Deposition Processes, Taylor & Francis, New York, USA, (1993).

[89]   U.J. Kroll, VHF-Plasmaabscheidung von amorphen Silizium: Einfluss der Anregungsfrequenz, der Reaktorgestaltung sowie Schichteigenschaften, University of Neuchâtel, Switzerland, (1995).

[90]   B. Rech, S.S. Schmidt, R. Schlatmann, Towards Photovoltaic Technology on the Terawatt Scale: Status and Challenges, D. Stolten, V. Scherer (Eds.), Transit. to Renew. Energy Syst., Wiley-VCH Verlag GmbH & Co. KG, Weinheim, Germany, (2013) 283-305.

[91]   F. Finger, P. Hapke, M. Luysberg, R. Carius, H. Wagner, M. Scheib, Improvement of grain size and deposition rate of microcrystalline silicon by use of very high frequency glow discharge, Appl. Phys. Lett. 65 (1994) 2588-2590.

[92]   O. Vetterl, On the Physics of Microcrystalline Silicon Thin Film Solar Cells From the Material to Devices with High Conversion Efficiencies, Universität Düsseldorf, Germany, (2001).

[93]   B. Rech, K. Ellmer, A. Klein, eds., Transparent Conductive Zinc Oxide-Basics and Applications in Thin Film Solar Cells, Springer Verlag, Berlin/Heidelberg, Germany, (2008).

[94]   J. Müller, O. Kluth, S. Wieder, H. Siekmann, G. Schöpe, W. Reetz, et al., Development of highly efficient thin film silicon solar cells on texture-etched zinc oxide-coated glass substrates, Sol. Energy Mater. Sol. Cells 66 (2001) 275-281.

[95]   B. Rech, J. Müller, T. Repmann, O. Kluth, T. Roschek, J. Hüpkes, et al., Amorphous and Microcrystalline Silicon Based Solar Cells and Modules on Textured Zinc Oxide Coated Glass Substrates, Mater. Res. Soc. Symp. Proc. 762 (2003) 285-292.

[96]   J.I. Owen, S.E. Pust, E. Bunte, J. Hupkes, J. Hüpkes, ZnO Etch-Feature Control via Concentration and Temperature of Various Acids, ECS J. Solid State Sci. Technol. 1 (2012) 11-17.

[97]   J. Hüpkes, J.I. Owen, S.E. Pust, E. Bunte, Chemical etching of zinc oxide for thin-film silicon solar cells, ChemPhysChem 13 (2012) 66-73.

[98]   K. Schwanitz, S. Klein, T. Stolley, M. Rohde, D. Severin, R. Trassl, Anti-reflective microcrystalline silicon oxide p-layer for thin-film silicon solar cells on ZnO, Sol. Energy Mater. Sol. Cells 105 (2012) 187-191.

[99]   P. Cuony, M. Marending, D.T.L. Alexander, M. Boccard, G. Bugnon, M. Despeisse, et al., Mixed-phase p-type silicon oxide containing silicon nanocrystals and its role in thin-film silicon solar cells, Appl. Phys. Lett. 97 (2010) 213502-1 - 213502-3.

[100]   K. Sriprapha, N. Sitthiphol, P. Sangkhawong, V. Sangsuwan, A. Limmanee, J. Sritharathikhun, p-Type hydrogenated silicon oxide thin film deposited near amorphous to microcrystalline phase transition and its application to solar cells, Curr. Appl. Phys. 11 (2011) 47-49.

[101]   C. Ulbrich, A. Gerber, K. Hermans, A. Lambertz, U. Rau, Analysis of short circuit current gains by an anti-reflective textured cover on silicon thin film solar cells, Prog. Photovoltaics Res. Appl. 21 (2012) 1672-1681.

[102]   W.B. Jackson, Optical absorption spectra of surface or interface states in hydrogenated amorphous silicon, Appl. Phys. Lett. 42 (1983) 105-107.

[103]   J. Klomfaß, Personal communication, (2013).

[104]   B. Rech, Solarzellen aus amorphem Silizium mit hohem stabilem Wirkungsgrad, Rheinisch-Westfälischen Technischen Hochschule Aachen, (1997).

[105]   A. Dasgupta, A. Lambertz, O. Vetterl, F. Finger, R. Carius, U. Zastrow, et al., P-layers of Microcrystalline Silicon Thin Film Solar Cells, Proc. 16th Eur. Photovolt. Sol. Energy Conf. Exhib. (2000) 557-560.

[106]   F. Yong, Stacked Solar Cells with Amorphous Silicon Germanium Red Absorber Layers, Graduate School, University of Science and Technology of China, Beijing, P. R. China, (2003).

[107]   R. Platz, D. Fischer, C. Hof, S. Dubail, J. Meier, U. Kroll, et al., H_2-Dilution vs. buffer layers for increased V_{oc}, Mater. Res. Soc. Symp. Proc. 420 (1996) 51-56.

[108]   V. Smirnov, C. Das, T. Melle, A. Lambertz, M. Hülsbeck, R. Carius, et al., Improved homogeneity of microcrystalline absorber layer in thin-film silicon tandem solar cells, Mater. Sci. Eng. B159-160 (2009) 44-47.

[109]   C. Ross, Y. Mai, R. Carius, F. Finger, Use of seed layers for structure, optical, and electronic transport measurements on microcrystalline silicon on glass, Prog. Photovoltaics Res. Appl. 19 (2011) 715-723.

[110]   K. Kihara, An X-ray study of the temperature dependence of the quartz structure, Eur. J. Mineral. 2 (1990) 63-67.

[111]   Http://www.mindat.org/min-3337.html, Quartz 24.11.2013,

[112]   Jmol: an open-source java viewer for chemical structures in 3D. http://www.jmol.org/, 3 (2013).

[113] S. Elliott, Medium-range structural order in covalent amorphous solids, Nature 354 (1991) 445-452.

[114] R. Temkin, An analysis of the radial distribution function of SiO_x, J. Non. Cryst. Solids 17 (1975) 215-230.

[115] U. Kahler, Darstellung, Charakterisierung und Oberflächenmodifizierung von Siliziumnanopartikeln in SiO_2, Martin-Luther-Universität Halle-Wittenberg, Germany, (2001).

[116] K. Hübner, Chemical Bond and Related Properties of SiO_2, Phys. Status Solidi A61 (1980) 665 - 673.

[117] K. Haga, H. Watanabe, A structural interpretation of Si-O-Si vibrational absorption of high-photoconductive amorphous a-SiO_x:H films, J. Non. Cryst. Solids 195 (1996) 72-75.

[118] A. Morimoto, H. Noriyama, T. Shimizu, Structure and defects in amorphous Si-O films, Jpn. J. Appl. Phys. 26 (1987) 22-27.

[119] G. Lucovsky, S. Lin, P. Richard, Local atomic structure of silicon suboxides (SiO_x, x < 2), J. Non. Cryst. Solids 75 (1985) 429-434.

[120] P.G. Pai, Infrared spectroscopic study of SiO_x films produced by plasma enhanced chemical vapor deposition, J. Vac. Sci. Technol. A Vacuum, Surfaces, Film. 4 (1986) 689-694.

[121] H. Wanatabe, K. Haga, T. Lohner, Structure of high-photosensitivity silicon-oxygen alloy films, J. Non. Cryst. Solids 164-166 (1993) 1085-1088.

[122] G. Lucovsky, J. Yang, S. S. Chao, J.E. Tyler, W. Czubatyj, Oxygen-bonding environments in glow-discharge-deposited amorphous silicon-hydrogen alloy films, Phys. Rev. B 28 (1983) 3225-3233.

[123] L. Houben, Plasmaabscheidung von mikrokristallinem Silizium: Merkmale und Mikrostruktur und deren Deutung im Sinne von Wachstumsvorgängen, Universität Düsseldorf, Germany, (1999).

[124] C.C. Tsai, Amorphous silicon and related materials, H. Fritzsche (Ed.), Adv. Disord. Semicond. Amorph. Silicon Relat. Mater. Vol. A, World Scientific, Singapore, (1989) 123-147.

[125] A. Janotta, R. Janssen, M. Schmidt, T. Graf, M. Stutzmann, L. Görgens, et al., Doping and its efficiency in a-SiO_x:H, Phys. Rev. B69 (2004) 115206-1 - 115206-16.

[126] R.A. Street, Hydrogenated amorphous silicon, Cambridge University Press, Cambridge, United Kingdom, (1991).

[127] A. Shabalov, M. Feldman, Optical properties and structure of thin SiO_x films, Thin Solid Films (1987) 317-323.

[128] H. Overhof, M. Otte, M. Schmidtke, U. Backhausen, R. Carius, The transport mechanism in micro-crystalline silicon, J. Non. Cryst. Solids 227-230 (1998) 992-995.

[129] K. Shimakawa, Percolation-controlled electronic properties in microcrystalline silicon: effective medium approach, J. Non. Cryst. Solids 269 (2000) 223-226.

[130] R. Landauer, Electrical conductivity in inhomogeneous media, AIP Conf. Proc. 40 (1978) 2-45.

[131] R. Janssen, A. Janotta, D. Dimova-Malinovska, M. Stutzmann, Optical and electrical properties of doped amorphous silicon suboxides, Phys. Rev. B60 (1999) 561-572.

[132] R. Flückiger, Microcrystalline Silicon Thin Films Deposited by VHF Plasmas for Solar Cell Applications, University of Neuchâtel, Switzerland, (1995).

[133] B. Goldstein, C.R. Dickson, I.H. Campbell, P.M. Fauchet, Properties of p+ microcrystalline films of SiC:H deposited by conventional rf glow discharge, Appl. Phys. Lett. 53 (1988) 2672-2674.

[134] K. Prasad, Microcrystalline silicon (μc-Si:H) prepared with very high frequency glow discharge (VHF-GD) process, University of Neuchâtel, Switzerland, (1991).

[135] W. Beyer, R. Carius, F. Einsele, D. Lennartz, L. Niessen, F. Pennartz, Highly conductive boron-doped hydrogenated microcrystalline silicon films obtained by hot wire deposition, Phys. Status Solidi C7 (2010) 557-560.

[136] W. Beyer, J. Herion, H. Wagner, Fermi energy dependence of surface desorption and diffusion of hydrogen in a-Si:H, J. Non. Cryst. Solids 114 (1989) 217-219.

[137] F. Finger, J. Müller, C. Malten, R. Carius, H. Wagner, Electronic properties of microcrystalline silicon investigated by electron spin resonance and transport measurements, J. Non. Cryst. Solids 266-269 (2000) 511-518.

[138] V.P. Gupta, N.M. Ravindra, Comments on the Moss Formula, Phys. Status Solidi B100 (1980) 715-719.

[139] P. Cuony, D.T.L. Alexander, I. Perez-Wurfl, M. Despeisse, G. Bugnon, M. Boccard, et al., Silicon filaments in silicon oxide for next-generation photovoltaics, Adv. Mater. 24 (2012) 1182-1186.

[140] A. Matsuda, S. Yamasaki, K. Nakagawa, H. Okushi, K. Tanaka, S. Iizoma, et al., Electrical and structural properties of phosphorous-doped glow-discharge Si:F:H and Si:H films, Jpn. J. Appl. Phys. 19 (1980) L305-L308.

[141] S. Kirner, O. Gabriel, B. Stannowski, B. Rech, R. Schlatmann, The growth of microcrystalline silicon oxide thin films studied by in situ plasma diagnostics, Appl. Phys. Lett. 102 (2013) 051906-1 - 051906-4.

[142] L.V. Mercaldo, P. Delli Veneri, I. Usatii, E.M. Esposito, G. Nicotra, Properties of mixed phase n-doped silicon oxide layers and application in micromorph solar cells, Sol. Energy Mater. Sol. Cells 119 (2013) 67-92.

[143] B.deB. Darwent, Bond Dissociation Energies in Simple Moleculs, United States Department of Commerce, (1970).

[144] O. Vetterl, P. Hapke, L. Houben, F. Finger, R. Carius, H. Wagner, Connection between hydrogen plasma treatment and etching of amorphous phase in the layer-by-layer technique with very high frequency plasma excitation, J. Appl. Phys. 85 (1999) 2991-2993.

[145] K. Uchida, A. Izumi, H. Matsumura, Novel chamber cleaning method using atomic hydrogen generated by hot catalyzer, Thin Solid Films 395 (2001) 75-77.

[146] S. Veprek, C. Wang, M.G.J. Veprek-Heijman, Role of oxygen impurities in etching of silicon by atomic hydrogen, J. Vac. Sci. Technol. A26 (2008) 313-320.

[147] H. Wanka, M. B. Schubert, High silicon etch rates by hot filament generated atomic hydrogen, J. Phys. D. Appl. Phys. 30 (1997) L28-L31.

[148] Y.S. Tsuo, Y. Xu, D.W. Baker, S.K. Deb, Etching properties of hydrogenated amorphous silicon, Mater. Res. Soc. Symp. Proc. 219 (1991) 805-810.

[149] P. Buehlmann, J. Bailat, D. Dominé, A. Billet, F. Meillaud, A. Feltrin, et al., In situ silicon oxide based intermediate reflector for thin-film silicon micromorph solar cells, Appl. Phys. Lett. 91 (2007) 143505-1 - 143505-3.

[150] P. Delli Veneri, L. V. Mercaldo, I. Usatii, P.D. Veneri, Silicon oxide based n-doped layer for improved performance of thin film silicon solar cells, Appl. Phys. Lett. 97 (2010) 023512-1 - 023512-3.

[151] S. Kim, J.-W.W. Chung, H. Lee, J. Park, Y. Heo, H.M. Lee, Remarkable progress in thin-film silicon solar cells using high-efficiency triple-junction technology, Sol. Energy Mater. Sol. Cells 119 (2013) 26-35.

[152] S.J. Jung, B.J. Kim, M. Shin, Low-refractive-index and high-transmittance silicon oxide with a mixed phase of n-type microcrystalline silicon as intermediate reflector layers for tandem solar cells, Sol. Energy Mater. Sol. Cells 121 (2014) 1-7.

[153] H. Schade, Z.E. Smith, J.H. Thomas, A. Catalano, Hydrogen plasma interactions with tin oxide surfaces, Thin Solid Films 117 (1984) 149-155.

[154] K. Winz, B. Rech, T. Eickhoff, Optoelectronic properties of thin amorphous and micro-crystalline p-type films developed for amorphous silicon-based solar cells, Mater. Res. Soc. Symp. Proc. 420 (1996) 819-824.

[155] M. Kubon, E. Boehmer, F. Siebke, B. Rech, C. Beneking, H. Wagner, Solution of the ZnO/p contact problem in a-Si:H solar cells, Sol. Energy Mater. Sol. Cells 41-42 (1996) 485-492.

[156] V. Demontis, C. Sanna, J. Melskens, R. Santbergen, A.H.M. Smets, A. Damiano, et al., The role of oxide interlayers in back reflector configurations for amorphous silicon solar cells, J. Appl. Phys. 113 (2013) 064508-1 - 064508-9.

[157]   F.-J. Haug, T. Söderström, O. Cubero, V. Terrazzoni-Daudrix, C. Ballif, Plasmonic absorption in textured silver back reflectors of thin film solar cells, J. Appl. Phys. 104 (2008) 064509-1 - 064509-7.

[158]   E. Moulin, U.W. Paetzold, K. Bittkau, J. Owen, J. Kirchhoff, A. Bauer, et al., Investigation of the impact of the rear-dielectric/silver back reflector design on the optical performance of thin-film silicon solar cells by means of detached reflectors, Prog. Photovoltaics Res. Appl. 21 (2013) 1236-1247.

[159]   M. Berginski, J. Hüpkes, A. Gordijn, W. Reetz, T. Wätjen, B. Rech, et al., Experimental studies and limitations of the light trapping and optical losses in microcrystalline silicon solar cells, Sol. Energy Mater. Sol. Cells 92 (2008) 1037-1042.

[160]   M. Berginski, J. Hüpkes, M. Schulte, G. Schöpe, H. Stiebig, B. Rech, The effect of front ZnO:Al surface texture and optical transparency on efficient light trapping in silicon thin-film solar cells, J. Appl. Phys. 101 (2007) 074903-1 - 074903-11.

[161]   K. Brecl, M. Topič, Simulation of losses in thin-film silicon modules for different configurations and front contacts, Prog. Photovoltaics Res. Appl. 16 (2008) 479-488.

[162]   M. Despeisse, G. Bugnon, a. Feltrin, M. Stueckelberger, P. Cuony, F. Meillaud, et al., Resistive interlayer for improved performance of thin film silicon solar cells on highly textured substrate, Appl. Phys. Lett. 96 (2010) 073507-1 - 073507-3.

[163]   G. Bugnon, G. Parascandolo, T. Söderström, P. Cuony, M. Despeisse, S. Hänni, et al., A New View of Microcrystalline Silicon: The Role of Plasma Processing in Achieving a Dense and Stable Absorber Material for Photovoltaic Applications, Adv. Funct. Mater. 22 (2012) 3665-3671.

[164]   N.P. Vaucher, B. Rech, D. Fischer, S. Dubail, M. Goetz, H. Keppner, et al., Controlled nucleation of thin microcrystalline layers for the recombination junction in a-Si stacked cells, Sol. Energy Mater. Sol. Cells 49 (1997) 27-33.

[165]   R.E.I. Schropp, M. Zeman, Amorphous and Microcrystalline Silicon Solar Cells: Modeling, Materials and Device Technology, Kluwer Academic Publishers, Boston/Dordrecht/London, (1998) 59-62.

[166]   K. Ellmer, Resistivity of polycrystalline zinc oxide films: current status and physical limit, J. Phys. D. Appl. Phys. 34 (2001) 3097-3108.

[167]   S. Hänni, G. Bugnon, G. Parascandolo, M.M. Boccard, J. Escarré, M. Despeisse, et al., High-efficiency microcrystalline silicon single-junction solar cells, Prog. Photovoltaics Res. Appl. (2013) 821-826.

[168]   P.D. Veneri, L. V. Mercaldo, I. Usatii, Improved micromorph solar cells by means of mixed-phase n-doped silicon oxide layers, Prog. Photovoltaics Res. Appl. 21 (2013) 148-155.

[169]   S. Kim, M.H. Lee, J. Chung, S.-W. Ahn, n-Type microcrystalline silicon oxide layer and its application to high-performance back reflectors in thin-film silicon solar cells, Curr. Appl. Phys. 13 (2013) 743-747.

[170] G. Bugnon, G. Parascandolo, S. Hänni, M. Stuckelberger, M. Charrière, M. Despeisse, et al., Silicon oxide buffer layer at the p-i interface in amorphous and microcrystalline silicon solar cells, Sol. Energy Mater. Sol. Cells 120 (2013) 140-150.

[171] B. Janthong, A. Hongsingthong, T. Krajangsang, L. Zhang, P. Sichanugrist, M. Konagai, Novel a-Si:H/μc-Si:H tandem cell with lower optical loss, J. Non. Cryst. Solids 358 (2012) 2478-2481.

[172] S. Kirner, S. Calnan, O. Gabriel, S. Neubert, M. Zelt, B. Stannowski, et al., An improved silicon-oxide-based intermediate-reflector for micromorph solar cells, Phys. Status Solidi C9 (2012) 2145-2148.

[173] S.-T. Hwang, D.J. You, S.H. Kim, S. Lee, H.-M. Lee, Large area Si thin film solar module applying n-μc-SiO$_x$:H intermediate layer with low refractive index, Sol. Energy Mater. Sol. Cells 113 (2013) 79-84.

[174] S. Guha, J. Yang, B. Yan, High efficiency multi-junction thin film silicon cells incorporating nanocrystalline silicon, Sol. Energy Mater. Sol. Cells 119 (2013) 1-11.

[175] B. Yan, G. Yue, L. Sivec, J. Yang, S. Guha, C.-S. Jiang, Innovative dual function nc-SiO$_x$:H layer leading to a >16% efficient multi-junction thin-film silicon solar cell, Appl. Phys. Lett. 99 (2011) 113512-1 - 113512-3.

[176] S. Ramser, New Record-Breaking PV Module Efficiency has been achieved - New photovoltaic module record with 12.24 % efficiency, TEL Sol. Press Release. (2014).

[177] M.A. Khashan, A.Y. Nassif, Dispersion of the optical constants of quartz and polymethyl methacrylate glasses in a wide spectral range: 0.2 - 3 μm, Opt. Commun. 188 (2001) 129-139.

Summary

The aim of the present study is to develop and investigate materials to improve the performance of thin-film silicon solar cells by (i) reducing the parasitic absorption of the ***doped layers*** and (ii) improving the in-coupling of light to gain considerably more in photo-current. Furthermore, to increase the stabilized efficiency of a-Si:H/μc-Si:H tandem solar cells most importantly (iii) the light-induced degradation of the a-Si:H top cell has to be reduced. For the latter, the intrinsic absorber layer of the a-Si:H top cell has to be as thin as possible. A thin absorber layer leads to an increased electrical carrier collection probability due to increased electrical field strength and reduced total number of defects. However, reducing the thickness of the a-Si:H i-layer results in a lower current due to reduced light-absorption. As the a-Si:H top cell and the μc-Si:H bottom cell are directly stacked, and thus, electrically connected in series, the cell with the lowest current limits the total device current. In order to achieve a high efficiency, the currents generated by the a-Si:H top cell and the μc-Si:H bottom cell have to be balanced. The amount of light absorbed in a thin top cell can be increased by using an ***intermediate reflector*** (IR) between the top cell and the bottom cell. To achieve a high internal reflection of the light, a high refractive index difference between the IR and the surrounding silicon ($n \approx 3.7$) is necessary.

In other words, the focus of the study is to develop materials and adapt their properties for the use as ***doped layers*** and as ***intermediate reflectors*** to achieve a higher stabilized solar cell efficiency and a potential to reduce the production cost. For the ***intermediate reflector*** and for the (other) ***doped layers*** in thin-film silicon solar cells, the following specific requirements of the material properties are desired:

- high transparency to minimize the parasitic absorption losses,

- an adequate conductivity $> 10^{-5} (\Omega cm)^{-1}$ in growth direction, for a sufficiently low series resistance of the solar cells,

- though $< 10^{-2} (\Omega cm)^{-1}$ in lateral direction for a sufficiently high shunt resistance for the fabrication of monolithic interconnections between cells, and

- applied as reflector, a low refractive index to reflect shorter wavelength light back into the cell, or

- applied as window layer, a suitable refractive index for improved in-coupling.

- In addition, if the subsequent layer is a microcrystalline silicon layer, they should also function as nucleation layer.

To achieve material with the aforementioned properties the present study focuses on the development and investigation of n- and p-type microcrystalline silicon oxide (μc-SiO$_x$:H) alloys

prepared by plasma enhanced chemical vapour deposition (PECVD). One purpose of the material development is to establish the relationship between the deposition process parameters and the material properties such as optical band gap (E_{04}), refractive index (n), conductivity (σ) and crystalline volume fraction (I_c). To understand the individual influences of the different structural phases of the composite material μc-SiO$_x$:H the link between the optoelectronic properties and the material structure as well as the material composition was investigated. Additionally, the n- and p-type μc-SiO$_x$:H layers were deployed in various types of thin-film silicon solar cells.

The findings suggest that doped μc-SiO$_x$:H material is a mixture of crystalline silicon nanoparticles (highly crystalline μc-Si:H) and amorphous silicon oxide (a-SiO$_x$:H), where the a-SiO$_x$:H phase itself consists of an a-SiO$_2$ and an a-Si:H phase. The phases can be thought of as providing the required optical and electrical properties individually: An oxygen rich amorphous silicon phase (a-SiO$_x$:H) has a wide optical band gap and a doped highly crystalline μc-Si:H phase ensures sufficiently high electrical conductivity.

The **optical properties** such as optical band gap E_{04} and refractive index n of the n- and p-type μc-SiO$_x$:H films can be conveniently adjusted by the CO$_2$/SiH$_4$ ratio (r_{CO2}) gas flow parameter. With increasing r_{CO2}, the oxygen content in the amorphous silicon fraction increases and the crystalline volume fraction decreases. The optical band gap E_{04} increases from 1.9 eV without oxygen incorporation ([O] $\approx$ 0) to 3.0 eV for an oxygen content [O] of 0.6 which corresponds to a stoichiometry factor x of 1.5. The refractive index n decreases from 3.8 to around 1.7 with increasing oxygen content. For both n- and p-type μc-SiO$_x$:H films the E_{04} increases and n decreases similarly with increasing oxygen content.

At a given r_{CO2}, the **electrical conductivity** σ depends on the crystalline volume fraction I_c. The I_c at a given r_{CO2} can be increased by decreasing the silane concentration process parameter $SC = \text{SiH}_4/(\text{SiH}_4 + \text{H}_2)$. This increase in SC results in an increased conductivity. The main difference in process gas parameters between both types of doping (n- and p-type) is the influence of the dopant gas flow on the crystalline volume fraction. The phosphine (PH$_3$) gas flow supports microcrystalline growth whereas the trimethylboron (TMB) gas flow hinders microcrystalline growth.

It is concluded that doped μc-SiO$_x$:H films having an a-SiO$_x$:H fraction with a high oxygen content (large a-SiO$_2$ fraction and small a-Si:H fraction) and a sufficiently high crystalline volume fraction (above the percolation threshold) is the preferable material with respect to the desired properties for the application in thin-film silicon solar cells.

From the material studies, a semi empirical phase model was proposed to predict the contribution of the phases on properties of the doped μc-SiO$_x$:H. The results on the contribution of the phases were elaborated by the effective medium theory (EMT), using Bruggeman's model. Additionally, the origin of influence of the dopant gases like TMB and phosphine on the doped μc-SiO$_x$:H growth behaviour was discussed. Moreover, the interdependence between the optical

and electrical properties is elaborated. Guiding principles for the development of doped μc-SiO$_x$:H for application in thin-film silicon solar cells are presented.

Application of the developed materials in solar cells show that by replacing the a-Si:H n-layer by an n-type μc-SiO$_x$:H layer in a-Si:H p-i-n solar cells, the parasitic absorption is reduced, which results in an increase in short circuit current density. For an a-Si:H single junction solar cell with a μc-SiO$_x$:H n-layer, a record efficiency of 10.3% after 1000 h light soaking is demonstrated.

Application of μc-SiO$_x$:H p-type window layers in μc-Si:H p-i-n solar cells, yield an increase in *EQE* of absolute 0.1 at a wavelength of 450 nm compared to solar cells with a conventional μc-Si:H p-layer. When replacing the a-Si:H n-layer by an n-type μc-SiO$_x$:H layer at the back of a μc-Si:H p-i-n solar cell one can further reduce parasitic absorption, which leads to an increase of J_{sc} of 1.4 mA/cm² and an efficiency of 9.6% for a solar cell with an thickness of 1 μm.

Finally, n- and p-type μc-SiO$_x$:H layers were applied to a-Si:H/μc-Si:H tandem solar cells as intermediate reflector at the n/p contact between both cells and as the n-layer of the μc-Si:H bottom cell. With an μc-SiO$_x$:H intermediate reflector the photogenerated current of the a-Si:H top cell increases with an decrease in refractive index of the n-type μc-SiO$_x$:H intermediate reflector due a larger difference in refractive index to the adjacent silicon layers. With this, the possible thickness reduction of the top cell i-layer thickness is around 40%.

Due to the adaptable refractive index of the μc-SiO$_x$:H films, it was possible to tailor the μc-SiO$_x$:H intermediate reflector to the particular a-Si:H/μc-Si:H tandem solar cell. By using an appropriate refractive index for the intermediate reflector, the parasitic absorption can be reduced and the current matching requirements between the a-Si:H top cell (340 nm) and the μc-Si:H bottom cell (3.2 μm) can be achieved. It was observed that the benefits of doped μc-SiO$_x$:H as the intermediate reflector and as the n-layer of the bottom cell are cumulative. For a-Si:H/μc-Si:H tandem solar cells on Asahi (VU) as substrate an efficiency of 13.5% in the initial state and of 11.8% after 1000 h light soaking was achieved with a short circuit current density of 14.1 mA/cm².

In conclusion, doped μc-SiO$_x$:H can be beneficially applied to thin-film silicon solar cells, reducing the parasitic absorption, improving light-incoupling, and acting as an intermediate reflector thanks to the low refractive index and the wide band gap at a sufficiently high conductivity.

Samenvatting het Nederlands

Het doel van het onderzoek beschreven in dit proefschrift is het ontwikkelen en onderzoeken van materialen om de prestatie van dunne-film silicium zonnecellen te verbeteren door (i) ongewenste absorptie in gedoteerde lagen te verminderen, en (ii) de inkoppeling van het licht in de zonnecel aanzienlijk te verbeteren. Bovendien moet (iii) de lichtdegradatie van de uit amorf silicium (a-Si:H) opgebouwde subcel gereduceerd worden ter verbetering van het rendement van gestapelde zonnecellen uit amorf silicium (a-Si:H) en microkristallijn silicium (μc-Si:H) subcellen. Hiertoe moet de a-Si:H subcel zo dun mogelijk gemaakt worden. Door een geringere dikte staat er een sterker elektrisch veld over de intrinsieke laag van de zonnecel en is de totale hoeveelheid defecten geringer. Beide effecten leiden ertoe dat meer ladingsdragers de contactlagen bereiken. Helaas resulteert een geringere dikte in een lagere gegenereerde kortsluitstroomdichtheid. Omdat de bovenste subcel uit a-Si:H met de onderste subcel uit μc-Si:H elektrisch in serie na elkaar zijn geschakeld, beperkt de subcel die de laagste stroomdichtheid genereert de totale stroomdichtheid van de gehele gestapelde cel. Voor een hoog omzettingsrendement moeten de gegenereerde stroomdichtheden in de bovenste en onderste sub cel gelijk zijn aan elkaar. Om dit te bereiken kan de gegenereerde stroom in de bovenste sub cel verhoogd worden door een zogenaamde intermediate reflector (IR) tussen beide subcellen in te bouwen. Voor een hoge interne reflectiviteit aan deze IR is een verschil in brekingsindex n tussen de IR en het silicium in zijn nabije omgeving (waarvan $n \sim 3{,}7$) vereist.

Om dit te bewerkstelligen, moet het materiaal van een IR in dunne-film silicium zonnecellen de volgende eigenschappen hebben:

- een hoge transparantie om de absorptie in de IR zelf te minimaliseren;
- een voldoende hoog geleidingsvermogen σ ($\sigma > 10^{-5} (\Omega cm)^{-1}$) langs de normaal van de zonnecel, voor een voldoende lage serieweerstand van de zonnecel;
- tegelijk moet het geleidingsvermogen in het vlak van de zonnecel laag genoeg zijn ($\sigma < 10^{-2} (\Omega cm)^{-1}$) om kortsluitingen te voorkomen bij serieschakelen van zonnecellen in modules;
- een brekingsindex n die laag genoeg is om licht met korte golflengtes terug in de bovenste subcel te reflecteren, of die geoptimaliseerd is om het licht in een volgende laag efficiënt in te koppelen.
- De IR moet bovendien over geschikte kiemeigenschappen beschikken voor de depositie vervolglagen met een microkristallijne component.

Teneinde een materiaal te ontwikkelen dat aan de bovengenoemde eigenschappen voldoet, wordt in dit werk n- en p-type gedoteerd μc-SiO$_x$:H ontwikkeld en onderzocht. Als depositietechniek wordt "plasma-enhanced chemical vapour deposition" (PECVD) gebruikt. Een van de doelen van het onderzoek is het bepalen van het verband tussen de gebruikte gasmengsels tijdens de depositie van de lagen en de materiaaleigenschappen van de verkregen lagen. De belangrijkste onderzochte materiaaleigenschappen zijn optische bandgap (E_{04}), brekingsindex (n), geleidingsvermogen (σ) en kristallijne volume fractie (I_c). Om de afzonderlijke invloeden van de gedoteerde kristallijn silicium nano-deeltjes en de zuurstofrijke amorfe fase in het μc-SiO$_x$:H in kaart te brengen, is het verband tussen enerzijds de opto-elektronische eigenschappen en anderzijds de structuur en samenstelling van het materiaal systematisch onderzocht. Bovendien zijn de n- en ptype gedoteerde μc-SiO$_x$:H lagen toegepast in verschillende types dunne-film silicium testzonnecellen.

De behaalde resultaten suggereren dat gedoteerd μc-SiO$_x$:H een mengsel is van kristallijn silicium (c-Si) nanodeeltjes, amorf silicium (a-Si:H) en amorf siliciumoxide (a-SiO$_x$:H). De laatstgenoemde fase bestaat op zijn beurt uit een a-SiO$_2$ en een a-Si:H fase. De verschillende fases dragen onafhankelijk van elkaar bij aan de vereiste materiaaleigenschappen: zuurstofrijk a-SiO$_x$:H heeft een grote optische bandgap terwijl de hoog-kristallijne μc-Si fase garant staat voor een voldoende groot geleidingsvermogen.

De optische materiaaleigenschappen zoals de bandgap E_{04} en de brekingsindex n van n- and p-type gedoteerde μc-SiO$_x$:H lagen kunnen worden ingesteld met de procesparameter r_{CO2}, een maat voor de verhouding tussen de toevoersnelheden van de procesgassen koolstofdioxide en silaan (CO$_2$/SiH$_4$). Zo neemt de optische bandgap E_{04} vanaf 1,9 eV zonder ingebouwde zuurstof ([O]$\approx$0) tot rond de 3 eV toe bij een toename van de zuurstofconcentratie [O] tot 0,6 (wat overeenkomt met een stoichiometriefactor van 1,5). Daarbij neemt de brekingsindex n af van 3,8 tot 1,7 voor een zelfde toename in zuurstofconcentratie. Gedoteerd μc-SiO$_x$:H vertoont een vergelijkbare afhankelijkheid van de zuurstofconcentratie.

Voor een gegeven procesgastoevoerverhouding r_{CO2} is de elektrische geleidingsvermogen σ afhankelijk van de kristallijne volumefractie I_c. De kristallijne volumefractie I_c kan erhoogd worden door de silaan concentratie van het toegevoerde procesgas (gegeven door $SC = $ SiH$_4$/(SiH$_4$+H$_2$)) te verlagen. Hierdoor wordt de elektrische geleidingsvermogen hoger. De invloed van de procesgassen ten behoeve van n- en p-dotering zijn verschillend: fosfinegas (PH$_3$), dat ingezet wordt voor n-dotering, bevordert de microkristallijne groei terwijl trimethylboon (TMB), ingezet voor p-dotering, juist een afremmende werking heeft op de groei van de kristallijne fase.

Er wordt geconcludeerd dat gedoteerde μc-SiO$_x$:H lagen met (i) een hoge zuurstofconcentratie in de amorfe fase en (ii) een voldoende grote fractie μc-Si:H (boven de drempelwaarde die nodig is

voor een aaneengesloten stroompad door de kristallijne fase) de voorkeur verdienen voor de toepassing in dunne-film silicium zonnecellen.

Gebaseerd op de experimentele gegevens wordt er in dit werk een semi-empirisch model opgesteld, dat de bijdrage van de verschillende fases aan de materiaaleigenschappen van gedoteerd μc-SiO$_x$:H voorspelt. De optische eigenschappen van de verschillende fases zijn bepaald met behulp van de effectieve medium theorie (EMT), gebruikmakend van Bruggeman's model. Daarnaast wordt ingegaan op de invloed van de doteergassen fosfine en trimethylboor op het ontstaan van het gedeponeerde materiaal. Bovendien wordt de afhankelijkheid tussen de optische en elektrische materiaaleigenschappen beschreven. Uiteindelijk wordt een leidraad voor het ontwikkelen van μc-SiO$_x$:H opgesteld.

De toepassing van de ontwikkelde materialen in zonnecellen leiden tot het inzicht dat in een enkelvoudige a-Si:H p-i-n zonnecel de a-Si:H n-laag kan worden vervangen door een n-gedoteerde μc-SiO$_x$:H laag. Hierdoor gaat er minder licht verloren door ongewenste absorptie in de n-laag, waardoor de zonnecel een grotere kortsluitstroomdichtheid kan leveren. Dit werk laat zien dat een enkelvoudige a-Si:H zonnecel waar zo'n μc-SiO$_x$:H n-laag ingebouwd is een omzettingsrendement van 10,3% na 1000 uur lichtblootstelling levert.

De toepassing van de μc-SiO$_x$:H p-lagen in enkelvoudige μc-Si:H p-i-n zonnecellen (aan kant waar het licht de zonnecel binnentreedt), leidt voor licht met een golflengte van 450 nm tot een toename in de *EQE* van 0,1 (absoluut). Er wordt tevens aangetoond dat als de a-Si:H n-laag door een n-gedoteerde μc-SiO$_x$:H laag wordt vervangen, de ongewenste absorptie in de n-laag verder afneemt zodat een zonnecel die 1 μm dik is, een kortsluitstroomdichthed J_{sc} van 1,4 mA/cm² en een omzettingsrendement van 9,6% kan bereiken.

Voorts beschrijft dit werk de preparatie van a-Si:H/μc-Si:H testzonnecellen waarin n- en p-gedoteerde μc-SiO$_x$:H lagen worden toegepast als IR (en dus tevens n/p contact tussen beide subcellen) en bovendien als de n-laag van de μc-Si:H onderste subcel.

Door het feit dat de brekingsindex van μc-SiO$_x$:H makkelijk aan te passen is, was het mogelijk de μc-SiO$_x$:H IR voor de a-Si:H/μc-Si:H gestapelde zonnecel te optimaliseren. Door een IR een geschikte brekingsindex te gebruiken kan de ongewenste absorptie kan worden teruggebracht en de stromen van de a-Si:H onderste subcel en de μc-Si:H bovenste subcel zo kunnen worden ingesteld dat ze aan elkaar gelijk zijn. Dit is een belangrijke voorwaarde voor dit type gestapelde zonnecellen. Voorts werd vastgesteld dat de voordelen van de implementatie van gedoteerd μc-SiO$_x$:H als IR en als n-laag van de bottomcel als cumulatief beschouwd kunnen worden. Voor a-Si:H/μc-Si:H gestapelde zonnecellen op met SnO$_2$:F gecoat glas van het type Asahi VU, wordt een omzettingsrendement van 13,5% in initiële toestand behaald en 11,8% na 1000 uur standaard lichtblootstelling.

Als hoofdconclusie geldt dat gedoteerd μc-SiO$_x$:H toegepast in dunne-film silicium zonnecellen een zeer positieve uitwerking op de celeigenschappen heeft door ongewenste absorptie te

verminderen, door de inkoppeling van licht te verbeteren, en door niet-geabsorbeerd licht terug te laten reflecteren. Hiertoe zijn de lage brekingsindex, de brede bandgap en het voldoende grote geleidingsvermogen van gedoteerd $\mu c\text{-SiO}_x$:H van essentieel belang.

List of publications

List of publications related to this thesis:

[1]   A. Lambertz, A. Dasgupta, W. Reetz, A. Gordijn, R. Carius, F. Finger, Microcrystalline Silicon Oxide as Intermediate Reflector For Thin Film Silicon Solar Cells, Proc. 22nd Eur. Photovolt. Sol. Energy Conf. Exhib., Milan, Italy, (2007) 1839-1842.

[2]   C. Das, A. Lambertz, J. Huepkes, W. Reetz, F. Finger, A constructive combination of antireflection and intermediate-reflector layers for a-Si/μc-Si thin film solar cells, Appl. Phys. Lett. 92 (2008) 053509-1 - 053509-3.

[3]   C. Das, A. Doumit, F. Finger, A. Gordijn, J. Huepkes, J. Kirchhoff, et al., Performance of superstrate multijunction amorphous silicon-based solar cells using optical layers for current management, Sol. Energy Mater. Sol. Cells 93 (2009) 973-975.

[4]   A. Lambertz, T. Grundler, F. Finger, n-type Hydrogenated Amorphous Silicon Oxide Containing a Microcrystalline Silicon Phase as an Intermediate Reflector in Thin-Film Silicon Solar Cells, Proc. 24th Eur. Photovolt. Sol. Energy Conf. Exhib., WIP Renewable Energies, Hamburg, Germany, (2009) 21-25.

[5]   V. Smirnov, W. Böttler, A. Lambertz, H. Wang, R. Carius, F. Finger, et al., Microcrystalline silicon n-i-p solar cells prepared with microcrystalline silicon oxide (μc-SiO$_x$:H) n-layer, Phys. Status Solidi C7 (2010) 1053-1056.

[6]   T. Grundler, A. Lambertz, F. Finger, N-type hydrogenated amorphous silicon oxide containing a microcrystalline silicon phase as an intermediate reflector in silicon thin film solar cells, Phys. Status Solidi C7 (2010) 1085-1088.

[7]   V. Smirnov, A. Lambertz, W. Böttler, R. Carius, F. Finger, N-type microcrystalline silicon oxide (μc-SiO$_x$:H) layer for n-side illuminated microcrystalline silicon solar cells, 25th Eur. Photovolt. Sol. Energy Conf. Exhib. / 5th World Conf. Photovolt. Energy Convers., Valencia, Spain, (2010) 3165-3168.

[8]   L. Xiao, O. Astakhov, R. Carius, A. Lambertz, T. Grundler, F. Finger, et al., Defects and structure of μc-SiO$_x$:H deposited by PECVD, Phys. Status Solidi C7 (2010) 941-944.

[9]   A. Lambertz, T. Grundler, F. Finger, Hydrogenated amorphous silicon oxide containing a microcrystalline silicon phase and usage as an intermediate reflector in thin-film silicon solar cells, J. Appl. Phys. 109 (2011) 113109-1 - 113109-10.

[10]   V. Smirnov, A. Lambertz, B. Grootoonk, R. Carius, F. Finger, Microcrystalline silicon oxide (μc-SiO$_x$:H) alloys: A versatile material for application in thin film silicon single and tandem junction solar cells, J. Non. Cryst. Solids 358 (2012) 1954-1957.

[11]   A. Lambertz, F. Finger, B. Hollaender, J.K. Rath, R.E.I. Schropp, Boron-doped
        hydrogenated microcrystalline silicon oxide (μc-SiO$_x$:H) for application in thin-film
        silicon solar cells, J. Non. Cryst. Solids 358 (2012) 1962-1965.

[12]   A. Lambertz, V. Smirnov, T. Merdzhanova, K. Ding, S. Haas, G. Jost, et al.,
        Microcrystalline silicon-oxygen alloys for application in silicon solar cells and modules,
        Sol. Energy Mater. Sol. Cells 119 (2013) 134-143.

[13]   V. Smirnov, A. Lambertz, S. Tillmanns, F. Finger, p- and n-type microcrystalline silicon
        oxide (μc-SiO$_x$:H) for applications in thin film silicon tandem solar cells, Can. J. Phys. 92
        (2014) 932-935.

List of other publications in the period of this study:

[1]   W. Böttler, V. Smirnov, A. Lambertz, J. Hüpkes, F. Finger, Front and back contacts for microcrystalline silicon solar cells in n-i-p configuration, 25th Eur. Photovolt. Sol. Energy Conf. Exhib. / 5th World Conf. Photovolt. Energy Convers., (2010) 3060-3063.

[2]   W. Böttler, V. Smirnov, A. Lambertz, J. Hüpkes, F. Finger, Window layer development for microcrystalline silicon solar cells in n-i-p configuration, Phys. Status Solidi C7 (2010) 1069-1072.

[3]   K. Ding, T. Kirchartz, B.E. Pieters, C. Ulbrich, S. Schicho, A. Lambertz, et al., Detailed Analysis of a-Si:H/μc-Si:H Tandem Solar Cell Characterization Data Using Numerical Simulation, Proc. 25th Eur. Photovolt. Sol. Energy Conf. Exhib., Valencia, Spain, (2010) 2908-2914.

[4]   M. Gunes, R.E. Johanson, S.O. Kasap, F. Finger, A. Lambertz, R.E.I. Schropp, The effect of aging on the dark conductivity and 1/f noise in hydrogenated microcrystalline silicon thin films, Phys. Status Solidi C7 (2010) 658-661.

[5]   J. Üpping, A. Bielawny, S. Fahr, C. Rockstuhl, F. Lederer, L. Steidl, et al., Micromorph silicon tandem solar cells with fully integrated 3D photonic crystal intermediate reflectors, R.B. Wehrspohn, A. Gombert (Eds.), Proc. SPIE 7725, Photonics Sol. Energy Syst. III (2010) 77250K-1 - 77250K-7.

[6]   J. Üpping, A. Bielawny, C. Ulbrich, M. Peters, J.C. Goldschmidt, L. Steidl, et al., 3D photonic crystals for photon management in solar cells, G.S. Subramania, S. Foteinopoulou (Eds.), Proc. SPIE 77560, Active Photonic Materials III (2010) 77560A-1 - 77560A-13.

[7]   K. Ding, T. Kirchartz, B.E. Pieters, C. Ulbrich, A.M. Ermes, S. Schicho, et al., Characterization and simulation of a-Si:H/μc-Si:H tandem solar cells, Sol. Energy Mater. Sol. Cells 95 (2011) 3318-3327.

[8]   S. Haas, A. Bauer, A. Lambertz, U. Rau, Innovative series connection concept for thin-film silicon solar modules, 26th Eur. Photovolt. Sol. Energy Conf. Exhib. (2011) 2375-2378.

[9]   C. Ulbrich, C. Zahren, J. Noll, A. Gerber, K. Hermans, A. Lambertz, et al., Analysis of the Short-Circuit Current Gains by an Anti-Reflective Texture Coating on Silicon Thin-Film Solar Cells, Proc. 26th Eur. Photovolt. Sol. Energy Conf. Exhib. (2011) 2329-2335.

[10]   C. Ulbrich, A. Gerber, K. Hermans, A. Lambertz, U. Rau, Analysis of short circuit current gains by an anti-reflective textured cover on silicon thin film solar cells, Prog. Photovoltaics Res. Appl. 21 (2012) 1672-1681.

[11]   A. Hoffmann, U.W. Paetzold, T. Merdzhanova, A. Lambertz, O. Höhn, C. Ulbrich, et al., Spectrally selective intermediate reflectors for tandem thin-film silicon solar cells, Proc. SPIE 8823, Thin Film Sol. Technol. V (2013) 882305-1 - 882305-8.

[12] S. Michard, V. Balmes, M. Meier, a. Lambertz, T. Merdzhanova, F. Finger, Microcrystalline silicon absorber layers prepared at high deposition rates for thin-film tandem solar cells, EPJ Photovoltaics 4 (2013) 45201-p1 - 45201-p6.

[13] E. Moulin, U.W. Paetzold, K. Bittkau, M. Ermes, L. Ding, L. Fanni, et al., Thin-film silicon solar cells applying optically decoupled back reflectors, Mater. Sci. Eng. B. 178 (2013) 645-650.

[14] C. Zhang, M. Meier, A. Lambertz, V. Smirnov, A. Gordijn, T. Merdzhanova, Development of p-Type μc-SiO$_x$:H for Thin-Film Silicon Solar Cells on Sputtered ZnO:Al, Proc. 28st Eur. Photovolt. Sol. Energy Conf., WIP Renewable Energies, Paris, France, (2013) 2554-2557.

[15] C. Zhang, M. Meier, A. Lambertz, V. Smirnov, B. Holländer, A. Gordijn, et al., Optical and Electrical Effects of p-type μc-SiO$_x$:H in Thin-Film Silicon Solar Cells on Various Front Textures, Int. J. Photoenergy (2014) 1-10.

[16] K. Ding, U. Aeberhard, A. Lambertz, V. Smirnov, B. Holländer, F. Finger, et al., Impact of doped microcrystalline silicon oxide layers on crystalline silicon surface passivation, Can. J. Phys. 92 (2014) 758-762.

[17] V. Smirnov, A. Lambertz, F. Finger, Bifacial microcrystalline silicon solar cells with improved performance due to μc-SiO$_x$:H doped layers, Can. J. Phys. 92 (2014) 913-916.

[18] F. Urbain, K. Wilken, V. Smirnov, O. Astakhov, A. Lambertz, J.-P. Becker, et al., Development of Thin Film Amorphous Silicon Tandem Junction Based Photocathodes Providing High Open-Circuit Voltages for Hydrogen Production, Int. J. Photoenergy 249317 (2014) 1-10.

[19] A. Hoffmann, U.W. Paetzold, C. Zhang, T. Merdzhanova, A. Lambertz, C. Ulbrich, et al., Advancing tandem solar cells by spectrally selective multilayer intermediate reflectors, Opt. Express. 22 (2014) A1271-A1277.

[20] M. Bär, D.E. Starr, A. Lambertz, B. Holländer, J.-H. Alsmeier, L. Weinhardt, et al., Microcrystalline silicon oxides for silicon-based solar cells: impact of the O/Si ratio on the electronic structure, Proc. SPIE 9177, Thin Film. Sol. Energy Technol. VI (2014) 91770E-1 - 91770E-3.

Patent applications

[1]   A. Lambertz, S. Haas, Method for the production and series connection of strip-shaped elements on a substrate, WO2011000361A2.

[2]   V. Smirnov, A. Lambertz, F. Finger, Method for producing a solar cell, and a solar cell, WO2012072065A2.

[3]   A. Lambertz, S. Haas, Method for the production and series connection of photovoltaic elements to a solar module a solar module, WO2010127656A2.

[4]   A. Lambertz, S. Bergfeld, Cleaning of surfaces in vacuum apparatuses using laser, WO2012072475A2.

Acknowledgements

Curriculum vitae

Andreas Lambertz was born on December 6th, 1968 in Opladen, Germany. Between 1985 and 1990, he completed an apprenticeship at the Bayer AG as process control technician. He attended the Berufskolleg Opladen and obtained a vocational diploma. In 1995, he completed a Diplom Ingenieur in applied physics at the Aachen University of Applied Science. The title of his diploma thesis was "Design of a Pump Test System for Solar Water Pumps", and the work for this thesis was carried out at Curtin University in Perth, Australia.

In 1996, he started his work on thin-film silicon solar cells at the Forschungszentrum Jülich. During this time, he received a year-long DAAD scholarship to work as research fellow at the University of New South Wales, Australia in the Group of Prof. Martin Green. In this time, he has worked on solid phase crystallized silicon for solar cell applications and completed the university course "High Efficiency Silicon Solar Cells". Following his return to Forschungszentrum Jülich, he has published more than 10 papers and 4 Patent applications on thin-film silicon solar cells, has been a research fellow at the Indian Association for the Cultivation of Science, Energy Research Unit, Kolkata/India and Korean Institute of Energy Research, Deadeok/Korea and has done consultancy work for several companies. His focus since he has started his work at the Forschungszentrum Jülich is the development of thin-film silicon solar cells and related materials at the 6-Chamber PECVD deposition system.